Trailing-Edge Blowing of Model Fan Blades for Wake Management

Margaret Elizabeth Craig

Thesis submitted to the faculty of the Virginia Polytechnic Institute and State University
in partial fulfillment of the requirements for the degree of

Master of Science
in
Aerospace Engineering

William J. Devenport, Chair

Joseph A. Schetz

Roger L. Simpson

December 2005
Blacksburg, Virginia

Keywords: aircraft engine, hot-wire, linear cascade, tone noise

Trailing-Edge Blowing of Model Fan Blades for Wake Management

Margaret Elizabeth Craig

ABSTRACT

Model fan blades designed to implement the wake management technique of trailing-edge blowing were tested in a linear cascade configuration. Measurements were made on two sets of blowing blades installed in the Virginia Tech low-speed linear cascade wind tunnel. The simple blowing blades were identical to the baseline GE Rotor B blades, aside from a slight difference in trailing-edge thickness, a set of internal flow passages, and a blowing slot just upstream of the trailing-edge on the suction side of the blade. The Kuethe vane blades were also slightly thicker at the trailing-edge, and had a set of nine evenly spaced vortex generators upstream of the blowing slot on the suction side. The cascade tunnel accommodates eight blades with adjustable tip-gap heights, although only the center four blades were replaced by blowing blades in this study. The tunnel has an inlet angle of 65.1°, a stagger angle of 56.9° and a flow turning angle of 11.8°. The tip-gap was set to 0.004125*c* and the freestream velocity of 24.7m/s led to a Reynolds number based on the chord of 385,000.

Blowing slot uniformity measurements made with a single hot-wire immediately behind the trailing-edge revealed that the blowing becomes more spanwise uniform as blowing rate is increased. The same occurs with the Kuethe vane blades, despite a spanwise serrated pattern that appears as a result of the upstream vortex generators.

Cross-sections made perpendicular to the blade span gave preliminary evidence that the simple blowing wake deficit increases from the passive suction case at a blowing

rate of 1.4% and becomes overblown by 2.6%. The Kuethe vane wake deficit does not increase at low blowing rates. Both sets of blowing blades indicated a slight angling of the wake towards the pressure side with blowing.

Pitot-static full cross-sections of the simple blowing blades at $x/c_a = 0.839$ and 1.877 verified the increase in wake depth and width at 1.4% as compared to the passive suction and non-blowing baseline cases, and the wake overblowing that occurs as blowing rate is increased to approximately 2.6%. The Kuethe vane blades only achieve partial wake cancellation at the maximum tested rate of 2.6% for these measurements.

The results of the baseline study of Geiger (2005) are used for comparison with the mid-span velocity profiles made at four downstream locations. The velocity profiles clearly confirm the results of the normal-to-span and full cross-sections, while also revealing a decrease from the baseline of at least 25% in most of the maximum Reynolds normal stresses and turbulent kinetic energies at all rates between 1.4% and 2.7% for both sets of blowing blades. Spectral measurements of the simple blowing blades show clear reductions of the energy in the wake for all blowing rates over the majority of the range of normalized frequencies, while the Kuethe vane blades show reductions at all rates and all frequencies.

By performing Fourier decompositions, the tone noise benefits over the non-blowing baseline blades are directly comparable in decibels. The optimum blowing rate for the simple blowing blades is clearly 2.5%, since this rate shows the most potential tone noise reduction. The Kuethe vane blades suggest decreases in tone noise over all of the tested blowing rates.

ACKNOWLEDGEMENTS

Most importantly, I thank the members of the Advanced Turbulent Flow Research Group – past and present – as well as those students and friends who have made my graduate work a much more pleasurable experience: Aurelien Borgoltz, Derek Geiger, Nicolas Spitz, Ben Smith, Josh Staubs, Dustin & Kathy Grissom, Nanya Intaratep, JV Larssen & Beatriz Díaz Acosta, Sumit Vasudeva, Laurent Mounaud, Amy Linklater, Luca Maddalena, Deirdre Hunter, and Sterling Hatcher. Many thanks to all of the people of the Aerospace & Ocean Engineering Department: Gail Coe, Betty Williams, Luke Scharf, Bruce Stanger, James Lambert, and Steve Edwards. I would like to recognize the members of my committee: Dr. Roger Simpson, Dr. Joseph Schetz, and especially Dr. William Devenport, for always believing, or at least appearing as such, that this research could be accomplished. I would also like to thank Dr. Brian Fite and Dr. Edmane Envia at NASA-Glenn for their support of this work through Grant NCC3-1026. I am extremely grateful to my parents, Jim and Thelma Craig, for having faith in me and my decisions for the last 23 years, and to my future husband Don Knize, for, well, everything.

TABLE OF CONTENTS

NOMENCLATURE

Roman

c	Total chord of blade
c_a	Axial chord of blade
C_p	Static pressure coefficient
C_{p0}	Total pressure coefficient
dS	Differential blade length
f	Spectral frequency
G_{uu}, G_{vv}, G_{ww}	Spectral functions in the three velocity directions
k	Turbulent kinetic energy
$\bar{k}$	Pitchwise-averaged turbulent kinetic energy
L_w	Standard wake half-width
$L_{u'}$	Wake half-width based on u'^2
P	Static pressure
P_b	Tunnel back pressure
P_∞	Freestream static pressure
P_0	Total pressure
$P_{0\infty}$	Freestream total pressure
u', v', w'	Fluctuating velocity components in wake-aligned coordinate system
u'^2, v'^2, w'^2	Time-averaged Reynolds normal stresses

$u'^3, v'^3, w'^3, u'v'^2, v'u'^2, v'w'^2, w'v'^2, u'w'^2, w'u'^2, u'v'w'$

	Time-averaged triple products
$\overline{u'^2}$	Pitchwise-averaged Reynolds stress
$u'v'$, $v'w'$, $-u'w'$	Time-averaged Reynolds shear stresses
U, V, W	Time-averaged mean velocity components in wake-aligned coordinate system
$\overline{U(x,t)}$	Mean velocity in the direction of wake propagation
U_e	Edge velocity of the wake
U_w	Standard velocity deficit, or square root of u'^2
U_{w-}	Maximum velocity deficit for blowing blades
U_{ref}	Reference freestream velocity
x, y, z	Blade row-aligned coordinate system, origin at trailing-edge of blade five
X, Y, Z	Wake-aligned coordinate system, origin at the trailing-edge of blade five

Greek

δ	Boundary layer thickness
δ^*	Displacement thickness
Γ	Circulation
θ	Momentum thickness

LIST OF TABLES

LIST OF FIGURES

1. INTRODUCTION

1.1. Aircraft Noise Restrictions

Air traffic has more than doubled over the past two decades, which is prompting an international effort to tighten noise regulations for aircraft (Krammer *et al*, 2003). The Advisory Council for Aeronautics Research in Europe (ACARE) has projected a 15dB cumulative reduction from today's standards by 2010, while NASA's Aerospace Technology Enterprise (ATE) is aiming for a 25dB reduction by the same year (Krammer *et al*, 2003). Over the next twenty years, the number of people exposed to aircraft noise disturbances will increase tremendously as more communities are built surrounding airports (Thomas *et al*, 2004). By this time, ACARE and ATE are hoping for 40dB and 75dB cumulative reductions respectively (Krammer *et al*, 2003). To achieve these goals, all engine noise sources must be examined for possible alterations that could assist in noise reduction.

1.2. Fan Noise Sources and Noise Reduction Techniques

The dominant source of noise in high-bypass ratio engines is the unsteady loading on the stators due to the wakes shed by the rotors (Figure 1-1). This unsteadiness in the flow consists of two parts: unsteadiness that is either periodic or non-periodic on the blade-passing period. The periodic unsteadiness causes unsteady pressures on the stators at multiples of the blade-passing frequency (BPF), which produces what is referred to as tone noise. The non-periodic unsteadiness is largely due to turbulence and is the leading source of broadband noise. Both tone noise and broadband noise contribute to the overall noise produced by turbofan engines ("Making Future Commercial Aircraft Quieter", 1999).

Fan noise reductions have been obtained over the last few decades by noise source control, including variation of rotor-stator blade count and variation of rotor-stator spacing to weaken the wakes. Multiple acoustic treatments, such as acoustic liners, have also served to reduce noise from fan sources. In 1992, NASA, the FAA, and the United States aerospace industry began the Advanced Subsonic Technology Noise Reduction Program (AST program) to conduct engine noise reduction research. The goal was a 6 EPNdB, or Effective Perceived Noise dB, reduction in engine source noise relative to 1992. The fan noise reduction portion of this program looked at new noise reduction techniques, including low-noise fan stage design, sweep and lean of the outlet guide vanes, active noise control, and wake management methods.

Pratt and Whitney built a model fan stage called the Advanced Ducted Propulsor (ADP) in order to study the possibility of achieving the 6 EPNdB reduction of the AST program. Sweep and lean of the outlet guide vanes showed potential noise reductions of up to 10dB at the exhaust (Envia, 2001). The active noise control method used actuators embedded in the surface of the engine casing or in the vanes to create an acoustic field of equal amplitude and opposite phase of the field produce by the engine. This method produced noise reductions of 18dB on average over a range of fan tip speeds (Envia, 2001).

The most recent studies on wake management of fan blades involves the injection of mass at the trailing edges to essentially “fill in” the wake deficit to create uniform flow into the stators. According to Sutliff *et al* (2002), this “trailing-edge blowing” technique produces noise reductions up to 12.4dB.

1.3. Wake Management

As mentioned above, wake management is the idea of altering the wakes shed by the upstream fan blades to affect the uniformity of the flow entering the downstream stator vanes. Due to limitations in aircraft engine sizing and weight, the spacing between the fan and the stator vanes is typically a distance of a few axial chords. The velocity deficit in the wake shed by the fan impinges upon the stator, serving as the major source of rotor-stator interaction. The trailing-edge blowing technique is thought to reduce this wake deficit before entering the stator row.

1.4. Previous Wake Management Research

Experimental research has been done on the topics of two-dimensional momentumless wakes and trailing-edge blowing. These studies have been done on flat plate airfoils, model aircraft engines and wind turbines. In the following sections, a review of these studies will be presented.

1.4.1. Experimental Studies of Momentumless Wakes

The most fundamental research on momentumless plane wakes was done by Cimbala and Park (1990). They studied pure wake (no injection), weak wake (injection insufficient to cancel the model drag), momentumless wake (enough injection to cancel the drag), and weak-jet (more injection than necessary to cancel the drag) effects on a flat plate airfoil with a rounded leading-edge and a blunt trailing-edge. The airfoil had an 89mm chord and a 965mm span. A narrow slit covering 80% of the total model span was located at the trailing-edge to allow for wake injection. Measurements were performed in a 0.3m by 0.97m cross-section low-turbulence test section with a freestream velocity of 4.2m/s. Single-sensor and dual-sensor hot-wire measurements, as well as smoke-wire flow visualization, were performed on all four types of wakes. From the flow visualization, Cimbala and Park found that the pure and weak wakes had Kármán-type vortex structures within a defined wake structure, whereas the momentumless and weak-jet wakes had wake-like structures at the edges of the wakes but were disorganized compared to the pure and weak wakes. The pure and weak wakes spread downstream with a wake scale that doubled in size, whereas the weak-jet wake spread at a slower rate while still containing eddy scales that doubled in size. The momentumless wake was observed to essentially decay downstream, containing only small eddy fluctuations. From the single hot-wire mean velocity measurements, the centerline velocity deficit (the difference between the freestream velocity and mean centerline velocity) of the momentumless wake decayed rapidly ($U_d \sim x^{-0.92}$) and had a slow spreading rate ($l \sim x^{0.30}$). In comparison, the pure wake had a slower velocity decay ($U_d \sim x^{-0.50}$) and a faster spreading rate ($l \sim x^{0.50}$). The mean shear of the momentumless wake essentially disappears downstream, and the flow becomes isotropic about 45 model diameters downstream. The turbulence behavior is more similar to that of grid turbulence rather than plane or pure jet wakes. It was also observed that mean velocity profiles were extremely sensitive to small mismatches of momentum injection and to misalignment of the model with the freestream.

Jet-injection geometry for momentumless wakes was further examined in Park and Cimbala (1991). The experimental setup was identical to that of Cimbala and Park (1990) except that three different model configurations were studied: a central single-jet injection model, an asymmetric single-jet injection model, and a dual-jet injection model. From smoke-wire flow visualization, it was observed that the wake of the central jet contained random features, while the other two models produced more organized, wavy flow patterns. The dual-jet configuration created a flapping effect in the wake cause by the merging of the upper and lower jets. This flapping effect was possibly enhanced by the interaction of the jets with the Kármán vortex shedding. The mean velocity profile of the dual-jet was similar to that of the central jet, but the profile of the asymmetric wake contained both jet-like and wake-like components while still maintaining the properties of a momentumless wake. The mean velocity deficit decayed faster for the dual-jet ($U_d \sim x^{-2.02}$) than for the asymmetric jet ($U_d \sim x^{-1.24}$) and the central jet ($U_d \sim x^{-0.92}$). Similarly, the spreading rate of the dual-jet ($l \sim x^{0.46}$) was more rapid than that of the asymmetric jet ($l \sim x^{0.36}$) and the central jet ($l \sim x^{0.30}$). For all momentumless wake configurations, it was observed that wake turbulence levels decay more rapidly and the wake width grows more slowly when compared to conventional wakes. The authors determined that the far-field mean velocity profiles and turbulence intensities were strongly dependent on the jet injection configuration of the models.

Other studies of momentumless wakes were done by Takami and Maekawa (1997) and Cherepanov and Babenko (1998). Similar to the study of Cimbala and Park (1990), Takami and Maekawa (1996) examined momentumless wakes for a flat plate. The hot-wire measurements showed the same results as Cimbala and Park (1990), especially for the turbulence intensity levels, the downstream decay of turbulence, and the isotropy of the turbulence. Cherepanov and Babenko (1998) completed a study of the momentumless wake from an airfoil. The model had a span of 74.0mm and a chord of 100.0mm. Measurements were performed in an 82.0mm square test section. The results were compared with other previous studies of momentumless wakes, including Cimbala and Park (1990). They observed that the decay rate of the mean velocity deficit was greater than that of the turbulence intensities. Turbulence models have been developed by Dmitrenko *et al* (1987) for wakes with zero excess momentum and by Ahn and Sung (1995) for momentumless wakes with coexisting wakes and jets.

1.4.2. Experimental Studies of Trailing-Edge Blowing in Blade Rows

Sell (1997) made profile measurements downstream of a two-dimensional linear cascade with trailing-edge blowing. He determined that the blowing could significantly fill the wake while also lowering turbulence levels within it. For a mass through-flow rate of 1.08%, the wake momentum thickness was reduced by 100%, the wake depth by 67%, the wake width by 6.85%, and the maximum turbulence levels by 44.5%. He estimated that these effects would result in tone noise reductions of 8.0dB to 24.4dB and broadband noise reduction of 7.0dB.

Brookfield (1998) and Brookfield and Waitz (2000) studied the trailing-edge blowing technique while also examining the difficulties associated with applying the technique to a model fan. The 558.8mm model had 16 fan blades with holes drilled in the trailing-edges, 40 stator blades, a separation between the blade rows of 1.7 chords, and a hub-to-tip ratio of 0.5. The fan tip speed was 265.2m/s. At a blowing rate of less than 2.0% mass through-flow, unsteady surface pressure measurements were made on the surface of the stator blades, and microphone measurements were made at 1.0 and 1.5 axial chords downstream of the rotors. The slight change in geometry of the blowing rotor blades did not cause a significant variation in performance from the solid baseline blades. The blowing was found to fill the wake profiles and reduce the turbulence levels within them, ultimately reducing tone noise levels by 10dB. It was concluded that significant noise reductions could be achieved by trailing-edge blowing while maintaining a given rotor-stator spacing.

Sutliff *et al* (2002) investigated the tone noise benefits of trailing-edge blowing on the 1.2m Active Noise Control Fan (ANCF) at NASA Glenn's Aero-Acoustic Propulsion Laboratory (AAPL). These are currently the only known acoustic measurements made on a realistic fan. The rotor had 16 blades with a tip-turning of 15° and the stator row had 14 blades. The tip speed was 129.5m/s with a blade-passing frequency (BPF) of 500Hz. The rotor blades had narrow internal passages which were supplied with air from an external plenum. Sutliff *et al* tested three different blowing configurations: no blowing (where the trailing-edges were fixed with inserts to eliminate vortex shedding or flow separation due to bluntness), self-blowing of 0.6% mass through-flow (blowing was induced by the pressure difference between the trailing-edges and the plenum), and blowing rates between 0.5% and 2.0% fan mass through-flow at fan speeds of 25Hz to 31.6Hz. Measurements were made with two-component hot-wires at one axial chord downstream of the rotors at 15-25 radial locations. Other measurements included unsteady stator surface pressure measurements by mounting three stator blades with 30 microphones each, mapping of ducted modes through the use of a rotating rake, and far-field acoustic measurements on the optimal blowing configuration with 28 microphones. From the hub to 50% span, the hot-wire measurements showed a reduction in the wake deficit for all three blowing cases. For the optimum blowing rate of 1.8% at 1BPF, the duct measurements predicted a tone noise reduction of 11.5dB at the inlet and an increase of 0.1dB at the exhaust. At 2BPF, the reductions were 7.2dB at the inlet and 11.4dB at the exhaust, and at 3BPF, the reductions were 11.8dB and 19.4dB. The far-field microphone measurements supported these findings. They measured noise reductions of 5.4dB at 1BPF, 10.6dB at 2BPF, and 12.4dB at 3BPF. Their results suggested that blowing may have broadband noise benefits, but that further study of this issue was needed.

Leitch *et al* (2000) used trailing-edge blowing on four 52.8mm stators located 0.75 chords upstream of an 18-blade 104.1mm turbofan simulator with 26 outlet guide vanes. The stators had six blowing holes located at the trailing-edges. Passive blowing measurements at fan speeds of 500Hz, 833.3Hz and 1166.7Hz were made in Virginia Tech’s 4.0m x 2.7m x 2.0m anechoic chamber. Pressure measurements across the fan face showed that the wakes of the stators could be filled with less than 1.0% of the total fan mass through-flow. Microphone measurements were made at 12 points from 0° to 110° on a circular arc 1.2m from the fan face. The maximum tone noise reduction was found to be 8.9dB tone noise at 80° for a fan speed of 500Hz. The average reduction was close to 6.2dB between 30° and 90°. At 833.3Hz and 1166.7Hz, the maximum reductions were 5.5dB and 2.6dB respectively. The higher fan speeds produced smaller maximum reductions, perhaps due to increased buzz-saw noise from the resulting higher tip speeds or due to insufficient injection from non-uniformity of the blowing holes.

Rao *et al* (2001) adapted the system used by Leitch *et al* (2000) into an active wake control system. The flow rate of each identically-sized blowing hole was monitored by a microelectro-mechanical system-based microvalve. This system could adjust the amount of injected air needed as a function of the fan speed so that the optimum blowing rate could be used automatically. They took similar measurements to those of Leitch *et al* (2000) at fan speeds of 491.7Hz and 666.7Hz. The maximum tone noise reductions were 8.2dB at 491.7Hz and 7.3dB at 666.7Hz. The noise reductions also decreased with increasing fan speed, as found by Leitch *et al* (2000).

Wo *et al* (2002) applied trailing-edge blowing to a low-speed compressor rotor with variable axial spacing. The compressor rotor had 60 upstream inlet guide vanes (IGV's), 58 rotors, and 60 stators, which all had a chord of 60.0mm. For this experiment, the spacing between the rotors and the stators was set to 30% chord and the IGVs were 1.75 chords upstream to provide room for the dissipation of the wake. The mass flow for blowing, which ranged from 1.3% to 3.7%, was injected through part-span slots near the mid-span of the trailing-edges.

Results of the pressure measurements showed that the development of the wake was dependent on the blade loading: the velocity deficit was not reduced at high blade loadings. Downstream measurements showed the expected velocity deficit reductions and a decrease in the traverse gust factor with the wake momentum defect factor. The stator unsteady force was found to decrease linearly with increased blowing momentum.

Corcoran (1992) and Naumann (1992) performed studies of a simulated turbofan blade with trailing-edge blowing in the 0.9m wide, 0.5m deep test section of a water channel using particle image velocimetry to obtain distributions of mean and fluctuating velocities and Reynolds stresses across the wake. The facility was capable of speeds up to 0.2m/s. Corcoran (1992) examined the wakes for single-slit and double-slit jet configurations at various blowing rates to determine the rate at which the wake deficit vanished. In Naumann (1992), a range of blowing rates for two trailing-edge configurations was examined while attempting to find the minimum blowing rate required for the maximum attenuation of the wake deficit, while still blowing at a rate less than necessary to achieve a momentumless wake. Jet velocities of two to four times the freestream velocity were required for successful attenuation. The author found that increased mixing in the near-wake region provided more effective attenuation of the velocity deficit and turbulence intensities. This mixing was created by discrete jet blowing rather than continuous blowing through slits, by vortex generators at the trailing-edge of the blades, or by a combination of both: discrete jet blowing with trailing-edge vortex generators was the most effective solution. Vortex generators were previously shown in Kuethe (1972) to increase mixing of the jet with the freestream in the wake region, which decreased the wake deficit and reduced turbulence levels.

1.5. Objectives for Study of Trailing-Edge Blowing

Despite the number of prior studies on trailing-edge blowing, a sufficient basis for the development of CFD codes to model this technique does not yet exist. A linear cascade configuration provides a practical arrangement to determine if trailing-edge blowing is a realistic solution for reducing the wake deficit of fan blades. The Virginia Tech Low-Speed Linear Cascade Tunnel was used for this study (Figure 1-2 (Ma, 2003)). The cascade tunnel blades are designed to simulate (at low speeds) the loading and flow generated by a subsonic high-bypass ratio aircraft engine fan at takeoff conditions. The cascade tunnel also provides a stationary frame of reference that can be measured more easily than the wake of a moving fan rotor. There are several other benefits to this configuration. Since the tunnel has no downstream stators, the exit turning angle of the blades does not have to be matched with the inlet angle of the stators. Also, the blades are not rotating, so there is no additional flow due to rotational forces. This allows the unaltered form of the wake to be studied.

The objectives of this study are as follows:

- To create an experimental database for blown wakes with realistic rotor blade geometries required for the development and testing of CFD codes
- To determine the practicality of trailing-edge blowing as a noise reduction solution
- To provide a basis for actual fan design

1.6. Previous Studies in the Virginia Tech Low-Speed Linear Cascade Tunnel

This cascade tunnel at Virginia Tech has been the location of multiple prior studies since 1996, when modifications were made to convert the tunnel from a turbine cascade configuration.

The first such study was made by Muthanna (1998), also reported in Muthanna *et al* (1998), in which basic properties of the flow were examined. Four-sensor hot-wires were used to measure the mean velocity field, the turbulence stress field, and velocity spectra at axial locations (x/c_a) of 1.366, 2.062, 2.831, 3.770 and 4.640 at tip-gap heights of 0.0165c, 0.0320c and 0.00825c. Oil flow visualizations were performed on the lower end-wall, tip-gap heights were varied, and boundary layer trip-strip positions were varied in order to study the tip-leakage vortex. It was found that the tip-leakage vortex is formed from the "rolling up" of the tip flow as it exits the tip-gap region. A secondary vortex is formed from the separation of the tip-gap flow off the end-wall. These vortices continue to develop as they move downstream, ultimately dominating the end-wall flow. The axial gradients in the vortices create the majority of the turbulence in this region. It was also found that wakes of the blades in this facility exemplify the properties of two-dimensional plane wakes.

Wenger *et al* (1998) and Wenger (1999) describe two-point hot-wire measurements taken at several locations in the blade wakes and tip-leakage vortices of the cascade tunnel. These measurements were made to calculate space-time correlations over a grid, which led to the conclusion that turbulence in the tip-leakage vortex is anisotropic and there are turbulent eddies along an axis 20° from the axis of the vortex. The helical shape of these eddies is a result of the large axial gradient present in the tip-leakage vortex. Because of the anisotropy of the turbulence, the correlation level seen by the downstream stators would likely depend on the engine operating speed and the configuration of the stators.

A moving end-wall was installed on the cascade tunnel to simulate the relative motion between the blade tips and the engine casing. Wang (2000) studied the effects of this motion on the tip-leakage vortex by making hot-wire measurements at axial locations (x/c_a) of 1.51, 2.74, and 3.75 at tip-gap heights of 0.0165*c*, 0.033*c*, and 0.0083*c*. The results (also shown in Wang and Devenport (2004)) were compared with those of Muthanna (1998) and Wenger (1999) for the stationary end-wall. The moving end-wall was found to reduce the strength of the tip-leakage vortex, while also altering its shape and direction. It does not affect the wakes of the blades.

Two-dimensional predictions based on Rapid Distortion Theory (RDT) were made by de la Riva (2001) (also presented in de la Riva *et al* (2004)) and compared with grid turbulence measurements of the flow in the cascade tunnel. Measurements were made at a tip-gap of 0.0165*c* with a stationary end-wall. Taking viscous effects into consideration, RDT calculations were able to show the general development of turbulent fluctuations in the cascade to within 10% of the measurements. As expected, RDT predictions in the near-wall region were less accurate, since blade-blocking effects were not modeled. A more detailed RDT model, including viscosity and blade-blocking effects, could more precisely model the turbulent flow.

Muthanna (2001, 2002) continued the study of Muthanna (1998) by taking hot-wire measurements at eight axial locations (x/c_a = 0.8 and 0.23 upstream, 0.27, 0.48, 0.77, 0.98 and 1.26 downstream) at a tip-gap of 0.0165*c* to inspect the tip-leakage vortex evolution downstream. The tip-leakage vortex appears at approximately 0.27 axial chords downstream, and its structure and behavior significantly change between axial locations of 0.77 and 0.98. The effects of grid-generated turbulence on the cascade flow were also studied, revealing a 4% decrease in blade loading and a 20% reduction in vorticity levels in the tip-leakage vortex. The path of the vortex was shifted by $0.05c_a$ towards the suction side of the blade at the trailing-edge due to the presence of the grid. This shift reduced the circulation of the vortex by 2.5%, while simultaneously increasing its size by about 30%. Results also found increased turbulence kinetic energy within the vortex around $x/c_a = 0.77$.

Ma (2003) studied the tip-leakage vortex downstream of the tunnel rotor blades, after attaching a set of triangular-shaped vortex generators to the moving end-wall to produce a periodic vortical inflow to represent the idealized flow from a set of upstream stator vanes. Three-component turbulence and pressure fluctuation measurements were made for tip-gaps of 0.0083c, 0.0165c, 0.022c and 0.033c at streamwise locations of 0.772 to 1.117 x/c_a. Measurements of the generated inflow showed a pair of asymmetric counter-rotating vortices existing in a 4.6% chord end-wall boundary layer. These vortices are nearly two orders of magnitude smaller than the tip-leakage vortices produced from the cascade tunnel's typical configuration. Single-point hot-wire measurements revealed that the vertical inflow alters the position and structure of the tip-leakage vortex, as well as its size and strength. These unsteady, yet periodic, effects were found to increase with tip-gap height. Two-point space-time correlation measurements were made to study the aperiodic fluctuations of the tip-leakage vortex. The author found that the aperiodic fluctuations produce organized large-scale structures and motions. Microphone measurements of pressure fluctuations verified the single-point and two-point hotwire measurements.

Motivated by the results of Ma (2003), unsteady pressure measurements were made by Mish (2003) on the suction and pressure sides of the two center cascade blades with an array of 24 sub-surface microphones. Vortex generators were also used in this experiment. Measurements were made at eight tip-gap heights between 0.00825c and 0.129c and phased-averaged with respect to the vortex generator positioning. Ma (2003) observed that the periodic fluctuations in the tip-leakage vortex increased with increasing tip-gap, suggesting that the tip-leakage vortex shedding with a periodic disturbance is influenced by the inviscid response of the blade. Unsteady pressure measurements by Mish (2003) found both inviscid and viscous responses, but that the inviscid response of the blade plays a major role in determining the tip-leakage vortex circulation.

The same vortex generators used by Ma (2003) were also used by Staubs (2005) for tip-gaps between 0.0083*c* and 0.129*c*. Tip blade loading measurements revealed that the minimum suction pressure coefficient increases linearly up to a tip-gap of 0.079*c*. Microphone measurements taken at the blade tip on both the suction and pressure sides found that the unsteady pressures at the blade tip are linearly related to the tip-gap height. Instantaneous pressure measurements at the tip showed that the inflow vortices stimulate the blade response, whether or not the vortex generators are present. Hot-wire measurements made in the tip-gap on the suction side found that the mass flux through the tip-gap is related to the pressure difference across the tip-gap.

Most recently, Geiger (2005) studied the effects of trailing-edge modifications for noise reduction made to the center four cascade blades. Four sets of serrated trailing-edge designs were studied at four downstream locations at a tip-gap of 0.0165*c*: 12.7mm serrations, 12.7mm serrations with trailing-edge camber, 25.4mm serrations, and 25.4mm serrations with trailing-edge camber. Blade loading was found to decrease with increasing serration size, but increase with the addition of camber. Pitot-static cross-sections revealed that peaks and valleys in the wake, which became less visible as the wake propagated downstream, represented the serrations. These cross-sections also showed that the structure of the tip-leakage vortex and the upper end-wall boundary layer were not altered by the presence of serrations. The hot-wire cross-sectional measurements showed that the streamwise velocity, turbulent kinetic energy, and turbulent kinetic energy production in the tip-leakage region were the same as those of the baseline GE Rotor B blades. Mid-span hot-wire cross-sectional measurements determined that the wake spreading rate and the velocity deficit decay rate increased with serration size. The addition of camber at the trailing-edge minimally improved these rates. The serrated blades were predicted to lead to a reduction in tone noise based on the improvement of these rates and the consequential reduction in periodic fluctuations in the wake. The wakes were also compared to the mean velocity and turbulence profiles of plane wakes. The blades with the smallest serrations and no camber best represented the self-similarity seen in plane wakes and in the baseline blades.

1.7. Thesis Organization

This thesis documents the results of an experimental study of trailing-edge blowing applied to a linear compressor cascade. Two sets of blowing blades were tested in this configuration. Chapter 2 includes a description of the apparatus and instrumentation used. It begins with a presentation of the wind tunnel facility, followed by the blowing system, set-up, and measurement techniques. Chapter 3 presents a brief examination of the non-blowing baseline flow, including various results of Geiger (2005). The results of the trailing-edge blowing are discussed and compared in Chapter 4. A conclusion of significant results can be found in Chapter 5, followed by an uncertainty analysis in the Appendix.

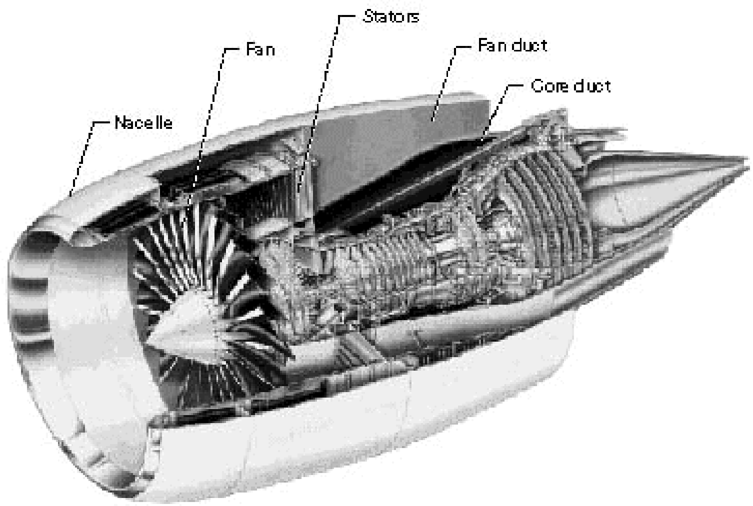

Figure 1-1: Model of aircraft engine from NASA's Quiet Aircraft Facts (1999)

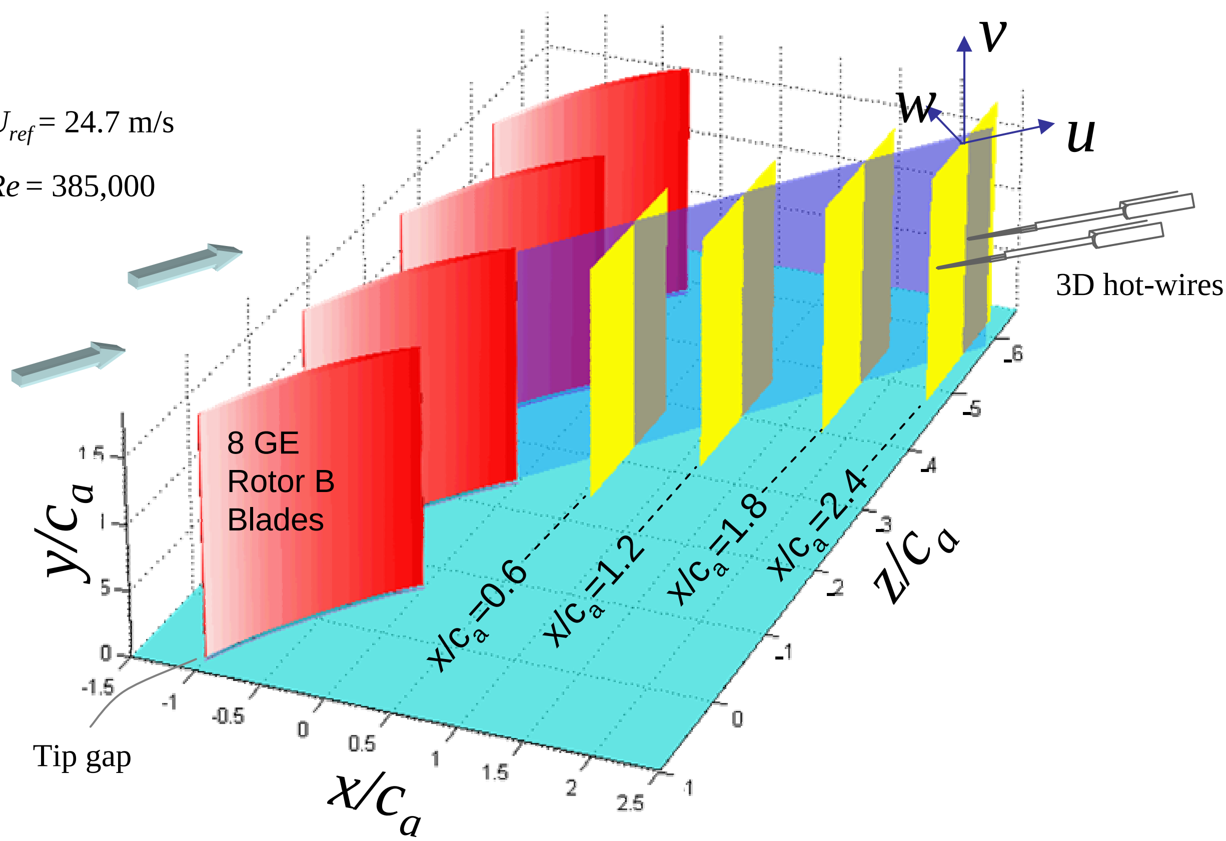

Figure 1-2: Orientation of cascade tunnel test section (Ma, 2003)

2. APPARATUS AND INSTRUMENTATION

This chapter presents a description of the facility and the modifications made for this experiment, as well as an explanation of the data acquisition equipment and techniques.

2.1. Virginia Tech Low-Speed Linear Cascade Wind Tunnel – Original Configuration

The low-speed linear cascade wind tunnel is an 8-blade (7-passage) linear compressor cascade facility that was converted from a turbine cascade in 1996 (Muthanna *et al*, 1998) (Figure 2-1). A moving end-wall system was added to simulate the relative motion between the blade tips and the engine casing (Wang, 2000). The tunnel configuration described in this section was used by Geiger (2005), whose results are used for comparison in the present study. This configuration was also used for the stabilizing pin testing, described in Section 2.2.2.

The tunnel is composed of two major sections: the upstream section and the test section. The upstream section includes the fan, diffuser, settling chamber, settling screens, and contraction. The test section includes the inlet section, blade row, blades, downstream section and the moving wall system.

2.1.1. Upstream Section

A 11.2kW AC motor with a diameter of 1.1m powers the centrifugal fan that supplies the flow to the test section of the tunnel. Flow from the fan then enters the diffuser and slows before reaching the settling chamber (Figure 2-2). The diffuser and settling chamber have a combined length of 4.3m, and the ratio of the cross-sectional area of the fan exit to that of the settling chamber is approximately 1:2.9. At the end of the settling chamber, the flow reaches a set of screens spanning the entire cross-section. The purpose of these screens is to reduce turbulence entering the test section. Finally, the flow passes through a contraction of 6.43:1, before reaching the test section inlet (Figure 2-3).

2.1.2 Test Section

2.1.2.1 *Inlet Section*

The inlet section begins at the exit of the contraction (Figure 2-4 and 2-1). It has a width of 762mm and a height of 305mm. The long side-wall is 2.4m in length and the short side-wall is 0.9m long, up to the location of the boundary layer suction slots. The walls are at an angle of 24.9° with respect to the blade row.

The boundary layer suction slots are located 187.6mm axially upstream of the blade row, on both the upper and lower end-walls. Each slot has a height of 25.4mm and serves to remove the boundary layer from the tunnel before the flow reaches the blade row. The new, smaller boundary layer that enters the blade row is tripped by a 2.4mm square metal rod attached to the lower end-wall about 7mm axially downstream of the suction slot leading-edge (Figure 2-5 and 2-1).

The boundary layer suction slot on the lower end-wall does not adequately remove the boundary layer on its own. To resolve this problem, an additional boundary layer bleed is located upstream of the suction slot, 483mm from the contraction section exit. The boundary layer bleed is a rectangular piece of perforated stainless steel, measuring 762mm (the entire width of the inlet section) by 63.5mm in length (Figure 2-6 and 2-1). An estimated 8% of the flow is removed through the bleed (Muthanna, 2002).

The freestream velocity in the inlet, U_{ref}, is a nearly constant 24.7m/s, leading to a Reynolds number based on the chord of about 385,000. According to Muthanna (2002), the inflow velocity measured at -0.80 x/c_a from the leading edge line is $0.993U_{ref}$. The streamwise turbulence intensity in the freestream, $\sqrt{\frac{u'^2}{U_{ref}}}$, is 0.2%.

2.1.2.2 *Blade Row*

The blades are housed in a 1.9m by 0.2m aluminum superstructure that is bolted to the top of the tunnel frame. Each of the eight blades is fixed to the superstructure by two 9.5mm diameter bolts. The blades are lowered into position through a partial 6.4mm thick Plexiglas roof and the superstructure is bolted to the frame while resting upon shims of a height appropriate for the desired tip-gap setting (Figure 2-7). The tip-gap for the original configuration used by Geiger (2005) was 0.0165*c*. Four 6.4mm diameter Allen bolts are then used to adjust the sweep and pitch of the blades, and to make minor adjustments in the tip-gap height at both the leading- and trailing-edges. The blade spacing is 236.0mm and the blade height inside the tunnel is nominally 254.0mm less the tip-gap.

Once the blades have been properly positioned, blade root covers are installed to partially seal the openings in the Plexiglas roof where the blades were inserted. The blade roots covers, made of 0.5mm thick galvanized steel, are 76.2mm by 342.9mm (Figure 2-8). They were taped to the inside surface roof, maintaining an approximately 1mm gap between the blade and cover on both the suction and pressure sides of the blade. This gap was necessary to minimize mass flow out of the roof openings, in order to match the CFD tunnel configuration being used by NASA.

Side-wall boundary layer scoops are found at each end of the blade row (Figure 2-9 and 2-1). The boundary layer escapes through the gap between these adjustable aluminum panels and the surface of blades one and eight. For this study, the gaps were set to 38.1mm and 41.3mm at the top and bottom for the long side-wall scoop and 28.6mm and 30.2mm for the short side-wall scoop.

The positioning of the blade row corresponds to a stagger angle of 56.9° and an inlet angle of 65.1°.

2.1.2.3 *Baseline Blades*

The baseline blades for this tunnel are General Electric Rotor B blades (Figure 2-10), which are 4% thick modified circular arc sections designed by Wisler (1977, 1981) for the third stage of an aircraft engine core compressor. The work of Moore *et al* (1996) concluded that the loading experienced by these compressor blades in this facility is similar to that seen near the tip of a subsonic aircraft engine fan at takeoff. All eight baseline blades are made of aluminum and have rounded leading- and trailing-edges. The total chord (c) is 254mm, the axial chord (c_a) is 138.7mm, the total span is 279mm, and the maximum thickness is approximately 10.9mm at 60% chord. The blade profile coordinates and a plot of the profile are shown in Figures 2-11 and 2-12. Spanwise boundary layer trip strips can be found 25.4mm from the leading-edge on both the suction and pressure sides of each blade. These 6.4mm-wide strips were created from double-sided tape, one side covered with 0.5mm diameter glass beads.

2.1.2.4 *Downstream Section*

Downstream of the blade row, the direction of the flow is adjusted by Plexiglas tailboards (Figure 2-1). The upstream ends of the tailboards are clamped to blade one on the short side and blade eight on the long side. The downstream ends extend past the tunnel exit. Once properly angled to 11.8° (determined by Ma (2003) to be the proper turning angle of this facility), the tailboards are clamped in position to the upper end-wall. This creates a 3mm gap to allow for the passage of the moving wall.

The upper end-wall is divided into two sections (Figure 2-13). The section adjacent to the blade row is an easily removable and replaceable piece of 12.7mm thick foamboard. Continuous slots are cut into the foam so that probes can be traversed to the desired locations for data acquisition. Different foamboard sections are used for different traverse paths. The edges of this roof section are cut such that it is flush with the existing tunnel roof sections when installed and taped into place. The roof section downstream of the foamboard is a permanent 6.4mm thick piece of Plexiglas. No probes were placed in this section in this experiment.

The back pressure in the tunnel is measured by three 0.8mm diameter pressure ports imbedded into the lower end-wall, 127mm upstream of the tunnel exit plane (Figure 2-1). The average pressure read by these ports was monitored with a Dwyer Series 475 Mark III hand-held digital manometer. Two framed screens can be clamped and taped into place across the exit plane to control the back pressure. Several strips of 25.4mm-wide duct tape were attached to the outer screen to increase the blocked area, and consequently the back pressure (Figure 2-14 and 2-1).

2.1.3. Moving Wall System

A moving end-wall was added to the tunnel configuration by Wang (2000) to simulate the relative motion between the blade tips and an engine casing. A 0.3mm thick belt of Mylar runs underneath the blades and around the entire lower end-wall on two rollers (Figure 2-15). The belt speed can be adjusted to within 1% of the desired speed. The moving wall was not used in the present work or the work of Geiger (2005), so the Mylar was removed and the Teflon beneath it served as the lower end-wall. The moving wall system is described in detail by Wang (2000) and Ma (2003).

2.2. Virginia Tech Low-Speed Linear Cascade Wind Tunnel – Modified Configuration

To implement the trailing-edge blowing, the center four cascade blades (blades three through six) were replaced with one of two sets of rapid-prototyped blowing blades.

A blowing system was developed in order to supply equal amounts of air to the blowing blades. The main components are a blower, a plenum, four nozzles, the two sets of four blowing blades, and a small air conditioner. The blower sends the required amount of air through delivery tubing to the plenum, where it is equally divided among four delivery pipes to the four nozzles attached to the root of the four center blades in the tunnel. Each blade had internal passages allowing air to be expelled from the trailing-edge.

A set of stabilizing pins were added to the tips of the new blades, which required a reduction of the tip-gap height.

2.2.1. Blowing System

2.2.1.1. *Blower*

A variable speed Cincinnati Fan Model HP-4C17 high pressure blower was installed outside of the tunnel, adjacent to the diffuser (Figure 2-16). It is powered by a 3.7kW Baldor industrial motor, model M3613T. It has a pressure rating of 5480.0Pa for 0.1m^3/s, which is the condition at a blowing rate of 2.6%. A section of 152.4mm diameter flexible tubing connects the blower to the plenum.

2.2.1.2. *Plenum*

A 152.4mm-diameter PVC pipe 1.4m in length served as the plenum (Figure 2-17). Four 50.8mm (outer diameter) PVC delivery pipes extend 330.2mm from the center of the plenum. Each pipe is connected to the 50.8mm diameter inlet of one of the four nozzles by a 0.5m section of 50.8mm (inner diameter) Tygon tubing (Figure 2-18). The tubing was selected because hose clamps could be used at both ends to eliminate any flow leakage, but the material was flexible enough that when lubricated with grease, the thin plastic of the nozzle entrance area was not damaged. Numerous small holes were drilled in the delivery pipes to alter the pressure so that the desired mass flow would reach each individual nozzle. Each pipe also contained a 76.2mm long section of 6.4mm diameter aluminum honeycomb fitted to the pipe exit to eliminate any swirling of the flow into the nozzles.

2.2.1.3 *Nozzles and Calibration*

Four nozzles were manufactured specifically for the blowing blades by NASA-Glenn using rapid-prototyping techniques (Figures 2-19, 2-20 and 2-21). The nozzles connected the air delivery pipes to the internal passage inlet at the root of each blowing blade. Each nozzle has a circular inlet area of 8100mm^2 and a roughly rectangular exit area of approximately 700mm^2. Scanned images of the nozzle exit and blade passage inlet were traced and overlaid by alignment of the attachment holes to compare their shapes, seen in Figure 2-22. It is apparent that the two traces are not identical, and thus small steps would have been present at the nozzle exit when the system was assembled. The length of the nozzle exit area is 103.9mm, but the length of the corresponding blade passage inlet is 102.6mm. Otherwise, the differences are less than 1mm. The nozzles were connected to the roots of the four center blades with four 4.8mm diameter screws each. Any potential flow leaks at this interface were sealed with silicone sealant.

In addition to ducting the airflow into the blade passages, the nozzles also provide a means to monitor the mass flow. Eight pressure taps were mounted in each nozzle: four equally spaced around the circular inlet, and four around the nozzle outlet (Figure 2-20). A Dwyer Series 475 Mark III hand-held manometer was used to read the pressure difference across each nozzle (the difference between the average of the four inlet and four outlet pressure taps), which was related to the total mass flow through the nozzle using a calibration performed before the installation of the blowing system in the tunnel. Since the nozzles were not completely identical, the calibration had to be performed separately on each nozzle by making measurements with a Dwyer Instruments Standard Model 160 Pitot-static Probe (Model 167-12, 304.8mm shaft length, 76.2mm tip length) over a grid of points covering the exit area as a function of flow speed. A coarse grid was used for 14 different blower speeds, equivalent to pressure differences in the range of 12.5Pa to 622.7Pa. The coarse grid included a point in the center of the passage at 11 locations across the passage (Figure 2-23). At three locations, two additional points were taken both above and below the center of the passage for a total of 23 points and a more complete mass flow calculation. At the time the nozzle calibrations were performed, it was assumed that a 2.7% mass flow rate was to be the focus of this study. In order to have the most accurate mass flow calculation, a fine grid was used at three pressure differences in the vicinity of 124.5Pa, which roughly corresponds to 2.7%. The fine grid included points along the passage center, plus three additional points both above and below the centerline at thirteen locations for a total of 91 points (Figure 2-24). A contour of the exit dynamic pressure for the nozzle of blade five at 2.71% is shown in Figure 2-25 with the fine grid points overlaid. To calculate the mass flow at each measurement point for one blower speed, the velocity measured by the Pitot-static probe was multiplied by the local air density and the differential area calculated from the grids. The total mass flow at each speed was simply the summation of the mass flow at all points. The complete set of mass flows as a percentage of the passage mass flow at 17 blower speeds (14 using the coarse grid plus 3 using the fine grid) was used to determine a calibration curve fit for each nozzle, which is plotted in Figures 2-26 through 2-29. Power law curve fits to this data were used to provide an estimate of the mass flow rate for any pressure difference across the nozzle. Table 2-1 shows the pressure difference required for the blade five nozzles to produce the mass flow rates used throughout this study, along with the corresponding blower speeds, for both sets of blowing blades.

Table 2-1. Pressure differences and blower frequencies for mass flow rates. Mass flow normalized on total mass flow through one cascade passage at normal cascade tunnel operating conditions. Frequencies listed are nominal operating frequencies for the variable speed blower fan.

Pressure Difference (in. H_2O)	**% Mass Flow**	**Simple Blowing Frequency (Hz)**	**Kuethe Vane Frequency (Hz)**
0.03-0.04	1.0	22.1	19.7
0.09-0.10	1.4	27.6	23.7
0.11-0.12	1.5	29.0	25.
0.15-0.16	1.7	32.1	27.9
0.19-0.20	1.9	34.9	30.4
0.21-0.22	2.0	35.9	31.4
0.24-0.25	2.1	37.6	33.1
0.30-0.31	2.3	41.1	35.9
0.35-0.36	2.5	43.7	38.3
0.39-0.40	2.6	45.9	39.9
0.42-0.43	2.7	47.1	41.6
0.52-0.53	3.0	-----	44.9

2.2.1.3.1. Base Plate Design

Each baseline blade attaches to the tunnel superstructure by a 9.5mm thick aluminum base plate secured to the blade root by three Allen bolts. However, the base plate design had to be modified to allow for the nozzle attached to the root of each blowing blade. New plates were created without the center section, leaving only two Allen bolts to join to the blade. Several of the hole diameters were decreased in size from the original base plates, but the new plates are interchangeable with the old. Drawings of the original plate and the new plate are shown in Figures 2-30 and 2-31 respectively.

2.2.1.4. *Blowing Blades*

The first set of trailing-edge blowing blades that were examined is referred to as the “simple blowing blades”. Externally, they are nearly identical to the non-blowing baseline GE Rotor B blades, except for the presence of the blowing slot on the suction side at the trailing-edge (Figure 2-32). The blowing slot creates a difference in trailing-edge thickness from the baseline blades. These differences are compared on Figure 2-33, as measured in Figure 2-34. At the slot exit, the simple blowing blades have a thickness of 5.0mm, and the baseline blades are 4.6mm thick. At the trailing-edge itself, the simple blowing blades are 3.0mm thick, while the baseline blades are actually 3.3mm thick. This difference in geometry was not found to significantly alter the flow in the trailing-edge region.

Internally, the blowing blades have a series of flow passages that were designed to create uniform blowing according to CFD predictions. The flow is accelerated from the nozzle exit through five separate passages to the trailing-edge of the blade, as shown in Figures 2-35 and 2-36.

The second set of blowing blades is referred to as the “Kuethe vane blowing blades”. These blades differ from the simple blowing blades by a set of angled ridges (vanes) located upstream of the blowing slot at the trailing-edge (Figure 2-37). The Kuethe vanes were used to increase the mixing of the blowing jet with the freestream in the wake region, as shown in Kuethe (1972). Kuethe showed that the presence of the vanes decreased the wake deficit and reduced turbulence levels.

Measurements of the four simple blowing blades and four Kuethe vane blades were made using a Mitutoyo 12-inch caliper (0.001" accuracy), and are listed in Tables 2-2 and 2-3. All dimensions are given in millimeters.

2.2.1.4.1. Simple Blowing Blade Geometry

The simple blowing blades have the same 254mm chord as the baseline blades, but a slightly longer span of 288.3mm outside of the tunnel. Even though the span of these blades is about 9.3mm longer than the baseline span, the span inside the tunnel remains 254mm minus the tip-gap height. The blowing slot is located approximately 9.6mm upstream of the trailing-edge of the blade on the suction side. The slot is 9.5mm chordwise from the trailing-edge and has a span of 241.0mm (Figure 2-38). It is located 6.3mm from the blade tip and 40.6mm from the root (Figure 2-39). The slot width is 1.4mm on average, with several locations less than 1.3mm around mid-span (Figure 2-40).

On the face of the blade root, the nozzle passage is visible (Figure 2-41). The width of the passage at the leading-edge is 4.9mm and 7.1mm at the trailing-edge. The passage length is 102.5mm on both the pressure and suction sides of the blade.

Table 2-2. Simple blowing blade geometry, dimensions in mm.

Parameter	**Measurement Location**	**Blade 3**	**Blade 4**	**Blade 5**	**Blade 6**
Chord	**Root** **Mid-span** **Tip**	253.5 253.5 253.5	253.6 253.3 253.6	253.7 253.2 253.3	253.5 253.4 253.6
Span	**Leading-edge**	287.8	288.3	288.8	288.3
Blowing Slot Chordwise Distance from Trailing-Edge	**Root** **Tip**	9.6 9.6	9.3 9.2	9.6 9.1	9.9 9.9
Blowing Slot Span	**Slot mouth on suction side**	241.3	240.9	240.8	241.0
Blowing Slot Width	**Root** **Tip**	1.4 1.4	1.4 1.4	1.4 1.4	1.4 1.4
Blowing Slot Location	**From root** **from tip**	40.7 6.3	40.5 6.2	40.6 6.4	40.6 6.4
Nozzle Passage Width	**Leading-edge** **Trailing-edge**	4.9 7.1	4.9 7.1	5.1 7.1	4.9 6.9
Nozzle Passage Length	**Pressure side** **Suction side**	102.8 102.4	102.4 102.4	102.5 102.6	102.5 102.5
Nozzle Passage Location	**Passage trailing-edge from root trailing-edge** **Passage leading-edge from root leading-edge**	85.1 57.0	85.1 56.9	85.1 56.9	85.0 57.0

2.2.1.4.2. Kuethe Vane Blade Geometry

Similar to the simple blowing blades, the Kuethe vane blowing blades have a chord of 254mm and a span of 288.3mm. The blowing slot is located 9.6mm upstream of the trailing-edge on the suction side, and the slot span 240.7mm. The slot is located 6.7mm from the blade tip and 40.9mm from the root. The slot is 1.4mm wide, except for areas near mid-span where it decreases to 1.3mm. The nozzle passage on the blade root is 5.2mm in width at the leading edge and 7.1mm wide at the trailing-edge. The overall length of the passage is 102.6mm.

The horizontal length of the ridges, labeled as the chordwise width in Figure 2-42, has a length of 47.1mm. The spanwise height is 12.7mm, so the total length of a ridge is 48.8mm. The nine ridges per blade are evenly spaced by 25.4mm, starting 46.3mm from the root and ending 31.5mm from the tip. The row of ridges is located 24.8mm upstream from the trailing-edge of the blade, which is 15.2mm from the blowing slot exit.

Table 2-3. Keuthe vane blowing blade geometry, dimensions in mm.

Parameter	**Measurement Location**	**Blade 3**	**Blade 4**	**Blade 5**	**Blade 6**
Chord	**Root**	253.6	253.4	253.6	253.7
	Mid-span	253.5	253.5	253.3	253.4
	Tip	253.5	253.4	253.5	253.5
Span	**Leading-edge**	288.5	288.4	289.3	288.3
Blowing Slot Chordwise Distance from Trailing-Edge	**Root**	9.3	8.9	9.8	9.2
	Tip	9.3	9.9	9.4	9.0
Blowing Slot Span	**Slot mouth on suction side**	240.7	240.1	241.0	240.7
Blowing Slot Width	**Root**	1.4	1.9	1.8	1.9
	Tip	1.5	1.5	1.5	1.8
Blowing Slot Location	**From root**	40.0	41.1	41.4	41.0
	from tip	6.4	6.7	6.9	6.8
Nozzle Passage Width	**Leading-edge**	5.1	5.2	5.2	5.1
	Trailing-edge	7.0	7.2	7.1	7.1
Nozzle Passage Length	**Pressure side**	102.6	102.6	102.5	102.5
	Suction side	102.6	102.6	102.6	102.6
Nozzle Passage Location	**Passage trailing-edge from root trailing-edge**	85.0	85.1	85.0	85.0

	Passage leading-edge from root leadin- edge	57.3	56.9	57.0	57.0
Ridge Dimension	**Chordwise width** **Spanwise height** **Total length**	47.0 12.7 48.7	47.4 13.7 49.3	47.1 12.5 48.7	46.9 11.8 48.4
Ridge Spacing		25.4	25.4	25.4	25.4

2.2.1.5. *Air Conditioner*

The air that passes through the blades emerges at the trailing-edge at up to three times the freestream velocity. Losses in the air delivery system are turned into heat, which can lead to a higher temperature in the trailing-edge blowing than in the rest of the wind tunnel flow. These temperature differences can cause substantial errors in hot-wire measurements. To counteract this effect, small window-unit air conditioner was used to cool the air entering the blower. The flow temperature had to be kept as constant as possible to ensure the accuracy of the hot-wire probes, described in Section 2.4.1. A Whirlpool ACQ158XPO 4.3kW air conditioner was stationed beneath the settling chamber. The face of the air conditioner was inserted 127mm into the width of a 673.1mm x 622.3mm x 444.5mm heat exchanger box (Figure 2-43). A pipe connected the opposite side of the box to the blower to supply air at the desired temperature.

2.2.2. Stabilizing Pins and Reduced Tip-Gap

Initially, the simple blowing blades were found to twist significantly when subjected to the aerodynamic loading of the tunnel. Figures 2-44a through 2-44g show the results of aligning a laser with the trailing-edge of blade five. With no flow, the laser is in good alignment with the trailing-edge. With flow, part of the laser is visible on the pressure side, indicating a deflection of the blade tip, estimated to be 2mm.

To resolve this issue, a set of two stabilizing pins per blade were designed and installed at the blade tips. Each conical pin is 2.54mm in diameter and projects an additional 9.1mm spanwise from the blade tip. As the tip-gap is decreased, the pins prevent any twisting of the blowing blades by piercing the lower end-wall of the tunnel. The leading-edge pin was placed 18.1mm from the leading-edge, while the trailing-edge pin was placed 26.5mm from the trailing-edge. This placement prevents any interference with the internal blade passages of the blowing blades.

The pins were first installed on the center four blades for the baseline blade row (Figure 2-45). Figure 2-46 shows a total pressure coefficient cross-section of the baseline blades taken at 0.839 x/c_a with a tip-gap of 0.004125c, while Figure 2-47 shows a cross-section of the pinned non-blowing baseline blades at the same conditions. There are no discernable differences between these two figures. Once it was determined that the pins had no influence on the flow downstream of the blades, the pins were installed on the simple blowing (Figure 2-48) and Kuethe vane blowing blades.

2.3. Data Acquisition

2.3.1. System

Data was acquired with an Agilent VXI system, which is composed of an Agilent E1432A module, an Agilent E8491A interface, and an Agilent E8408A VXI mainframe. The Agilent E1432 module is a 16-channel digitizer that is installed in one of four slots on the mainframe. The module performs digital signal processing, transducer signal conditioning, alias protection, digitization, and high-speed measurement computation. The interface links the mainframe to the serial bus and to a computer. A laptop computer running the Agilent VEE programming language controls the data acquisition and the movement of the traverse.

2.3.2. Three-Axis Traverse

A three-axis traversing system controls the position of the probes in the test section (Figure 2-49). Each axis is moved by Compumotor model S57-83-MO stepper motors driven by Parker PDX-13 single-axis mini-step drivers. The resolution of the traverse movement is 0.025mm per step.

2.4. Pressure Measurements

Pitot-static probes were used to measure the static, dynamic, and total pressures in the cascade tunnel, while static ports on the blades measured the pressure distribution of the blades. Uncertainties in pressure measurements are listed in the appendix.

2.4.1. Pitot-Static Probes

A Dwyer Instruments Standard Model 160 Pitot-static Probe (Model 167-12) was fixed in the inlet of the test section, approximately 0.95m downstream of the contraction exit (Figure 2-50). The shaft length is 304.8mm and the tip length is 76.2mm. This probe was used to measure the freestream conditions. A second Dwyer 167-12 model probe was used to measure the conditions downstream of the blade row to check periodicity and for the Pitot-static cross-sections (Figure 2-51). An additional bent Pitot probe was used to verify uniform inflow upstream of the blade row (Figure 2-52). There is only one upstream slot in the roof for probe insertion, directly above the junction of the inlet section floor and the Teflon bed. The ideal probe location to measure the inflow is immediately before it enters the blade row, but the Dwyer Pitot-static probes are not capable of reaching this position. Because of the geometry of the bent probe, measurements can be made closer to the downstream blade row when it is inserted into the upstream roof slot.

2.4.2. Blade Loading

The pair of blade surfaces forming the center passage of the cascade (the suction side of blade four and the pressure side of blade five) were instrumented with a series of pressure taps near mid-span for each set of blades (baseline, simple blowing and Kuethe vane). They are located at mid-span, which is 127.1mm from the blade tips. Table 2-4 shows the port locations normalized on the total chord, *c*. The ports are connected to tubing embedded in the blade surface, which emerges at the blade root where it is connected to a set of Tygon tubes that attach to a scanivalve system. The CTLR2P/S2-S6 Scanivalve Corp scanivalve can automatically measure and record pressures from a maximum of 48 pressure taps using a built-in stepper motor that rotates the tubing from the pressure ports. The scanivalve uses two pressure transducers and is activated either by a 386 PC or manually.

Table 2-4. Static pressure port locations, normalized on the blade total chord, where the *x*-direction is perpendicular to the blade row.

Port Number	**Pressure Side, *x/c***	**Suction Side, *x/c***
0	1.31108E-06	0.021353296
1	0.009910775	0.035547062
2	0.021444658	0.050270465
3	0.033403604	0.065331773

4	0.045810974	0.080686959
5	0.078724561	0.120348154
6	0.114257790	0.161746308
7	0.152295090	0.204778177
8	0.192706716	0.249343811
9	0.235377036	0.295330709
10	0.280180369	0.342635659
11	0.327010251	0.391176214
12	0.375810713	0.440925660
13	0.426557791	0.491883888
14	0.479266505	0.543975485
15	0.534208964	0.596990017
16	0.591722333	0.650976198
17	0.651985584	0.706213853
18	0.715169152	0.762927871
19	0.781296147	0.821384077
20	0.850371445	0.881814862
21	0.878816765	0.906586114
22	0.907711045	0.931721835
23	0.937051964	0.957228769
24	0.966858177	0.983092222

2.4.3. Transducers

Three Setra model 239 pressure transducers were used in this experiment. The reference transducer has a range of ±1868.2Pa with an output of ±2.5V DC (slope of 3), and the primary measurement transducer has a range of ±3736.3Pa and an output of ±2.5V DC (slope of 6). The secondary measurement transducer, used mainly during hot-wire calibrations, has a range of ±17.4kPa and an output of ±2.5V DC (slope of 28.26). The output voltages measured by the transducers is recorded by the channels of the Agilent E1432A module.

2.5. Hot-wire Anemometry

Hot-wire anemometry was the primary measurement technique used in this experiment. The probes, the system, and the probe calibration method are described below. Uncertainties in velocity and turbulence measurements are listed in the appendix.

2.5.1. Hot-wire Probes

A miniature Kovaznay type four-sensor hot-wire probe, type AVOP-4-100, manufactured by the Auspex Corporation was used for three-component velocity measurements and is shown in Figure 2-53. The probe consists of eight 75μm tip-diameter prongs that suspend four 5μm tungsten wires with lengths of 1.4mm. The wires are arranged in two orthogonal X-wire arrays with each wire inclined at 45° to the probe axis. The measurement volume achieved with this configuration is approximately 0.5mm^3. The development of this probe and a more detailed description can be found in Wittmer *et al* (1998).

An Auspex Corporation single-wire probe was used to measure blowing slot uniformity and normal-to-span cross-sections (Figure 2-54). This probe uses either a 3.8μm or 5μm tungsten wire of length 0.5μm suspended between two prongs.

2.5.2. StreamLine System

Both types of hot-wire probes are operated by a Dantec Dynamics StreamLine Constant Temperature Anemometry (CTA) System. The system requires a frame containing four CTA modules, a calibration unit, and the Agilent E1432A module. A serial connection links the computer to the frame and the CTA output reaches the computer through the E1432A. Agilent VEE codes were used to assist in set-up, calibration and data acquisition. StreamWare signal conditioning contains low- and high-pass filters, DC-offset, and gain options to automatically optimize the hot-wire signal.

2.5.3. Hot-wire Calibration

Velocity calibrations are performed on each probe to correlate the wire output voltage to the flow velocity through King's Law. The calibration is performed with a calibrator jet using the HP-4C blower (Figure 2-55). An Agilent VEE program takes a voltage reading over a range of blower frequencies from 5Hz (7.5m/s) to 60Hz (93m/s).

An angle calibration is required only for the four-sensor probe. This type of calibration involves pitching and yawing the probe to angles of ±45° from the flow direction. The relationship between velocity and flow angle can then be obtained, as described in Wittmer *et al* (1998).

2.6. Tunnel Coordinate Systems

Two coordinate systems were used in the tunnel, as shown on Figure 2-56. The first coordinate system (x,y,z) is aligned with the blade row. The origin is at the trailing-edge of blade five. The x-axis is perpendicular to the blade row, measured axially downstream. The y-axis is aligned with the blade span, measured from the lower end-wall, and the z-axis is pitchwise, perpendicular to the blades. The second coordinate system (X,Y,Z) also originates from the trailing-edge of blade five, but is aligned with the wake. The X-axis is aligned with the wake of blade five, the Y-axis is aligned with the blade span, and the Z-axis is perpendicular to the plane of the wake. The wake-aligned system is mainly used to define the wake-aligned mean velocity components (U,V,W) and the fluctuating velocity components (u',v',w').

The inlet freestream velocity, U_{ref}, and the potential core (or 'edge') velocity downstream of the cascade, U_e, (~$0.75U_{ref}$) are used to normalize many of the velocity components. Some distances are normalized on the axial blade chord, c_a, of 138.9mm. Blowing rates are defined in terms of the total mass flow injected through a single blade, normalized on the total mass flow through a single blade passage.

These coordinate systems and the axial measurement locations were drawn on a sheet of Mylar that could be accurately placed on the lower end-wall. The Mylar could be inserted for each measurement to ensure the correct measurement location.

2.7. Tunnel Calibration

The cascade tunnel was calibrated to correctly model the flow by meeting the following conditions of Ma (2003):

1. There is no acceleration or deceleration of the flow as it passes the boundary layer side or end-wall scoops
2. There are no net pitchwise pressure or velocity gradients upstream of the blade row
3. There is no net pitchwise pressure gradient downstream of the blade row, and equal blade wake spacing
4. The difference between the back pressure and the freestream static pressure, $P_b - P_\infty$, was 144.5±5.0Pa.

Several adjustments can be made to meet the above requirements. The side-wall scoop openings can be increased or decreased to make sure the flow does not accelerate or decelerate. Altering the back pressure screen configuration can change the pressure in the test section, and therefore the amount of flow removed by all of the scoops. Proper angling of the tailboards prevents any pitchwise pressure gradients in the wake region.

2.7.1. Inflow and Periodicity

Figures 2-57 and 2-58 show the inflow to the center passage of the modified cascade for the simple and Kuethe vane blowing blades, measured from just above the lower end-wall at 0.01*c* to a height of 0.75*c* at -1.28 x/c_a with the bent Pitot-probe. Figures 2-59 through 2-80 show the mid-span pitchwise pressure and velocity distributions for the simple blowing blades at 1.877 x/c_a and the Kuethe vane blades at 0.839 x/c_a respectively, with the Dwyer 167-12 Pitot-static probe. The pressure coefficients and normalized local velocity in the figures are defined as follows:

$$C_p = \frac{P - P_\infty}{P_{0\infty} - P_\infty}$$

$$C_{p0} = \frac{P_0 - P_\infty}{P_{0\infty} - P_\infty}$$

$$\frac{U}{U_{ref}} = \sqrt{C_{p0} - C_p}$$

where P is the measured static pressure, P_∞ is the freestream static pressure, P_0 is the measured total pressure, and $P_{0\infty}$ is the freestream total pressure.

In Figures 2-57 and 2-58, the normalized inflow velocity, U/U_{ref}, is plotted against the normalized pitchwise distance, z/c_a, where $z/c_a = 0$ is the trailing-edge of blade five. At $x/c_a = -1.28$, U/U_{ref} is equal to one, except in the vicinity of the lower end-wall boundary layer seen at the bottom of the figure. Inflow measurements were taken with no blowing, with the blowing slots left uncovered.

In Figures 2-59 through 2-80, the pressure coefficients and the velocity across the mid-span of blades three to six is shown versus the normalized pitchwise distance, where $z = 0$ is the wake center of blade five. The C_p line shows that the downstream pressure gradient is less than 0.001, so the static pressure in the test section is essentially constant.

The value of C_{p0} shows the periodicity. Between the wakes, C_{p0} is one, indicating that the flow did not accelerate or decelerate as it passed through the blade row. The local velocity has decreased to approximately $0.75U_{ref}$ from $1.00U_{ref}$ as seen in the inflow measurement. The wakes are nearly equally spaced at 236mm fulfilling the requirements for tunnel calibration. Periodicity was verified at all blowing rates up to 2.7%.

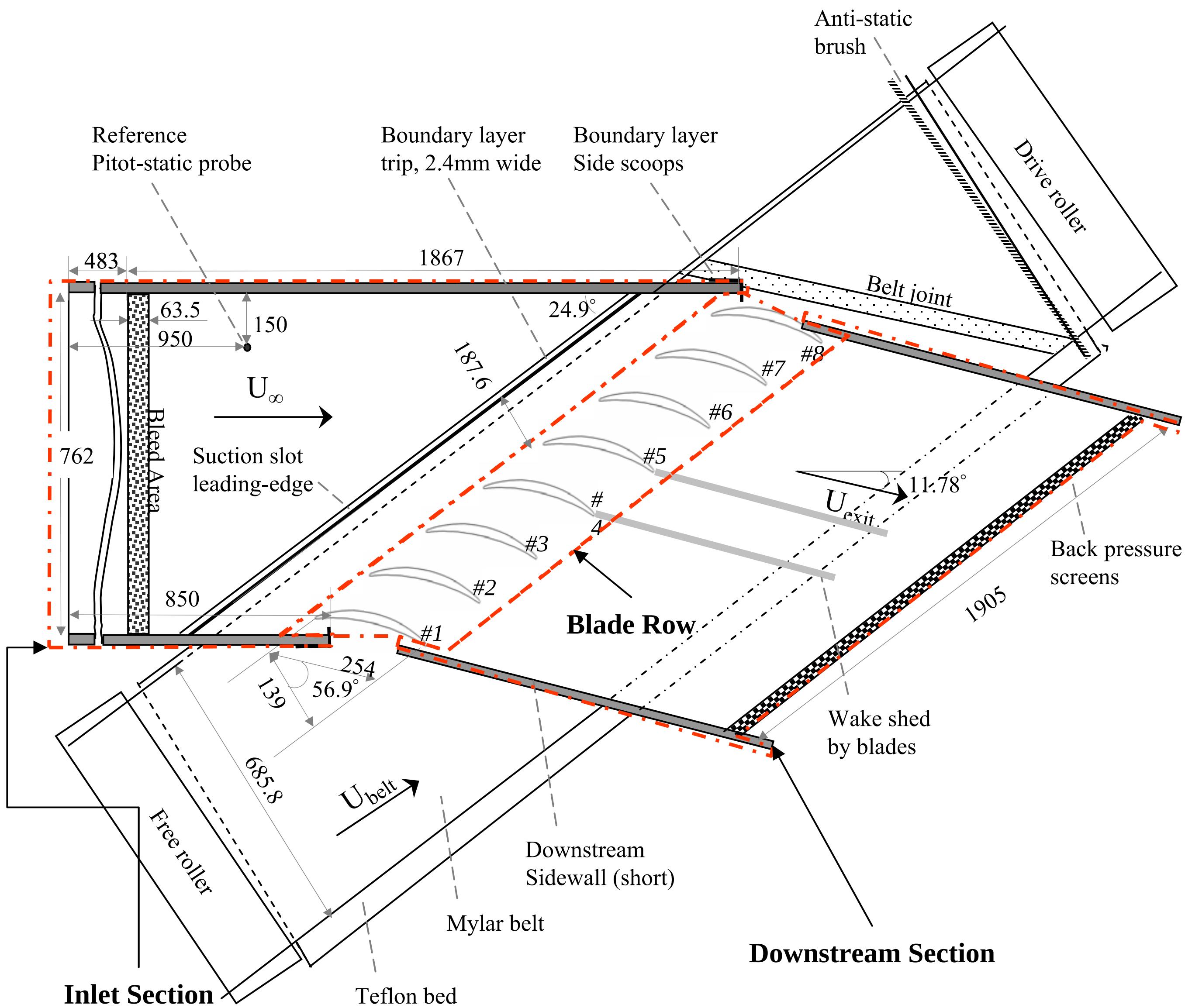

Figure 2-1: Top view of the test section of Virginia Tech's Low-Speed Linear Cascade Tunnel, dimensions in mm (Ma, 2003)

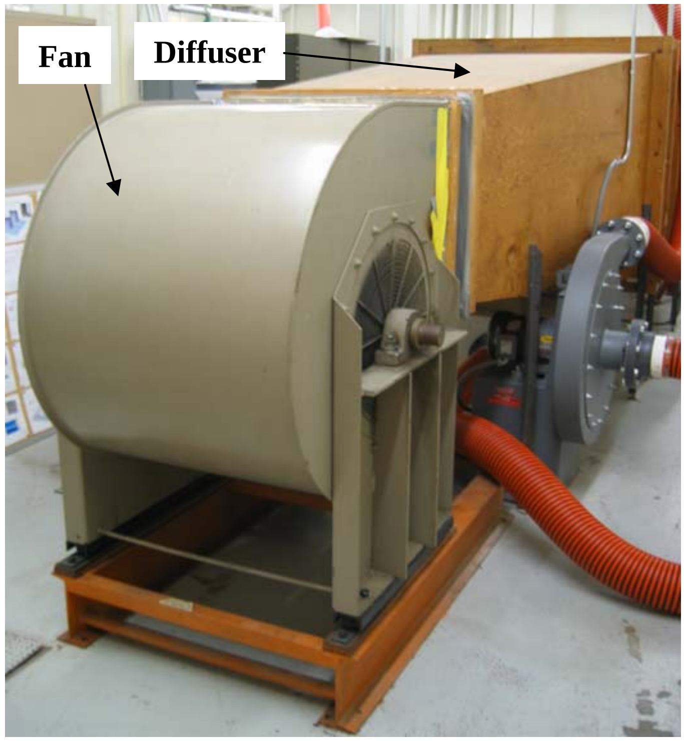

Figure 2-2: Cascade tunnel fan and diffuser (Geiger, 2005)

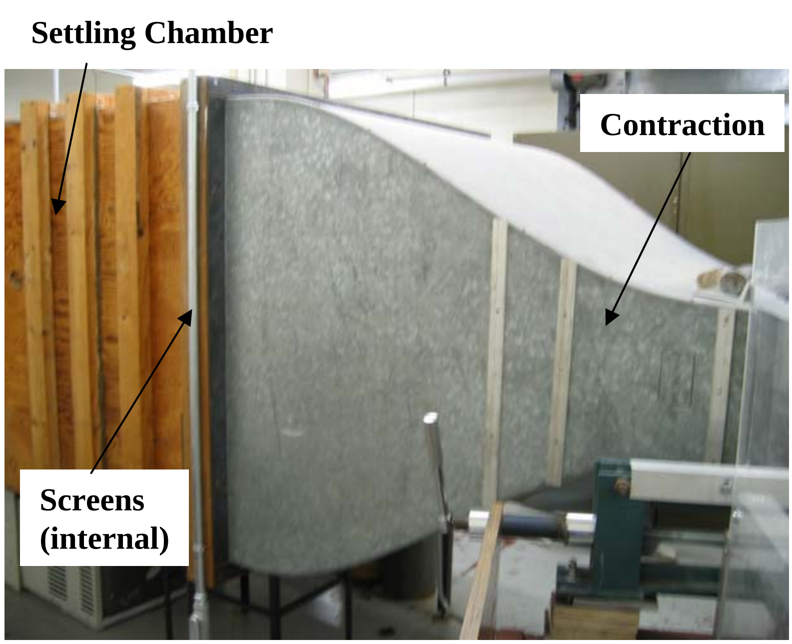

Figure 2-3: Cascade tunnel settling chamber and contraction (Geiger, 2005)

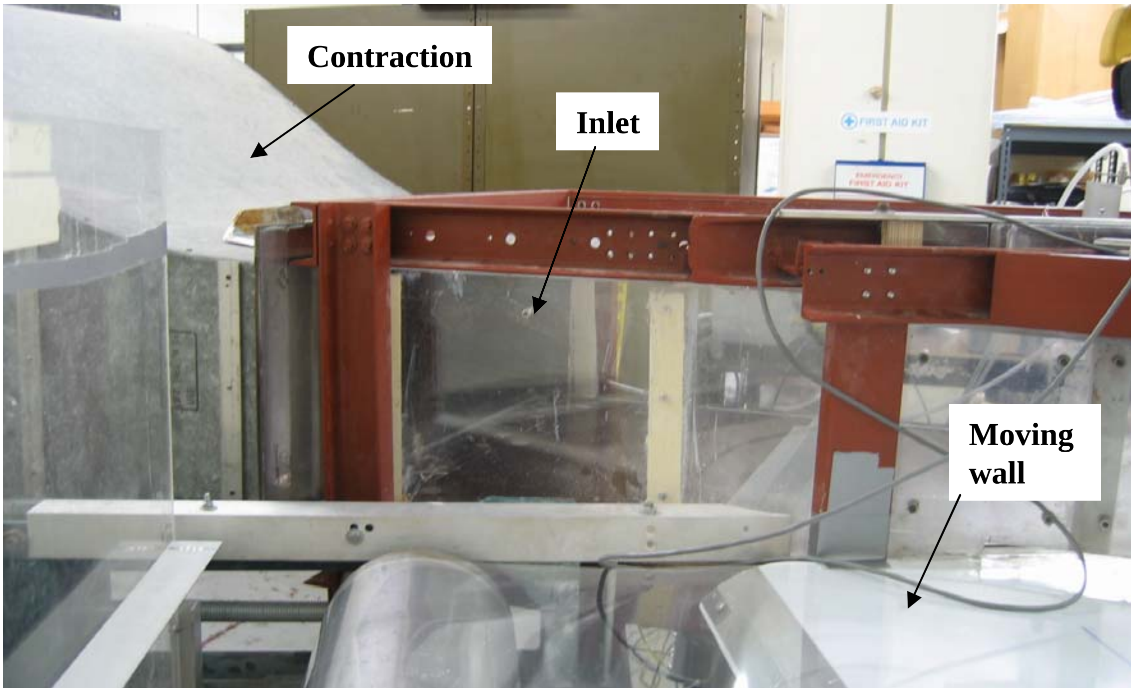

Figure 2-4: Cascade tunnel contraction exit and test section inlet (Geiger, 2005)

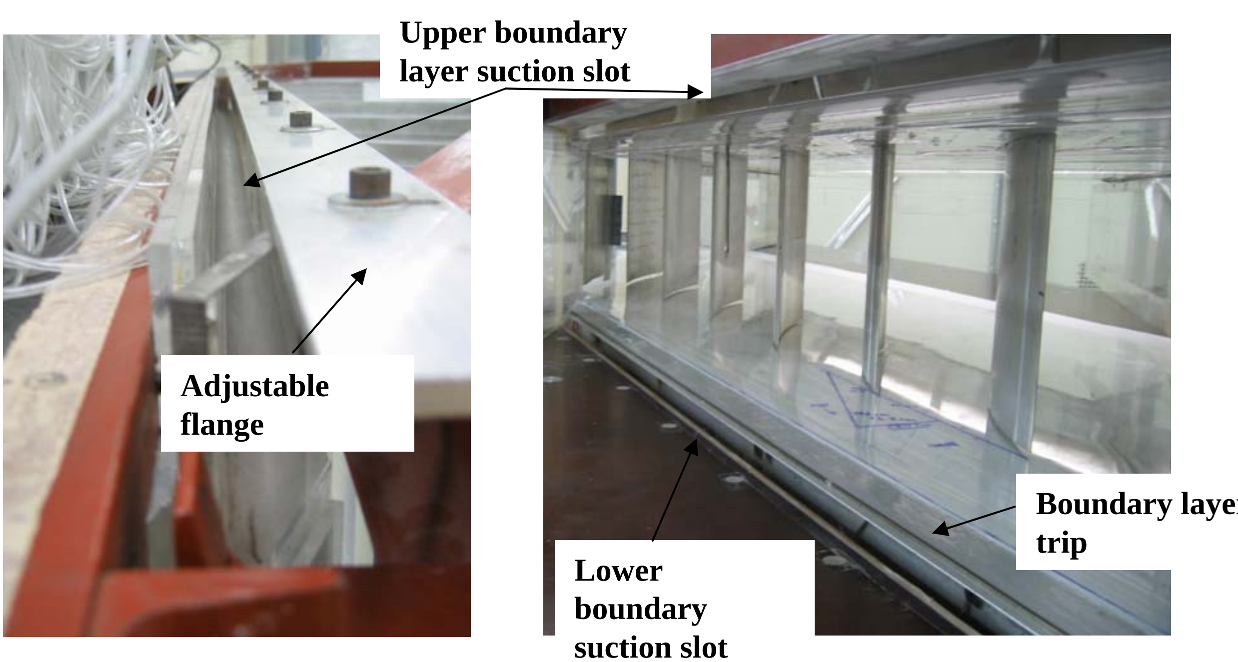

Figure 2-5: Boundary layer suction slots and boundary layer trip, upstream of blade row (Geiger, 2005)

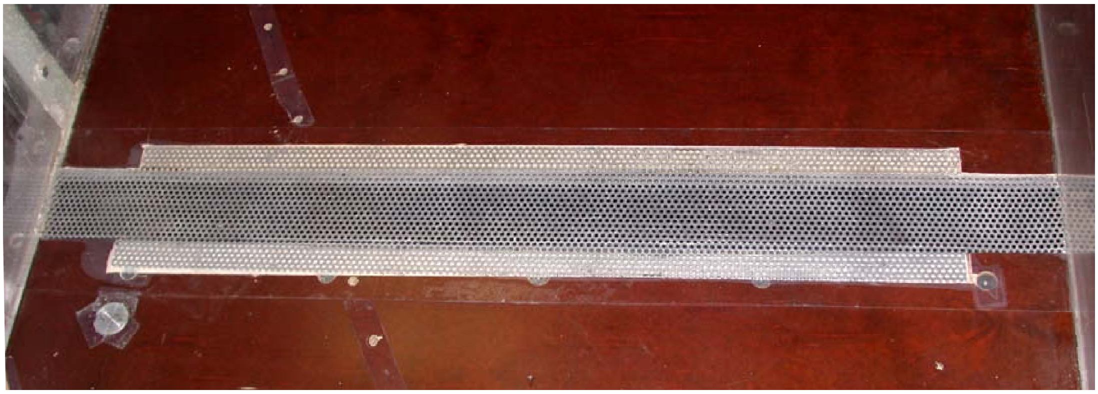

Figure 2-6: Upstream boundary layer bleed (Ma, 2003)

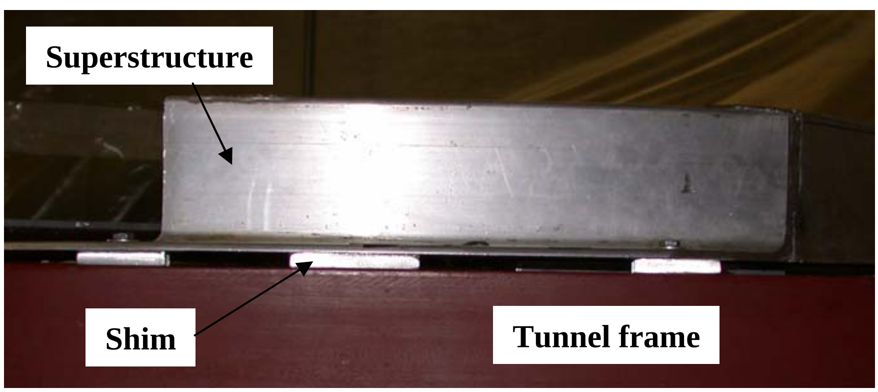

Figure 2-7: Superstructure resting on shims, situated on top of tunnel frame (Ma, 2003)

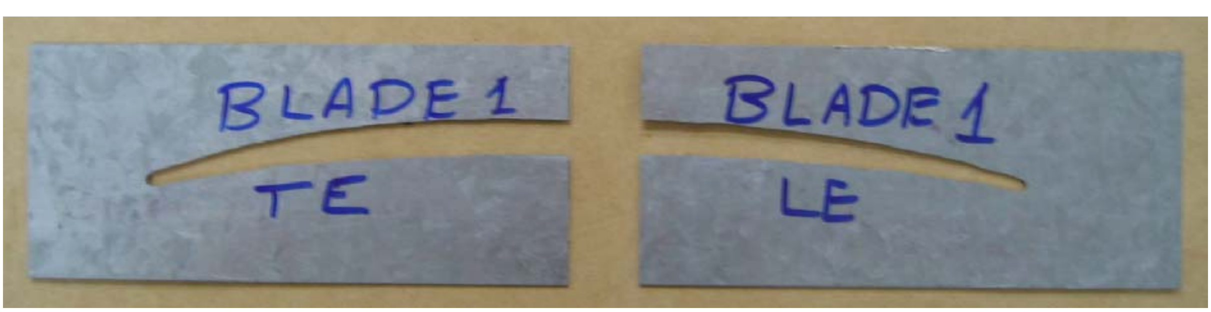

Figure 2-8: Blade root covers (Geiger, 2005)

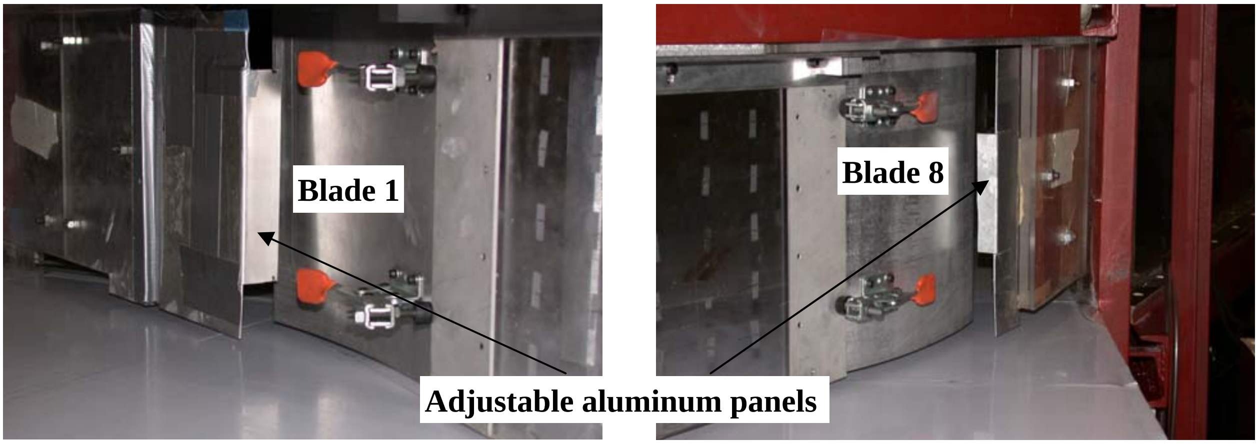

Figure 2-9: Side-wall boundary layer scoops (Ma, 2003)

Figure 2-10: Baseline GE Rotor B blade (Geiger, 2005)

Lower surface		Upper surface	
x/c	z/c	x/c	z/c
0.000000	0.000000	0.000000	0.000000
0.000435	0.000596	0.000060	-0.001491
0.001413	0.001047	0.000923	-0.003169
0.002926	0.001323	0.002598	-0.005009
0.004966	0.001388	0.005091	-0.006975
0.007524	0.001209	0.008414	-0.009021
0.010599	0.000777	0.012579	-0.011102
0.014200	0.000137	0.017595	-0.013180
0.019048	-0.000748	0.023465	-0.015238
0.029117	-0.002550	0.030187	-0.017291
0.039178	-0.004300	0.037745	-0.019400
0.049233	-0.006001	0.045855	-0.021590
0.096961	-0.013419	0.093151	-0.033478
0.144562	-0.019783	0.140592	-0.043940
0.192059	-0.025156	0.188155	-0.053027
0.239468	-0.029599	0.235822	-0.060789
0.286809	-0.033171	0.283572	-0.067278
0.334100	-0.035929	0.331389	-0.072544
0.381356	-0.037929	0.379254	-0.076640
0.428588	-0.039220	0.427156	-0.079613
0.475794	-0.039826	0.475098	-0.081487
0.522983	-0.039750	0.523069	-0.082262
0.570167	-0.038991	0.571058	-0.081938
0.617353	-0.037568	0.619059	-0.080492
0.664516	-0.035603	0.667097	-0.077670
0.711679	-0.032997	0.715151	-0.073277
0.758887	-0.029596	0.763179	-0.067158
0.806192	-0.025241	0.811130	-0.059163
0.853654	-0.019769	0.858947	-0.049143
0.901342	-0.013007	0.906564	-0.036954
0.949328	-0.004778	0.953911	-0.022461

Figure 2-11: Baseline GE Rotor B blade profile coordinates, normalized on the total chord

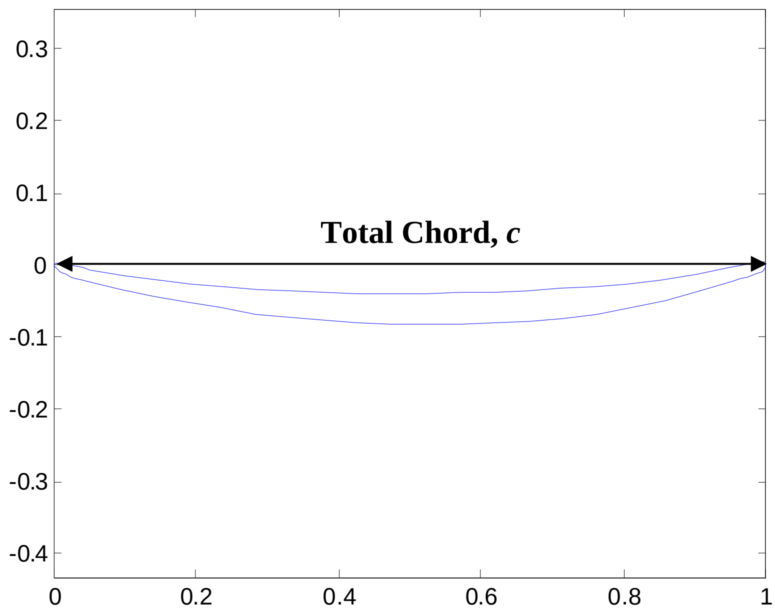

Figure 2-12: GE Rotor B blade profile (Geiger, 2005)

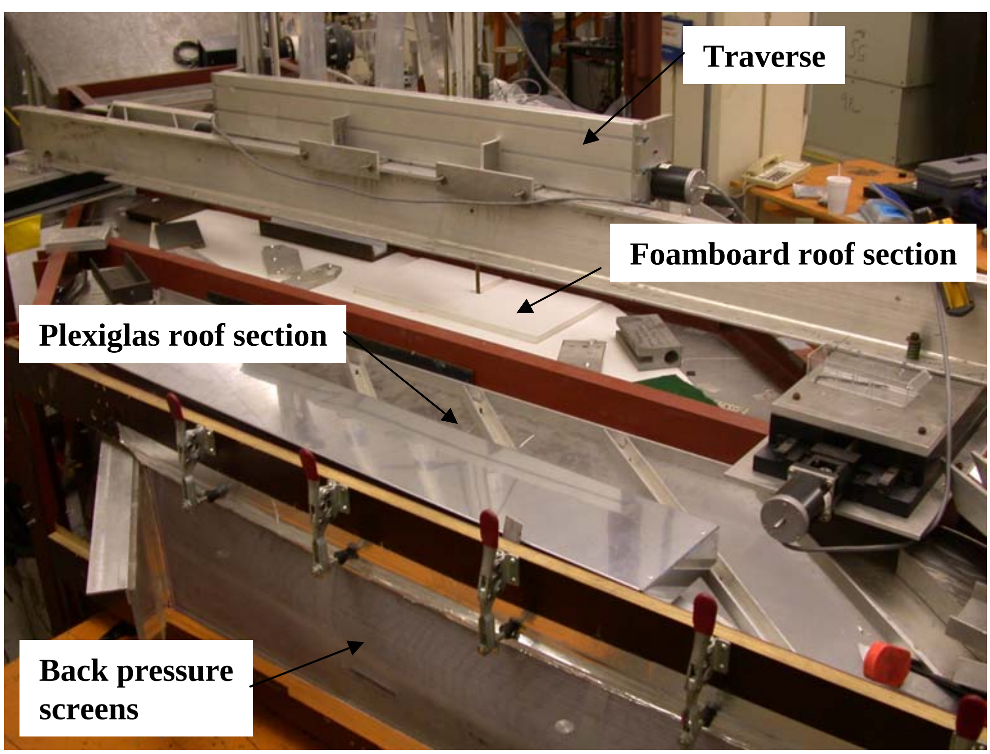

Figure 2-13: Downstream section roof

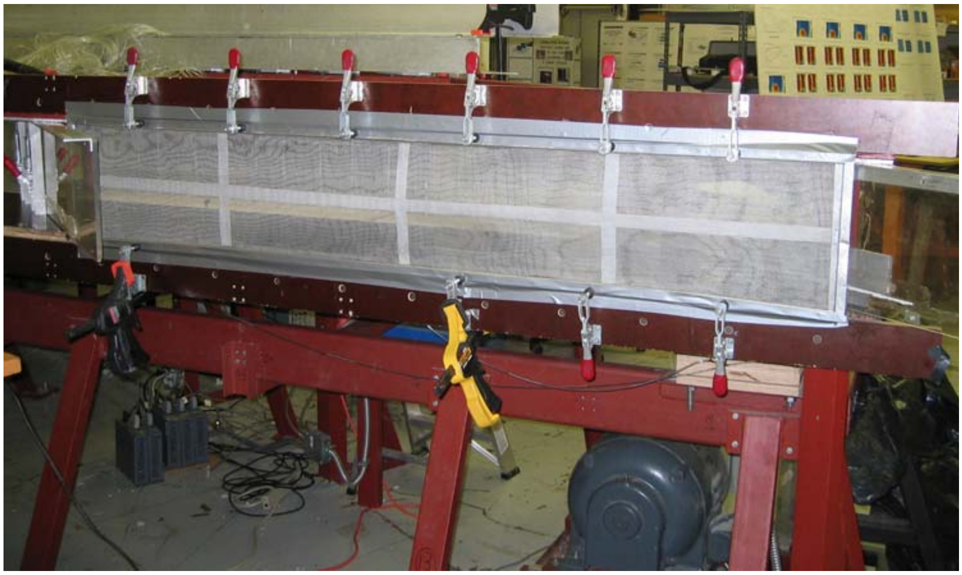

Figure 2-14: Back pressure screens clamped to tunnel exit (Ma, 2003)

Figure 2-15: Moving wall system

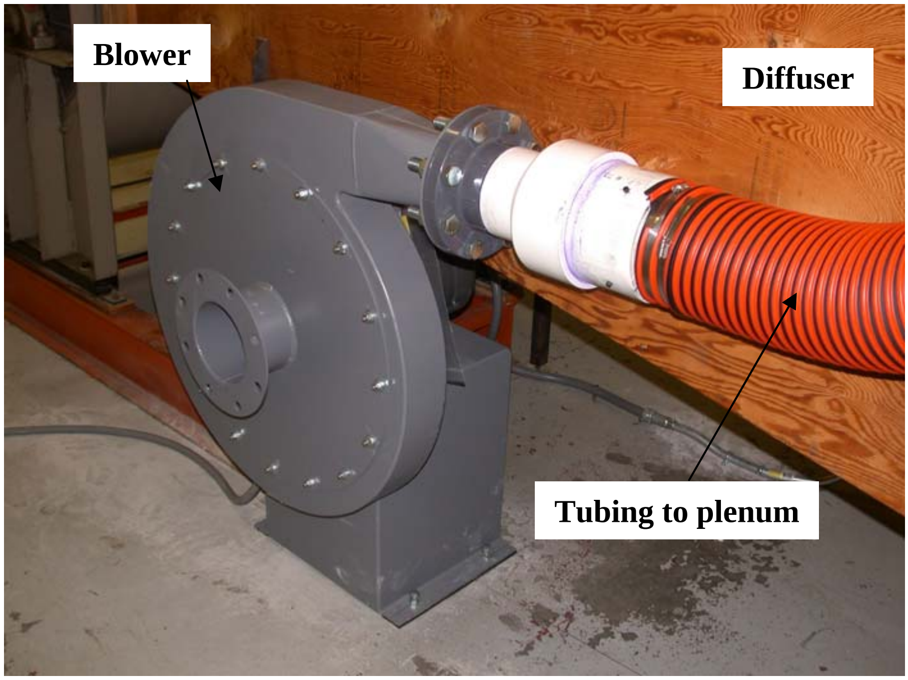

Figure 2-16: Cincinnati Fan Model HP-4C17 high pressure blower and delivery tubing

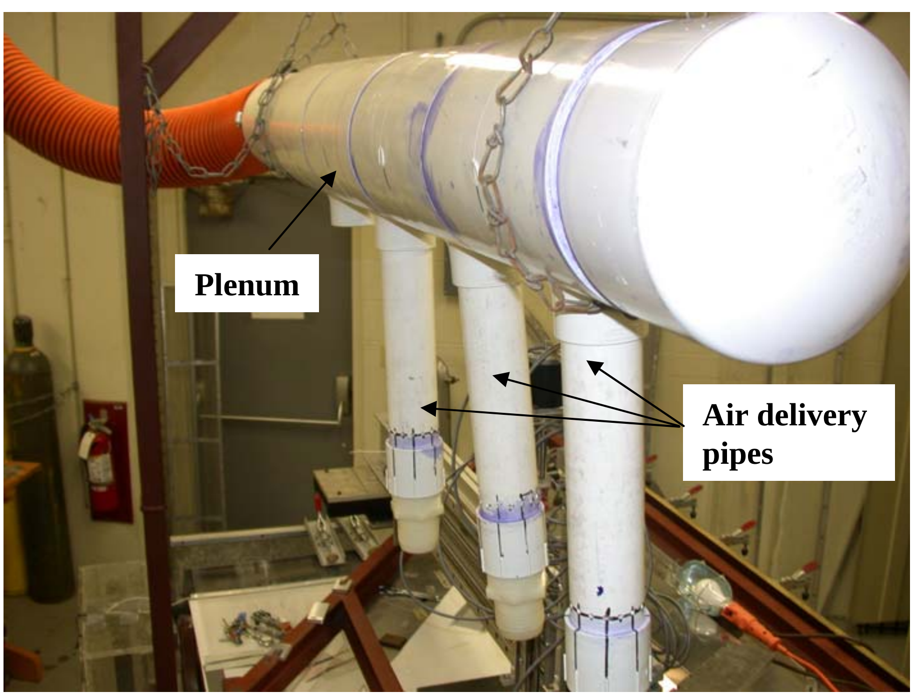

Figure 2-17: PVC plenum with attached delivery pipes

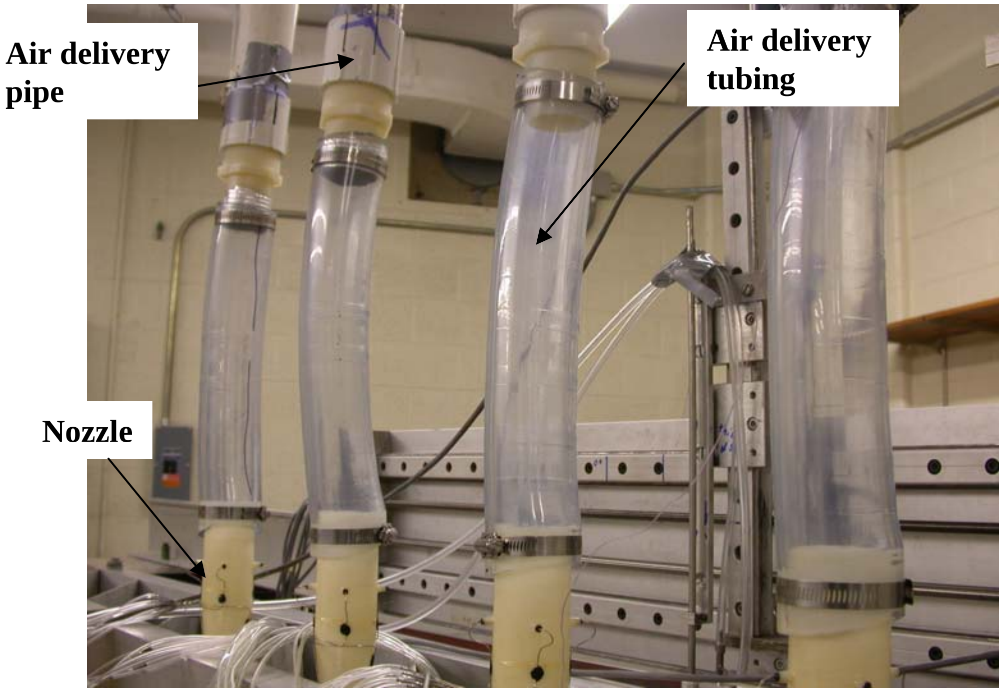

Figure 2-18: Tygon tubing connecting delivery pipes to nozzle inlets

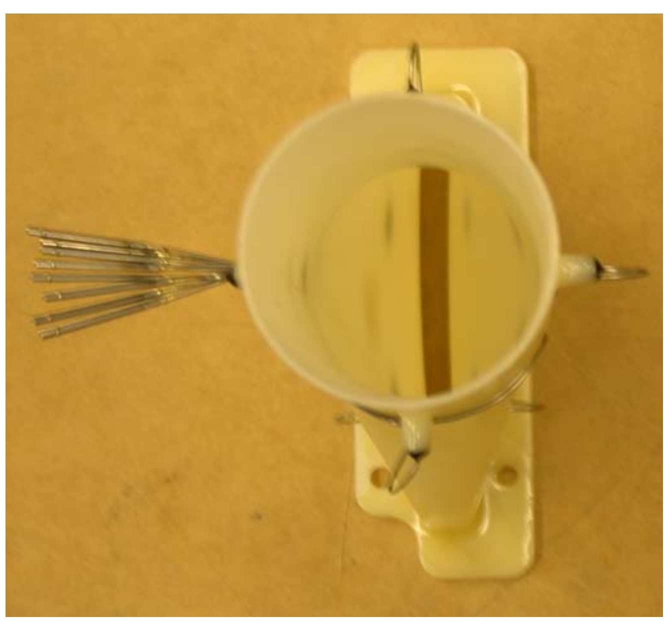

Figure 2-19: Top view of a nozzle, showing nozzle inlet area and pressure taps

Figure 2-20: Side view of a nozzle

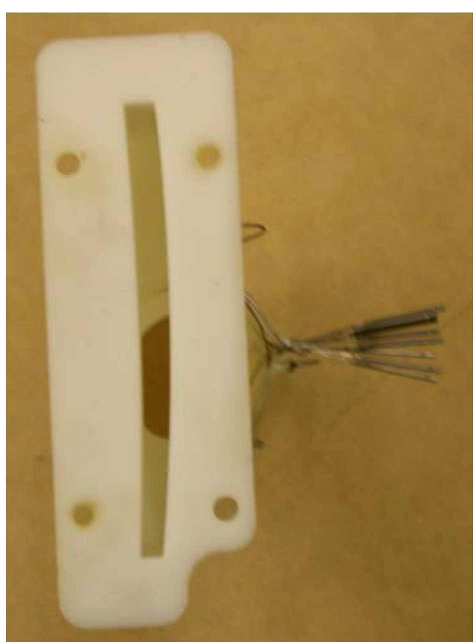

Figure 2-21: Bottom view of a nozzle, showing nozzle exit area

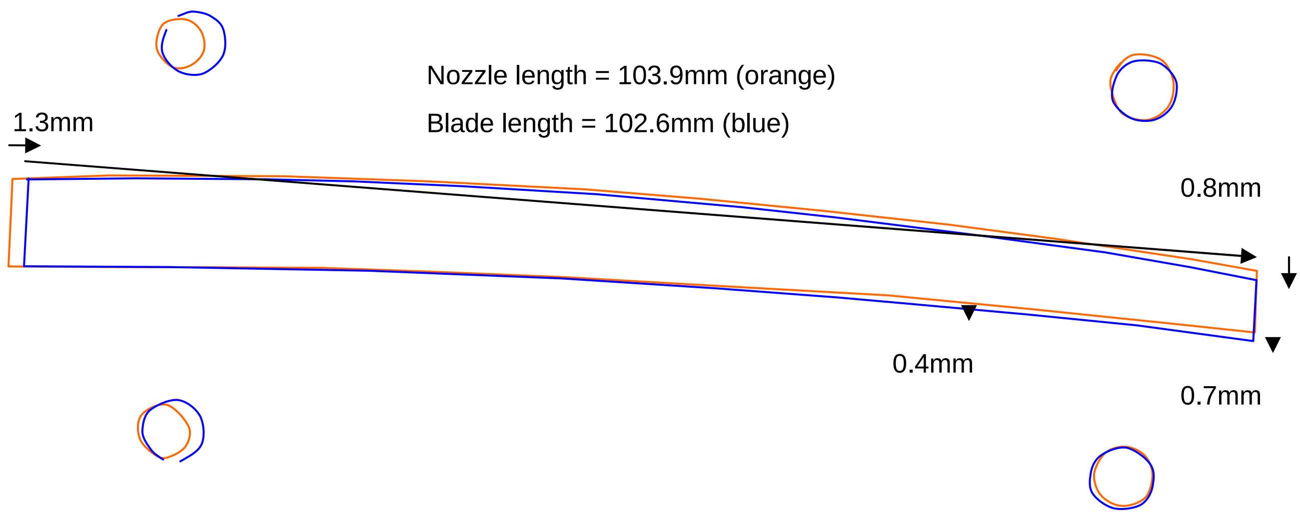

Figure 2-22: Alignment of nozzle exit area and attachment holes with blade root inlet area and attachment holes

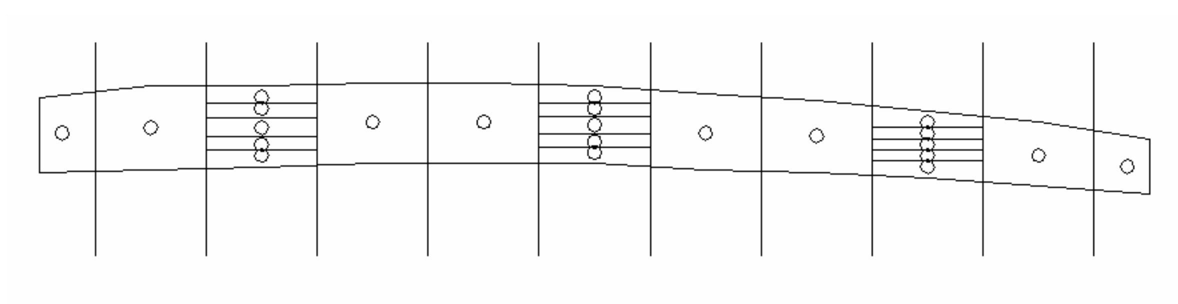

Figure 2-23: Coarse nozzle exit grid with 23 measurement locations

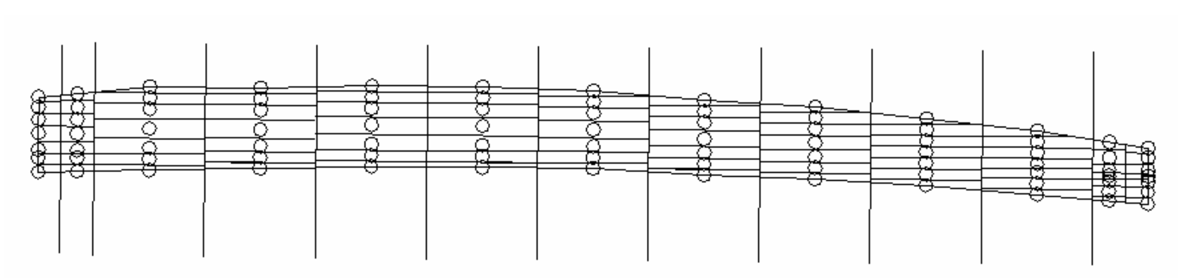

Figure 2-24: Fine nozzle exit grid with 91 measurement locations

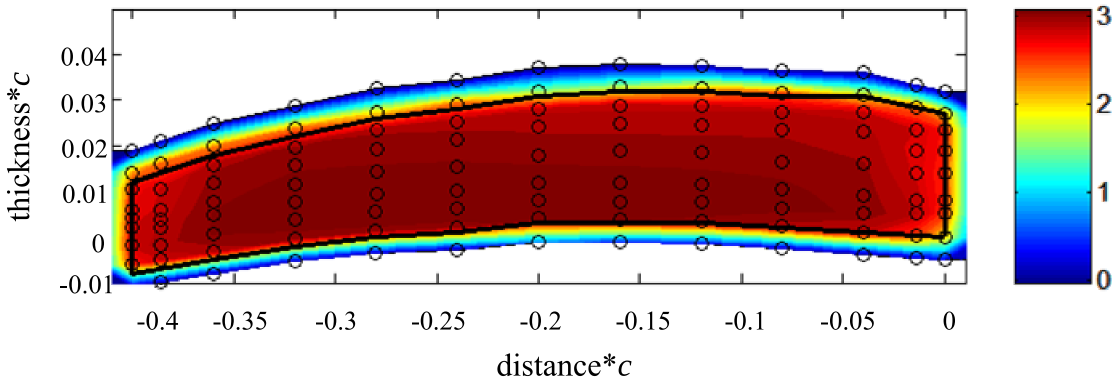

Figure 2-25: Nozzle exit dynamic pressure contour for a 2.71% mass flow rate

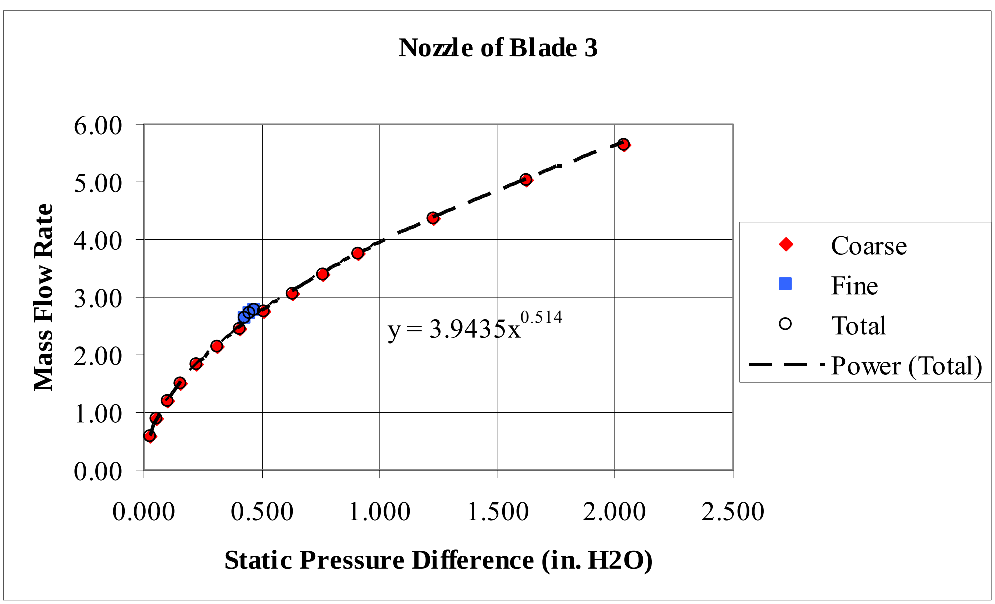

Figure 2-26: Nozzle 3 power curve to determine mass flow rate from static pressure difference between the nozzle exit and inlet

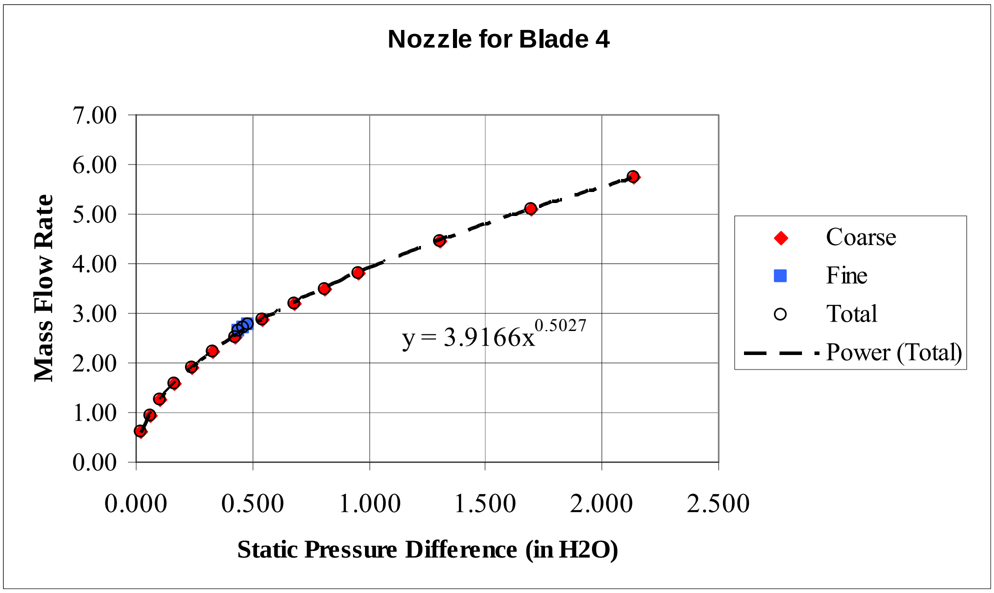

Figure 2-27: Nozzle 4 power curve to determine mass flow rate from static pressure difference between the nozzle exit and inlet

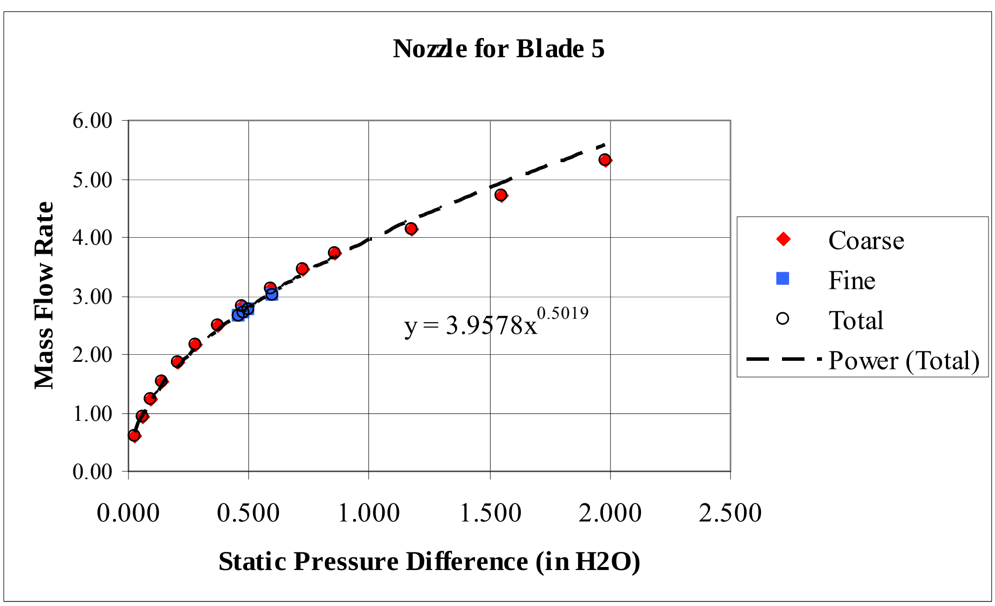

Figure 2-28: Nozzle 5 power curve to determine mass flow rate from static pressure difference between the nozzle exit and inlet

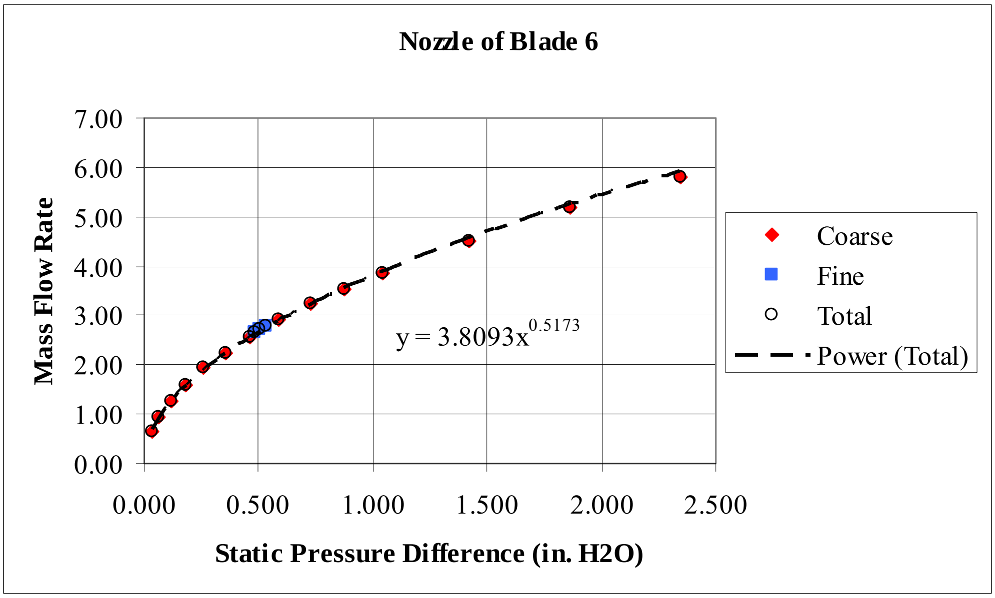

Figure 2-29: Nozzle 6 power curve to determine mass flow rate from static pressure difference between the nozzle exit and inlet

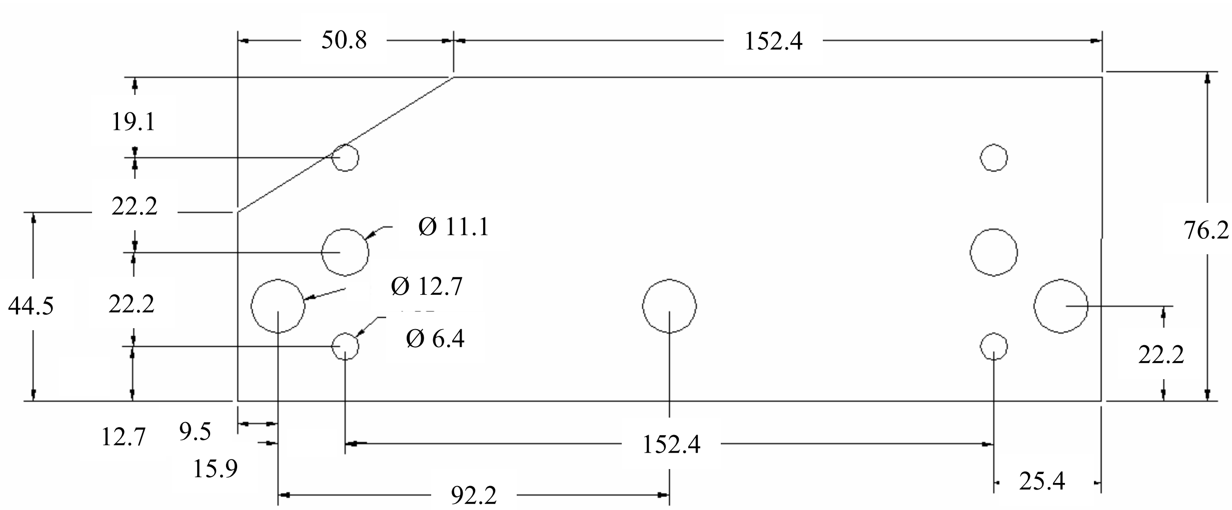

Figure 2-30: Original base plate used for non-blowing baseline blades, dimensions in mm

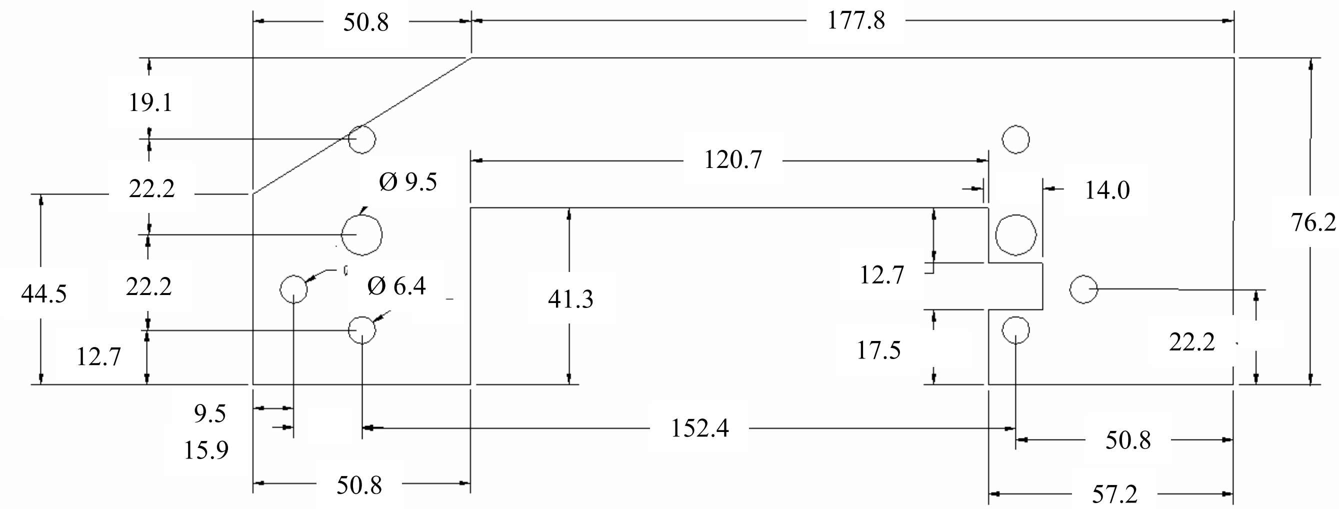

Figure 2-31: New base plate used for both sets of blowing blades, dimensions in mm

Figure 2-32: Simple blowing blade

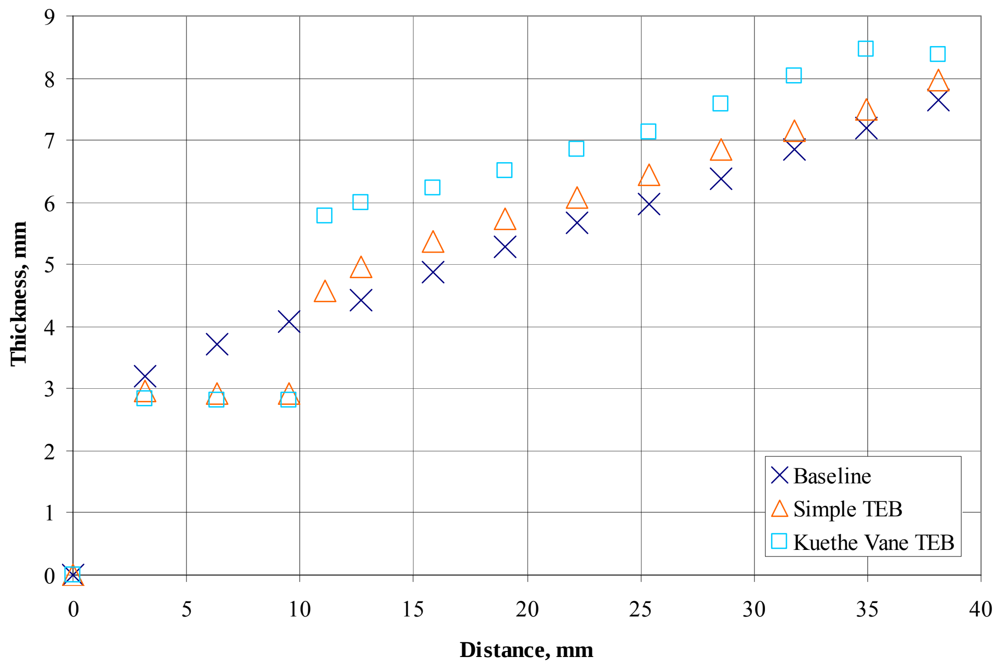

Figure 2-33: Comparison of blowing blade trailing-edge thicknesses to baseline trailing-edge thickness

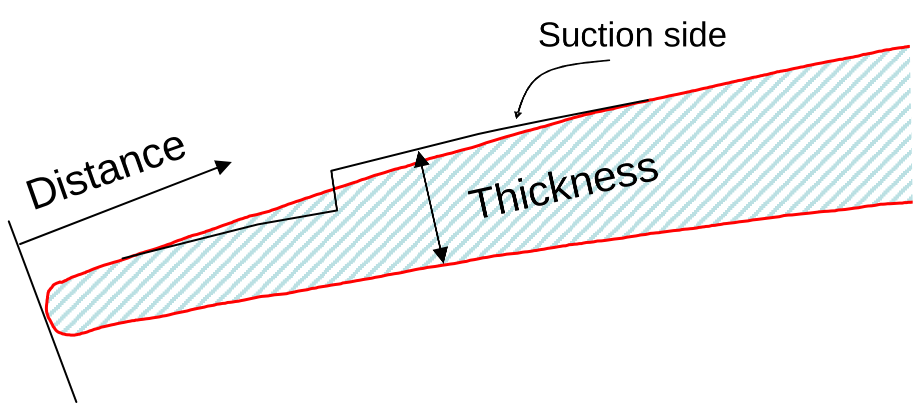

Figure 2-34: Locations of trailing-edge distance and thickness, plotted in *Figure 2-33*

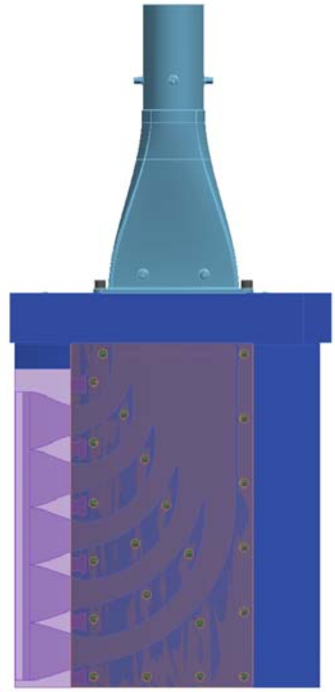

Figure 2-35: Internal blowing blade passages (NASA Glenn)

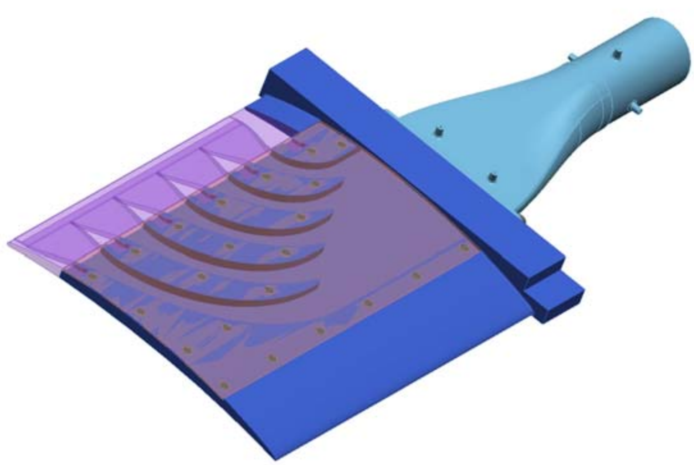

Figure 2-36: Internal blowing blade passages (NASA Glenn)

Figure 2-37: Kuethe vane blowing blade

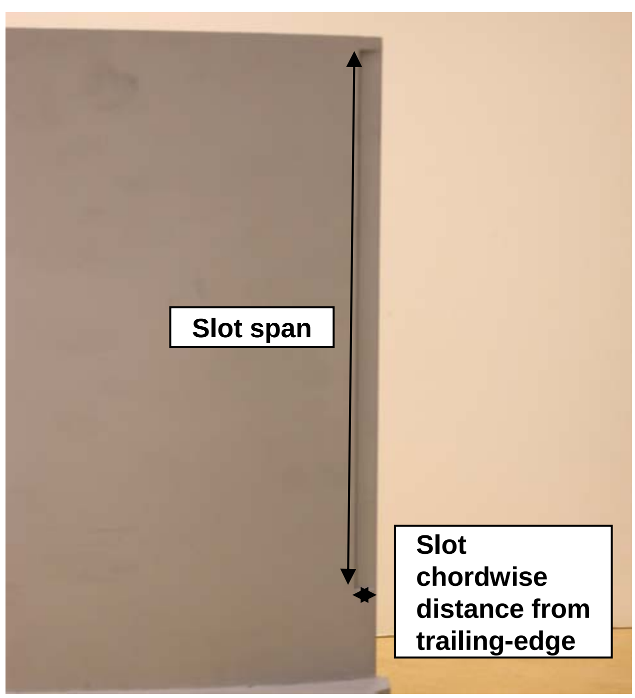

Figure 2-38: Location of blowing slot span and chord

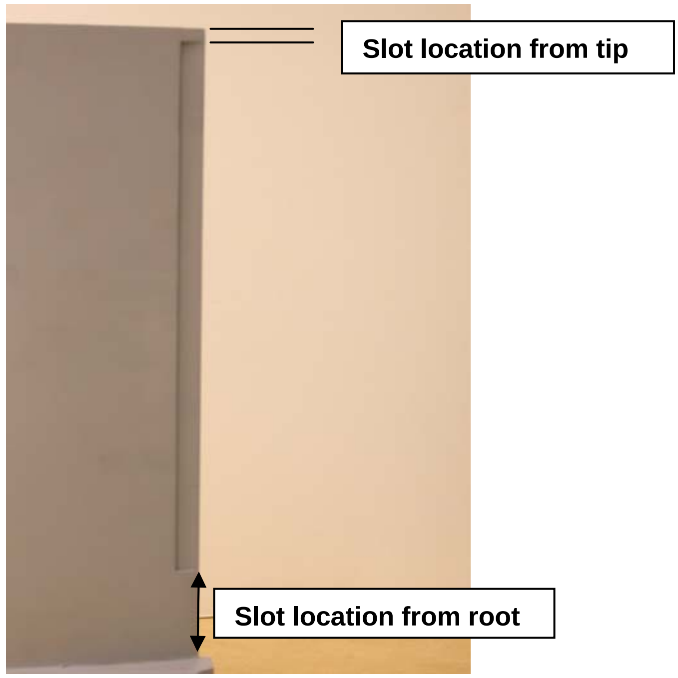

Figure 2-39: Blowing slot location from blade tip and root

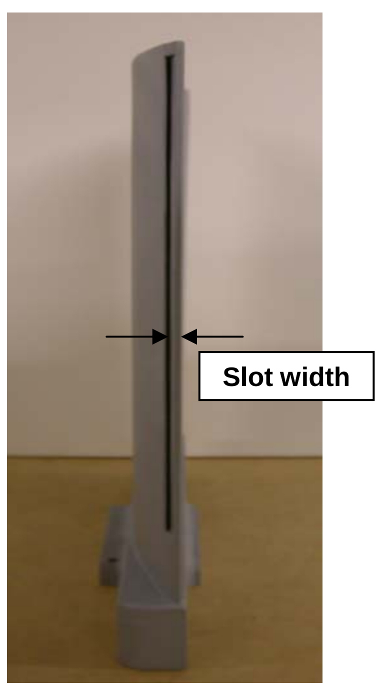

Figure 2-40: Location of slot width

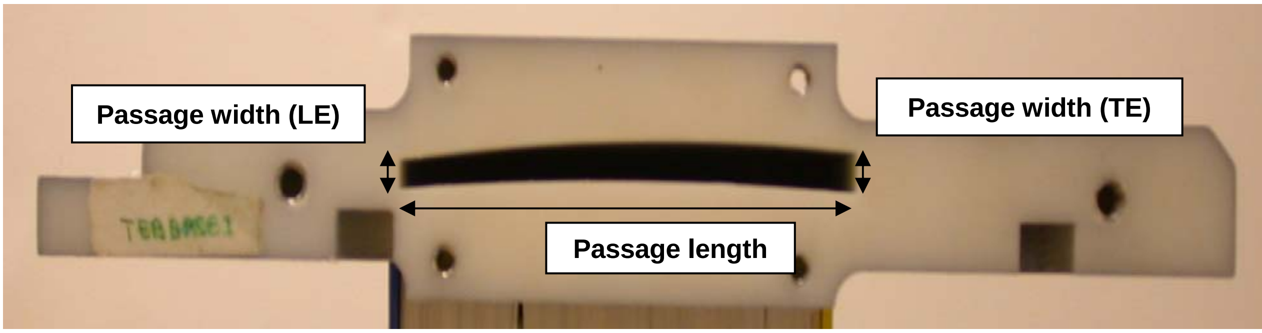

Figure 2-41: Blowing blade root with passage inlet area corresponding to nozzle exit area

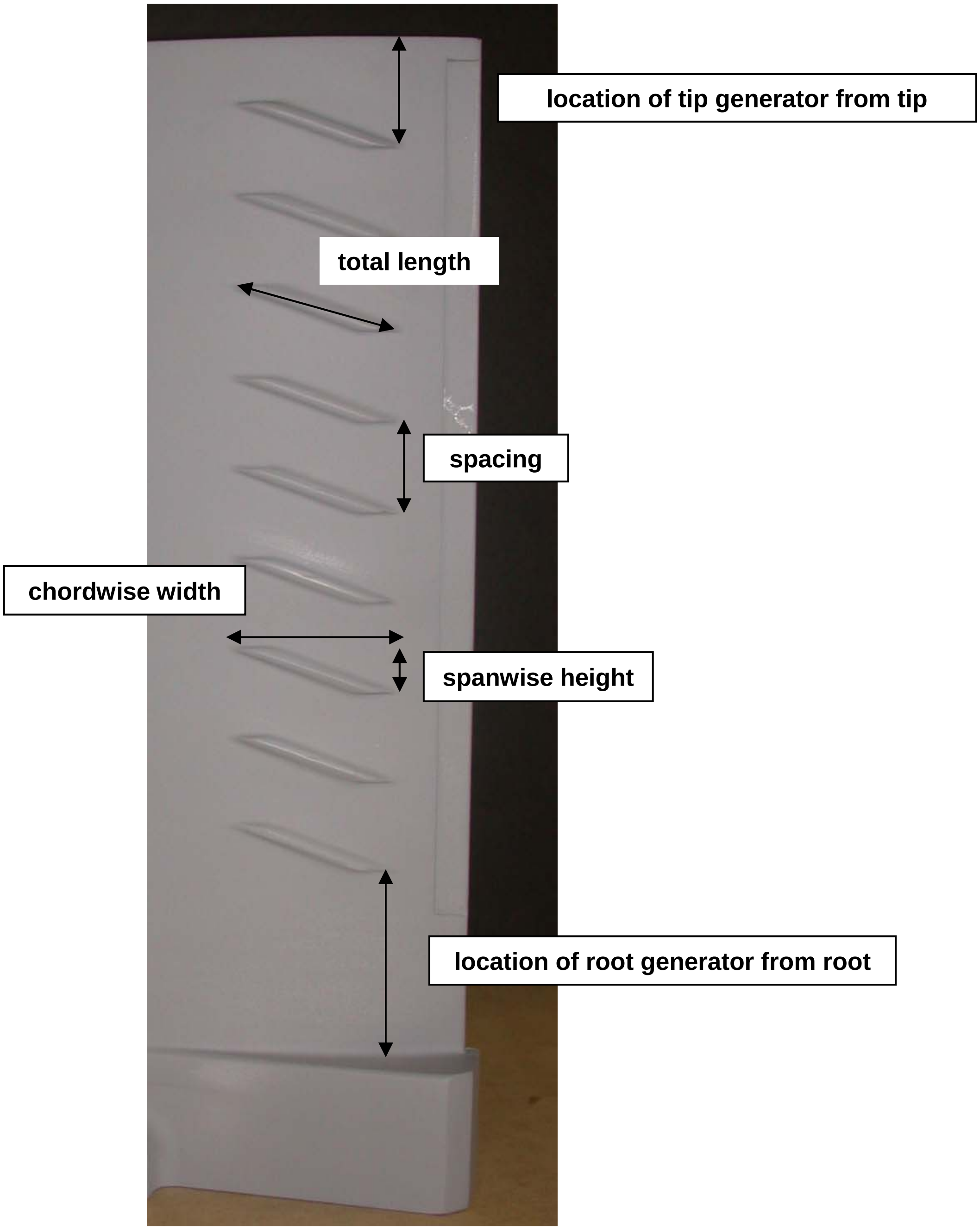

Figure 2-42: Location of Kuethe vane generators and their geometry

Figure 2-43: Heat exchanger box with face of air conditioner exposed

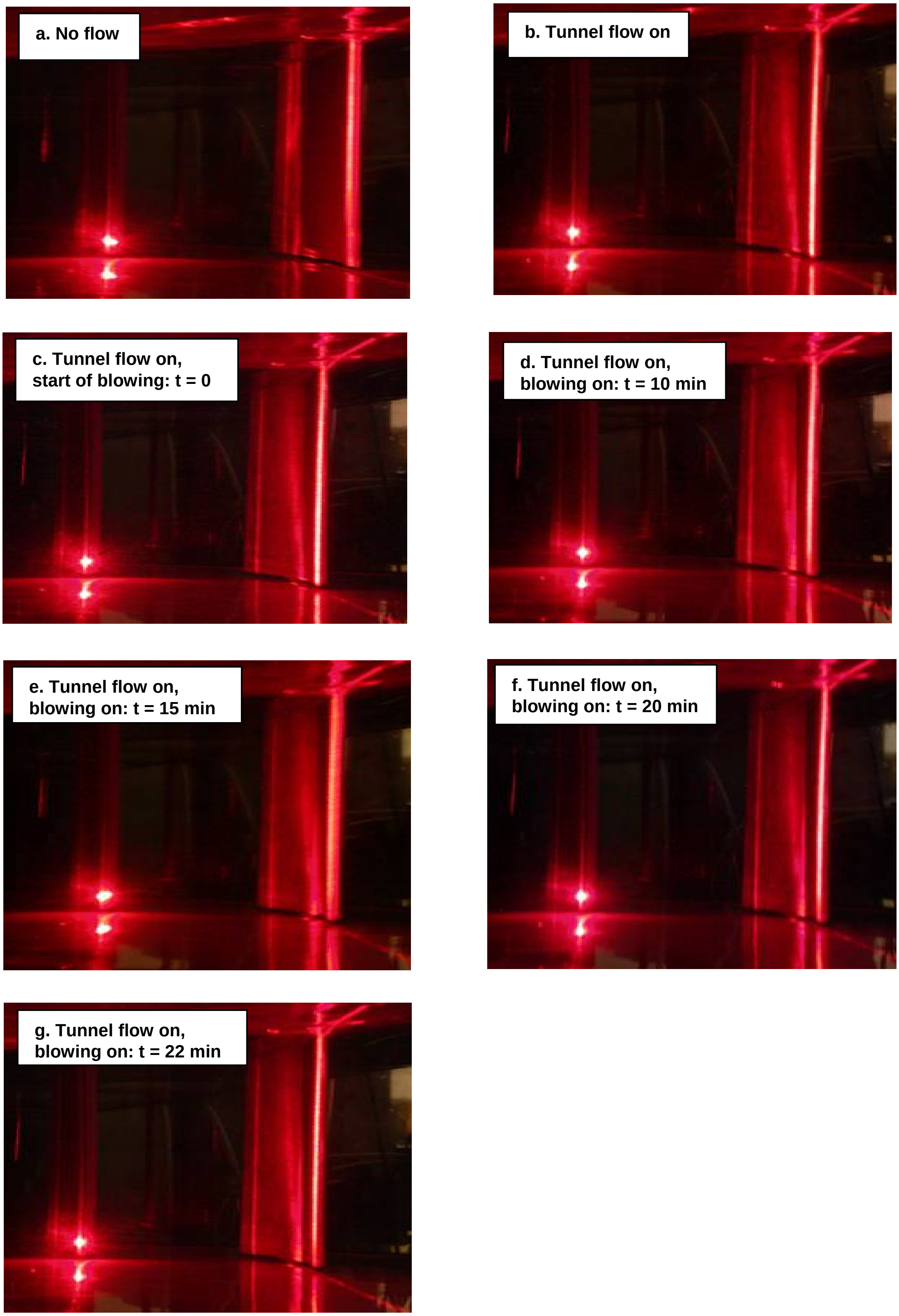

Figures 2-44a – 2-44g: Results of aligning a laser beam with the trailing-edge of blade five, indicating a deflection of the blade over time

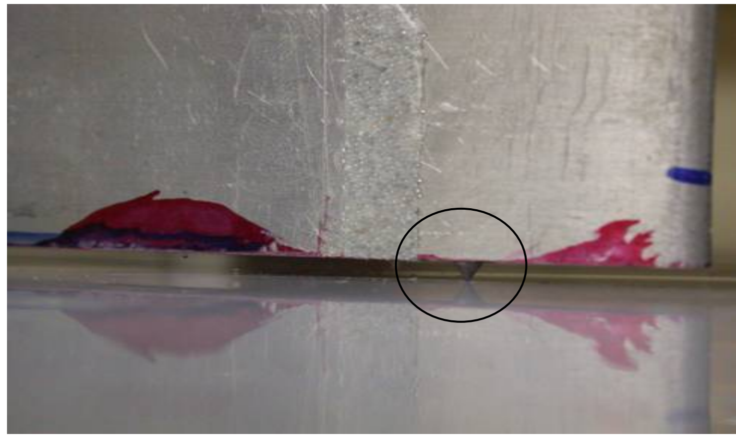

Figure 2-45: Location of leading-edge stabilizing pin on non-blowing baseline blades

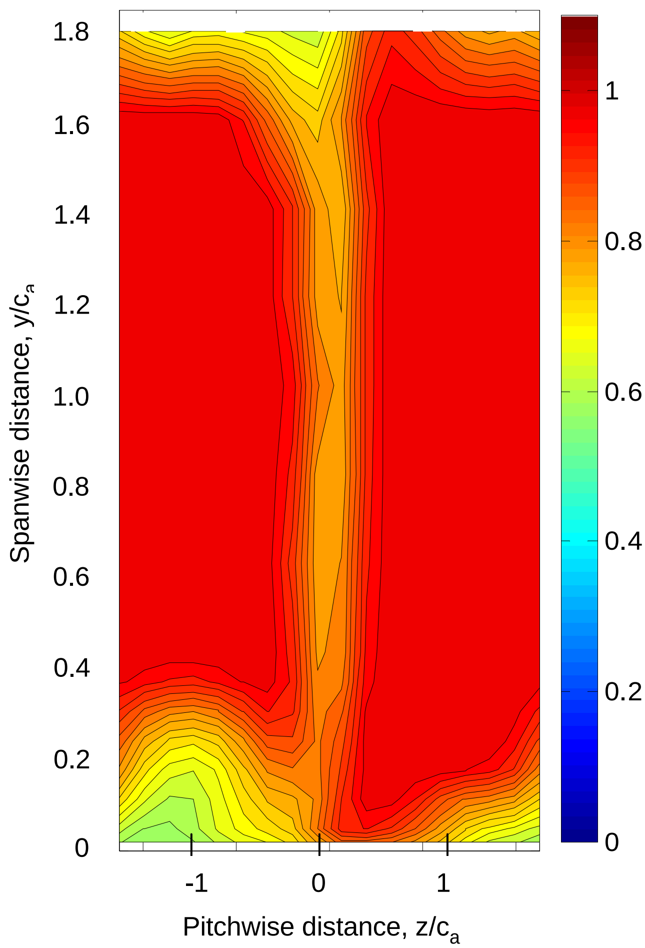

Figure 2-46: C_{p0} cross-section at x/c_a = 0.839 of non-blowing baseline with stabilizing pins for 0.004125c tip-gap

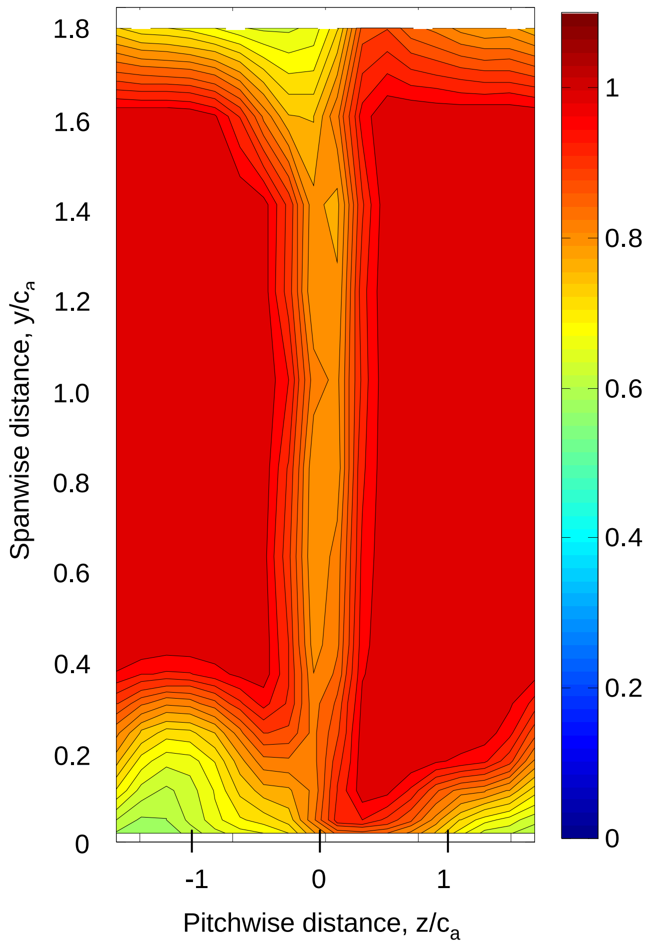

Figure 2-47: C_{p0} cross-section at $x/c_a = 0.839$ of non-blowing baseline without stabilizing pins for 0.004125*c* tip-gap

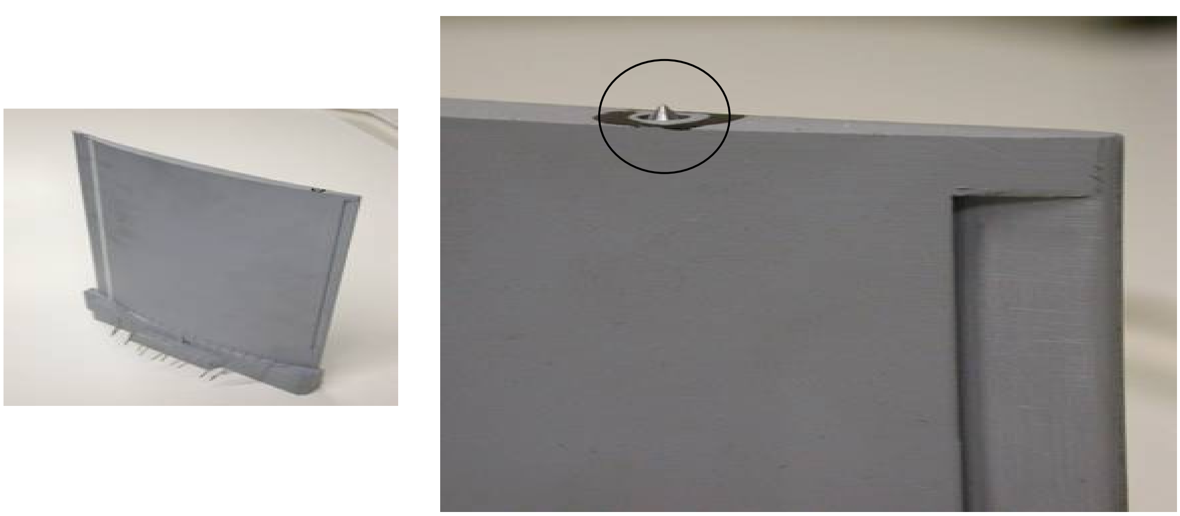

Figure 2-48: Location of trailing-edge stabilizing pin on simple blowing blades

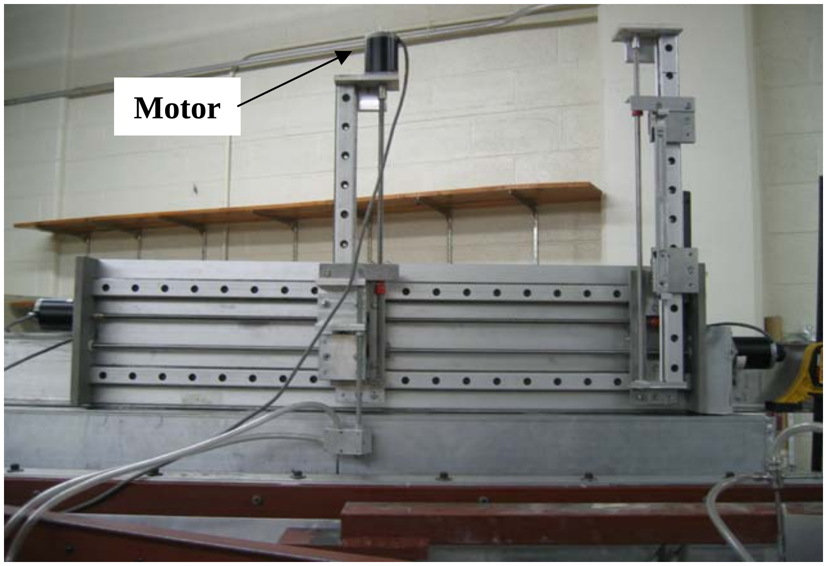

Figure 2-49: Three-axis traverse system

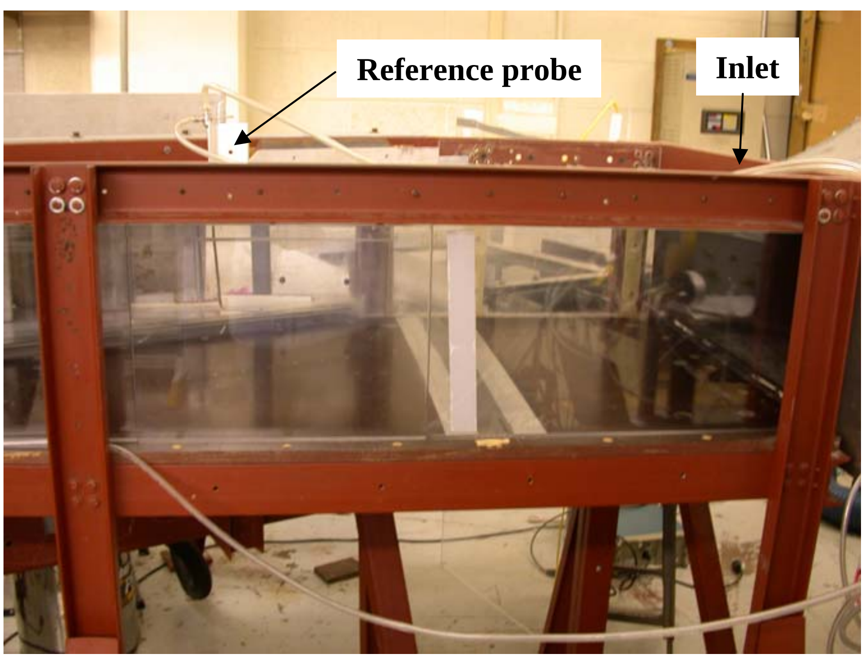

Figure 2-50: Reference Pitot-static probe fixed in the inlet section

Figure 2-51: Dwyer Instruments Standard Model 160 Pitot-static probe (Model 167-12) with 304.8mm shaft length and 76.2mm tip length

Figure 2-52: Bent Pitot probe used for cascade inflow measurements

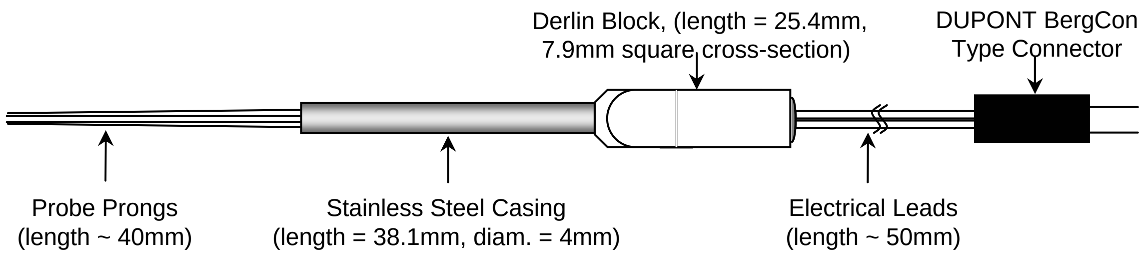

Figure 2-53: Miniature Kovaznay type four-sensor hot-wire probe, type AVOP-4-100 manufactured by Auspex Corporation

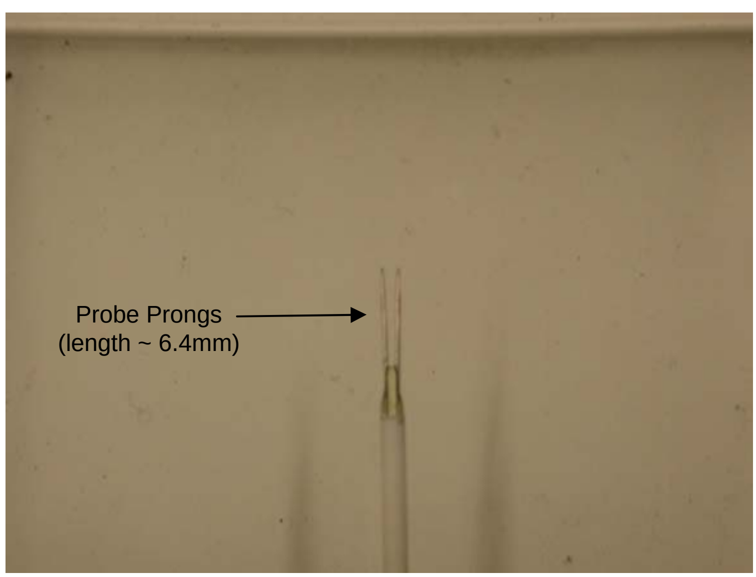

Figure 2-54: Auspex Corporation single-wire probe

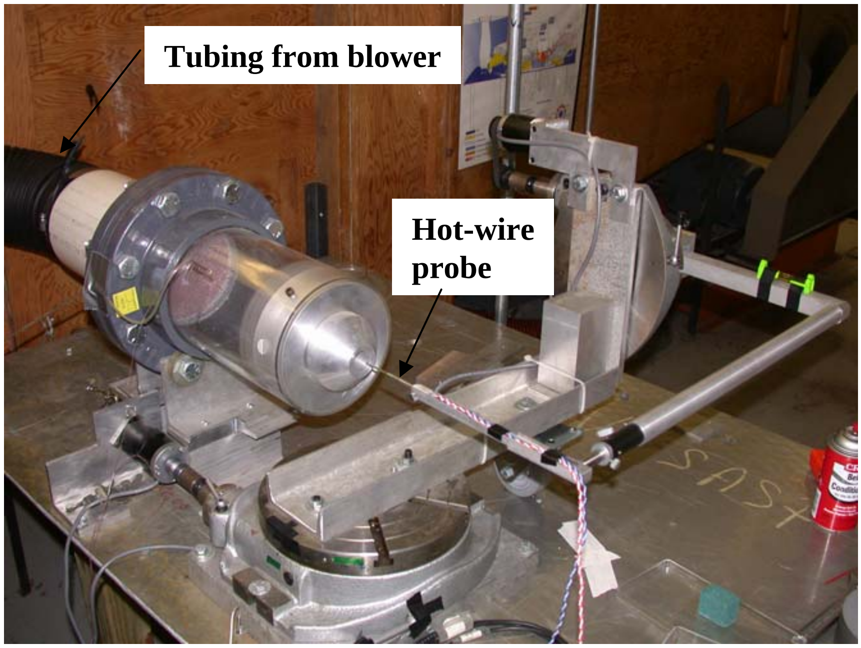

Figure 2-55: Hot-wire probe in calibration jet

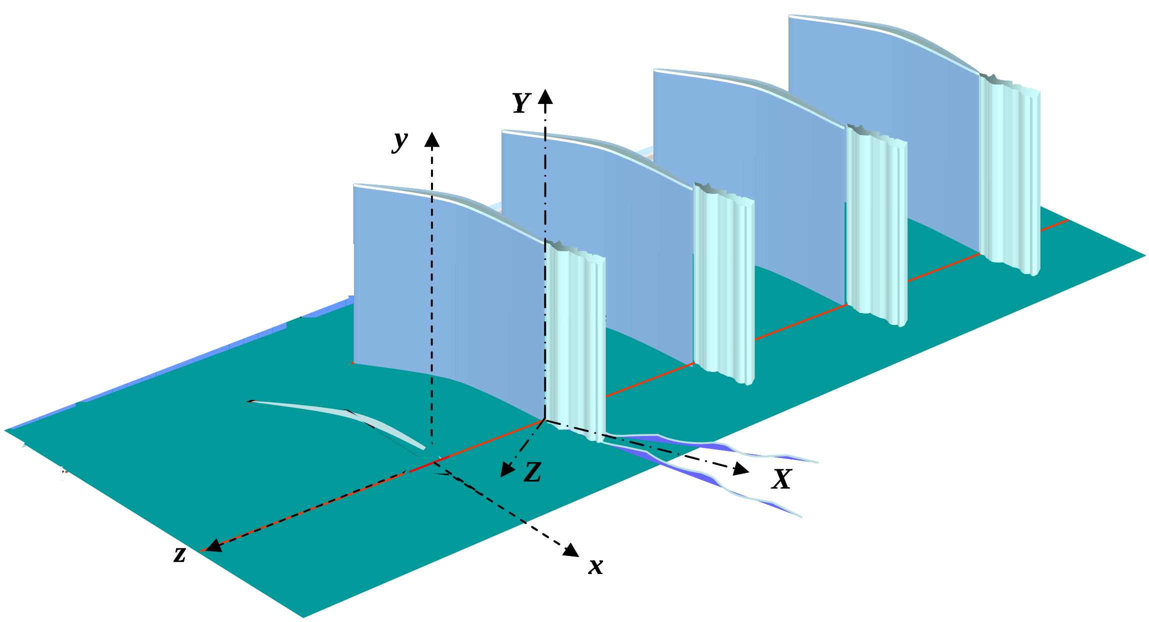

Figure 2-56:

- - - - - - - - - -	***cascade coordinate system (x,y,z)***
–·–·–·–·–	***wake-aligned coordinate system (X,Y,Z)***

Both coordinate systems referenced to the trailing-edge of blade five

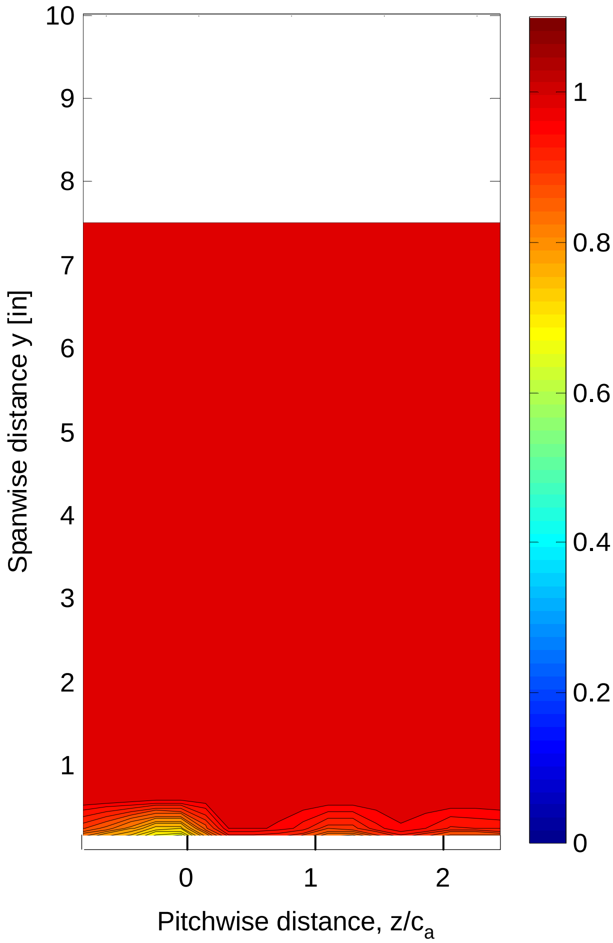

Figure 2-57: U/U_{ref} cascade inflow for the simple blowing blades

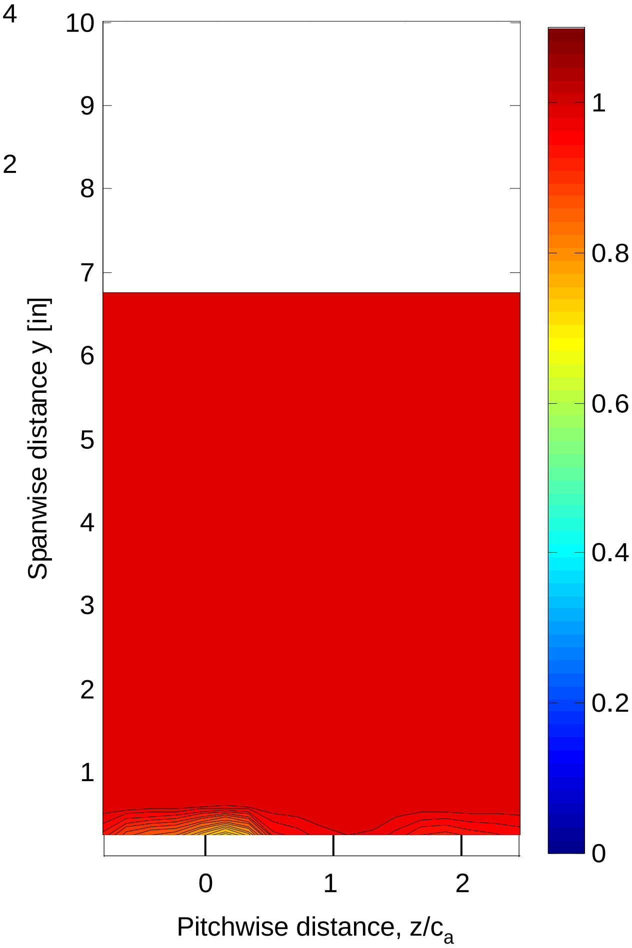

Figure 2-58: U/U_{ref} cascade inflow for the Kuethe vane blades

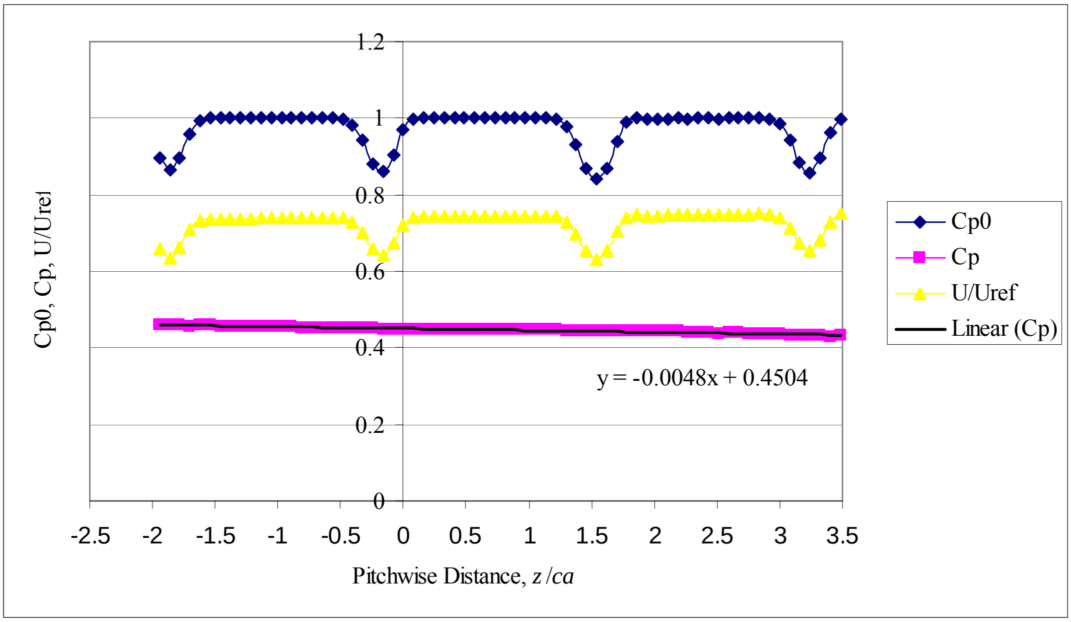

Figure 2-59: Simple blowing mid-span pitchwise pressure and velocity distributions (passive suction) at x/c_a = 1.877

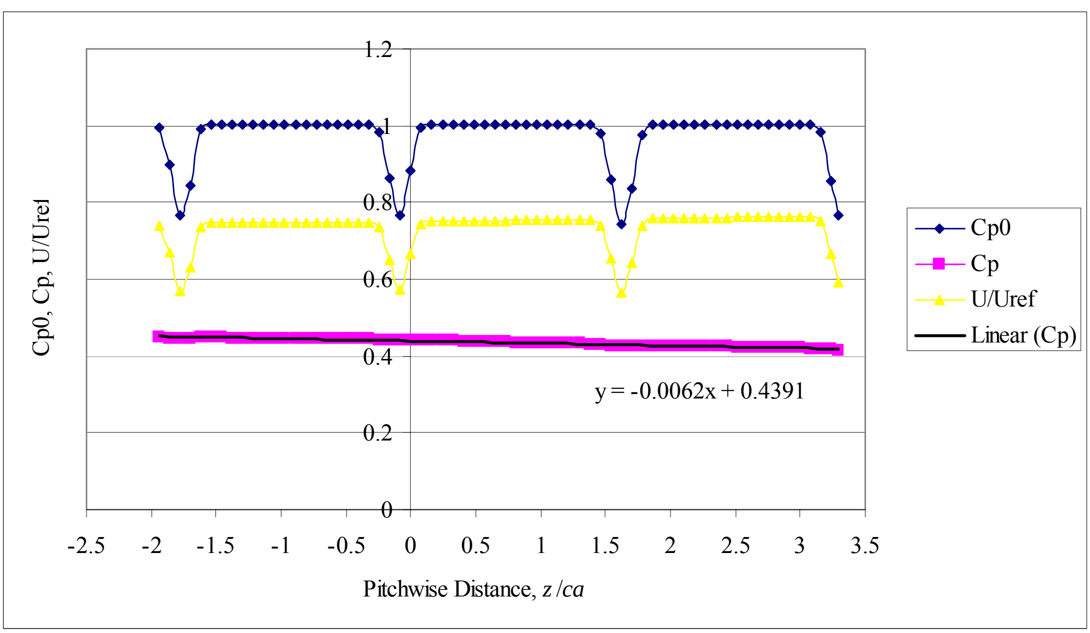

Figure 2-60: Simple blowing mid-span pitchwise pressure and velocity distributions (1.4%) at x/c_a = 1.877

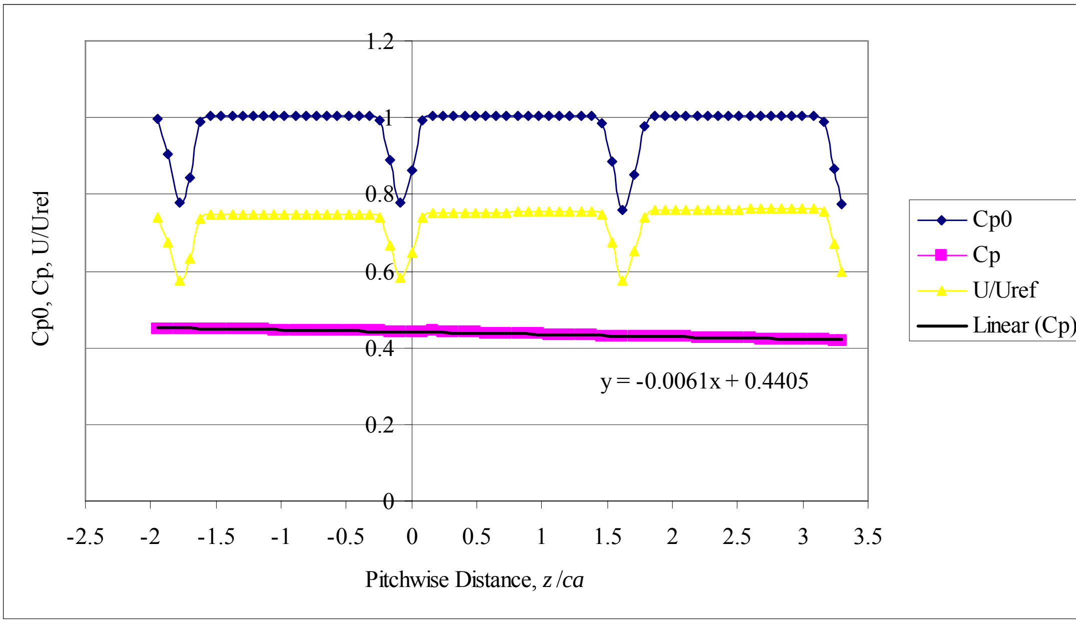

Figure 2-61: Simple blowing mid-span pitchwise pressure and velocity distributions (1.5%) at $x/c_a = 1.877$

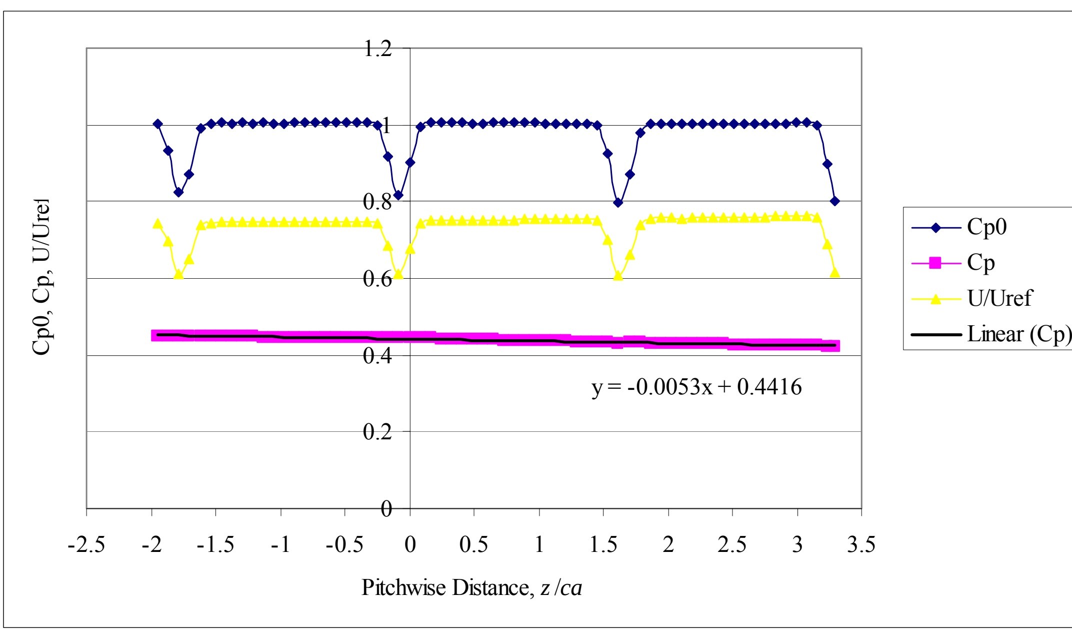

Figure 2-62: Simple blowing mid-span pitchwise pressure and velocity distributions (1.7%) at $x/c_a = 1.877$

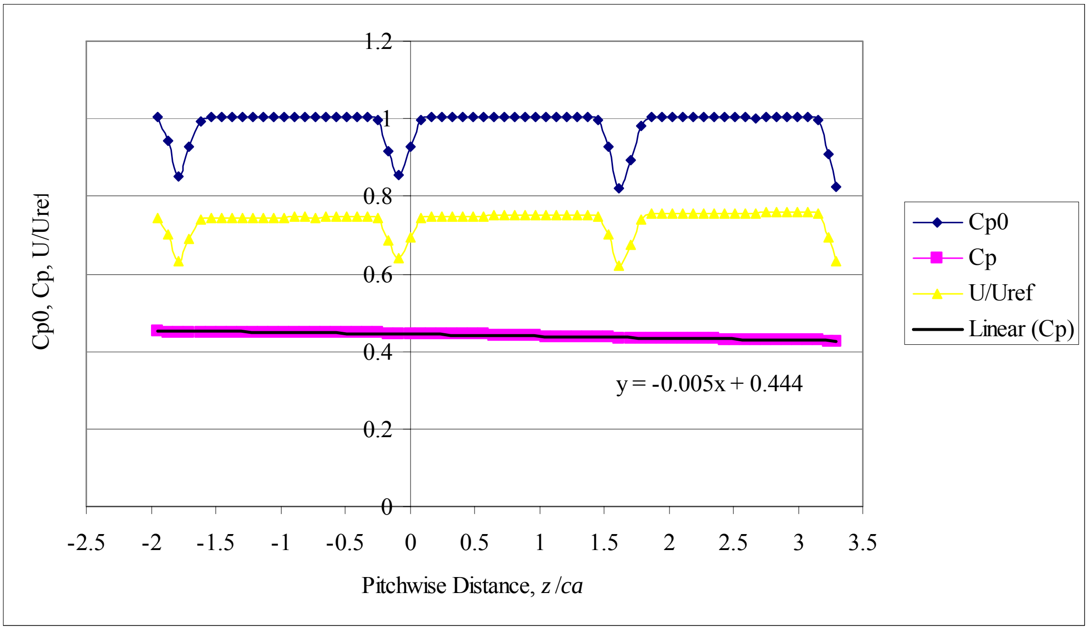

Figure 2-63: Simple blowing mid-span pitchwise pressure and velocity distributions (1.9%) at $x/c_a = 1.877$

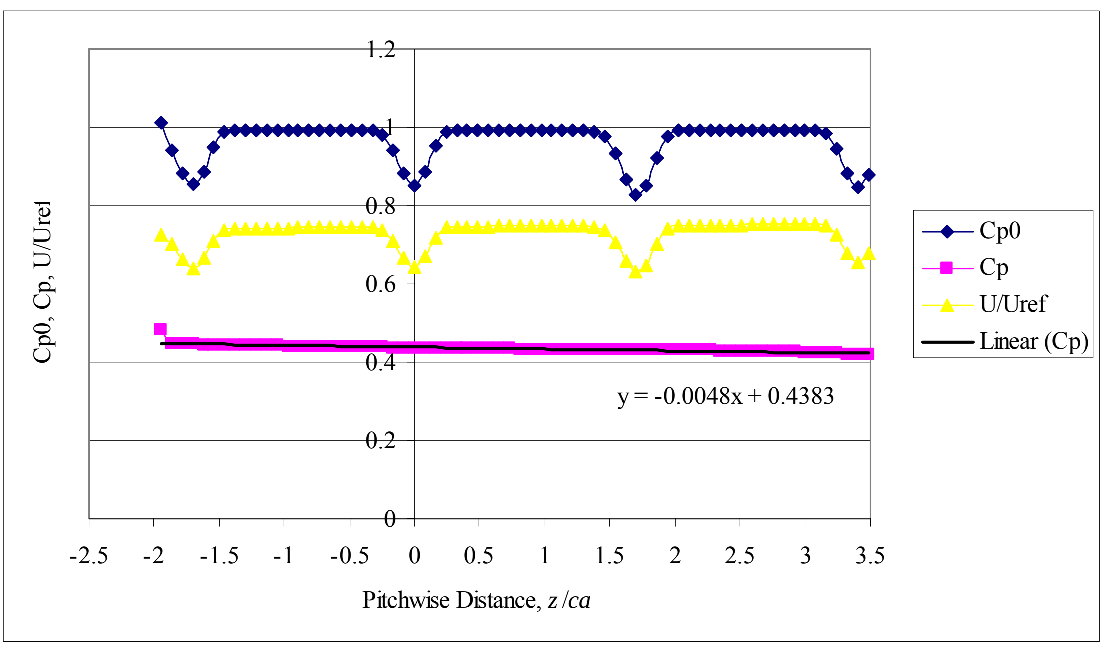

Figure 2-64: Simple blowing mid-span pitchwise pressure and velocity distributions (2.0%) at $x/c_a = 1.877$

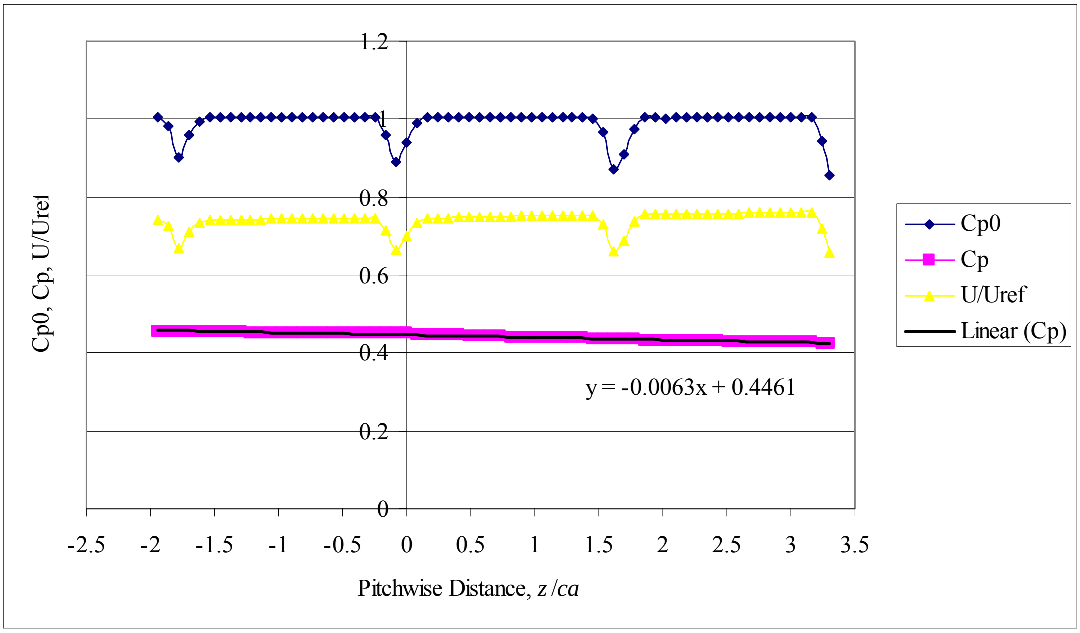

Figure 2-65: Simple blowing mid-span pitchwise pressure and velocity distributions (2.1%) at x/c_a = 1.877

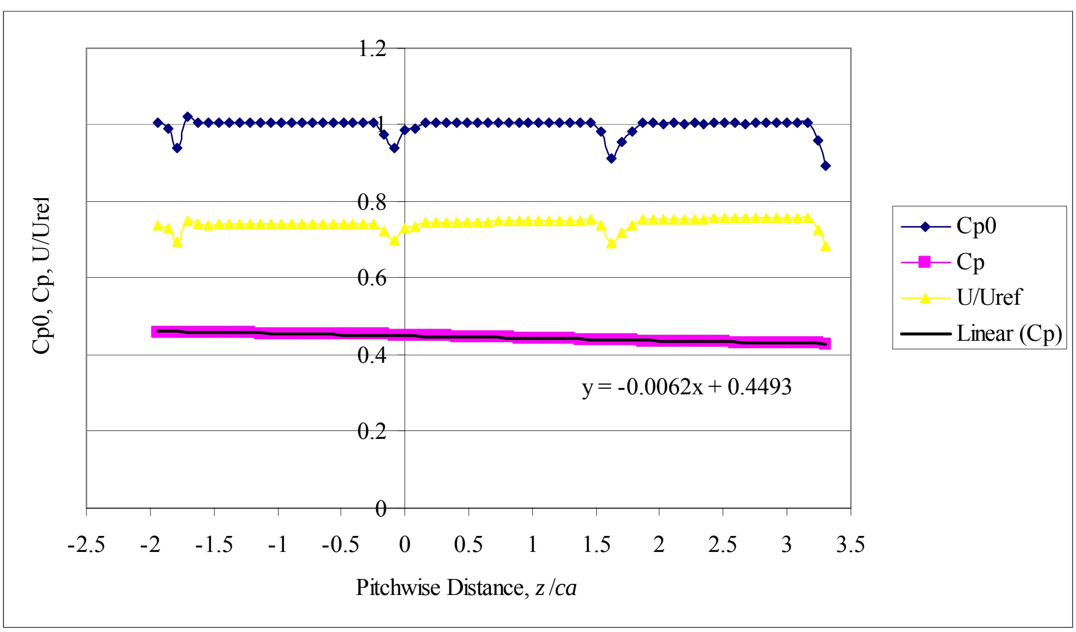

Figure 2-66: Simple blowing mid-span pitchwise pressure and velocity distributions (2.3%) at x/c_a = 1.877

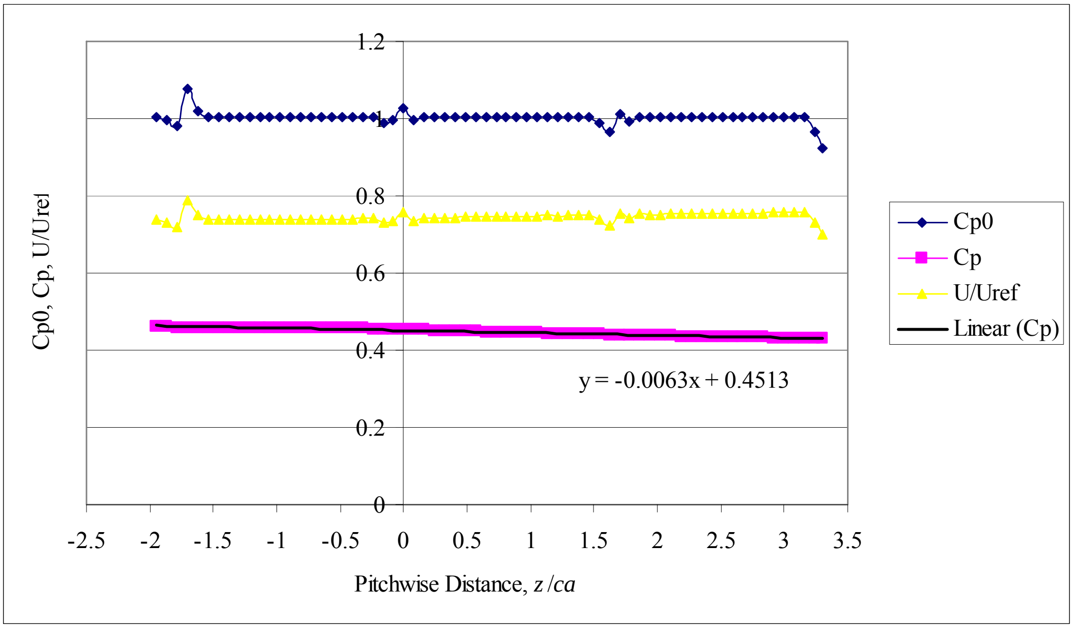

Figure 2-67: Simple blowing mid-span pitchwise pressure and velocity distributions (2.5%) at x/c_a = 1.877

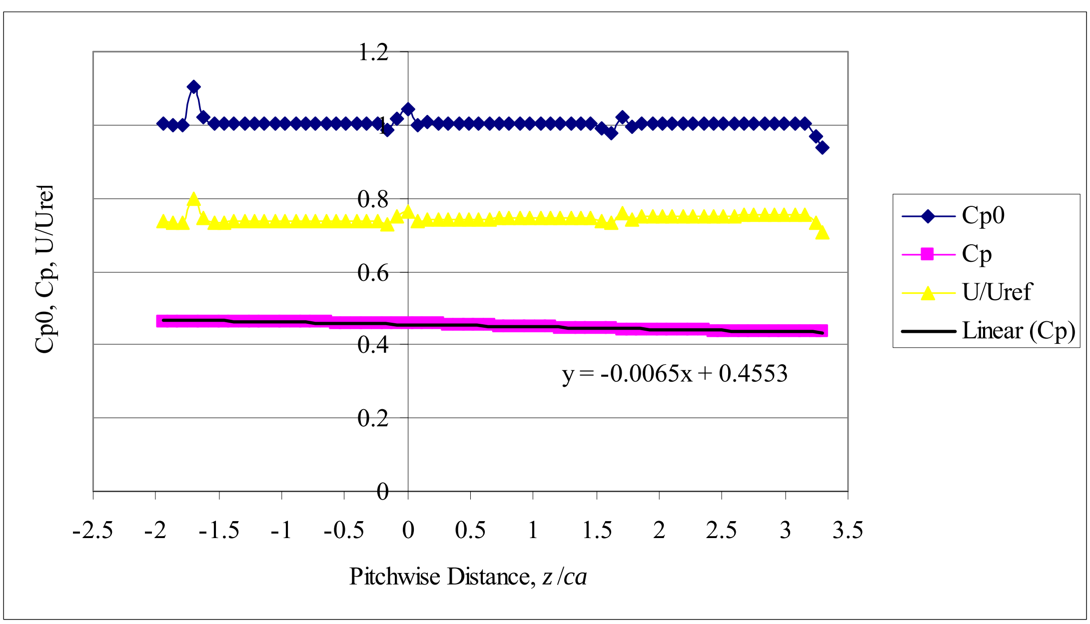

Figure 2-68: Simple blowing mid-span pitchwise pressure and velocity distributions (2.6%) at x/c_a = 1.877

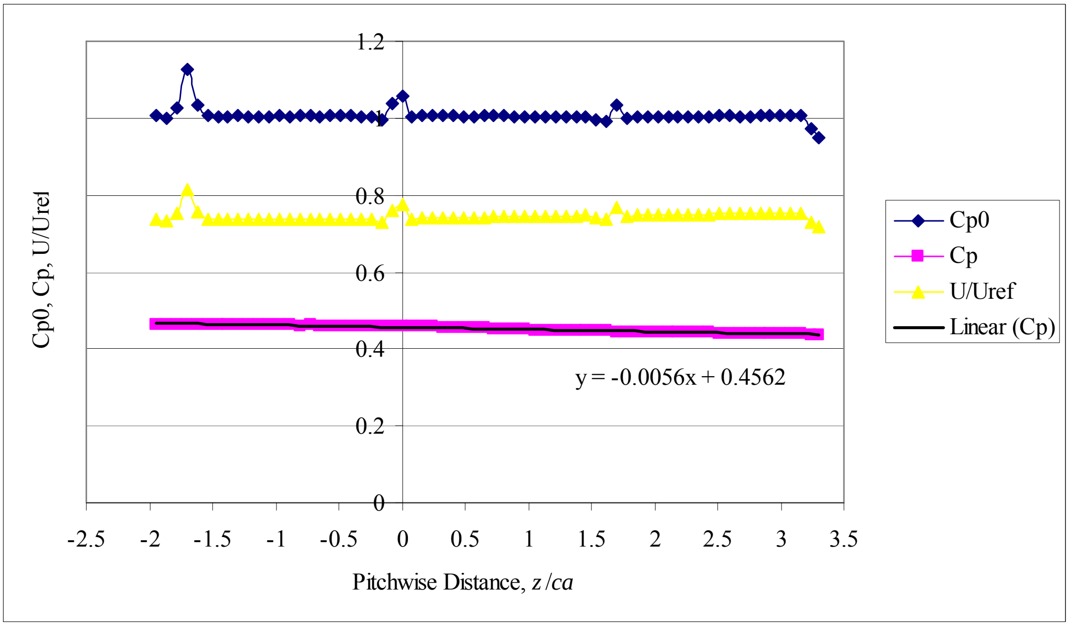

Figure 2-69: Simple blowing mid-span pitchwise pressure and velocity distributions (2.7%) at x/c_a = 1.877

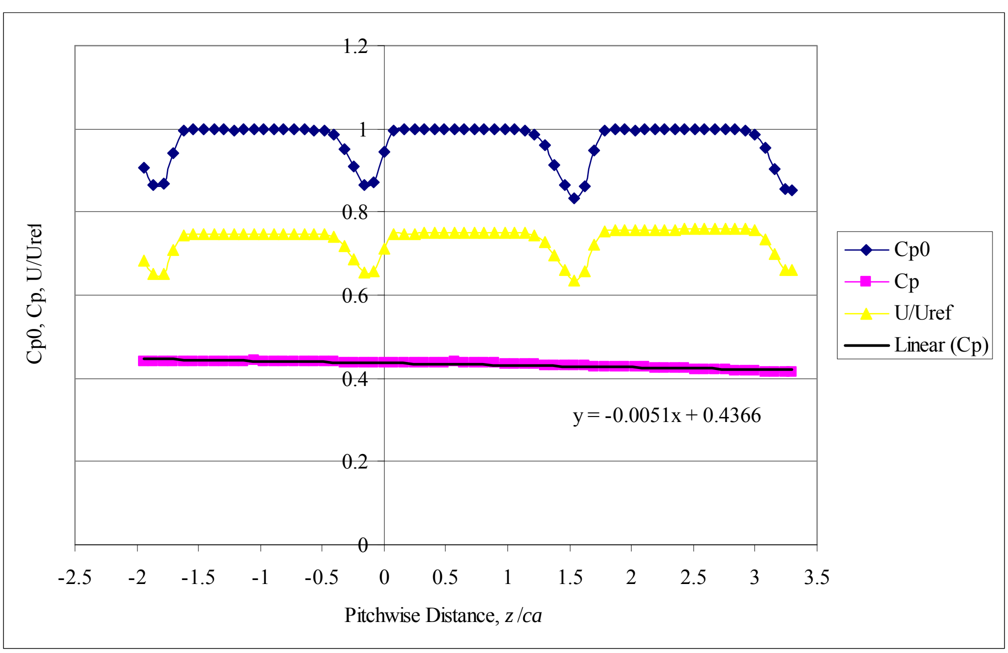

Figure 2-70: Kuethe vane mid-span pitchwise pressure and velocity distributions (passive suction) at x/c_a = 0.839

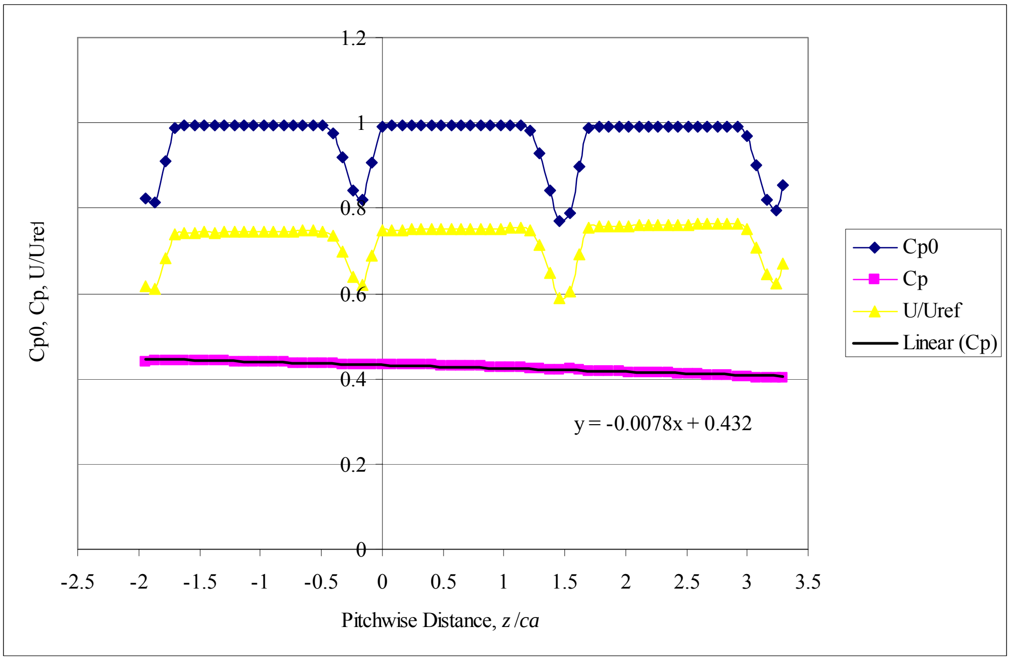

Figure 2-71: Kuethe vane mid-span pitchwise pressure and velocity distributions (1.4%) at x/c_a = 0.839

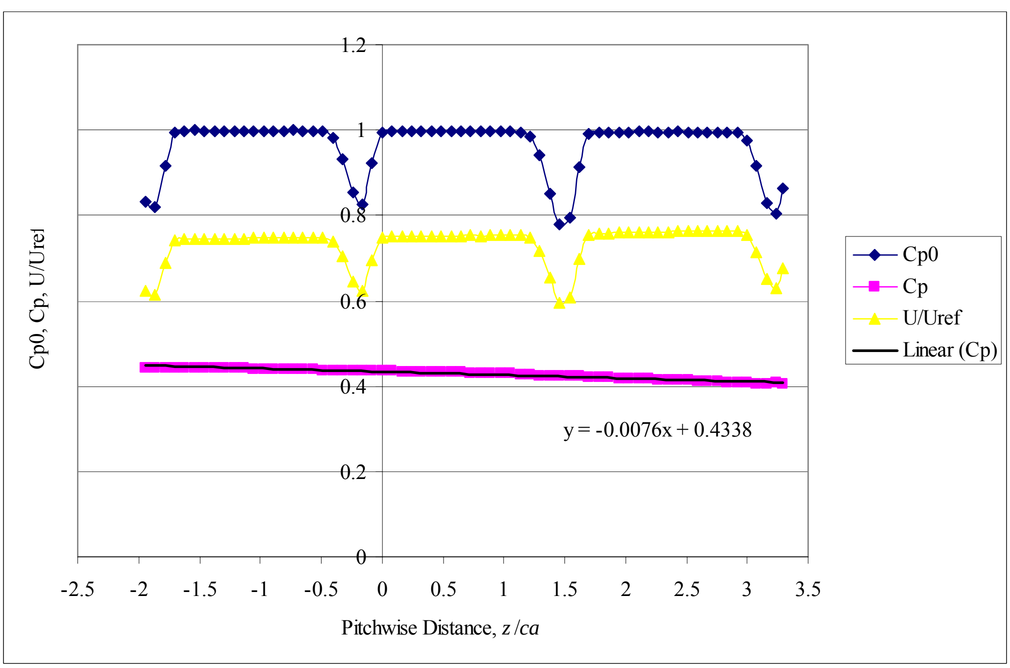

Figure 2-72: Kuethe vane mid-span pitchwise pressure and velocity distributions (1.5%) at x/c_a = 0.839

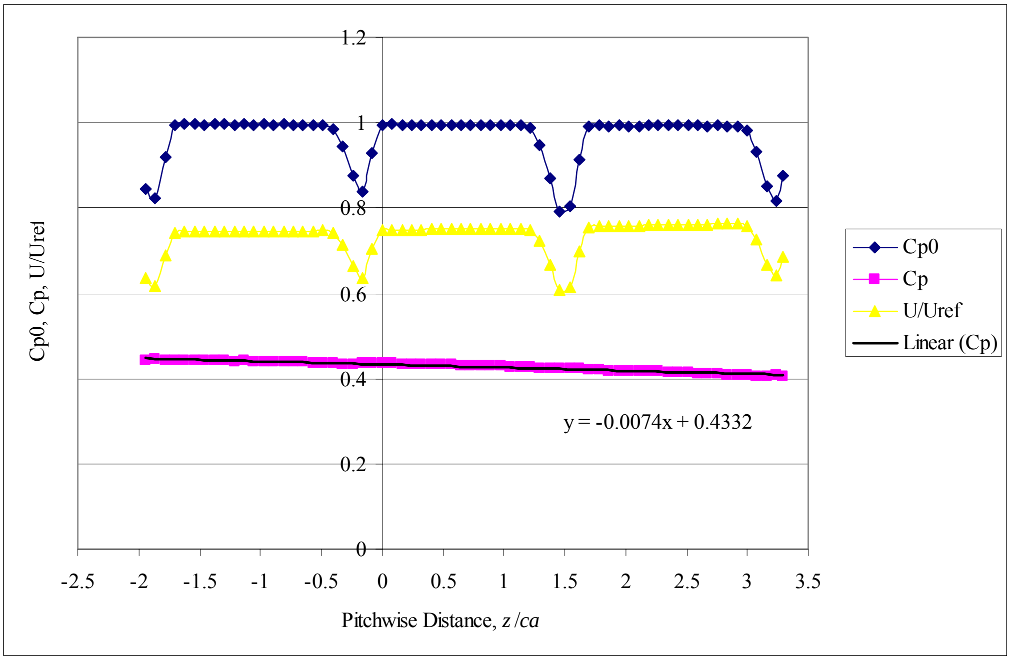

Figure 2-73: Kuethe vane mid-span pitchwise pressure and velocity distributions (1.7%) at x/c_a = 0.839

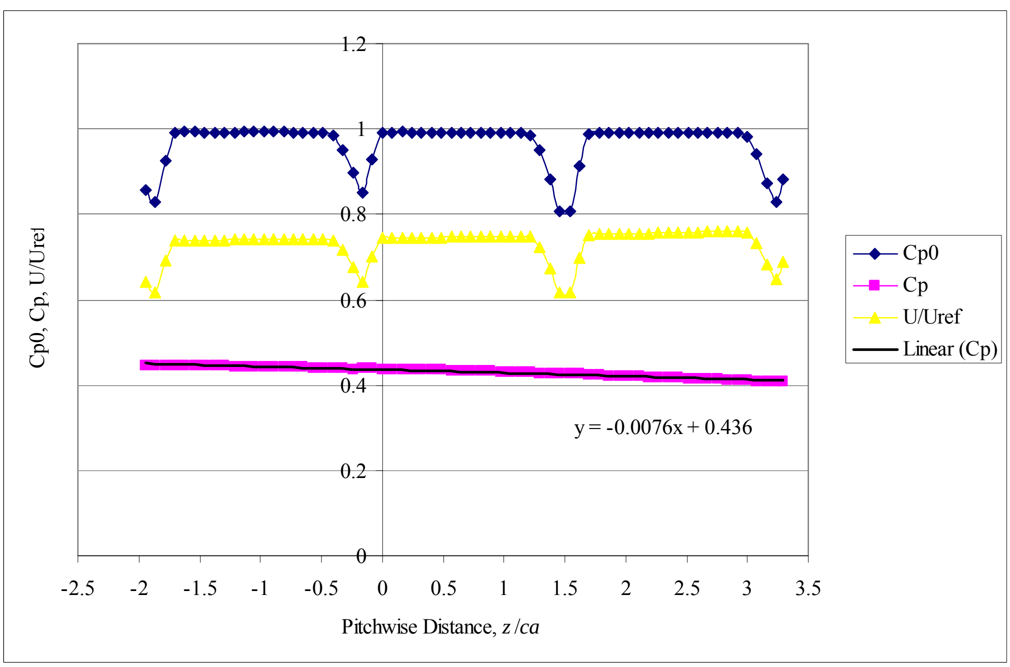

Figure 2-74: Kuethe vane mid-span pitchwise pressure and velocity distributions (1.9%) at x/c_a = 0.839

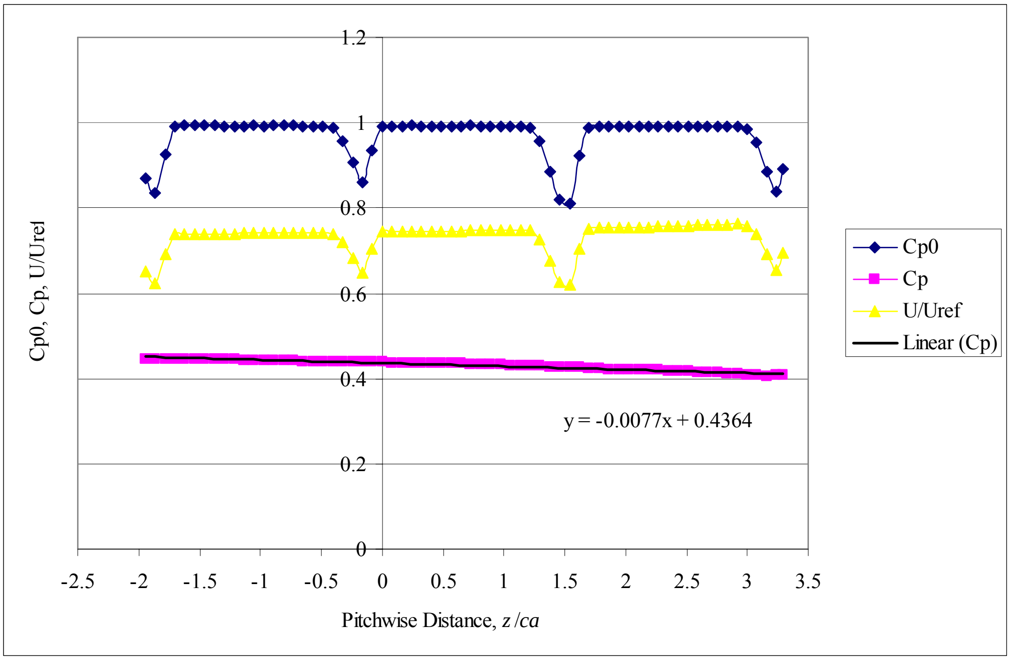

Figure 2-75: Kuethe vane mid-span pitchwise pressure and velocity distributions (2.0%) at $x/c_a = 0.839$

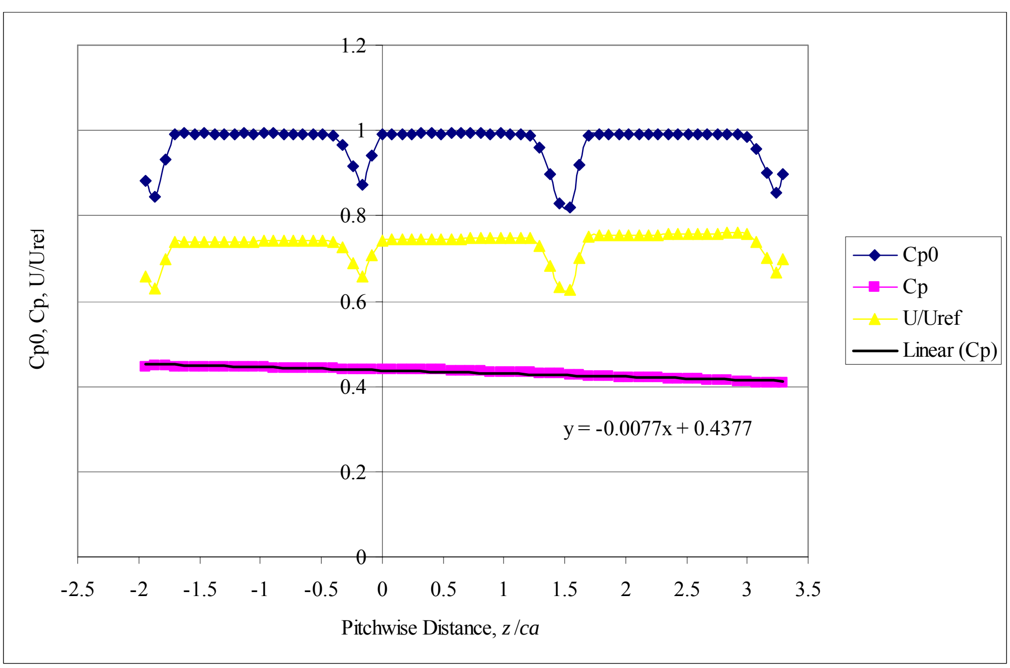

Figure 2-76: Kuethe vane mid-span pitchwise pressure and velocity distributions (2.1%) at $x/c_a = 0.839$

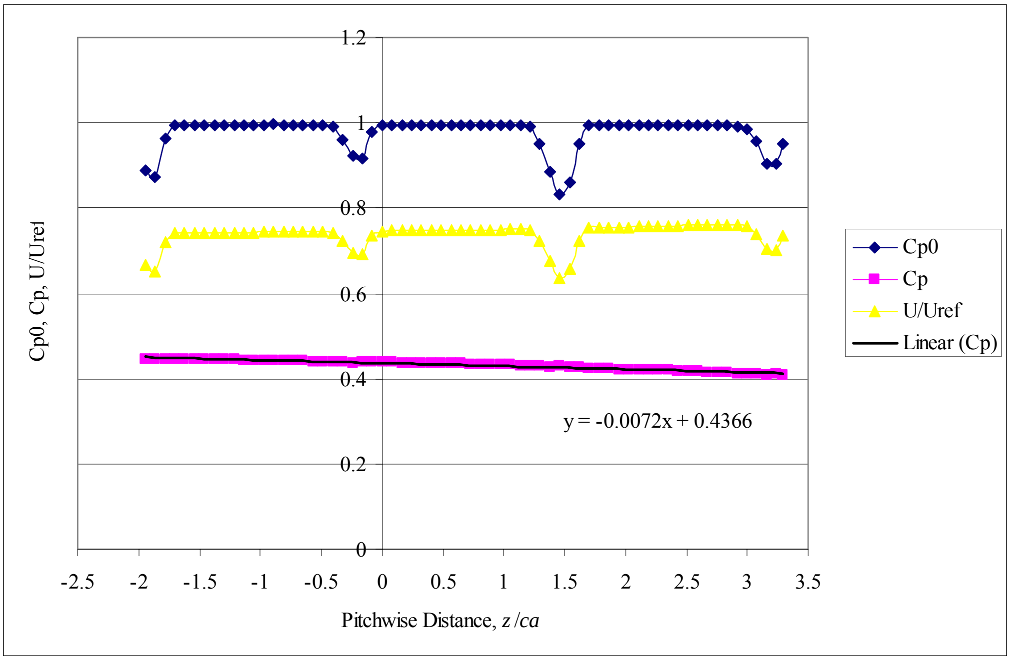

Figure 2-77: Kuethe vane mid-span pitchwise pressure and velocity distributions (2.3%) at $x/c_a = 0.839$

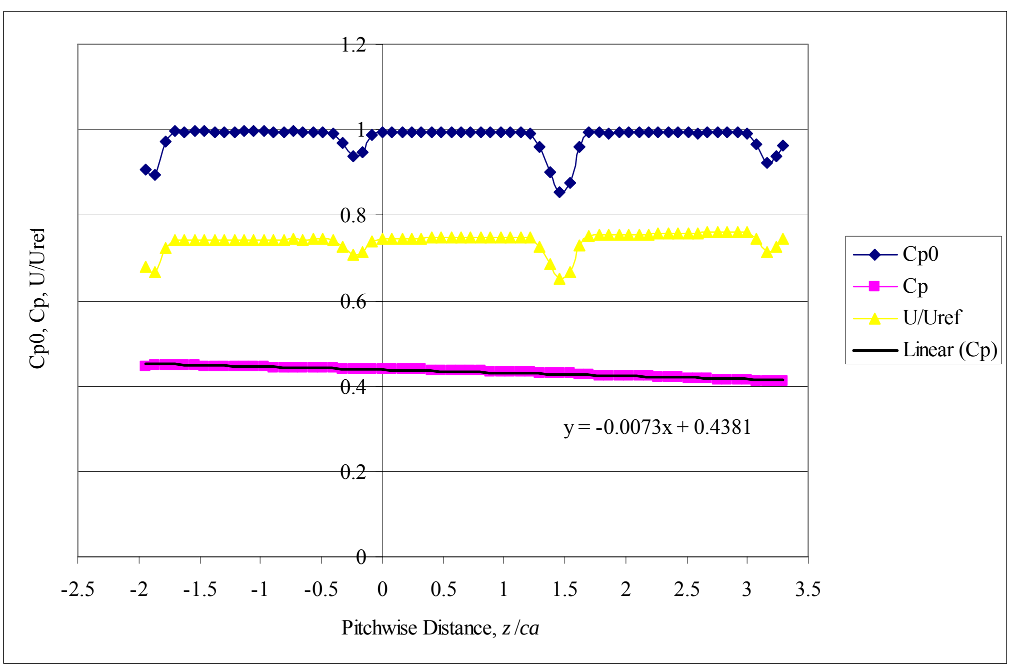

Figure 2-78: Kuethe vane mid-span pitchwise pressure and velocity distributions (2.5%) at $x/c_a = 0.839$

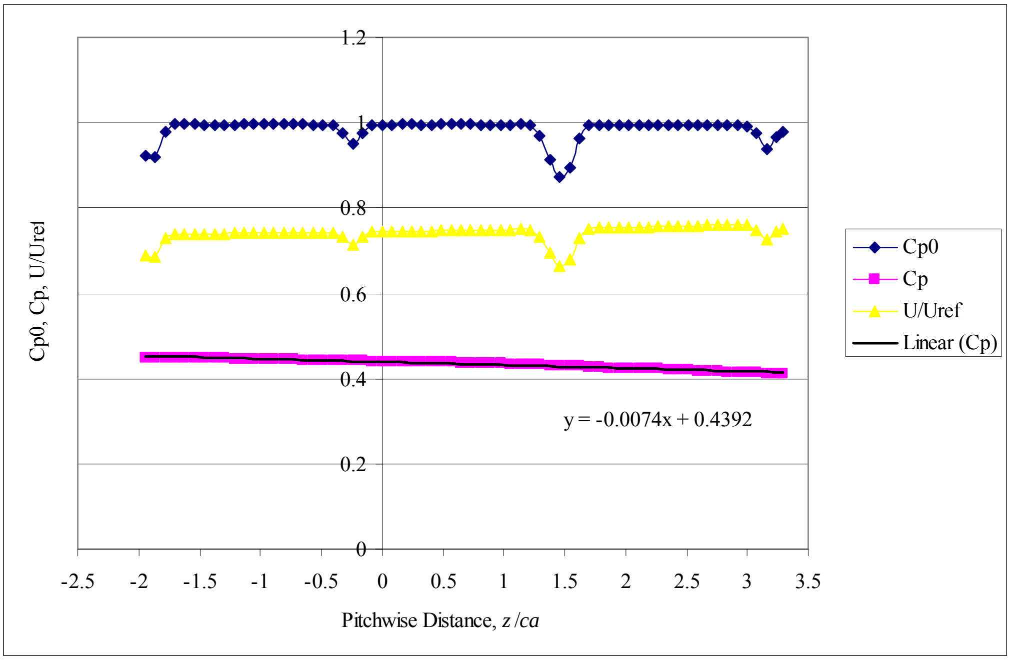

Figure 2-79: Kuethe vane mid-span pitchwise pressure and velocity distributions (2.6%) at $x/c_a = 0.839$

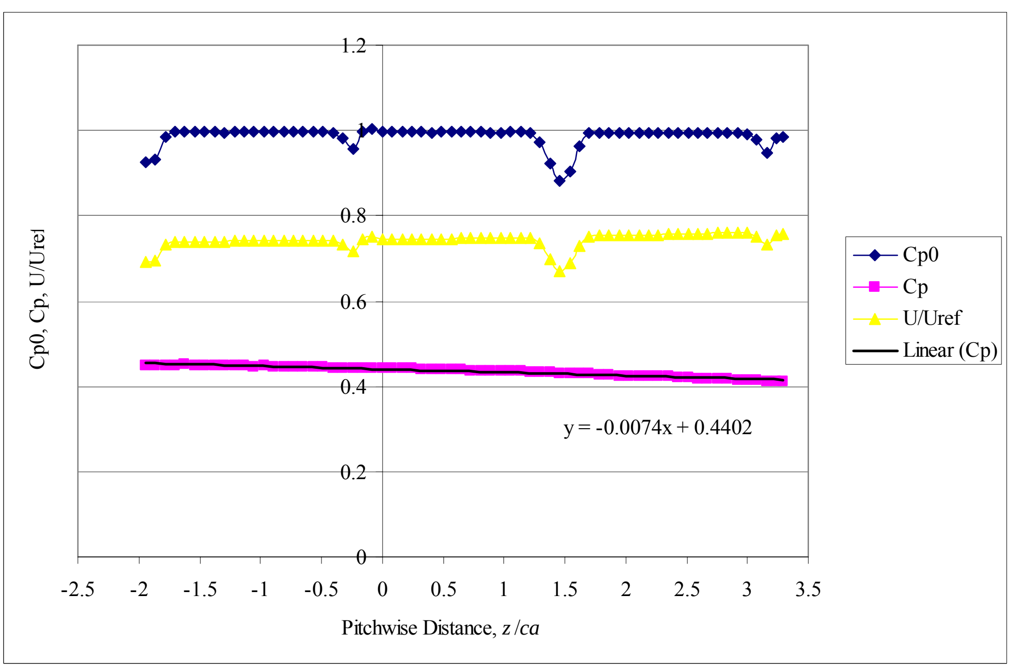

Figure 2-80: Kuethe vane mid-span pitchwise pressure and velocity distributions (2.7%) at $x/c_a = 0.839$

3. ANALYSIS OF BASELINE GE ROTOR B BLADES

3.1 Introduction

In order to discuss the effectiveness of trailing-edge blowing, the cascade tunnel flow with the baseline GE Rotor B blades must first be examined. Blade loading was measured, Pitot-static cross-sectional measurements were made at downstream locations of 0.839 and 1.877 x/c_a, and four-sensor hot-wire mid-span measurements were made at 0.608, 1.178, 1.819 and 2.384 x/c_a. The data presented in this chapter is a combination of that of Geiger (2005) and data taken as part of the present study.

3.2. Presentation of Figures Produced by Geiger (2005)

3.2.1. Pitot-Static Full Cross-Sections

In order to address a more complete set of data on the baseline blades, the cross-sectional plots of the total pressure coefficient (C_{p0}) of blade five created by Geiger (2005) are presented in Figures 3-1 through 3-4. They show the Pitot-static measurements that were made at downstream locations of both 0.839 and 1.877 x/c_a. The pitchwise distance normalized on the axial chord is on the horizontal axis, while the normalized spanwise distance is on the vertical axis. The flow is seen as looking upstream, with the pressure side on the left of the figure and the suction side on the right. The blade is vertical and the tip-gap of 0.0165c at the bottom of the figure. The top of the figure would represent the hub of a real fan, and the bottom would represent the tip. Mid-span is marked by the horizontal dashed line.

In Figure 3-1 of C_{p0} at x/c_a = 0.839, the wake centerline is slightly curved because of the vorticity from the end-walls induced on the wake. Between 0.608 y/c_a and 1.178 y/c_a, the wake is relatively two-dimensional. The upper end-wall boundary layer is of inconsistent thickness, reaching $0.18c_a$ on the suction side but a minimum of $0.082c_a$ on the pressure side. In the lower left of the figure, the tip-leakage vortex shed from blade four is present as a region of low pressure coefficient on the pressure side of blade five. The location of the vortex center is approximately 1.25 z/c_a and 0.15 y/c_a. The normalized streamwise velocity, U/U_{ref}, is shown in Figure 3-2. The same characteristics of Figure 3-1 are found here. The velocity along the wake centerline is approximately $0.56U_{ref}$, while the velocity outside the wake is $0.76U_{ref}$. The lowest velocity is in the vortex center, with a value of $0.35U_{ref}$.

Several alterations to the wake are noticeable by $x/c_a = 1.877$. From Figure 3-3 of the total pressure coefficient, the wake width is larger and the pressure in the vortex center has increased. The wake is still curved and thicker on the suction side, and it remains two-dimensional in the mid-span region. Also, the upper end-wall boundary layer is about the same thickness as at $x/c_a = 0.839$. In Figure 3-4 of the normalized velocity, the velocity outside of the wake is still $0.76U_{ref}$, although the centerline velocity has increased slightly to $0.60U_{ref}$. The vortex center velocity has changed from $0.35U_{ref}$ at $x/c_a = 0.839$ to $0.51U_{ref}$ at $x/c_a = 1.877$.

3.3. Analysis of Baseline Data from Geiger (2005)

3.3.1. Blade Loading

Blade loading was measured by Geiger (2005) using the static pressure ports on the blades forming the center passage of the cascade. The ports are located 127mm from the blade tip, and the instrumentation is described in Section 2.4.2. The pressure coefficient can be calculated from the measured static pressure as follows:

$$C_p = \frac{P - P_\infty}{P_{0\infty} - P_\infty} \qquad \text{Eqn. 3-1}$$

where P is the measured static pressure, P_∞ is the freestream static pressure, P_0 is the measured total pressure, and $P_{0\infty}$ is the freestream total pressure. Figure 3-5 shows C_p plotted at each pressure port location, normalized on the total chord, c, for a tip-gap of 0.0165c.

Small fluctuations in pressure coefficient are visible between the leading-edge and 0.15c, on both the pressure and suction sides of the blade due to the trip strip at 0.10c. Following the analysis of Geiger (2005), the suction side shows a favorable pressure gradient from the leading-edge up to 0.22c, where the pressure coefficient reaches a minimum value of -0.24. After this point, an adverse pressure gradient continues over the remainder of the blade until the maximum suction side pressure coefficient of 0.30 is reached near the trailing-edge. After 0.15c on the pressure side, the pressure coefficient increases steadily to a maximum of 0.49 at roughly 0.70c. From this point onwards, the pressure decreases, presumably in an effort to match the value at the trailing-edge of the suction side.

The circulation around the blade can be calculated by the following equation:

$$\Gamma = \oint U \bullet dS \qquad \text{Eqn. 3-2}$$

where dS is the differential blade length and the local velocity, U, is determined from Bernoulli's equation:

$$\frac{U}{U_{ref}} = \sqrt{1 - C_p} \qquad \text{Eqn. 3-3}$$

The circulation calculated by Geiger (2005) is $0.45 U_{ref} c_a$.

3.3.2. Wake Mid-Span Profiles

Geiger (2005) made velocity measurements behind the blade mid-span at downstream locations of 0.608, 1.178, 1.819 and 2.382 x/c_a. The fluid velocity has two components, expressed through Reynolds decomposition as:

$$U(x,t) = \overline{U(x,t)} + u(x,t) \qquad \text{Eqn. 3-4}$$

where $U(x,t)$ is the velocity, $\overline{U(x,t)}$ is the mean velocity and $u(x,t)$ is the fluctuating velocity. The four-sensor hot-wire measures both the mean and fluctuating velocity fields in the cascade.

After taking the mean of the momentum equation and substituting the Reynolds decomposition, the non-linear term $\overline{U_i U_j}$ becomes:

$$\overline{U_i U_j} = \overline{U_i}\,\overline{U_j} + \overline{u_i}\,\overline{u_j} \qquad \text{Eqn. 3-5}$$

The velocity covariances, $\overline{u_i}\,\overline{u_j}$, are referred to as Reynolds stresses, which can be expressed in matrix form as:

$$u_i u_j = \begin{bmatrix} \overline{u'u'} & \overline{u'v'} & \overline{u'w'} \\ \overline{v'u'} & \overline{v'v'} & \overline{v'w'} \\ \overline{w'u'} & \overline{w'v'} & \overline{w'w'} \end{bmatrix} \qquad \text{Eqn. 3-6}$$

The diagonal elements are the normal stresses and the non-diagonal elements are the shear stresses, which are symmetrical about the diagonal. The Reynolds stresses are used to quantify the turbulence of the flow (Pope, 2001).

In the following sections, the mid-span velocity profiles are provided along with definitions and descriptions of the wake parameters. The associated Reynolds stresses and turbulent kinetic energy are shown as well.

3.3.2.1. *Mean Velocity Profiles*

Figure 3-6 shows the mean velocity deficit normalized on U_{ref} for locations of 0.608, 1.178, 1.819 and 2.382 x/c_a generated from the data of Geiger (2005). Each nearly symmetric profile has been adjusted so that $z/c_a = 0$ coincides with the wake center. The spreading of the wake is visible, as well as the decay of the velocity deficit downstream. The deficit at x/c_a=1.819 is of high interest, since this location will be used for comparison with the blowing blades in Chapter 4. The wake is not purely two-dimensional, since a small velocity component exists in the spanwise direction (Figure 3-7). At an x/c_a of 1.819, the magnitude of this component is never more than 0.80%U_{ref}, and the variations do decrease with downstream distance. Three-dimensionality is also apparent in Figure 3-8 of W/U_{ref}. This component varies up to 2.0%U_{ref} at 0.608 x/c_a, but by 2.382 x/c_a it is no more than 0.50%U_{ref}.

3.3.2.2. *Definition of Wake Parameters*

The displacement thickness is defined by the following equation:

$$\delta^* = \int_{wake} (1 - \frac{U}{U_e}) dy \qquad \text{Eqn. 3-7}$$

where δ is the boundary layer thickness and U/U_e is the viscous profile velocity normalized on the wake edge velocity. The mass flow in the boundary layer region is less for a viscous flow than it would be for a hypothetical inviscid flow. To create an inviscid profile with the same mass flow as the viscous profile, the surface would have to be displaced some distance upward, represented by δ^*. The momentum thickness can be defined in a similar manner:

$$\theta = \int_{wake} (1 - \frac{U}{U_e}) \frac{U}{U_e} dy \qquad \text{Eqn. 3-8}$$

Shifting the profile outward by a distance of θ creates an inviscid profile that has an equivalent flow of momentum through the wake to the viscous profile (Schetz, 1993).

The wake half-width, L_w, is typically calculated as the distance between the locations where the velocity deficit is a maximum and where it is half of the maximum. The velocity deficit is defined as follows:

$$U_w = U_e - U \qquad \text{Eqn. 3-9}$$

Therefore the maximum deficit occurs at the point of minimum velocity in the wake. Due to the inversion of the wake profiles of the blowing blades at higher blowing rates, the maximum deficit could not be calculated and properly compared in this manner. Instead, two new quantities were defined. The maximum deficit was renamed U_{w-}, which reaches a value of zero when the wake deficit becomes a surplus. The new U_w became the square root of the maximum value of the streamwise Reynolds normal stress, u'^2. Since the shape of the u'^2 profile is consistent for all blowing rates, the wake half-width was calculated as the distance between the locations of the maximum streamwise Reynolds normal stress and where it is half of the maximum. It was renamed $L_{u'}$ for clarity.

3.3.2.3. *Wake Parameters*

The wake parameters are often used to normalize various lengths, velocities, and turbulence quantities. The wake profiles of Geiger (2005) were measured parallel to the pitchwise (z) direction. Wake parameters calculated directly from these profiles represent what would be seen by a downstream stator row. The parameters were converted to the wake-aligned coordinate system, parallel to the Z-direction, by multiplying by the cosine of the angle between the z- and Z-axes. According to Geiger (2005), this angle is 53.3° for the baseline blades. The pitchwise and wake-aligned values of the displacement thickness, momentum thickness and the wake half-width and the pitchwise U_w and velocity deficit calculated from the data of Geiger (2005) for the baseline blades are presented in Table 3-1. These values are comparable to those presented in Geiger (2005).

Table 3-1. Normalized baseline wake parameters.

	Pitchwise					**Wake-Aligned**		
x/c_a	δ^*/c_a	θ/c_a	$L_{u'}/c_a$	U_w/U_{ref}	U_{w-}/U_{ref}	δ^*/c_a	θ/c_a	$L_{u'}/c_a$
0.6	0.052	0.042	0.257	0.068	0.201	0.031	0.025	0.153
1.2	0.048	0.042	0.392	0.050	0.136	0.029	0.025	0.234
1.8	0.046	0.042	0.430	0.042	0.108	0.028	0.025	0.257
2.4	0.049	0.045	0.467	0.038	0.099	0.029	0.027	0.279

The displacement thickness and momentum thickness are nearly constant with axial location. In the wake-aligned system, the average displacement and momentum thicknesses are 0.029 and 0.026, respectively. The wake half-width increases from x/c_a = 0.608 to x/c_a = 2.382, meaning that the wake is spreading as it travels downstream. Between these two locations, the half-width nearly doubles to 0.279 from 0.153.

3.3.2.4. *Reynolds Stresses and Turbulent Kinetic Energy*

Figures 3-9, 3-10 and 3-11 show the normalized Reynolds normal stresses, u'^2/U_{ref}^2, v'^2/U_{ref}^2 and w'^2/U_{ref}^2 plotted against the cross-wake distance on the axial chord, and Figures 3-12, 3-13 and 3-14 show the normalized shear stresses, $u'v'/U_{ref}^2$, $v'w'/U_{ref}^2$ and $-u'w'/U_{ref}^2$ against z/c_a. The normal stresses are symmetric about the wake center and decrease in value with downstream location. The peak streamwise normal stress, u'^2/U_{ref}^2 at 1.819 is roughly $1.8\text{x}10^{-3}U_{ref}^2$, while the maximum values of v'^2/U_{ref}^2 and w'^2/U_{ref}^2 are $1.5\text{x}10^{-3}U_{ref}^2$ and $2.1\text{x}10^{-3}U_{ref}^2$ respectively.

For a plane wake, $u'v'/U_{ref}^2$ and $v'w'/U_{ref}^2$ are zero. However, Figures 3-12 and 3-13 show that these two stresses are present in the baseline flow, though they are on the order of 10^{-4}. The dominant shear stress, $-u'w'/U_{ref}^2$, is more clearly defined and is shown in Figure 3-14. Its maximum value at $x/c_a = 1.819$ is approximately $0.5 \text{x} 10^{-3} U_{ref}^2$.

The turbulent kinetic energy (*TKE*) is the mean kinetic energy per unit mass of the fluctuating velocity field (Pope 2001). It is defined by the normal stresses as:

$$k = \frac{1}{2}(u'^2 + v'^2 + w'^2) \qquad \text{Eqn. 3-10}$$

In Figure 3-15 it is easy to see how the *TKE* favors u'^2/U_{ref}^2 and v'^2/U_{ref}^2 with the symmetrical double-peaked shape. The peaks are less prominent than in u'^2/U_{ref}^2 and v'^2/U_{ref}^2 alone, due to the effects of w'^2/U_{ref}^2. The maximum *TKE* is $6.7 \text{x} 10^{-3} U_{ref}^2$ at x/c_a=0.608 but by x/c_a=1.819, it has reduced by nearly two-thirds.

3.4. Baseline Data from the Present Study

3.4.1. Pitot-Static Full Cross-Sections

To verify the Pitot-static cross-sections of Geiger (2005), the cross-sectional measurement of the total pressure coefficient of blade five that was made at a downstream location of 0.839 x/c_a while testing the blade stabilizing pins is presented in Figure 3-19. This figure is opposite of Figures 3-1 through 3-4, with the flow seen here as looking downstream. The pressure side is to the right of the wake and the suction side is to the left. The tip-gap was set to 0.004125c which is a quarter of the 0.0165c setting used by Geiger (2005).

At 0.839 x/c_a, the upper end-wall boundary layer is present and appears to be about 0.18c_a thick. The nearly vertical wake is widest near the upper end-wall, as the flow merges with the boundary layer, whereas around mid-span, the wake is approximately 0.37c_a wide in the pitchwise direction. The wake here is less curved than that of Geiger (2005), since less end-wall vorticity is induced at this lower tip-gap. The flow outside of the wake is an area of nearly constant pressure coefficient. The tip-leakage vortex shed from the tip-gap of blade five is visible in the lower left corner as a region of low total pressure coefficient. The vortex center is located at z/c_a = -1.25 and y/c_a = 0.15, which is the area of lowest velocity in the cross-section. The reduction in tip-gap height here does not seem to affect the wake flow itself. Aside from diminishing the height and strength of the tip-leakage vortex, this cross-section validates Figures 3-1 through 3-4 of Geiger (2005).

3.5. Summary

This chapter analyzed the baseline GE Rotor B blades in the Virginia Tech Linear Cascade Tunnel by presenting results of Geiger (2005) and of the present study. The Pitot-static cross-sections behind blade five at x/c_a = 0.839 and 1.877 created by Geiger (2005) clearly show the mid-span two-dimensionality, tip-leakage vortices, boundary layers and wake spreading associated with the original tunnel configuration. Even with the modified tip-gap setting, the Pitot-static cross-section taken during the present study exhibits the same features. The blade loading measurements reveal the pressure gradients that the blowing blades should be comparable to in order to represent GE Rotor B blades. Mid-span velocity and turbulence profiles created from the data of Geiger (2005) demonstrate wake spreading and wake deficit reductions that occur with streamwise distance.

These results thoroughly describe the original baseline configuration that the trailing-edge blowing results will be compared to in the following chapter. Chapter 4 includes similar measurements of blade loading, Pitot-static cross-sections and mid-span velocities, as well as the potential for fan noise reduction with trailing-edge blowing.

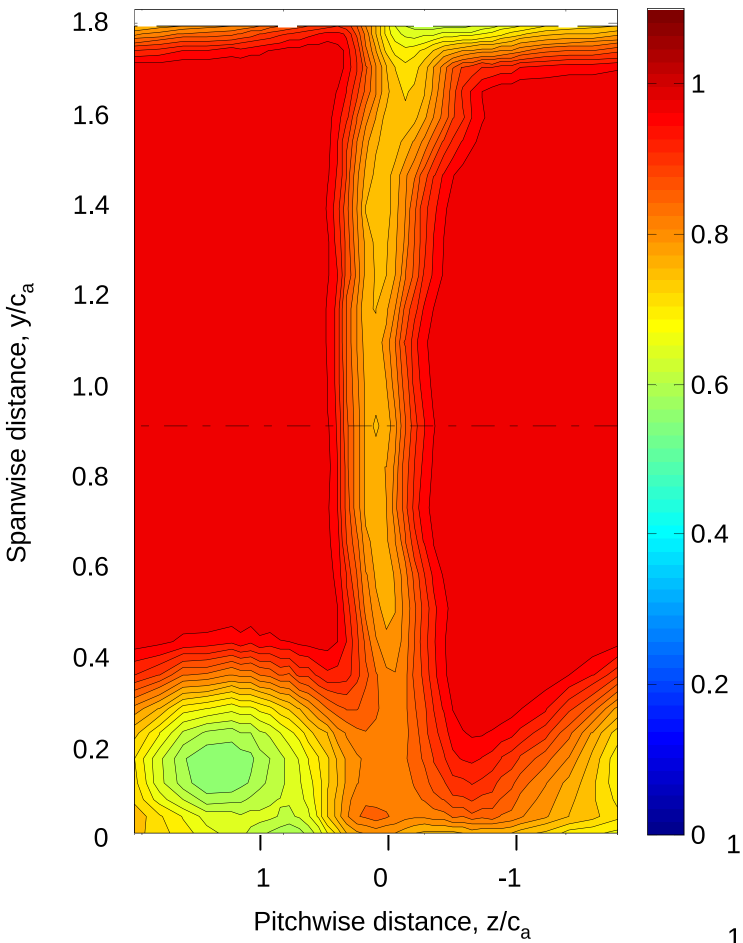

Figure 3-1: Non-blowing baseline C_{p0} cross-section at $x/c_a = 0.839$ and tip-gap 0.0165*c* (Geiger, 2005)

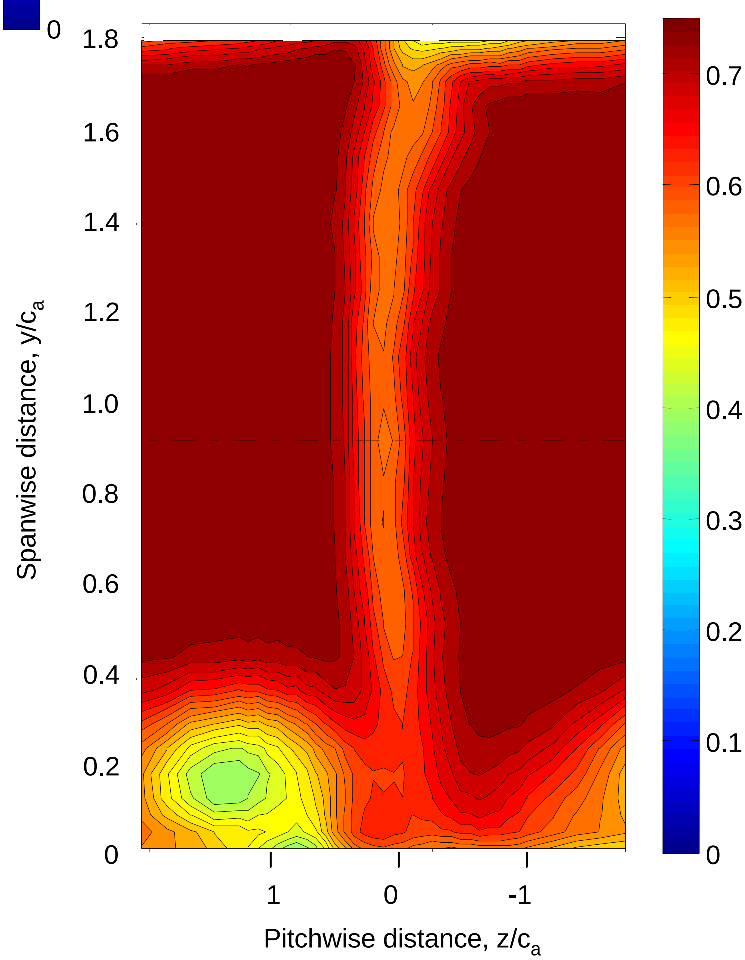

Figure 3-2: Non-blowing baseline U/U_{ref} cross-section at $x/c_a = 0.839$ and tip-gap 0.0165*c* (Geiger, 2005)

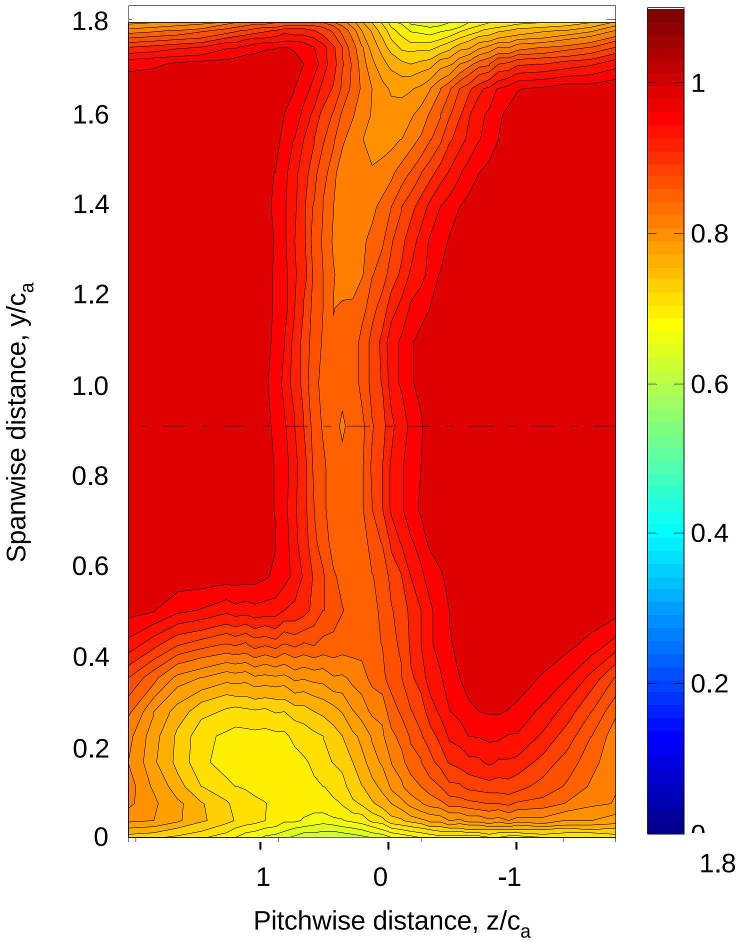

Figure 3-3: Non-blowing baseline C_{p0} cross-section at x/c_a = 1.877 and tip-gap 0.0165c (Geiger, 2005)

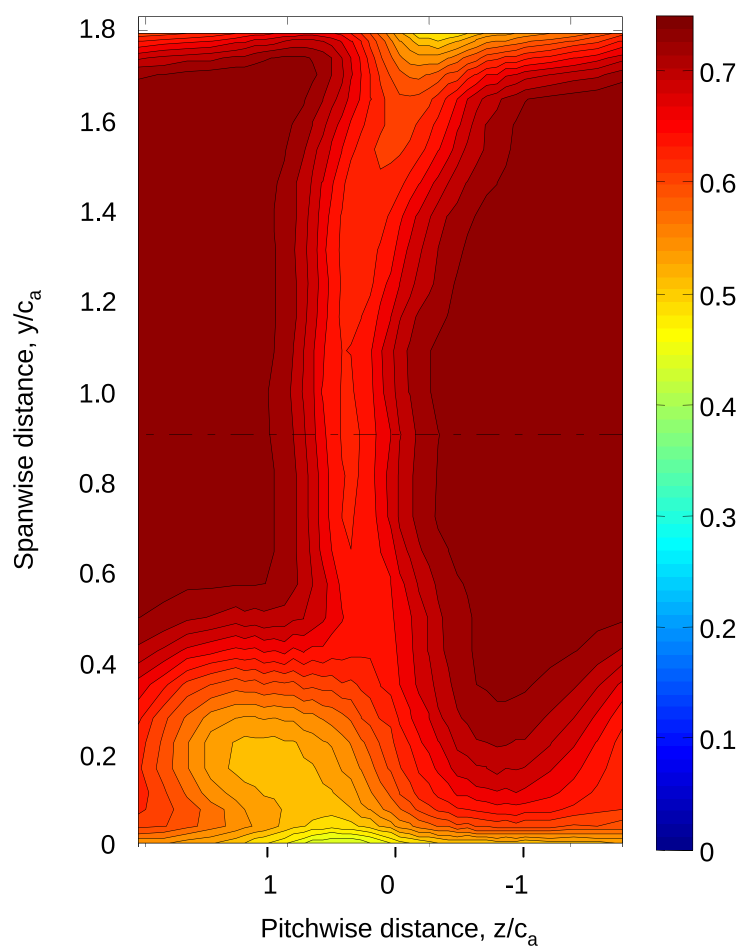

Figure 3-4: Non-blowing baseline U/U_{ref} cross-section at x/c_a = 1.877 and tip-gap 0.0165c (Geiger, 2005)

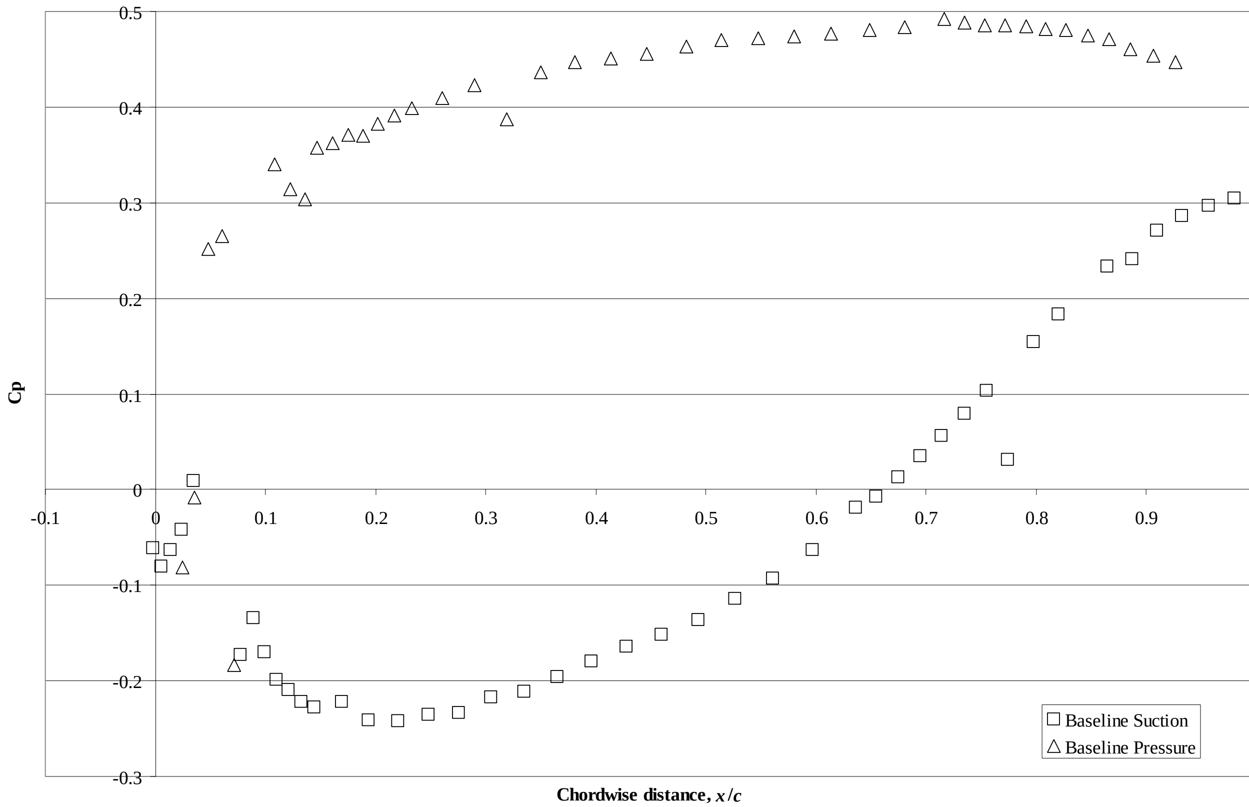

Figure 3-5: Mean pressure coefficient distribution at mid-span for the GE Rotor B baseline

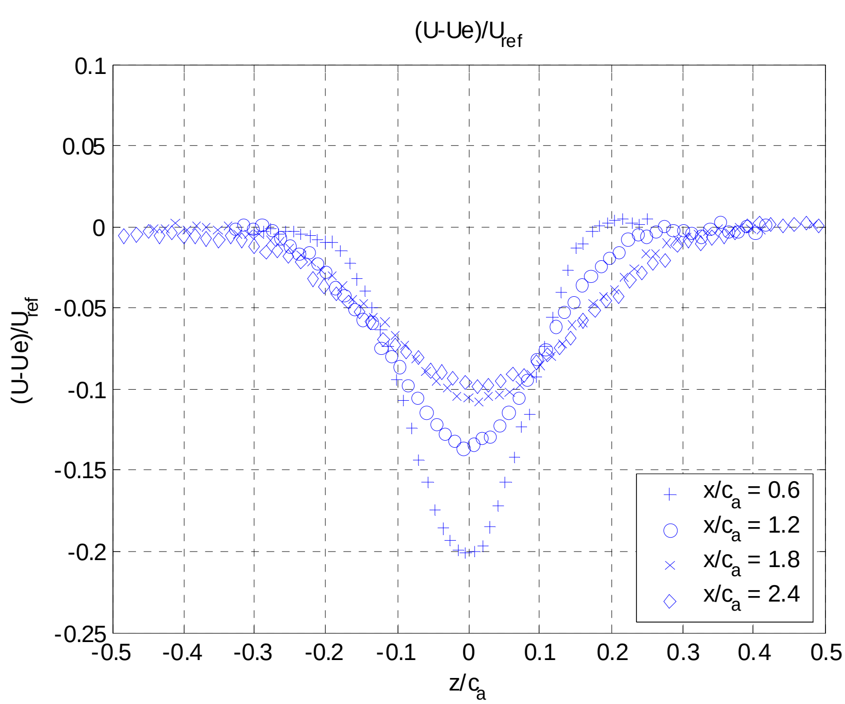

Figure 3-6: Baseline streamwise mean velocity profile $(U-U_e)/U_{ref}$ at x/c_a = 0.608, 1.178, 1.819 and 2.382

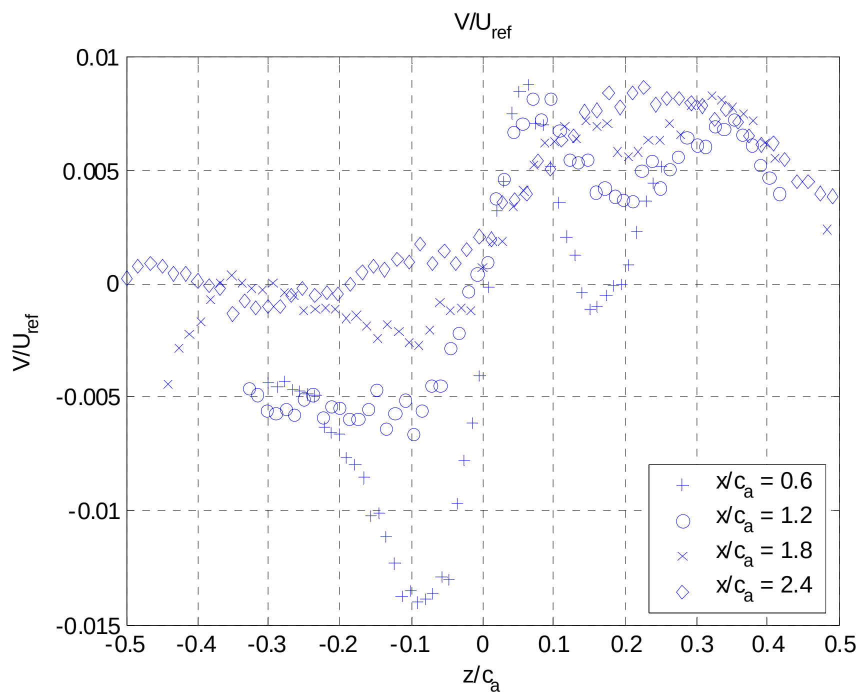

Figure 3-7: Baseline spanwise mean velocity profile V/U_{ref} at x/c_a = 0.608, 1.178, 1.819 and 2.382

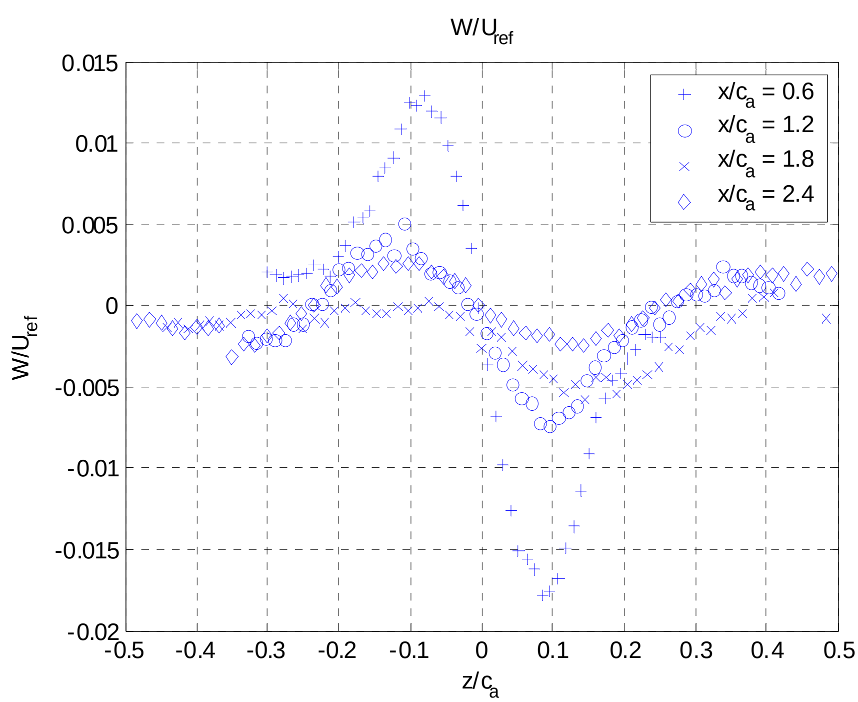

Figure 3-8: Baseline cross-wake mean velocity profile W/U_{ref} at x/c_a = 0.608, 1.178, 1.819 and 2.382

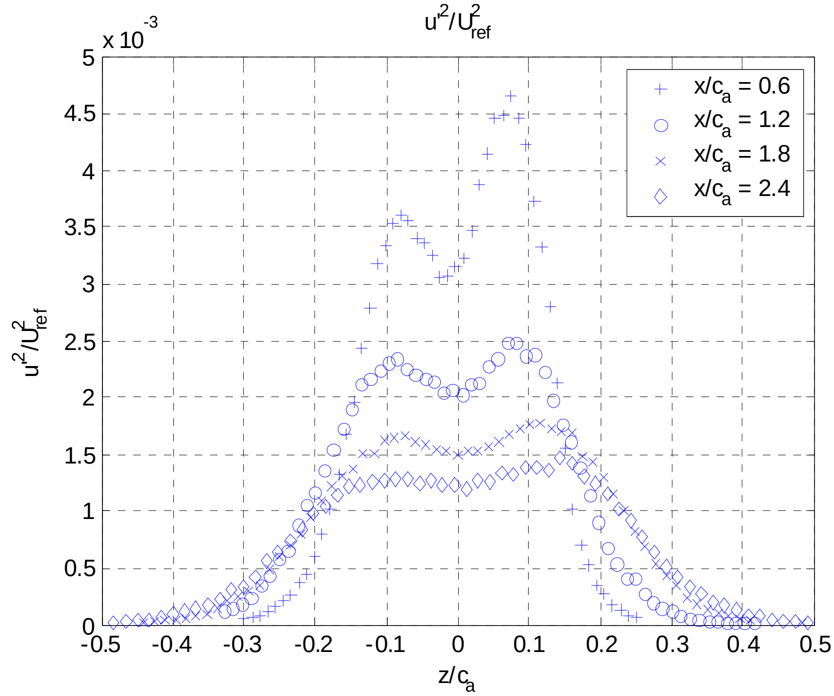

Figure 3-9: Baseline streamwise Reynolds normal stress profile u'^2/U_{ref}^2 at x/c_a = 0.608, 1.178, 1.819 and 2.382

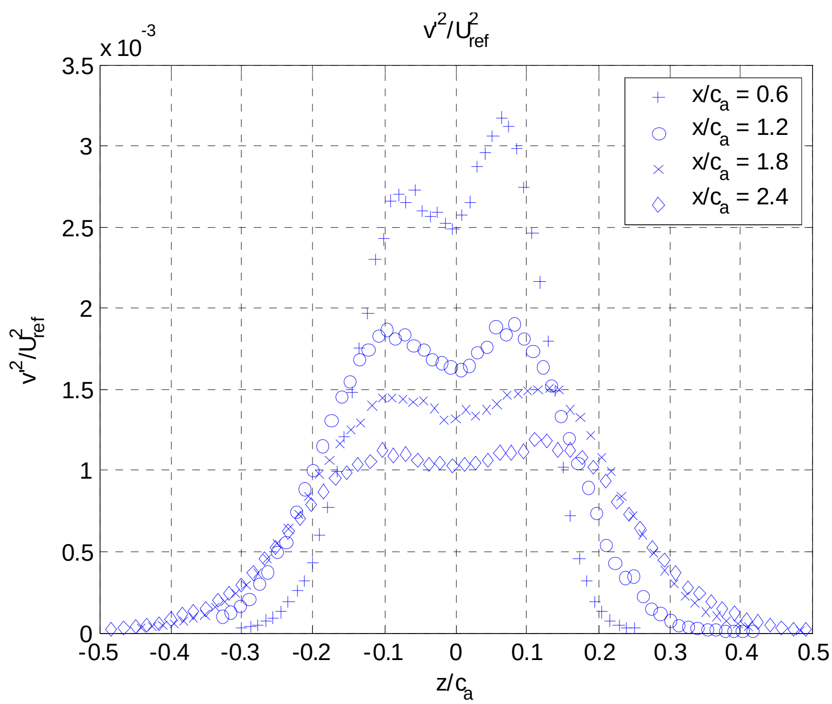

Figure 3-10: Baseline spanwise Reynolds normal stress profile v'^2/U_{ref}^2 at x/c_a = 0.608, 1.178, 1.819 and 2.382

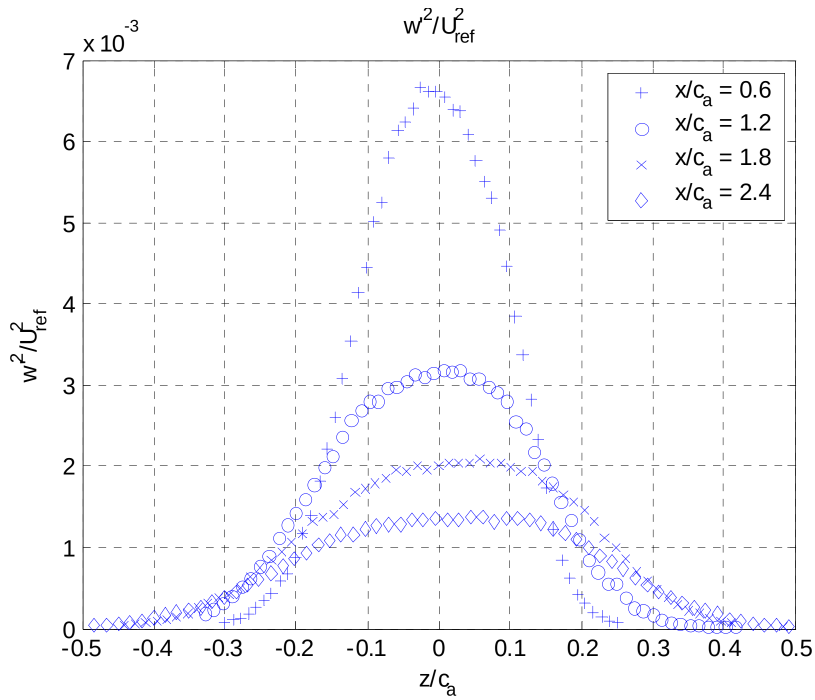

Figure 3-11: Baseline cross-wake Reynolds normal stress profile w'^2/U_{ref}^2 at x/c_a = 0.608, 1.178, 1.819 and 2.382

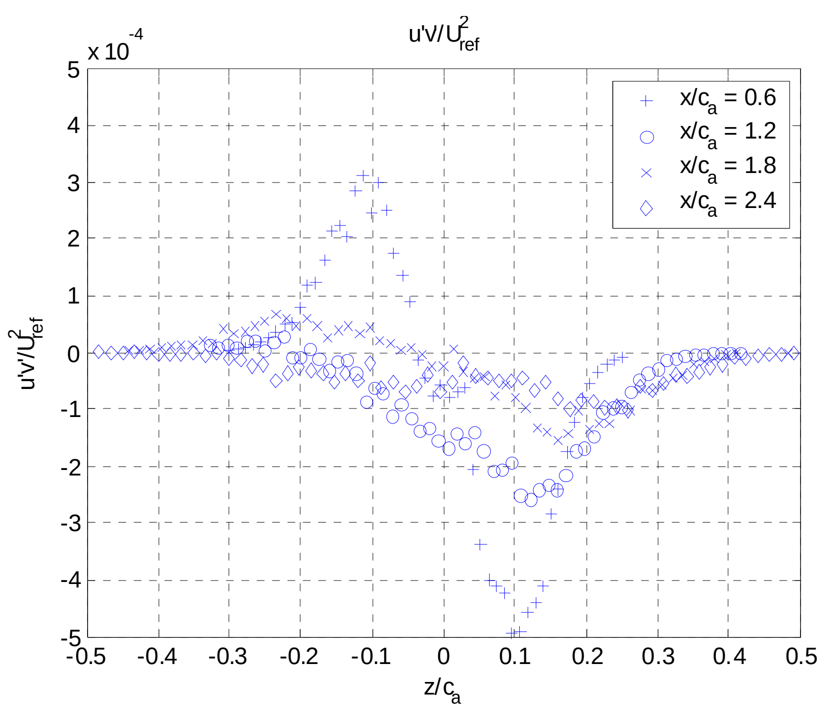

Figure 3-12: Baseline Reynolds shear stress profile $u'v'/U_{ref}^2$ at x/c_a = 0.608, 1.178, 1.819 and 2.382

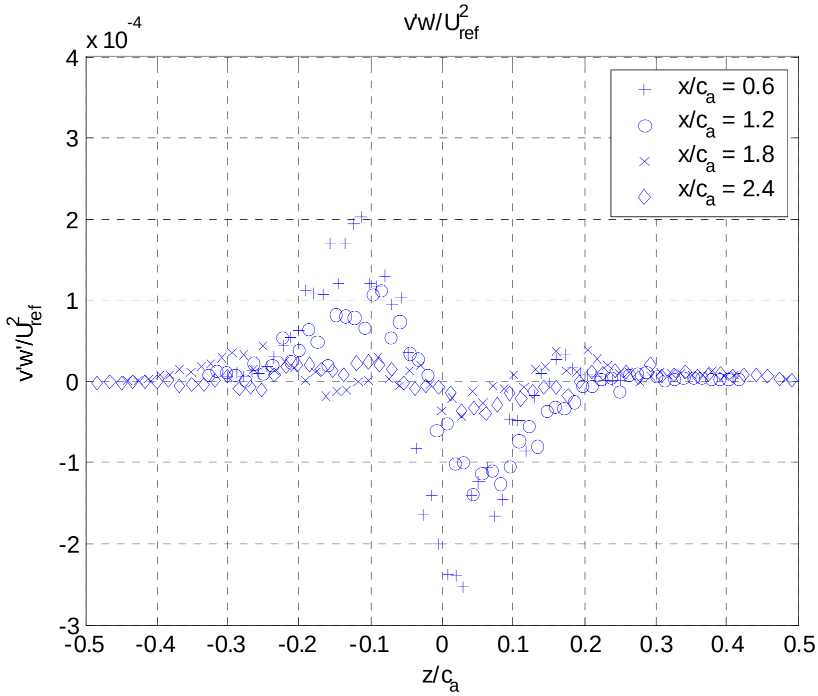

Figure 3-13: Baseline Reynolds shear stress profile $v'w'/U_{ref}^2$ at x/c_a = 0.608, 1.178, 1.819 and 2.382

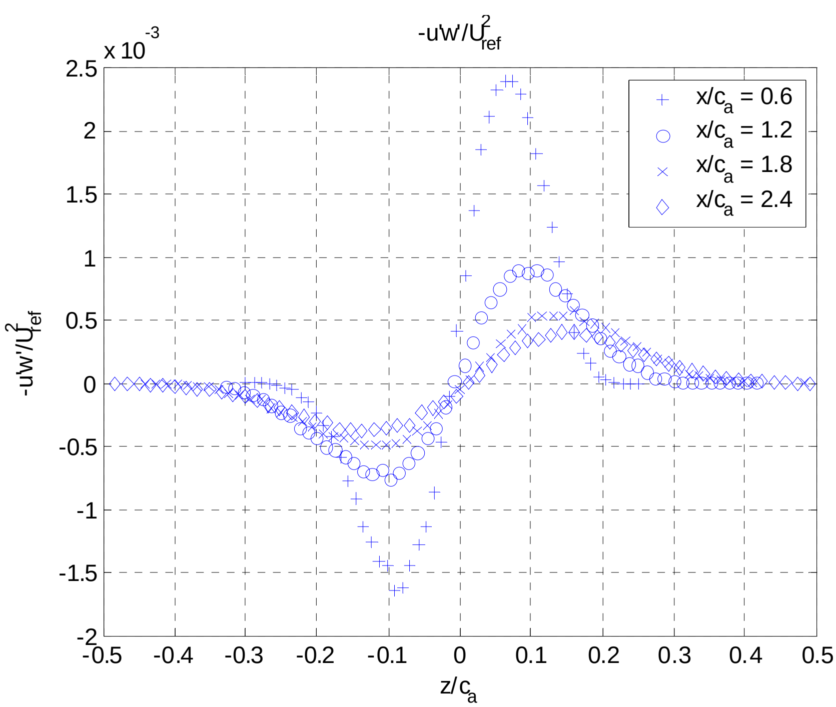

Figure 3-14: Baseline Reynolds shear stress profile $-u'w'/U_{ref}^2$ at x/c_a = 0.608, 1.178, 1.819 and 2.382

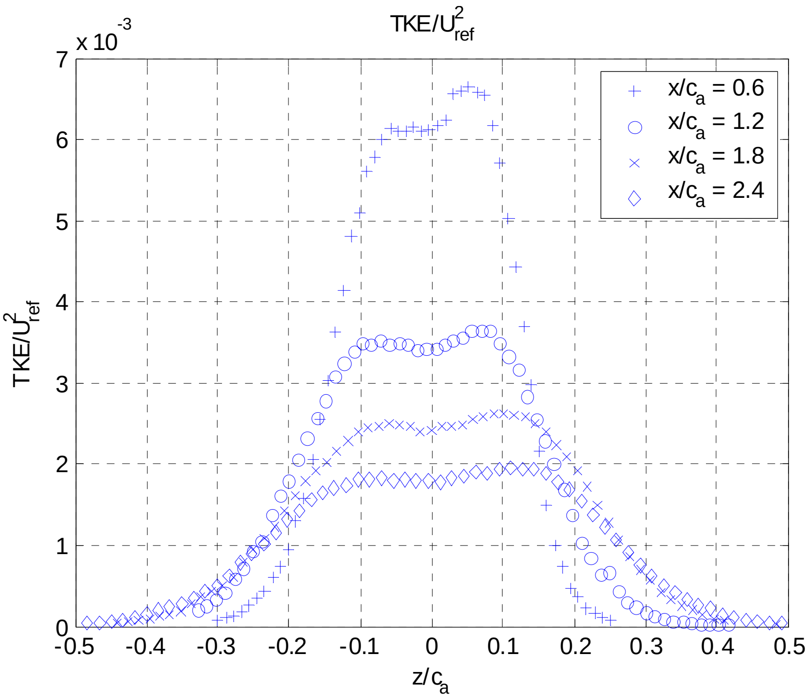

Figure 3-15: Baseline turbulent kinetic energy profile k/U_{ref}^2 at x/c_a = 0.608, 1.178, 1.819 and 2.382

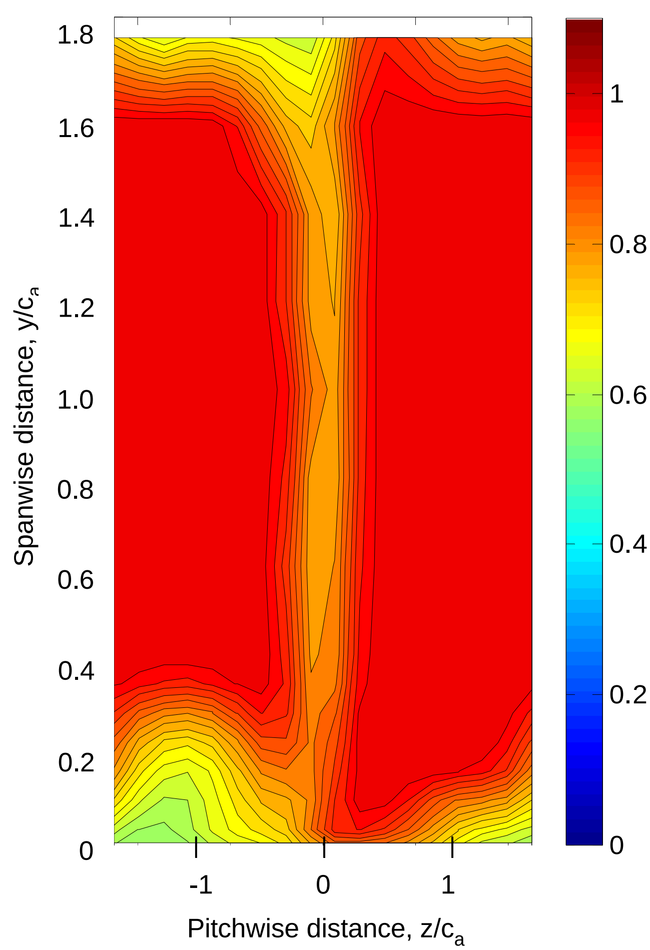

Figure 3-16: Baseline C_{p0} cross-section at x/c_a = 0.839 and tip-gap 0.004125c

4. EFFECTS OF TRAILING-EDGE BLOWING

The center four blades of the cascade were replaced by the simple blowing blades with internal flow passages and trailing-edge slots created by rapid-prototype techniques at NASA-Glenn. They were produced to create uniform blowing according to CFD predictions. The simple blowing blades were later replaced by the Kuethe vane blowing blades, identical except for a series of vertically spaced vortex generators on the suction side of the blade.

4.1. Flow Conditions

This section presents blade loading, the blade flow conditions and the basic flow structure before the more direct effects of trailing-edge blowing are examined in Sections 4.2 and 4.3. Blade loading was measured using the static pressure ports described in Section 2.3.2. Single hot-wire measurements were made at the blowing slot exit to determine flow uniformity out of the slot. Oil flow visualizations were performed to see what was occurring to the flow just upstream of the blowing slot. Finally, single hot-wire cross-sections were taken perpendicular to the span in the vicinity of the trailing-edge. All three of these measurement sets were taken at multiple blowing rates to obtain the best possible understanding of the flow. Pitot-static cross-sections are included as a first look into the changes to the trailing-edge flow that occur with increasing blowing rate.

4.1.1. Blade Loading

Figures 4-1 and 4-2 show the mean pressure coefficient distributions of the blowing blade sets, plotted at each mid-span pressure port location, normalized on the total chord, *c*. Each plot includes the blade loading of the non-blowing baseline GE Rotor B blades for comparison.

4.1.1.1 *Simple Blowing*

Blowing rate was calculated as a percentage of the mass flow through a single cascade passage. Figure 4-1 shows the simple blowing blade loading for blowing rates of 1.4%, 2.0% and 2.6%, plus two different 0% blowing cases: the 0% case with the trailing-edge slot covered by aluminum foil tape and the 0% case with the slot left open. The tape was used to make a true 0% blowing case, by preventing the small amount of suction that occurs with no blowing. Therefore, the taped case is now referred to as "0%" case and the un-taped case is called "passive suction". On Figure 4-1, the scattering on both the pressure and suction sides between the leading-edge and 0.15c is due to the placement of the trip strip at 0.10c. None of the blowing rates fully match the baseline blade loading, though they all create generally the same shaped figure. On the suction side, the 0% and the passive suction loadings are nearly identical until 0.40c. These two cases diverge by more than 0.1 from the non-blowing baseline, especially in the trailing-edge region between 0.5c and 0.9c. The 1.4% case has the closest loading to the baseline, while 2.0% and 2.6% are progressively farther away, yet significantly better than the non-blowing cases. On the pressure side, the passive suction, 1.4%, 2.0% and 2.6% loadings are very closely grouped over most of the chord, differing by less than 0.04. The passive suction loading does increase near the trailing-edge, to 0.47, as opposed to 0.43 for the other blowing cases. The 0% loading is surprisingly the most unlike the baseline loading. Taping the slot was intended to eliminate the effects of the differences in trailing-edge geometry from the non-blowing baseline. However, this case appears to be the least representative of the baseline, over both sides of the blade. Pressure coefficients of the baseline and the 0% cases differ in excess of 0.1, especially on the suction side trailing-edge region. The circulation for the 0% case is $0.55U_{ref}c_a$.

4.1.1.2 *Kuethe Vane*

The Kuethe vane blowing blade loading with passive suction and at rates of 0%, 1.0%, 1.4%, 2.0%, 2.6% and 3.0% are shown on Figure 4-2. Overall, the largest fluctuations in pressure coefficient are in the vicinity of the trip strip at 0.10c. On the suction side, the passive suction loading differs greatly from the baseline loading, in some locations by more than 0.2. Unlike the 0% case for the simple blowing blades, the 0% loading here is the most comparable to the non-blowing baseline, while the other five blowing rates fall in between. A similar situation is evident on the pressure side: all cases except for 0% are closely grouped over the entire chord, but are offset by at least 0.05 from the baseline. The 0% loading matches the baseline between 0.10c and 0.40c. Although the loading decreases beyond 0.40c, it is still the most representative of the non-blowing baseline. The circulation for the 0% case is $0.58U_{ref}c_a$.

4.1.2. Blowing Slot Uniformity

Measurements were made with a single hot-wire at the blowing slot exit of blade five to check the spanwise uniformity of the blowing. Figures 4-3 and 4-4 show the position of the hot-wire probe relative to the trailing-edge blowing slot. Starting at $y/c_a = 0.09$ and continuing spanwise every 25.4mm until $y/c_a = 1.37$, a set of six to eight points were taken at each spanwise location. The points were 0.25mm apart, and came as close to the suction side of the blade as possible without risk of damaging the hot-wire. These points were used to create the contour plots at multiple blowing rates of the simple blowing blades in Figures 4-5 through 4-12 and the Kuethe vane blades in Figures 4-13 through 4-22.

4.1.2.1. *Simple Blowing*

Figure 4-5 shows the slot uniformity of the simple blowing blades with passive suction (no applied blowing). The flow is seen as looking downstream, the normalized pitchwise distance is on the horizontal axis and the normalized spanwise distance is on the vertical axis. The suction side is to the left of the figure and the pressure side is to the right. The region between 0.36 y/c_a and 0.67 y/c_a has the lowest velocity, at about $0.30U_{ref}$, though this is unrelated to the effects of blowing. The uniformity at 1.4% blowing is shown in Figure 4-6. The four dark areas equivalent to the freestream velocity are a result of the shape of the internal blade passages. The rounded projection of higher velocity at 1.10 y/c_a and the thinner area immediately above is most likely due to an unintended blockage of the blowing slot. As the blowing rate is increased from 1.5%, to 1.7%, to 2.0% and to 2.3% (Figures 4-7 through 4-10), the vertical area of very low blowing ($0.10U_{ref}$ to $0.30U_{ref}$) becomes thinner and is replaced by areas of higher blowing ($0.75U_{ref}$ to $1.0U_{ref}$). The blocked area at 1.10 y/c_a remains essentially unchanged. At 2.5% and 2.6% (Figures 4-11, 4-12), the dark areas related to the internal passages are noticeably smaller, as the blowing around them has increased to the range of $0.75U_{ref}$ to $0.85U_{ref}$. The area immediately adjacent to the suction side blade surface is now approximately two-thirds of its thickness at 1.5%. The majority of the measured area has a velocity of at least $0.80U_{ref}$.

4.1.2.2. *Kuethe Vane*

The Kuethe vane slot uniformity plots are quite distinctive from the simple blowing plots, especially with passive suction and at 0.5% blowing. In the passive suction case, the vortex generators are solely responsible for the pattern seen in Figure 4-13. They are evenly spaced by 25.4mm, creating the vertical pattern of areas $0.01c_a$ in width with speeds equivalent to the freestream velocity at the trailing-edge. The areas of low velocity above mid-span are perhaps indicative of stalled flow on the suction side near the upper end-wall. This possibility is investigated further in the following oil flow visualization section. Initializing the blowing to 0.5% does not seem to disperse these areas significantly. Figure 4-14 shows that the some of the velocities in the patterned areas have been reduced to $0.85U_{ref}$, but the spanwise regions of higher velocity are still quite evident. Velocity varies in value from nearly zero up to the freestream value, from the suction side to the pressure side (Figure 4-15). Three localities of high velocity centered at y/c_a = 0.50, 0.85 and 1.25 are due to the internal blade passages, as is also seen in the simple blowing blade slot uniformity figures. The intensity of these spots increases as the blowing is raised to 1.4% and 1.5% (Figures 4-16, 4-17). A new zigzag pattern extending over the span is noticeable in Figure 4-18 at 1.7%, as well as a strengthening of the three high velocity locations towards the freestream level. A fourth centered at y/c_a = 0.20 is just emerging. However, it is no longer discernable by 2.0% (Figure 4-19) and 2.3% (Figure 4-20), although the serrated pattern remains. No major differences at 2.5% (Figure 4-21) and 2.6% (Figure 4-22) are apparent, aside from a slight strengthening of the velocity at the internal passage exits.

4.1.3. Oil Flow Visualization

The oil substance used for flow visualization was a mixture of 15 parts kerosene, 5 parts titanium dioxide (TiO_2), and 1 part oleic acid. An estimated 5 parts of extra kerosene was added to increase flow visibility, since the cascade tunnel flow speed is a relatively low 24.7m/s. A series of oil flow pictures were taken for both sets of blowing blades with passive suction and at 0%, 1.0%, 1.4%, 2.0% and 2.6% blowing.

4.1.3.1. *Simple Blowing*

For the simple blowing blades, the flow for the 0% case appears to show a region of low surface friction roughly 0.20*c* upstream from the trailing-edge (Figure 4-23). A similar region is seen near the same location for the passive suction case and all of the remaining rates: between 0.05*c* and 0.10*c* upstream from the blowing slot (Figures 4-24 through 4-28). Near the top of Figure 4-25 of 1.4% blowing, an important characteristic of all the rates is most visible: there is some suggestion of a connected region of low surface momentum above approximately 0.70*c* and continuing to the upper end-wall.

4.1.3.2. *Kuethe Vane*

Photographs of the oil flow visualization of the Kuethe vane blades do not differ much from rate to rate. The flow shows an area of low momentum around 0.10*c* from the trailing-edge, that could be a separation, for the 0%, 1.0% and 1.4% cases (Figures 4-29, 4-30 and 4-31). As the blowing is increased to 2.0% and 2.6%, the separation seems to occur slightly closer to the trailing-edge (Figures 4-32, 4-33).

4.1.4. Normal-to-Span Cross-Sections

To obtain a better understanding of the flow in the immediate trailing-edge region, single hot-wire cross-section were taken at mid-span, normal to the span (parallel to the upper and lower end-walls) at multiple blowing rates. Figure 4-34 was made to visualize the path of the probe to avoid a collision of the probe and the blade during a manual traverse movement. The trailing-edge of blade five as seen from above is plotted in the lower right of the figure, and the data acquisition points are represented by small dots. For the simple blowing blades, these cross-sections were made only at mid-span ($0.92c_a$). Three spanwise locations were used for the Kuethe vane blades: $0.84c_a$, $0.92c_a$, and $0.97c_a$. The first location was chosen because the suction side surface at this height is not obstructed by an upstream vane. The second location is mid-span, which happens to fall near the mid-span of a vane. The third lies at the height corresponding to the top surface of a vane. These three spanwise locations are shown in Figure 4-35.

The cross-sections are plotted in terms of pitchwise distance on the horizontal axis and axial distance on the vertical axis. The streamwise velocity normalized on maximum velocity was interpolated both pitchwise and in the direction of the flow. The theoretical position of the blade is indicated by the filled area and the actual measurement locations are denoted by small 'x' markings. This measurement grid is relatively sparse, leaving much of the plot subject to interpolation. The area within the dotted line surrounding the blade contains very few measurement points and is therefore largely interpolated.

4.1.4.1. *Simple Blowing*

Figures 4-36 and 4-37 compare the trailing-edge flows with no blowing applied. The blowing slot is covered by aluminum foil tape in Figure 4-36 (0%) and left open and unaltered in Figure 4-37 (passive suction). With the slot taped, the flow surrounding the trailing-edge appears fairly uniform at about $0.80U_{ref}$. At the slot exit and immediately downstream of the trailing-edge, the flow is significantly slowed over a distance of $0.37c_a$, nearly to zero velocity in some locations. In the passive suction cross-section, the flow outside of the wake appears slightly lower than that of the 0% flow, closer to the edge velocity (U_e) of $0.75U_{ref}$. The wake is somewhat angled towards the pressure side. Overall, the passive suction case has higher velocities, with only a 0.18c_a length of flow at 0.20U_{ref} or less.

With 1.0% blowing, the wake is no longer angled towards the pressure side (Figure 4-38). The wake with even this minimal amount of blowing has a lower range of velocities than the wake of the blade with 0% blowing. The 0% blowing is more representative of a true “baseline” case, implying that blowing at 1.0% is actually accentuating the undesirable low velocities of the wake. A small increase to 1.4% visibly increases the velocities in the wake, especially farther downstream (Figure 4-39). The wake deficit is smaller than with 1.0% blowing, though it is nearly identical or perhaps slightly greater than the deficit of the passive suction cross-section. The mid-span velocity profile at 1.4% demonstrates a larger deficit than with passive suction, which will be presented in Section 4.2. The area of locally high velocity at the blade tip is the result of a measurement point coinciding directly with the blowing jet. At 2.0%, the wake velocities are 0.50-0.60U_{ref}, which is rapidly approaching the velocity outside of the wake (Figure 4-40). By 2.3%, a thin section of flow on the pressure side of the wake has surpassed the edge velocity, to about 0.80U_{ref} (Figure 4-41). This flow enlarges in Figure 4-42 to cover half of the distance across the wake at 2.5%. The majority of the wake is overblown once the blowing has reached 2.7% in Figure 4-43, though dominantly on the pressure side, which complements the mid-span velocity profile to be presented in Section 4.2.1.1.

4.1.4.2. *Kuethe Vane*

The Kuethe vane normal-to-span cross-sections demonstrate the effects of the blowing and the vanes themselves on the trailing-edge flow. Figures 4-44, 4-45 and 4-46 were all measured at 0% blowing, though they are each at a different spanwise location. At 0.84c_a and

$0.97c_a$ the cross-sections are nearly identical. The wake at spanwise locations beneath the lower surface of a vane and at the top surface of a vane seem to produce a wake that is deep ($0.10U_{ref}$ or less) and symmetrical. However, the wake at the mid-span of a vane ($0.92c_a$) is strikingly different. The deficit is decreased to only 0.50-$0.60U_{ref}$ over roughly 90% of the wake. This indicates that the vanes are perhaps increasing the mixing of the trailing-edge flow as found by Kuethe (1972). With 1.0% blowing (Figures 4-47, 4-48 and 4-49), the wake velocities have increased, unlike the simple blowing blades at low blowing rates. The enhanced mixing at the vane mid-span is present at this rate as well. Figures 4-50, 4-51 and 4-52 of 1.4% show minimal improvement of the deficit at all spanwise levels, but there are no further differences from the 1.0% cross-sections.

4.1.5. Pitot-Static Full Cross-Sections

Pitot-static full cross-sections were taken at two downstream locations (0.839 and 1.877 x/c_a) for four blowing rates (passive suction, 1.4%, 2.0%, and 2.6%). Figures 4-53 through 4-84 show the total pressure coefficient cross-sections (C_{p0}) and velocity (U/U_{ref}) cross-sections behind blade five, the center cascade blade, with the normalized pitchwise distance on the horizontal axis and the normalized spanwise distance on the vertical axis. The view is downstream, with the suction side to the left of the figure and the pressure side to the right. The origin is at the wake center. Pairs of C_{p0} and U/U_{ref} cross-sections are presented for each station and blowing rate.

4.1.5.1. *Simple Blowing*

The passive suction C_{p0} cross-section at 0.839 x/c_a (Figure 4-53) looks nearly identical to the non-blowing baseline cross-section taken at the same location (Figure 3-1). The vortex structure appears unaffected by the presence of the stabilizing pins. The main difference from the non-blowing baseline appears to be a decrease of $0.1c_a$ in the width of the two-dimensional portion of the wake. This effect may be produced by the slightly blunter trailing-edge associated with the presence of the blowing slot. Overall, an increase in blowing rate decreases the depth of the wake, but upon closer examination, the wake at 1.4% is actually slightly deeper and roughly $0.1c_a$ wider than the passive suction case and the baseline case (Figure 4-55). This is examined further in the mid-span velocity profile measurements of Section 4.2.1.1. The 2.0% cross-section has a reduced deficit, with a visible surplus at the tip (Figure 4-57). The 2.6% cross-section is overblown across the full span, specifically in the tip region, which suggests either non-uniformity of the blowing slot or an interaction with the tip-leakage vortex (Figure 4-59).

As expected, the passive suction C_{p0} cross-section at 1.877 x/c_a is wider than at 0.839 x/c_a (Figure 4-61). The boundary layer thickness on the upper end-wall is still $0.20c_a$ thick, but the bulge on the root suction side around $y/c_a = 7$ has increased in size with downstream location. Perhaps due to flow separation, this phenomenon is also visible in the oil flow visualization pictures of Section 4.1.3.1. The tip-leakage vortex has increased in size, as well as strength. The wake at 1.4% is still wider and deeper than for the passive suction and baseline cases (Figure 4-63). A surplus at 2.0% is no longer visible here, but the 2.6% cross-section is essentially identical to the one taken at 0.839 x/c_a (Figures 4-65 and 4-67).

The U/U_{ref} cross-sections at $x/c_a = 0.839$ show the same flow characteristics as the C_{p0} plots. The minimum velocity occurs in the spanwise direction, along the center of the wake for the passive suction, 1.4% and 2.0% blowing cases (Figures 4-54, 4-56 and 4-58). The wake at 2.6% is overblown and does not display this characteristic (Figure 4-60). Equivalent characteristics are present for the U/U_{ref} cross-sections at x/c_a = 1.877 (Figures 4-62, 4-64, 4-66 and 4-68).

4.1.5.2. *Kuethe Vane*

On the four 0.839 x/c_a C_{p0} cross-sections, the upper end-wall boundary layer does not have a uniform thickness, and in fact nearly disappears on the pressure side of the blade. This is most likely due to an undesirable leak in the foamboard roof of the test section. It is unlikely that this leak had a significant effect on the rest of the tunnel flow, since it was estimated to be no larger than 12.7mm. The passive suction cross-section appears to be thicker than the non-blowing baseline cross-section, at $0.75c_a$ wide (Figure 4-69). The suction side bulge at y/c = 7.0 is most pronounced here. At a 1.4% blowing rate, the wake is again deeper than for the passive suction case (Figure 4-71). As the blowing is increased to 2.0%, the deficit is only reduced slightly, from $0.75U_{ref}$ to $0.80U_{ref}$ (Figure 4-73). However, as the blowing reaches 2.6%, the wake is quite overblown in multiple locations, corresponding to the spanwise positioning of the Kuethe vanes (Figure 4-75). The overblown regions are approximately $0.2c_a$ in spanwise height. Similar to the simple blowing blades, the tip region experiences a greater blowing surplus than other spanwise locations.

The upper end-wall boundary layer on the 1.877 x/c_a cross-sections has a wavy structure, again due to a leak in the test section roof. The C_{p0} cross-section with no blowing at 1.877 x/c_a matches the one at 0.839 x/c_a except for an increase in width (Figure 4-77). The same characteristics visible at 0.839 x/c_a can be seen here for each blowing rate, although the high velocity regions associated with the Kuethe vane placement have decreased in spanwise height, to $0.1c_a$. The bulge has become a main feature of the cross-section by 1.877 axial chords downstream, even at the higher blowing rates (Figures 4-79, 4-81 and 4-83).

The U/U_{ref} cross-sections at $x/c_a = 0.839$ indicate the minimum velocity outside of the tip-leakage vortex occurs in the center of the wake ($0.60U_{ref}$ to $0.70U_{ref}$) for the passive suction, 1.4% and 2.0% blowing cases (Figures 4-70, 4-72 and 4-74). As with the simple blowing case at 2.6%, the Kuethe vane cross-section confirms that the wake is overblown (Figure 4-76). Figures 4-78, 4-80, 4-82 and 4-84 at $x/c_a = 1.877$ are nearly the same as at $x/c_a = 0.839$, aside from the increased wake width.

4.2. Wake Mid-Span Profiles at $x/c_a = 1.819$

On all of the cross-sections described above, the wake is essentially two-dimensional and vertical around mid-span, $y/c_a = 0.92$. Velocity measurements were then made at mid-span with the expectation that they would be representative of two-dimensional flow without any end-wall effects.

Mid-span velocity measurements of the blowing blades were made with a four-sensor hot-wire at downstream locations of 0.608, 1.178, 1.819 and 2.382 x/c_a for eleven different blowing rates between 0% and 2.7%. In the following sections, the mean velocity profiles, the wake parameters calculated from these measurements and the turbulence profiles are presented, for $x/c_a = 1.819$. The figures do not include the 0% case, but instead show the non-blowing baseline as a more practical comparison.

Results of the 2.0% mid-span profile for the Kuethe vane blades should be regarded with caution. It is highly likely that this profile was subject to irreparable instrumentation errors. The three-component mean velocity profiles are not suspicious and are therefore included in this report. The unsteady velocity components deviated from their expected curves in such an illogical manner, that the Reynolds stresses and triple products are not presented for 2.0%.

4.2.1. Mean Velocity Profiles

4.2.1.1. *Simple Blowing*

Figure 4-85 shows the mean velocity in the X-direction, minus the edge velocity, normalized on U_{ref} versus the pitchwise distance normalized on the axial chord, at a downstream location of 1.819 x/c_a for the baseline and ten blowing cases. The pitchwise origin lies at the wake center. The baseline profile is wider that all of the blowing profiles, though not as deep: the velocity deficit at x/c_a = 1.819 appears to increase by $0.01U_{ref}$ at blowing rates of 1.4% and 1.5%, confirming the results of the Pitot-static full cross-sections. This indicates an increase in wake strength at low blowing rates and implies that trailing-edge blowing is not simply a superposition of the blowing jet to the blade wake. Between 1.7% and 2.7%, the velocity deficit does decrease as expected with increasing blowing rate. While 2.6% and 2.7% are completely overblown, both wake-like and jet-like components are present at 2.5%. This rate most effectively cancels the wake, which may lead to a decrease in tone noise. The overblown profiles are asymmetric and stronger on the pressure side. As the normal-to-span cross-sections indicated, the blown wake is angled towards the pressure side.

The above results can be alternatively visualized with the maximum velocity deficit, U_{w-}. Table 4-1 and Figure 4-86 show the maximum deficit normalized on U_{ref} at all four streamwise locations. By a blowing rate of 2.5%, the maximum deficit has decreased to $0.03U_{ref}$ or less. As the wake becomes overblown at 2.6% and 2.7%, the deficit reverses and U_{w-} is nearly zero.

Figures 4-87 and 4-88 show the velocity components in the *Y*- and *Z*-directions, respectively, at an x/c_a of 1.819. Each is normalized on U_{ref} and is plotted against the pitchwise distance normalized on the axial chord. The left side of the figure is the suction side of the blade and the right of the figure is the pressure side. Neglecting the baseline profiles, the profiles at the other ten rates are of the same shape. On the pressure side of the graphs the profiles overlap at all blowing rates (as a result of the method of data rotation), while on the suction side they are influenced by the blowing. For V/U_{ref} the velocities on the suction side decreases continuously between the 1.4% and 2.7%, and for W/U_{ref} the opposite occurs, although these velocities are extremely small over the entire pitchwise range, as is characteristic of two-dimensional plane wakes.

4.2.1.2. *Kuethe Vane*

Figure 4-89 shows (U-U_e) normalized on U_{ref} versus the normalized pitchwise distance at an x/c_a of 1.819. As with the simple blowing blades, the baseline profile is wider than the blowing profiles. At the wake center, it appears that 1.4% and 1.5% are nearly as deep as the baseline wake. Beyond 1.7%, the deficit decreases steadily, although the wake never achieves complete cancellation. At 2.7%, simultaneous wake-like and jet-like parts are just beginning to emerge, with the pressure side overblown by $0.005U_{ref}$. The blown wakes of the Kuethe vane blades are angled towards the pressure side as the simple blowing wakes are.

The maximum velocity deficit, U_w/U_{ref}, can be seen in Table 4-2 and Figure 4-90. At an x/c_a of 1.819, the deficit reduces from $0.10U_{ref}$ at 1.4% to $0.02U_{ref}$ at 2.7%. The Kuethe vane blowing blades do not eliminate the maximum deficit as the simple blowing blades have been shown to do, but they do substantially reduce it.

The components of velocity in the *Y*- and *Z*-directions at $x/c_a = 1.819$ are shown in Figures 4-91 and 4-92. The simple blowing profiles are only aligned on the pressure side from the rotation process, but these profiles seem much more aligned with each other over both the pressure and suction sides. The baseline case still lies away from the others, as is especially obvious in W/U_{ref}. The 2.5% through 2.7% V/U_{ref} profiles vary slightly from the group on the suction side, decreasing by roughly 0.005. Both sets of velocity profiles are comparable in magnitude to the simple blowing blades.

4.2.2. Wake Parameters

The wake parameters were converted from the pitchwise *z*-direction to the wake-aligned coordinate system, parallel to the *Z*-direction, by multiplying by the cosine of the angle between the *z*- and *Z*-axes, which is 53.3° for the non-blowing baseline blades, according to Geiger (2005). From records of the wake center position for the simple blowing and Kuethe vane blades relative to that of the baseline, a rotation angle was calculated for each blowing rate at an x/c_a of 1.819 (Table 4-1).

Table 4-1. Blown wake center position relative to the baseline (mm) and blown wake rotation angles (deg).

Blowing Rate	**Wake Center Position (mm) Relative to Baseline**	**Rotation Angle (deg)**
Baseline	0	53.3
1.4	-2.54	53.1
1.5	-2.54	53.1
1.7	-2.54	53.1
1.9	-2.54	53.1
2.0	-2.54	53.1
2.1	-2.54	53.1
2.3	-2.54	53.1
2.5	-7.62	52.7
2.6	-10.16	52.5
2.7	-10.16	52.5

4.2.2.1. *Simple Blowing*

The pitchwise and wake-aligned values of the displacement thickness, momentum thickness and the wake half-width and the pitchwise U_w and velocity deficit for the baseline and the simple blowing blades are presented in Table 4-2.

Table 4-2. Normalized simple blowing wake parameters.

		Pitchwise					Wake-Aligned		
Blowing Rate	x/c_a	δ^*/c_a	θ/c_a	L_u/c_a	U_w/U_{ref}	U_w/U_{ref}	δ^*/c_a	θ/c_a	L_u/c_a
Baseline	0.6	0.052	0.042	0.257	0.068	0.201	0.031	0.025	0.153
1.4	0.6	0.044	0.036	0.208	0.051	0.202	0.027	0.021	0.125
1.5	0.6	0.039	0.032	0.194	0.049	0.197	0.024	0.019	0.116
1.7	0.6	0.032	0.027	0.190	0.041	0.157	0.019	0.016	0.114
1.9	0.6	0.022	0.020	0.182	0.036	0.115	0.013	0.012	0.109
2.0	0.6	0.019	0.018	0.181	0.033	0.102	0.012	0.011	0.109
2.1	0.6	0.017	0.015	0.181	0.031	0.089	0.010	0.009	0.109
2.3	0.6	0.009	0.008	0.168	0.035	0.056	0.005	0.005	0.101
2.5	0.6	0.000	0.000	0.158	0.039	0.031	0.000	0.000	0.096
2.6	0.6	-0.005	-0.005	0.155	0.043	0.015	-0.003	-0.003	0.094
2.7	0.6	-0.008	-0.009	0.152	0.046	0.009	-0.005	-0.005	0.092
		Pitchwise					**Wake-Aligned**		
Blowing Rate	x/c_a	δ^*/c_a	θ/c_a	L_u/c_a	U_w/U_{ref}	U_w/U_{ref}	δ^*/c_a	θ/c_a	L_u/c_a
Baseline	1.2	0.048	0.042	0.392	0.050	0.136	0.029	0.025	0.234
1.4	1.2	0.038	0.033	0.257	0.043	0.144	0.023	0.020	0.154
1.5	1.2	0.034	0.030	0.240	0.038	0.136	0.021	0.018	0.144
1.7	1.2	0.029	0.026	0.225	0.034	0.119	0.017	0.015	0.135
1.9	1.2	0.022	0.020	0.223	0.028	0.094	0.013	0.012	0.134
2.0	1.2	0.019	0.017	0.221	0.025	0.083	0.011	0.010	0.133
2.1	1.2	0.016	0.015	0.220	0.024	0.073	0.010	0.009	0.132
2.3	1.2	0.009	0.009	0.214	0.021	0.046	0.005	0.005	0.129
2.5	1.2	0.001	0.001	0.205	0.023	0.020	0.001	0.001	0.125
2.6	1.2	-0.003	-0.003	0.206	0.026	0.010	-0.002	-0.002	0.126
2.7	1.2	-0.006	-0.006	0.207	0.027	0.003	-0.004	-0.004	0.126
		Pitchwise					**Wake-Aligned**		
Blowing Rate	x/c_a	δ^*/c_a	θ/c_a	L_u/c_a	U_w/U_{ref}	U_w/U_{ref}	δ^*/c_a	θ/c_a	L_u/c_a
Baseline	1.8	0.046	0.042	0.430	0.042	0.108	0.028	0.025	0.257
1.4	1.8	0.036	0.032	0.330	0.036	0.110	0.022	0.019	0.198
1.5	1.8	0.033	0.030	0.313	0.034	0.107	0.020	0.018	0.188
1.7	1.8	0.027	0.024	0.279	0.029	0.094	0.016	0.015	0.168
1.9	1.8	0.021	0.019	0.263	0.024	0.077	0.012	0.011	0.158
2.0	1.8	0.018	0.017	0.265	0.022	0.069	0.011	0.010	0.159
2.1	1.8	0.015	0.014	0.267	0.020	0.059	0.009	0.009	0.161
2.3	1.8	0.008	0.008	0.293	0.016	0.032	0.005	0.005	0.176
2.5	1.8	0.001	0.001	0.318	0.017	0.010	0.001	0.001	0.193
2.6	1.8	-0.004	-0.004	0.280	0.020	0.003	-0.002	-0.002	0.171

2.7	1.8	-0.007	-0.007	0.292	0.022	0.001	-0.004	-0.004	0.178
		Pitchwise					**Wake-Aligned**		
Blowing Rate	x/c_a	δ^*/c_a	θ/c_a	L_u/c_a	U_w/U_{ref}	U_w/U_{ref}	δ^*/c_a	θ/c_a	L_u/c_a
Baseline	2.4	0.049	0.045	0.467	0.038	0.099	0.029	0.027	0.279
1.4	2.4	0.036	0.033	0.304	0.033	0.097	0.022	0.020	0.183
1.5	2.4	0.034	0.031	0.309	0.030	0.094	0.020	0.018	0.186
1.7	2.4	0.027	0.025	0.301	0.026	0.082	0.016	0.015	0.181
1.9	2.4	0.021	0.020	0.305	0.022	0.069	0.013	0.012	0.183
2.0	2.4	0.018	0.017	0.298	0.020	0.061	0.011	0.010	0.179
2.1	2.4	0.016	0.015	0.312	0.019	0.057	0.010	0.009	0.187
2.3	2.4	0.009	0.009	0.309	0.014	0.032	0.005	0.005	0.185
2.5	2.4	0.001	0.001	0.324	0.015	0.009	0.001	0.001	0.196
2.6	2.4	-0.004	-0.004	0.330	0.018	0.001	-0.003	-0.003	0.201
2.7	2.4	-0.009	-0.009	0.355	0.020	0.002	-0.005	-0.005	0.216

Figure 4-93 shows the displacement thickness normalized on the axial chord for each of the cases. A set of data points is displayed for each of the four axial locations. The values do not change significantly as the wake moves downstream, as expected from the definition of displacement thickness (Eqn. 3-7). There is a reduction of 0.005 in the displacement thickness from x/c_a = 0.608 to 2.382 at a blowing rate of 1.4%, and an increase of 0.001 over this range for a blowing rate of 2.5%. However, at a given location, the displacement thickness does diminish with increasing blowing rate, if the passive suction case is neglected. The passive suction case here means that no blowing was applied even though the blowing slot was left open, which is not at all representative of the non-blowing baseline blades. The average (over the four axial locations) wake-aligned displacement thickness for the baseline blades is 0.029, while the maximum measured simple blowing displacement thickness is 0.027, occurring at x/c_a = 0.608 for a 1.4% blowing rate. The thickness decreases to essentially zero at a blowing rate of 2.5%, before becoming negative over the remaining two rates. This indicates an optimum blowing rate near 2.5% for the simple blowing. Interestingly, the displacement thickness appears to decrease in two linear segments of different slopes. The break in slope occurs between 2.1% and 2.3%.

The normalized momentum thickness at each location and blowing rate is shown in Figure 4-94. These values are nearly constant with downstream location, as Eqn. 3-8 suggests. While again neglecting the passive suction case, the momentum thickness decreases at two separate linear rates from its maximum value of 0.021 at 1.4% to zero at 2.5%. This confirms the optimum blowing rate of 2.5% suggested by the displacement thickness values, and provides a reasonable comparison to the average momentum thickness of 0.026 achieved by the baseline blades. The two linear rates appear to be the same as those seen in the displacement thicknesses. Smaller momentum thicknesses indicate a possible reduction in drag.

Figure 4-95 shows the wake half-width based on the maximum streamwise Reynolds stress, $L_{u'}/c_a$. Overall, the half-width is roughly 0.05 larger at each progressive downstream location. At both 0.608 and 1.178 x/c_a, the wake half-width is decreasing by 0.05 over the entire range of blowing rates, though the data is still consistent with approximately square root growth. The blowing is effectively decreasing the size of the wake. However, at 1.819 and 2.382 x/c_a, the half-width seems to reach a minimum around 2.0% before increasing again. This suggests that the blowing is losing effectiveness around 1.819 axial chords downstream while the wake spreading effect dominates. The largest values of $L_{u'}/c_a$ occur with passive suction and at 1.4%, but they are all significantly less than the wake half-widths of the non-blowing baseline blades (Table 3-1) for a given location, implying that the wakes of the baseline blades are wider than the wakes of the simple blowing blades at all blowing rates, as was seen in Figure 4-85. Although the wake half-widths decrease with blowing rate, they do not decrease as dramatically as the displacement thicknesses and momentum thicknesses.

4.2.2.2. *Kuethe Vane*

The pitchwise and wake-aligned values of the displacement thickness, momentum thickness and the wake half-width and the pitchwise U_w and velocity deficit for the baseline and the Kuethe vane blowing blades are presented in Table 4-3.

Table 4-3. Normalized Kuethe vane wake parameters.

		Pitchwise					Wake-Aligned		
Blowing Rate	x/c_a	δ^*/c_a	θ/c_a	L_u/c_a	U_w/U_{ref}	U_{w-}/U_{ref}	δ^*/c_a	θ/c_a	L_u/c_a
Baseline	0.6	0.052	0.042	0.257	0.068	0.201	0.031	0.025	0.153
1.4	0.6	0.038	0.030	0.231	0.059	0.177	0.023	0.018	0.139
1.5	0.6	0.044	0.036	0.229	0.057	0.171	0.026	0.022	0.137
1.7	0.6	0.037	0.032	0.220	0.051	0.149	0.022	0.019	0.132
1.9	0.6	0.032	0.028	0.217	0.047	0.131	0.019	0.017	0.130
2.0	0.6	0.028	0.025	0.212	0.044	0.118	0.017	0.015	0.128
2.1	0.6	0.024	0.022	0.206	0.042	0.107	0.015	0.013	0.124
2.3	0.6	0.017	0.015	0.198	0.037	0.082	0.010	0.009	0.119
2.5	0.6	0.011	0.011	0.196	0.034	0.062	0.007	0.006	0.119
2.6	0.6	0.006	0.006	0.187	0.036	0.048	0.004	0.003	0.114
2.7	0.6	0.003	0.003	0.181	0.038	0.038	0.002	0.002	0.110
		Pitchwise					**Wake-Aligned**		
Blowing Rate	x/c_a	δ^*/c_a	θ/c_a	L_u/c_a	U_w/U_{ref}	U_{w-}/U_{ref}	δ^*/c_a	θ/c_a	L_u/c_a
Baseline	1.2	0.048	0.042	0.392	0.050	0.136	0.029	0.025	0.234
1.4	1.2	0.041	0.036	0.307	0.044	0.128	0.025	0.022	0.184
1.5	1.2	0.039	0.035	0.302	0.043	0.122	0.024	0.021	0.182
1.7	1.2	0.034	0.031	0.283	0.038	0.112	0.021	0.018	0.170
1.9	1.2	0.029	0.027	0.274	0.034	0.010	0.018	0.016	0.165
2.0	1.2	0.028	0.025	0.268	0.033	0.093	0.017	0.015	0.161
2.1	1.2	0.023	0.021	0.265	0.030	0.081	0.014	0.013	0.159
2.3	1.2	0.017	0.016	0.253	0.026	0.060	0.010	0.009	0.152
2.5	1.2	0.011	0.010	0.247	0.023	0.045	0.007	0.006	0.150
2.6	1.2	0.006	0.006	0.241	0.022	0.033	0.004	0.004	0.147
2.7	1.2	0.004	0.004	0.232	0.023	0.027	0.003	0.002	0.141
		Pitchwise					**Wake-Aligned**		
Blowing Rate	x/c_a	δ^*/c_a	θ/c_a	L_u/c_a	U_w/U_{ref}	U_{w-}/U_{ref}	δ^*/c_a	θ/c_a	L_u/c_a
Baseline	1.8	0.046	0.042	0.430	0.042	0.108	0.028	0.025	0.257
1.4	1.8	0.041	0.037	0.348	0.036	0.105	0.025	0.022	0.209
1.5	1.8	0.038	0.035	0.351	0.035	0.102	0.023	0.021	0.211
1.7	1.8	0.033	0.030	0.340	0.031	0.092	0.020	0.018	0.204
1.9	1.8	0.028	0.026	0.324	0.029	0.083	0.017	0.015	0.195
2.0	1.8	0.025	0.023	0.320	0.027	0.078	0.015	0.014	0.192
2.1	1.8	0.022	0.021	0.315	0.025	0.070	0.013	0.012	0.189
2.3	1.8	0.015	0.015	0.309	0.021	0.053	0.009	0.009	0.186
2.5	1.8	0.010	0.010	0.307	0.017	0.036	0.006	0.006	0.186
2.6	1.8	0.006	0.006	0.300	0.016	0.026	0.004	0.004	0.183

2.7	1.8	0.004	0.004	0.297	0.017	0.019	0.002	0.002	0.181
		Pitchwise					**Wake-Aligned**		
Blowing Rate	x/c_a	δ^*/c_a	θ/c_a	L_u/c_a	U_w/U_{ref}	U_w/U_{ref}	δ^*/c_a	θ/c_a	L_u/c_a
Baseline	2.4	0.049	0.045	0.467	0.038	0.099	0.029	0.027	0.279
1.4	2.4	0.043	0.039	0.439	0.034	0.100	0.026	0.023	0.264
1.5	2.4	0.041	0.037	0.428	0.033	0.097	0.025	0.022	0.257
1.7	2.4	0.039	0.036	0.370	0.030	0.088	0.023	0.022	0.222
1.9	2.4	0.031	0.029	0.374	0.027	0.082	0.019	0.017	0.225
2.0	2.4	0.028	0.026	0.368	0.026	0.076	0.017	0.016	0.221
2.1	2.4	0.025	0.023	0.363	0.024	0.070	0.015	0.014	0.218
2.3	2.4	0.019	0.018	0.355	0.020	0.056	0.011	0.011	0.213
2.5	2.4	0.014	0.013	0.378	0.018	0.044	0.008	0.008	0.229
2.6	2.4	0.011	0.010	0.324	0.015	0.035	0.006	0.006	0.198
2.7	2.4	0.007	0.007	0.328	0.014	0.026	0.004	0.004	0.200

Figure 4-96 is a plot of the normalized displacement thickness. Variation with axial location is minimal. Between 1.4% and 2.7%, displacement thickness at x/c_a = 1.819 decreases from 0.025 to 0.002. The two rates of reduction with blowing rate for the Kuethe vane blowing blades appear to be very similar to those of the simple blowing blades, with the change in slope occurring between 2.1% and 2.3%. Whereas Figure 4-93 showed an optimum blowing rate at 2.5% for the simple blowing blades, Figure 4-96 does not indicate that the optimum rate has been achieved over the tested range.

Figure 4-97 of the normalized momentum thickness at an x/c_a of 1.819 versus blowing rate shows two linear decays from 0.022 to 0.002 between 1.4% and 2.7%. These occur at roughly the same rates as for the displacement thickness and simple blowing displacement and momentum thicknesses. No optimum blowing rate is apparent, supporting the same conclusion from the plot of displacement thickness, though extrapolation suggests a rate near 3.3% might force the displacement thickness and momentum thickness to zero.

The normalized wake half-width, in Figure 4-98, displays the same trend as Figure 4-95 does for the simple blowing blades. The wake half-width increases overall between x/c_a = 0.608 and x/c_a = 2.382, by about 0.05 at each location. At any given station, the values decrease, also by 0.05, between the passive suction case and 2.7%. The set of points for $x/c_a = 2.382$ is slightly scattered, though they do show the same overall trend as the other sets. Blowing effects are dominant over wake spreading effects this far downstream, although blowing is not as beneficial here as it is with reduction of displacement and momentum thicknesses.

4.2.3. Reynolds Stresses and Turbulent Kinetic Energy

The Reynolds normal stresses and Reynolds shear stresses for the simple blowing blades and Kuethe vane blades are described in the following section. As combinations of the unsteady parts of the three velocity components, the Reynolds stresses illustrate the effect of the fluctuating velocity field (Pope 2001). The turbulent kinetic energy (*TKE*) is also presented here, since it is defined by the Reynolds normal stresses (Eqn 3-6). Figures 4-99 through 4-116 show the Reynolds stresses and *TKE* normalized on U_{ref} and plotted against the cross-wake distance normalized on the axial chord, z/c_a.

4.2.3.1. *Simple Blowing*

Figure 4-99 shows the streamwise Reynolds normal stress, u'^2/U_{ref}^2, for the simple blowing blades. The maximum normal stress of $1.8\text{x}10^{-3}U_{ref}^2$ is achieved by the baseline. Unlike the mean velocity profiles, the stress levels continuously decrease to a sixth of the maximum with increasing blowing rate, up to 2.3%. At 2.5%, the stress levels decrease slightly on the suction side while increasing on the pressure side because of the dual wake-like and jet-like components of the velocity profile. As the blowing rate is increased further, normal stress increases even more on the pressure side, although it is roughly one-quarter of the passive suction normal stress.

The pitchwise-averaged streamwise Reynolds normal stress, $\overline{u'^2}/U_{ref}^2$, was calculated for each blowing rate by integrating over the range of *z*-locations in the profile and dividing by the blade spacing of 236.0mm. Figure 4-100 shows the curve generated by this process. The local minimum between 2.3% and 2.5% indicates the optimum blowing rate for minimizing this stress.

The spanwise and pitchwise normal stresses (Figures 4-101 and 4-102) are characteristically the same as the streamwise normal stress. The maximum stress occurs with the baseline blades, and the stress decreases to a fourth (v'^2/U_{ref}^2) and a sixth (w'^2/U_{ref}^2) of the maximum at 2.3% blowing. The Reynolds shear stresses ($u'v'/U_{ref}^2$, $v'w'/U_{ref}^2$, $-u'w'/U_{ref}^2$) show significant reductions with increasing blowing rate through 2.3%, but with values at least one order of magnitude smaller than the normal stresses, they are not discussed further (Figures 4-103, 4-104 and 4-105).

Figure 4-106 of k/U_{ref}^2 illustrates the combined effect of the three Reynolds normal stresses. The maximum energy of the fluctuating velocity field ($2.7\text{x}10^{-3}U_{ref}^2$) occurs with the baseline. All blowing profiles have at least 1/3 less energy than the baseline. The energy drops dramatically through the range of low blowing rates, and then the successive decreases become smaller as 2.3% is approached. By this rate, the maximum *TKE* in the wake has been reduced by a factor of five. Above 2.3%, the partially overblown wake (2.5%) and totally overblown wakes (2.6%-2.7%) contain slightly amplified energy levels, comparable to the levels of the 1.9% to 2.1% wakes.

The pitchwise-averaged *TKE* was calculated in the same manner as the pitchwise-averaged streamwise normal stress. Figure 4-107 shows $\overline{k}/U_{ref}^2$ for each blowing rate. The lowest observed average energy occurs between 2.3% and 2.5%, supporting the findings from Figure 4-55.

4.2.3.2. *Kuethe Vane*

The Reynolds normal stresses of the Kuethe vane blowing blades are notably similar to those of the simple blowing blades, in both value and behavior. The streamwise normal stress (Figure 4-108) has a maximum of $1.8\text{x}10^{-3}U_{ref}^2$ for the baseline and of $1.3\text{x}10^{-3}U_{ref}^2$ for 1.4%, and steadily decreases to a peak of approximately $0.3\text{x}10^{-3}U_{ref}^2$ at 2.5%. At this point, reduction continues on the suction side through 2.7%, but the pressure side does not appear to experience a change in streamwise normal stress at higher blowing rates.

The pitchwise-averaged streamwise normal stress is plotted in Figure 4-109. The points do not form a curve with a distinct minimum as the simple blowing points do in Figure 4-99. This suggests that the optimum blowing rate has not yet been achieved.

As with the simple blowing blades, the spanwise and pitchwise normal stresses are comparable to the streamwise normal stress (Figures 4-110 and 4-111). Both fail to show reduction on the pressure side above 2.5% blowing. The Reynolds shear stresses are more responsive to changes in blowing: despite their extremely small values, they do continuously decrease through all blowing rates (Figures 4-112, 4-113 and 4-114).

Although the Kuethe vane blowing blades do not achieve even partial wake cancellation, their turbulent kinetic energy (Figure 4-115) is not tremendously different from the *TKE* of the simple blowing blades. The reductions with increasing blowing rate are steady through 2.5%, at which point the suction side levels continue to drop slightly and the pressure side levels remain unchanged with additional blowing.

The pitchwise-averaged *TKE* curve is represented in Figure 4-116. The points decrease nearly identically to those in the plot of $\overline{u'^2}/U_{ref}{}^2$ (Figure 4-109), again indicating that optimum blowing rate is greater than 2.7%.

4.2.4. Triple Products

The triple product profiles for both sets of blowing blades are found in Figures 4-117 through 4-136. Each simple blowing plot shows ten different blowing rates plus the baseline, and the Kuethe vane plots include all but the 2.0% profile. All profiles are presented with the pitchwise distance normalized on $L_{u'}$ on the horizontal axis and each triple product component normalized on U_w on the vertical axis. Triple products normalized in this manner should be constant with streamwise location, if the wakes were fully developed (Devenport *et al*, 1999).

4.2.4.1. *Simple Blowing*

Figures 4-117 through 4-126 show the ten triple products for the simple blowing blades: u'^3, v'^3, w'^3, $u'v'^2$, $v'u'^2$, $v'w'^2$, $w'v'^2$, $u'w'^2$, $w'u'^2$ and $u'v'w'$ all normalized on U_w, the square root of the maximum streamwise normal stress. In a two-dimensional plane wake, the triple products w'^3, $w'v'^2$, $w'u'^2$ and $u'v'w'$ are exactly zero (Devenport *et al*, 1999). They are not zero here, which can be attributed to a combination of measurement uncertainty and the small *W* velocity components that are displayed in Figure 4-88. Because of the wake inversion that occurs at blowing rates of 2.5%, 2.6% and 2.7%, these profiles do not follow the trend of the others on the many figures.

4.2.4.2. *Kuethe Vane*

Triple products for the Kuethe vane blades are plotted in Figures 4-127 through 4-136. They demonstrate three-dimensionality in the same manner as the simple blowing blades. Profiles for 2.6% and 2.7% are distinctive, since the wake is just beginning to produce a jet-like portion. All triple product profiles are representative of the baseline, aside from a small offset of $0.25L_{u'}$ in some cases.

4.2.5. Spectra

A spectral measurement was made at every fifth data point of the mid-span profiles. The resulting spectral plots will reveal periodic behavior within the turbulence and the amount of energy contained by that behavior. Figures 4-137 through 4-142 are the spectral plots for both sets of blowing blades. The frequency (f) on the horizontal axis is normalized by (c_a/U_{ref}) and the spectral functions (G_{uu}, G_{vv} and G_{ww}) on the vertical axis are normalized by $(1/U_{ref})(1/c_a)$. Each plot shows the spectra at the pitchwise location of maximum streamwise turbulence. The non-blowing baseline spectra at the same location are plotted as a solid line for comparison.

4.2.5.1. *Simple Blowing*

Figures 4-137, 4-138 and 4-139 are normalized spectral plots for the simple blowing blades. These figures indicate that the energy in the wake at all blowing rates is less than that of the baseline at normalized frequencies below $2x10^1$. The energy decreases with decreasing blowing rate, down to 1.5%. Although the wake at 1.4% has been determined to be deeper and wider than the wake with passive suction, the three spectral plots show the least energy in the wake with passive suction. Above a frequency of $2x10^1$, the baseline and 2.7% are roughly equivalent, but the energy does continue to decrease with decreasing blowing rate as it does below this frequency. In Figure 4-139 of the normalized G_{ww}, the simple blowing blade spectra do not show the sharp peak displayed by the baseline at a normalized frequency of $2x10^0$.

4.2.5.2. *Kuethe Vane*

The normalized spectral plots of the Kuethe vane blades are found in Figures 4-140, 4-141 and 4-142. These plots differ from the simple blowing plots in that the energy in the wake at all blowing rates over the entire range of normalized frequencies is less than that of the baseline wake at this downstream location. However, the least energy in the wake occurs at 1.5% here instead of at 1.4% in all three figures. The Kuethe vane blades do not possess the G_{ww} peak of the baseline blades at a normalized frequency of $2x10^0$.

4.3. Potential Noise Reduction – Fourier Decomposition

In an aircraft engine, the downstream stator vanes are subject to a periodic fluctuation due to the motion of the upstream rotor blade wakes. Tone noise is the result of this blade passing frequency and its multiples. To examine the effect of trailing-edge blowing on this phenomenon, the periodic fluctuation must be monitored. The fluctuation has already been measured as the pitchwise variation in mean velocity in the cascade. Performing a Fourier transform in the pitchwise direction produces a spectrum that is proportional to what the leading-edges of the stator vanes would experience.

A Matlab code was written to extract all three components of the mid-span velocity profiles. The profiles are interpolated to 256 points over one period in the pitchwise direction, where the period is equivalent to the blade spacing of 236.0mm, and then Fourier transformed.

After squaring the magnitude of the transformation, the results are converted to decibels and plotted in Figures 4-143 through 4-146. The change in decibels with blowing rate should be noted, not the actual decibel values.

4.3.1. Simple Blowing

Figure 4-143 shows spectral levels of the three velocity components at the four streamwise locations of 0.608, 1.178, 1.819 and 2.382 x/c_a. Each of the twelve sub-plots includes the first 20 modes of the non-blowing baseline and blowing rates of 1.4%, 1.5%, 1.7%, 1.9%, 2.0%, 2.1%, 2.3%, 2.5%, 2.6% and 2.7% for the simple blowing blades. The passive suction case is not included here, since it is not directly comparable with the non-blowing baseline. Spectral levels in *U* are dominant over those in *V* and *W* at all four locations. Some reductions in tone noise with low blowing rates over the non-blowing baseline are seen in the *U* component.

The first five modes of the streamwise velocity component are displayed in Figure 4-144, with each of the four sub-plots showing a different streamwise location. Similar trends in noise levels are present at each location, such as the occurrence of the maximum tone noise reduction at 2.5% for all modes, though there are slight differences particular to each one.

At 0.608 x/c_a, the non-blowing baseline is dominant in the first three modes. In the first mode, the tone noise decreases at each successively higher blowing rate up to 2.5%, where the difference from the non-blowing baseline is greater than 25dB. From there, the noise levels increase at 2.6% and 2.7% by 7dB and 10dB respectively. Similar reductions occur over the second and third modes. In the fourth mode, the non-blowing baseline and the 1.4% blowing case produce equivalent tone noise. The difference between this level and the noise level at the optimum blowing rate of 2.5% is less than 20dB. Mode five is distinct in that the 1.4% and 1.5% blowing cases produce more noise than the baseline. All modes show an overall trend of tone noise reduction to 2.5% followed by an increase over 2.6% and 2.7%.

The blowing at 2.5% has an even greater effect at x/c_a = 1.178. A reduction of close to 30dB from the non-blowing baseline can be observed. A blowing rate of 1.4% is not effective at noise reduction in modes three through five. In fact, rates between 2.3% and 2.7% are the only ones successful in creating less noise than the non-blowing baseline in the fifth mode.

A blowing rate of 2.5% reaches its ultimate effectiveness in the cascade at 1.819 x/c_a. The tone noise level is decreased roughly 33dB from the non-blowing baseline. With each successive mode, the difference in noise level between the baseline and the optimum rate becomes smaller. By the fifth mode, only a 5dB reduction is produced by the 2.5% blowing.

Although the plots do not differ much with streamwise location, 2.7% blowing does seem to have more effect on the tone noise as downstream location increases. At 0.608 and 1.178 x/c_a, the decibel level remains essentially unchanged over the first five modes, although at 1.819 x/c_a it does decrease slightly with each mode. By an x/c_a of 2.382, the tone noise lessens by approximately 10dB between the first and the fifth mode.

4.3.2. Kuethe Vane

The spectral levels of the three velocity components at the four downstream locations are shown in the sub-plots of Figure 4-145. Over roughly the first five modes, the noise levels associated with the *U*-component decrease with increasing blowing rate at each axial location. This complements the mean velocity profiles, whose deficits decreased consistently with increased blowing over the entire range. At x/c_a = 0.608 and x/c_a = 1.178, the spectral levels of the *V*-component with blowing are practically indistinguishable from one another in the first five modes, though they are all greater than the non-blowing baseline. There does not seem to be a particularly consistent trend associated with the *W*-component.

The first five modes of the streamwise velocity component for the non-blowing baseline and ten blowing rates are plotted for each location in the sub-plots of Figure 4-146. This set of plots is much more consistent with location than the simple blowing plots. At 0.608 x/c_a, tone noise for all five modes steadily decreases from the non-blowing baseline to the maximum blowing rate of 2.7%. The total reduction in the first mode is about 23dB. Between the non-blowing baseline and 2.5% for the simple blowing blades, the total reduction was closer to 25dB, indicating that the Kuethe vane blades are less effective at this location.

The tone noise reduction in the first mode at 2.7% for x/c_a = 1.178 is a little lower, at approximately 20dB. The low blowing rates are responsible for higher tone noise levels than the non-blowing baseline in the third, fourth and fifth modes. At this location, the lower blowing rates create lower noise levels at higher multiples of the blade passing frequency while the higher blowing rates remain relatively unchanged from mode to mode.

At 1.819 and 2.382 axial chords downstream, the blowing is valuable up to the maximum tested for the first three modes. Blowing rates greater than or equal to 2.3% are the only ones capable of suppressing tone noise in the fourth mode at x/c_a = 1.819. At x/c_a = 2.382, 2.6% and 2.7% are the beneficial rates in the fourth mode. At both locations, all blowing rates induce higher noise levels than the non-blowing baseline at five BPF.

4.4. Summary

Unlike Sell (1997) who found that the altered geometry of the blowing blades did not significantly change the performance as compared to the baseline blades, it is apparent here that trailing-edge blowing is a more complex additional effect. From the results of the blade loading measurements, the pressure distribution of the simple blowing blades – at any blowing rate – does not completely match the distribution of the baseline GE Rotor B blades. However, the simple blowing blades are more representative of the baseline than the Kuethe vane blades are. Pressure coefficient differences between the baseline and the Kuethe vane blades reach 0.2, between x/c = 0.7 and 0.9.

Slot uniformity measurements of the simple blowing blades revealed that the blowing becomes more uniform with blowing rate. Pitchwise, the blowing is stronger towards the pressure side of the blade. As blowing rate is increased, regions of velocity approaching the freestream value appear in spanwise positions corresponding to the internal blade passages. The Kuethe vane slot uniformity measurements also revealed these regions, although a new serrated pattern associated with the Kuethe vane spacing of 25.4mm is also apparent.

Oil flow visualizations of the simple blowing blades showed regions of low surface momentum occurring streamwise between 0.05c and 0.10c upstream of the blowing slot for the blowing rates tested at 1.4% and above. The oil flow photographs of both sets of blowing blades, show a low momentum region on the blade suction side extending spanwise from 0.70c to the upper end-wall.

Cross-sections perpendicular to the blade span were made in the trailing-edge region for multiple blowing rates. The first evidence of the increase in wake deficit for the simple blowing blades at 1.4% as compared to passive suction is seen here. The wake velocities increase with blowing, and by 2.3% partial wake cancellation has been achieved. Cross-sections taken at 2.6% and 2.7% indicate overblown wakes, since the velocity inside the wake has surpassed the edge velocity of $0.76U_{ref}$. Kuethe vane normal-to-span cross-sections were only taken at blowing rates of 0%, 1.0% and 1.4%, although each rate included three spanwise locations to determine the effects of the vortex generators. At low blowing rates, no wake filling occurs, but there is no increase of wake deficit as with the simple blowing blades. All blowing rates for both sets of blowing blades indicate a slight angling of the wake towards the pressure side.

Pitot-static cross-sections were made at x/c_a = 0.839 and 1.877 for both set of blowing blades. The wake of the simple blowing blades increases between passive suction and 1.4%, though all blowing rates for these blades have a narrower wake than the baseline GE Rotor B blades at these two streamwise locations. Overblowing is present on the 2.6% cross-sections. The Kuethe vane blades also have a smaller wake width than the baseline, and partial wake cancellation occurs at 2.6% in a vertically spaced pattern corresponding to the locations of the internal passages and the vortex generators on the suction side of the blade.

The mid-span velocity profiles confirm the results of the normal-to-span cross-sections and the Pitot-static full cross-sections, while also providing comparison the results of the baseline study of Geiger (2005). The mean spanwise and cross-wake velocities of both sets of blowing blades are very different from the baseline, even in direction. The blowing displacement thicknesses and momentum thickness are at least $0.005c_a$ smaller than those of the baseline at the four measured streamwise locations of x/c_a = 0.608, 1.178, 1.819 and 2.382. The wake half-widths indicate that the baseline blades do indeed have wider wakes than the blowing blades. Reynolds normal stresses and turbulent kinetic energy are at least 25% lower than the baseline for both blowing blade sets, at all rates between 1.4% and 2.7%. The Kuethe vane spanwise normal stress is the only stress not following this trend. Spectral measurements of the simple blowing blades show clear reductions of the energy in the wake for all blowing rates over the majority of the range of normalized frequencies, while the Kuethe vane blades show reductions at all rates and all frequencies.

The Fourier decomposition technique produces a spectrum proportional to the periodic fluctuations produced by these blades by extracting the pitchwise variation in velocity from the mid-span velocity profiles of both the baseline and the blowing blades. This process allows the mean velocities of the blades to be compared in terms of decibels. The simple blowing blades show tone noise benefits at the blade passing frequency at all blowing rates and streamwise locations. As all other results confirm, 2.5% is the optimum blowing rate, since it shows the most promise for tone noise reduction. At the blade passing frequency, the Kuethe vane blades suggest tone noise reductions through all blowing rates tested in this study.

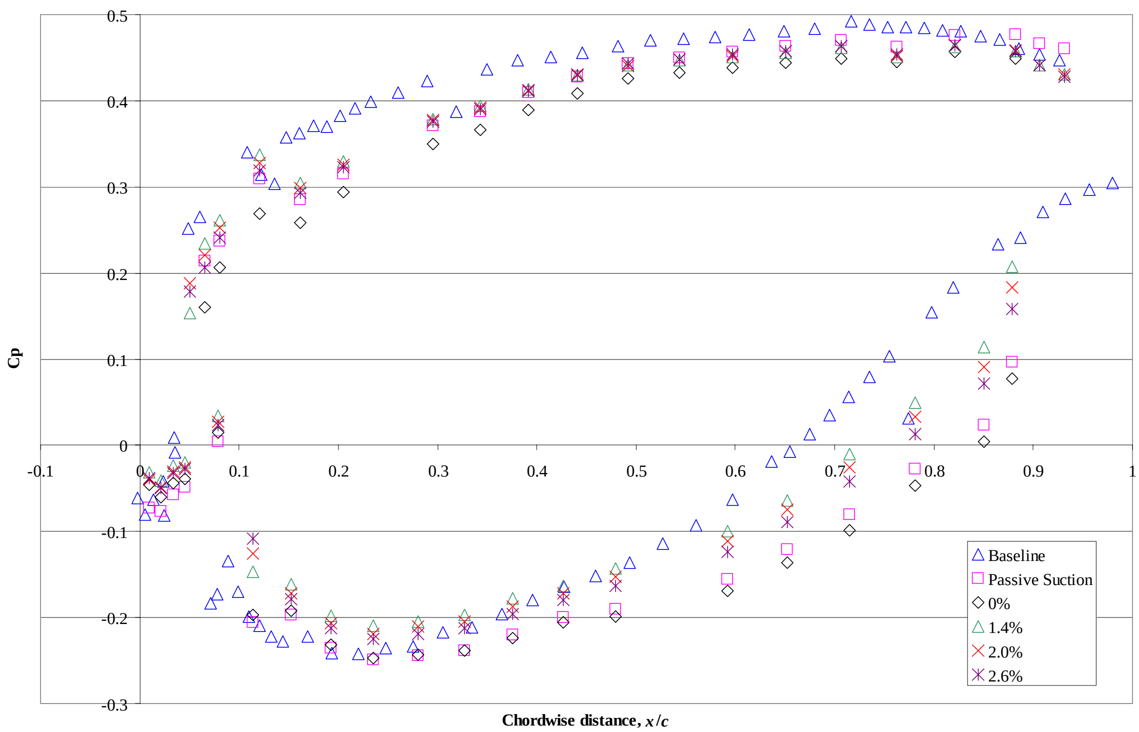

Figure 4-1: Mean pressure coefficient distributions at mid-span for the baseline and the simple blowing blades as a function of blowing rate.

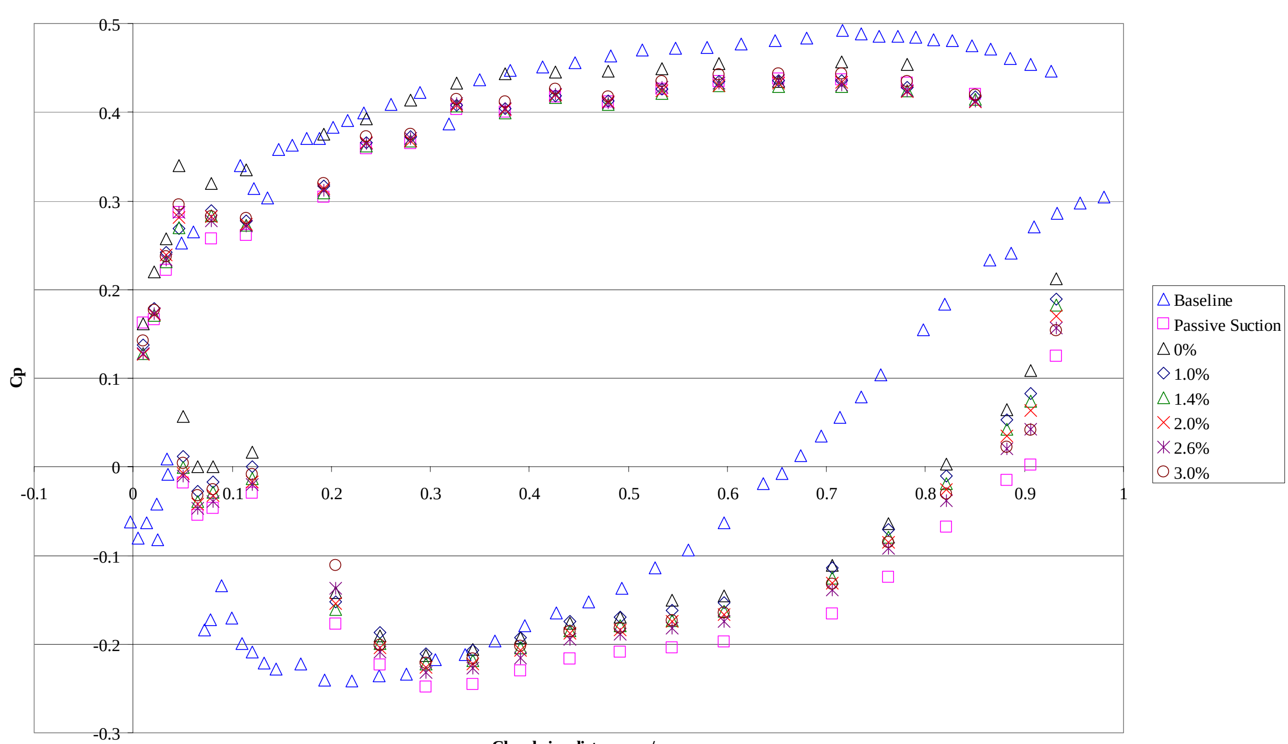

Figure 4-2: Mean pressure coefficient distributions at mid-span for the baseline and the Kuethe vane blowing blades as a function of blowing rate.

Figure 4-3: Rear view of hot-wire probe location for slot uniformity measurements

Figure 4-4: Side view of hot-wire probe location for slot uniformity measurements

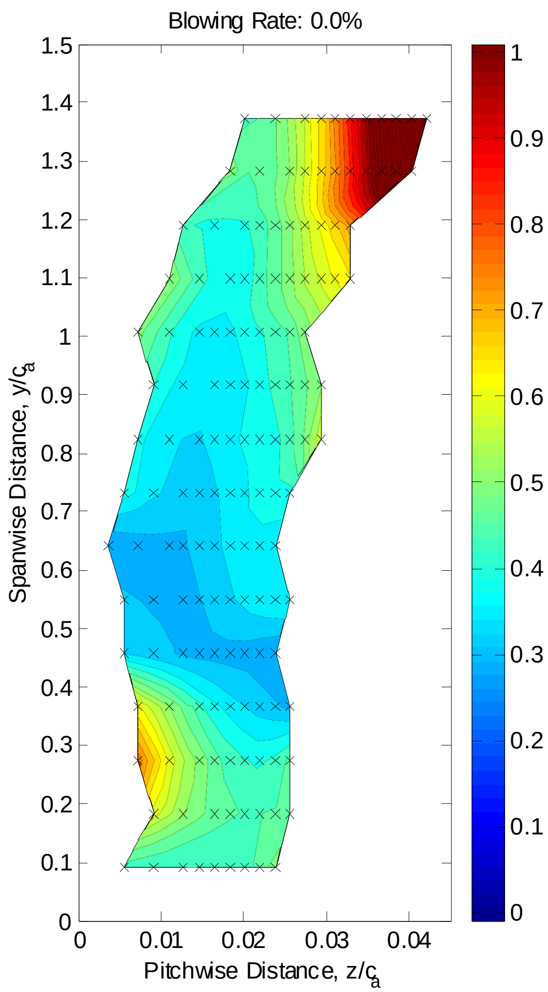

Figure 4-5: Simple blowing slot uniformity U/U_{ref} cross-section (passive suction)

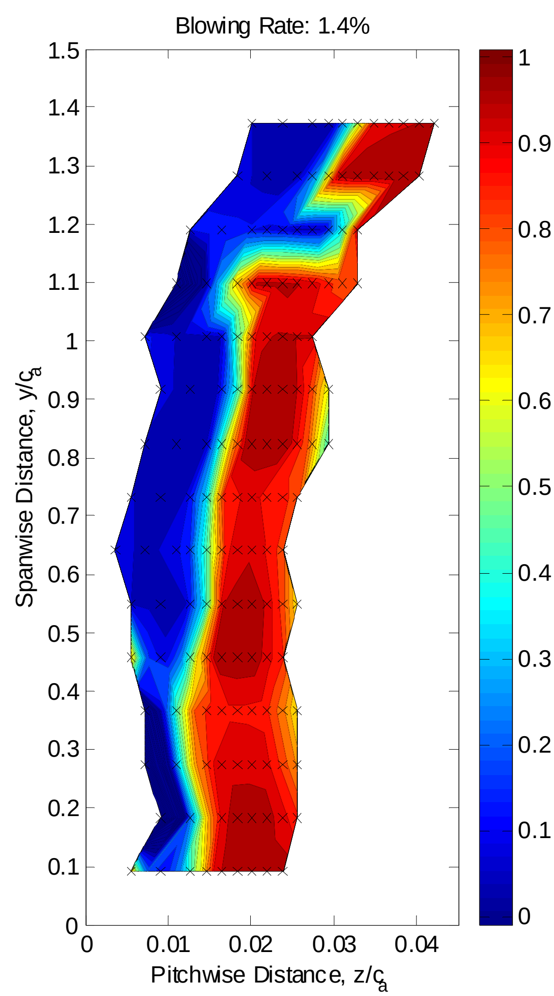

Figure 4-6: Simple blowing slot uniformity U/U_{ref} cross-section (1.4%)

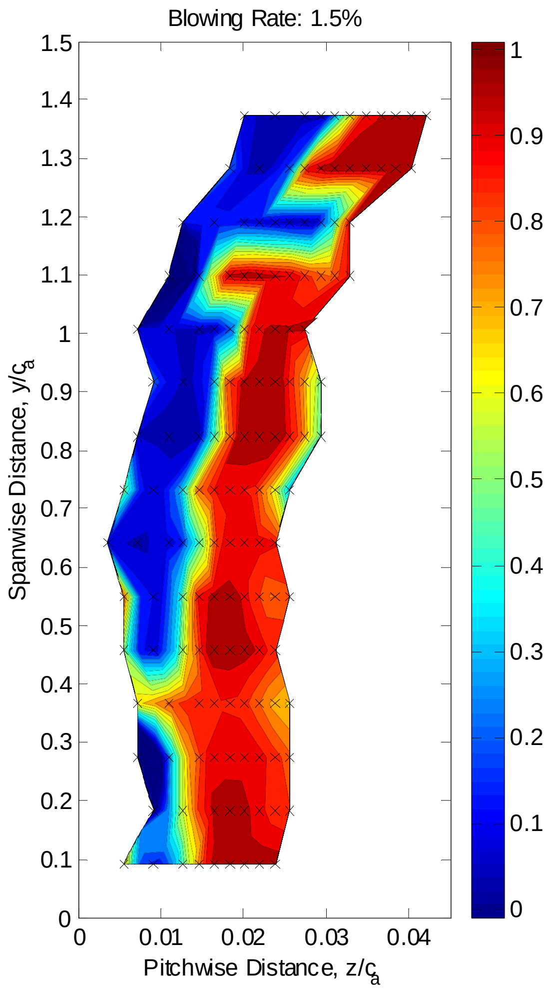

Figure 4-7: Simple blowing slot uniformity U/U_{ref} cross-section (1.5%)

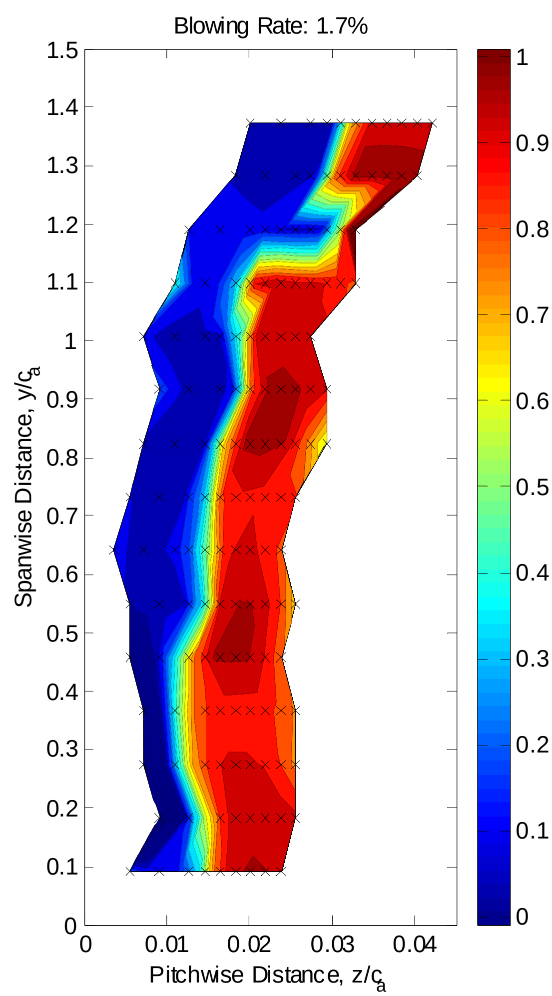

Figure 4-8: Simple blowing slot uniformity U/U_{ref} cross-section (1.7%)

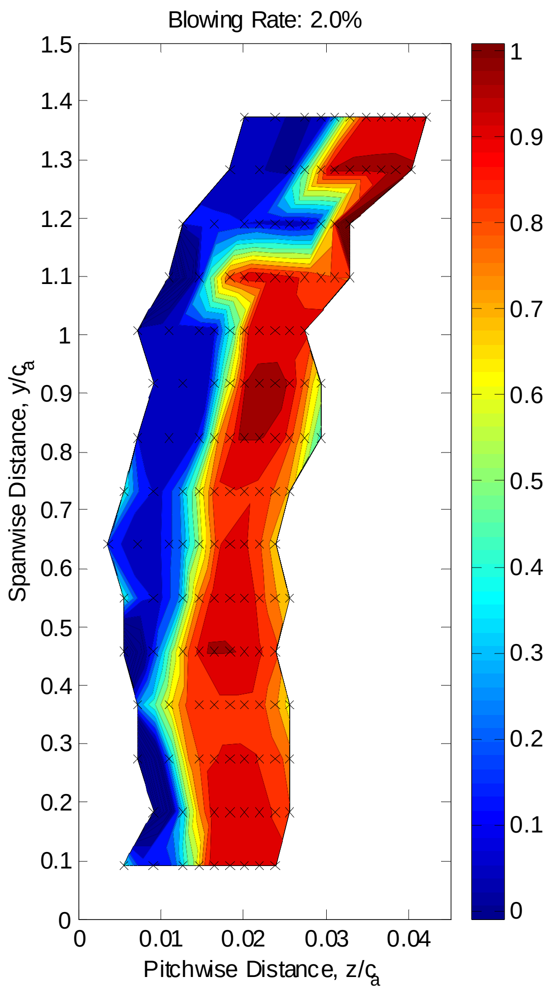

Figure 4-9: Simple blowing slot uniformity U/U_{ref} cross-section (2.0%)

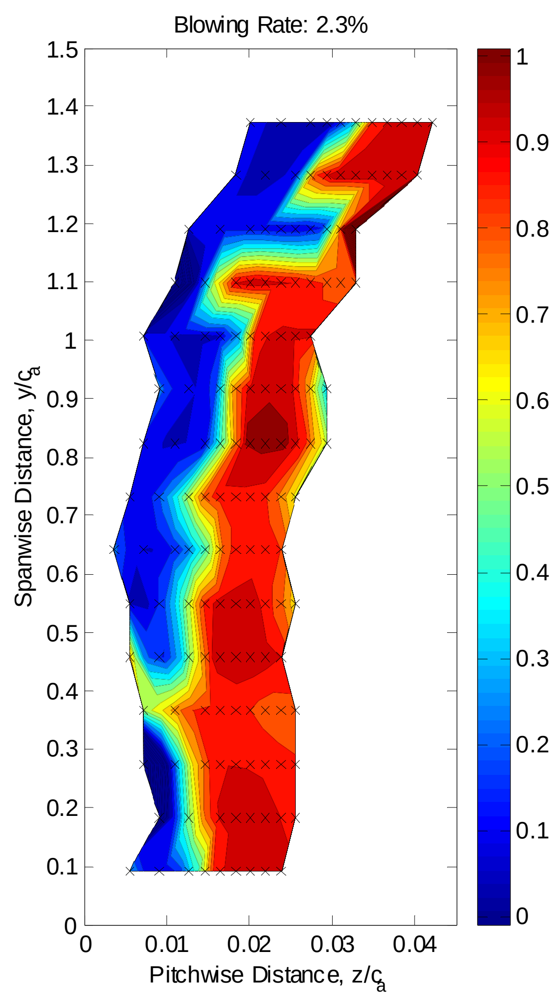

Figure 4-10: Simple blowing slot uniformity U/U_{ref} cross-section (2.3%)

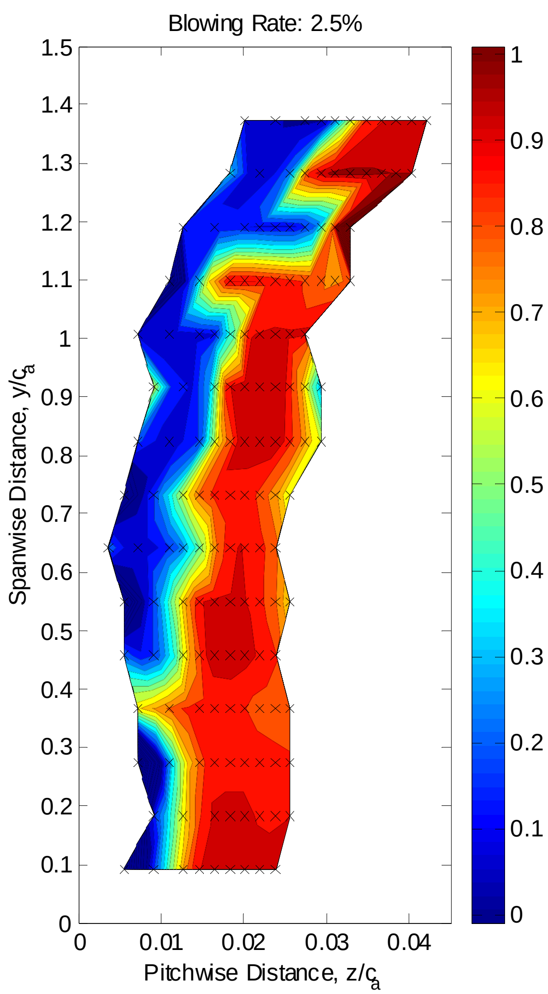

Figure 4-11: Simple blowing slot uniformity U/U_{ref} cross-section (2.5%)

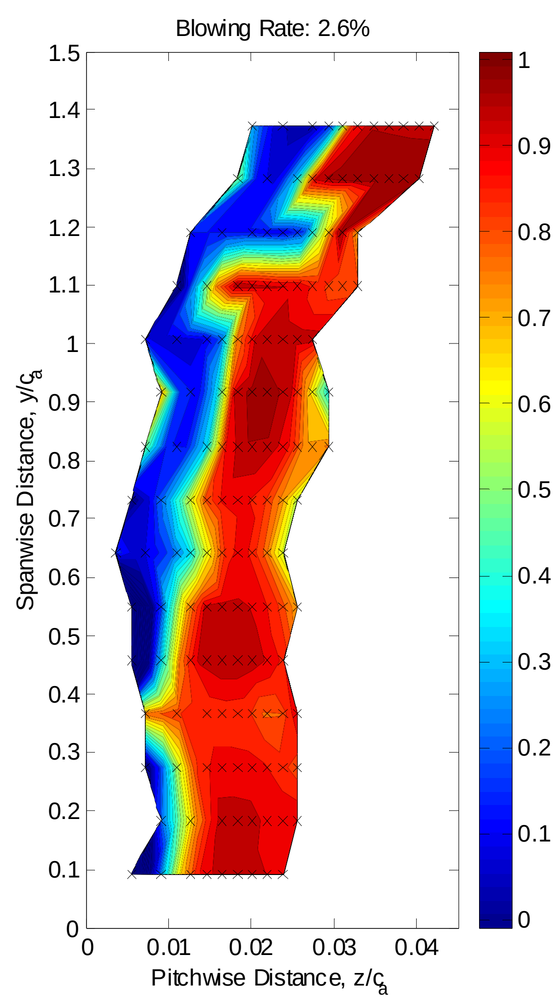

Figure 4-12: Simple blowing slot uniformity U/U_{ref} cross-section (2.6%)

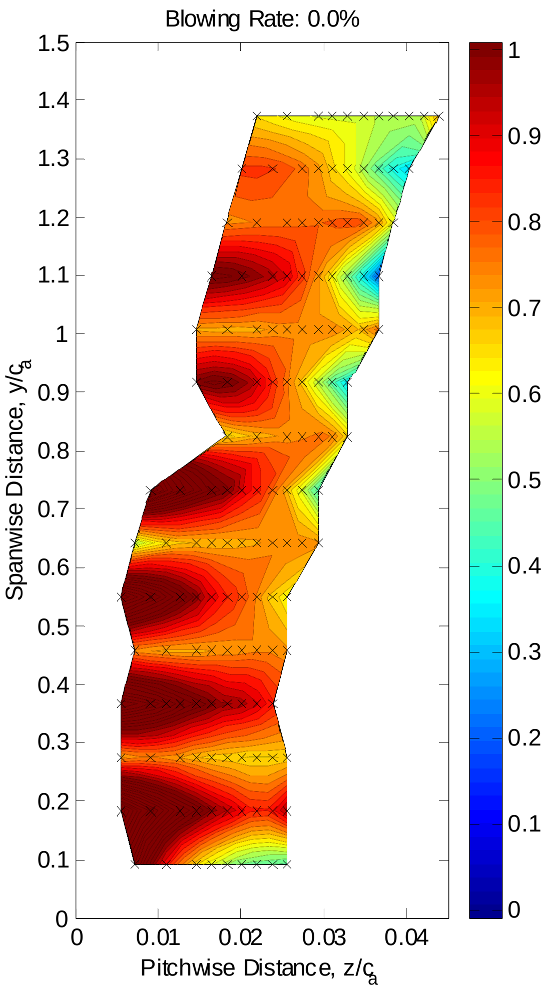

Figure 4-13: Kuethe vane slot uniformity U/U_{ref} cross-section (passive suction)

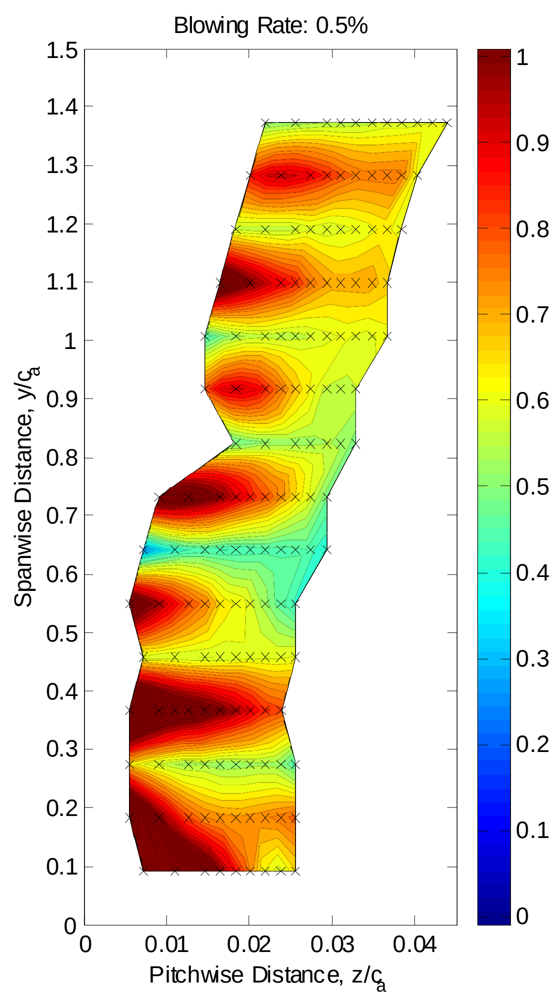

Figure 4-14: Kuethe vane slot uniformity U/U_{ref} cross-section (0.5%)

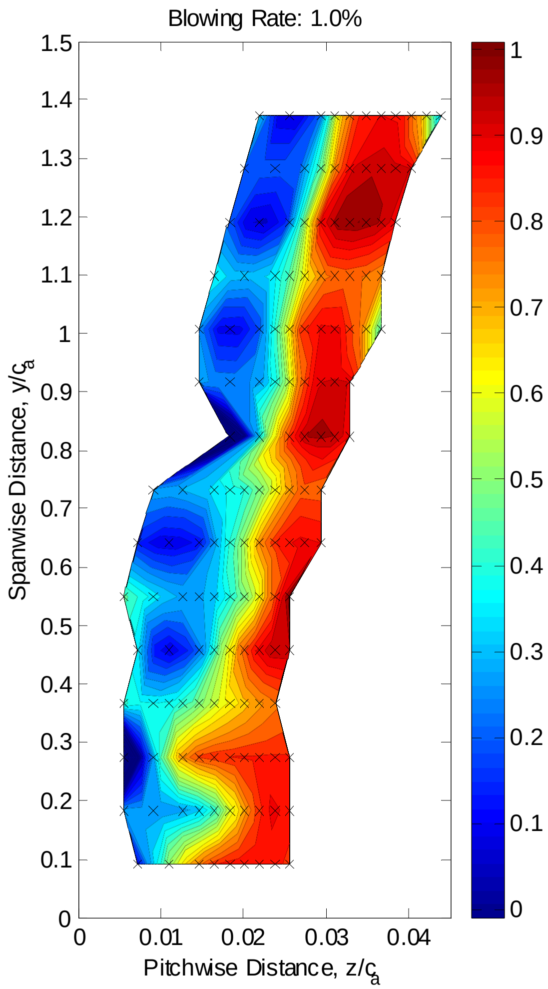

Figure 4-15: Kuethe vane slot uniformity U/U_{ref} cross-section (1.0%)

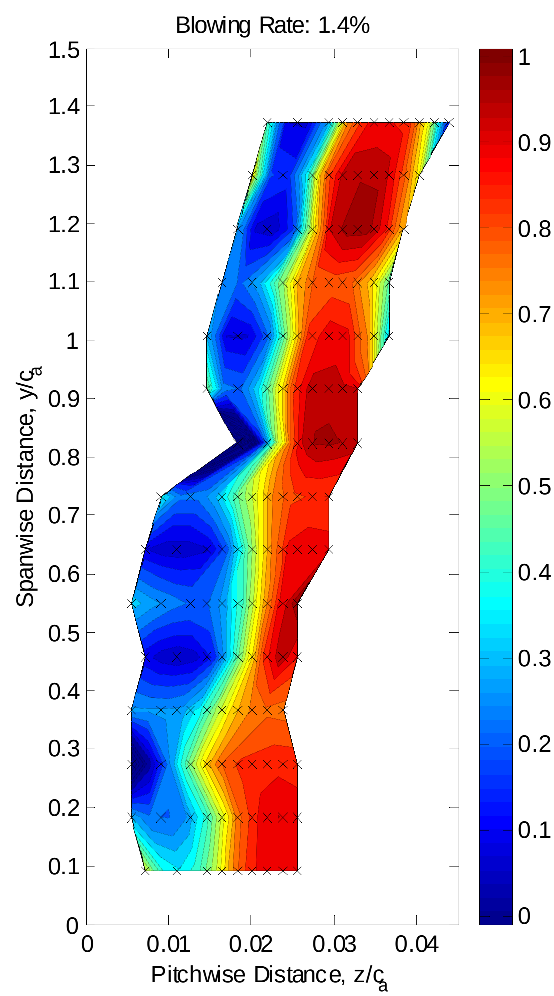

Figure 4-16: Kuethe vane slot uniformity U/U_{ref} cross-section (1.4%)

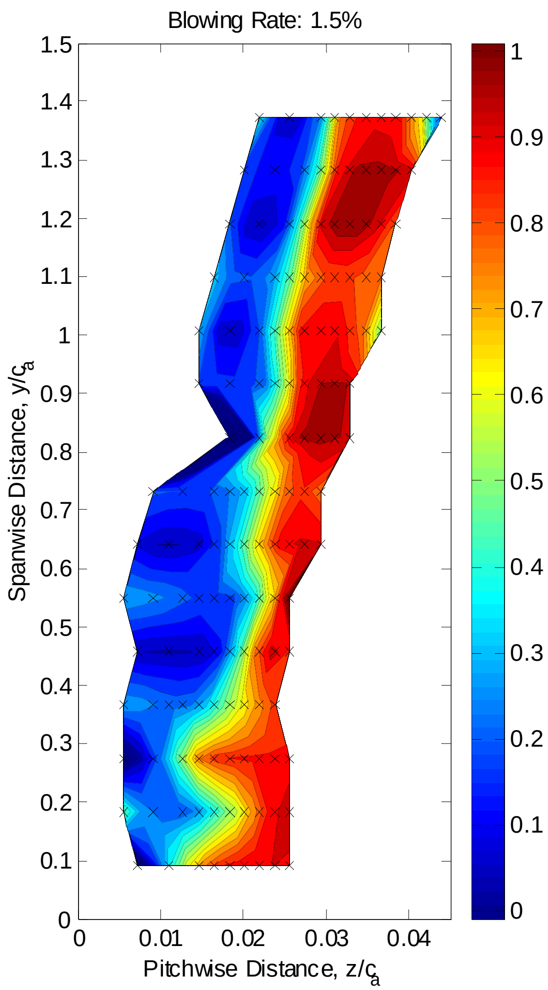

Figure 4-17: Kuethe vane slot uniformity U/U_{ref} cross-section (1.5%)

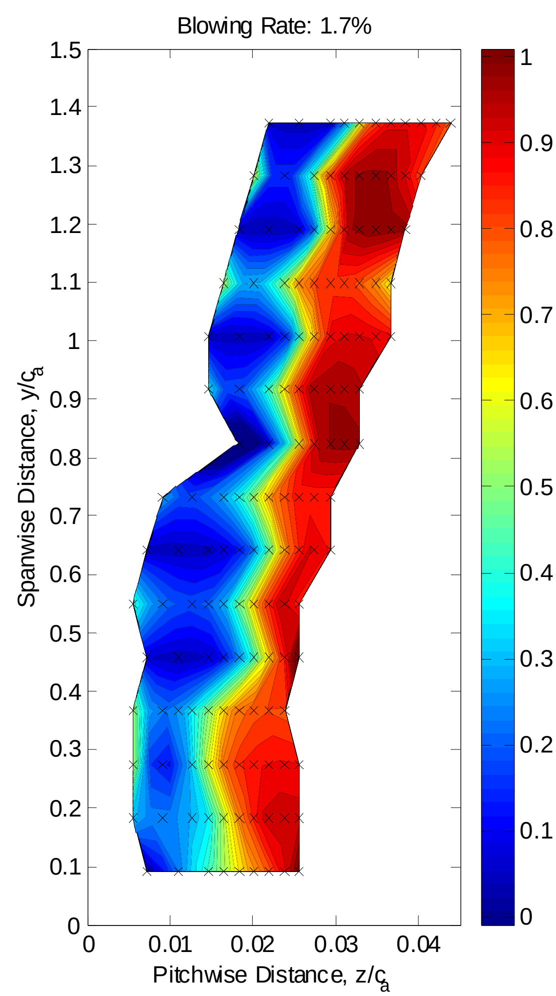

Figure 4-18: Kuethe vane slot uniformity U/U_{ref} cross-section (1.7%)

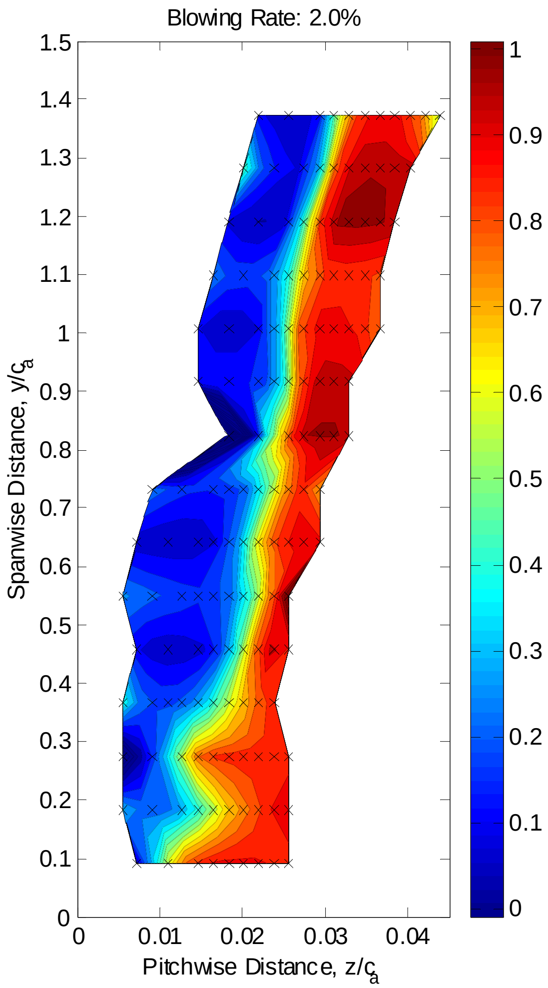

Figure 4-19: Kuethe vane slot uniformity U/U_{ref} cross-section (2.0%)

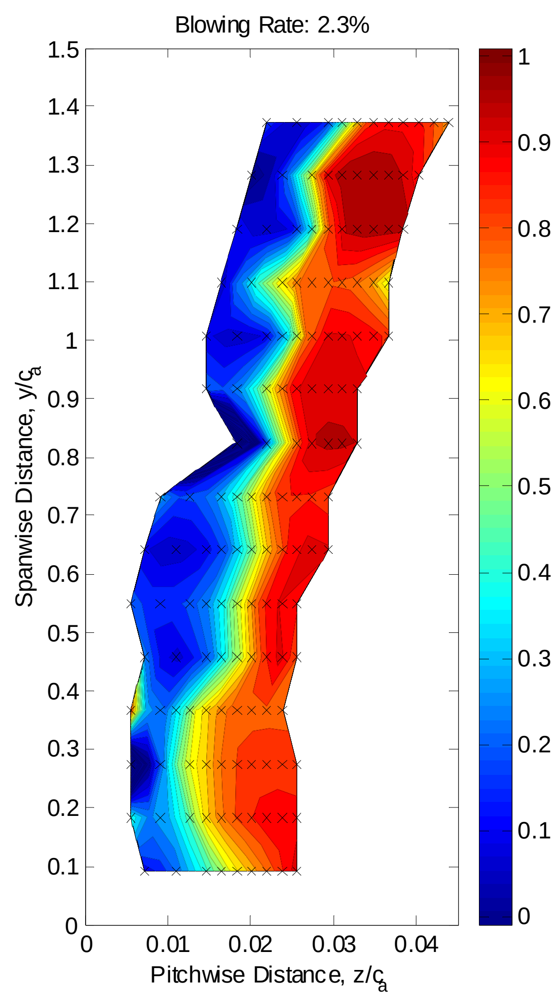

Figure 4-20: Kuethe vane slot uniformity U/U_{ref} cross-section (2.3%)

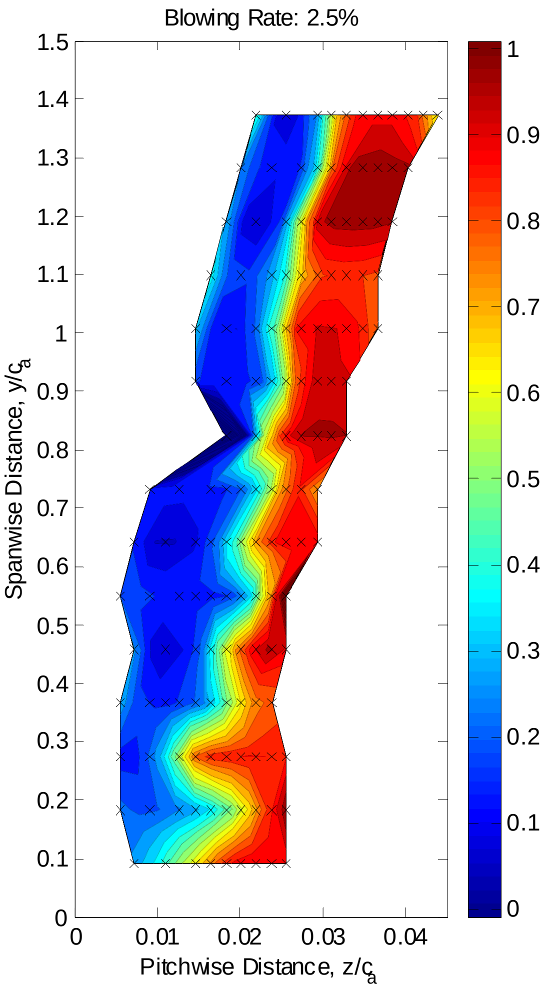

Figure 4-21: Kuethe vane slot uniformity U/U_{ref} cross-section (2.5%)

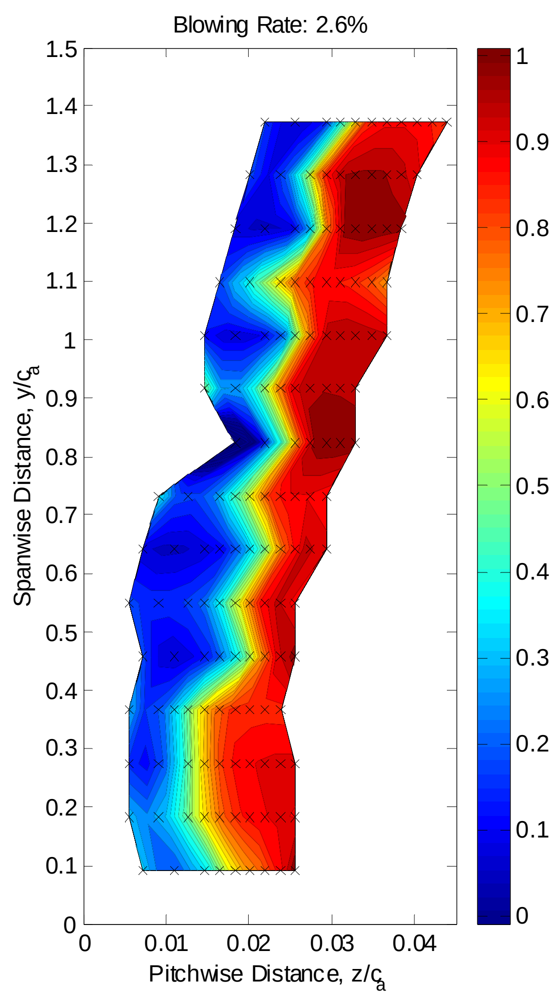

Figure 4-22: Kuethe vane slot uniformity U/U_{ref} cross-section (2.6%)

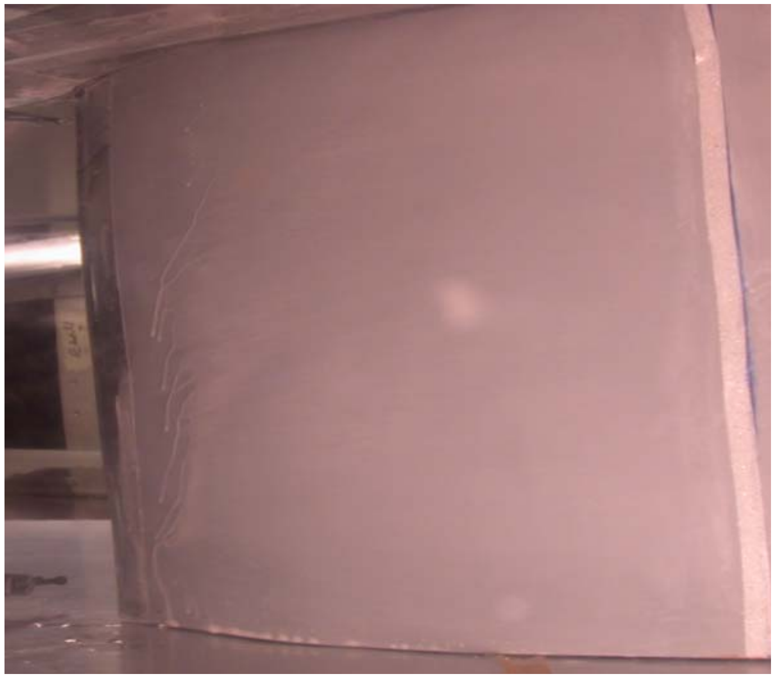

Figure 4-23: Simple blowing oil flow visualization at 0%

Figure 4-24: Simple blowing oil flow visualization with passive section

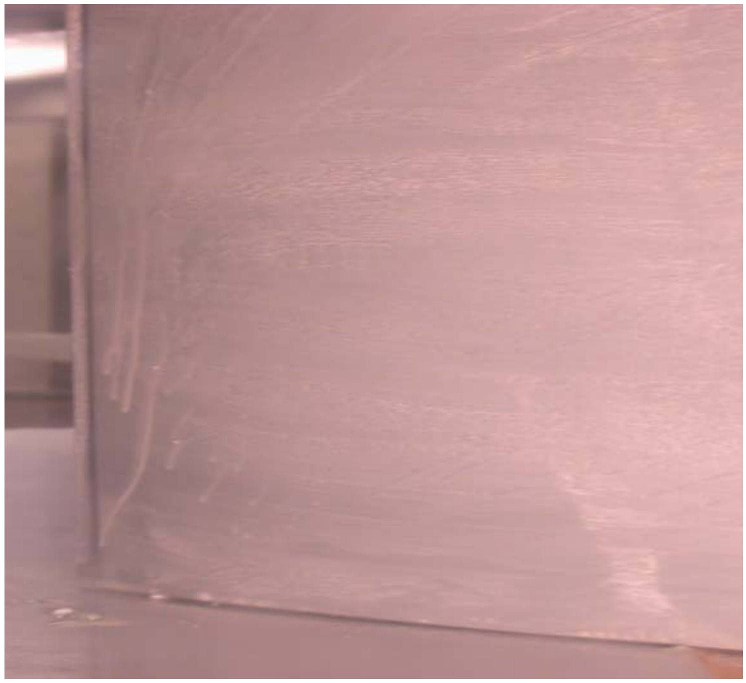

Figure 4-25: Simple blowing oil flow visualization at 1.0%

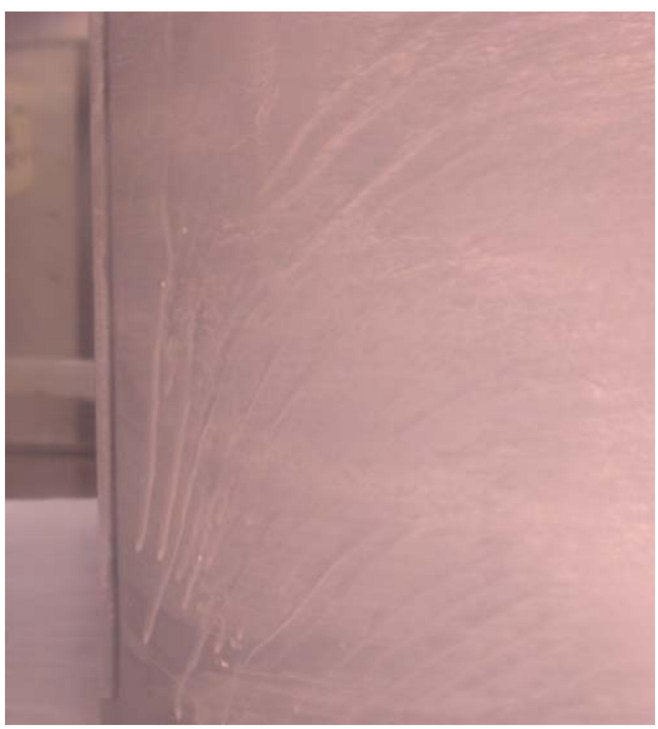

Figure 4-26: Simple blowing oil flow visualization at 1.4%

Figure 4-27: Simple blowing oil flow visualization at 2.0%

Figure 4-28: Simple blowing oil flow visualization at 2.6%

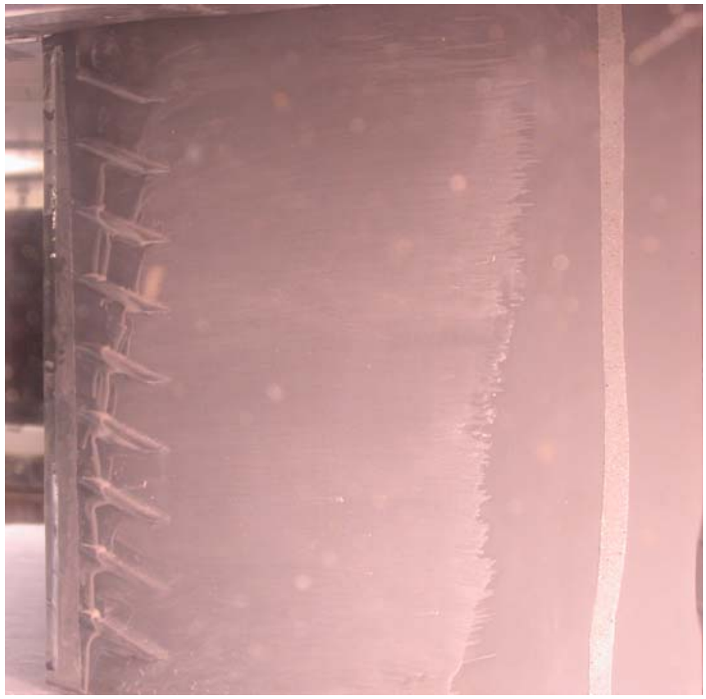

Figure 4-29: Kuethe vane oil flow visualization at 0%

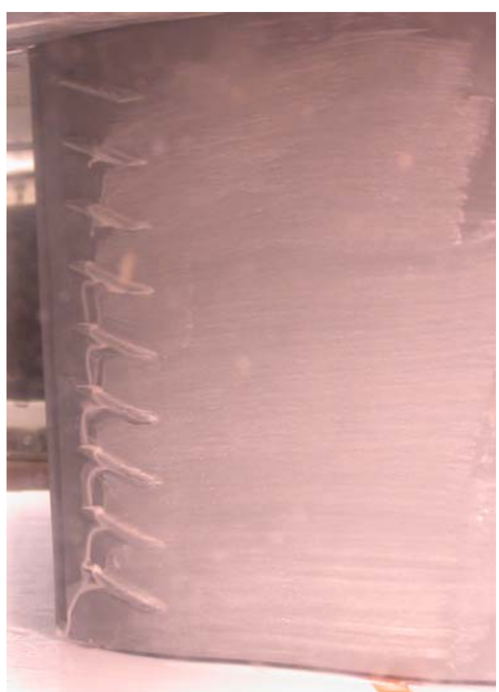

Figure 4-30: Kuethe vane oil flow visualization at 1.0%

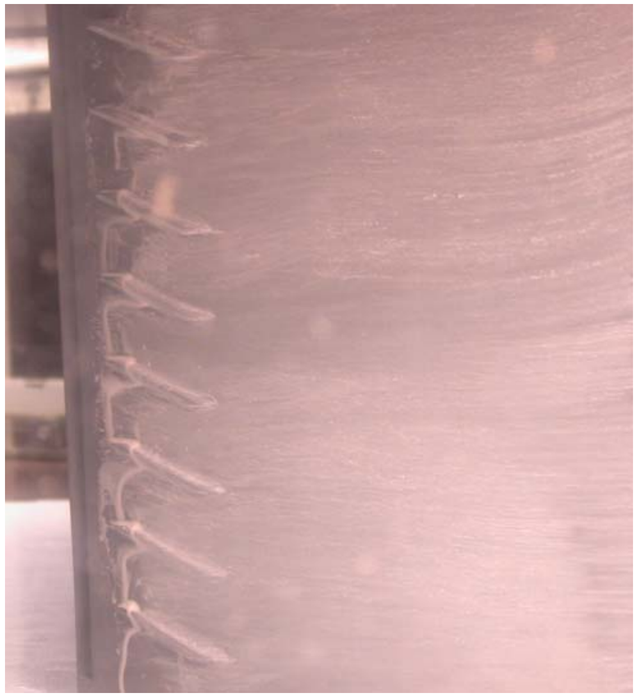

Figure 4-31: Kuethe vane oil flow visualization at 1.4%

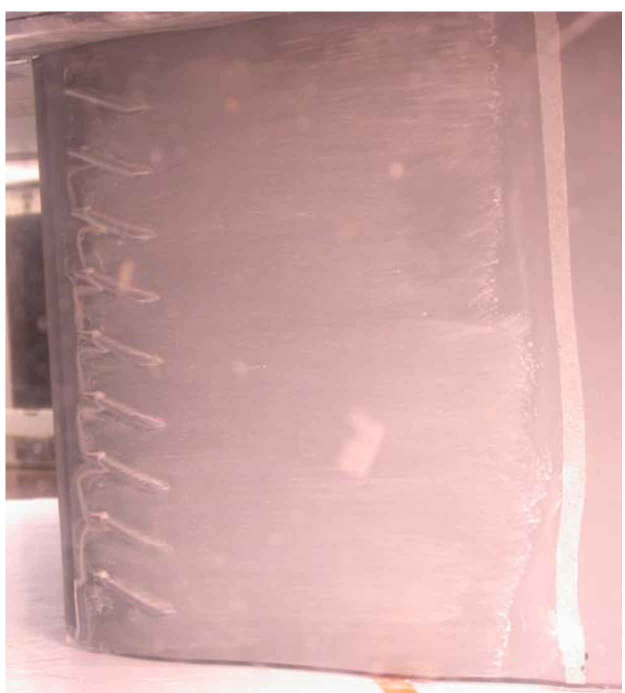

Figure 4-32: Kuethe vane oil flow visualization at 2.0%

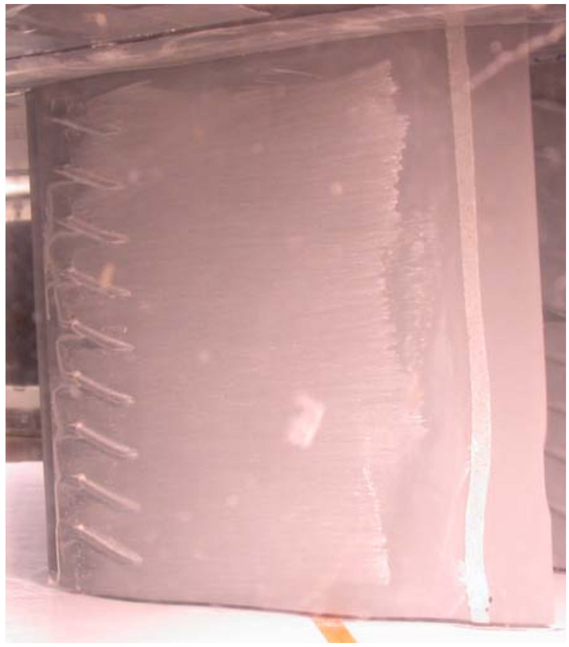

Figure 4-33: Kuethe vane oil flow visualization at 2.6%

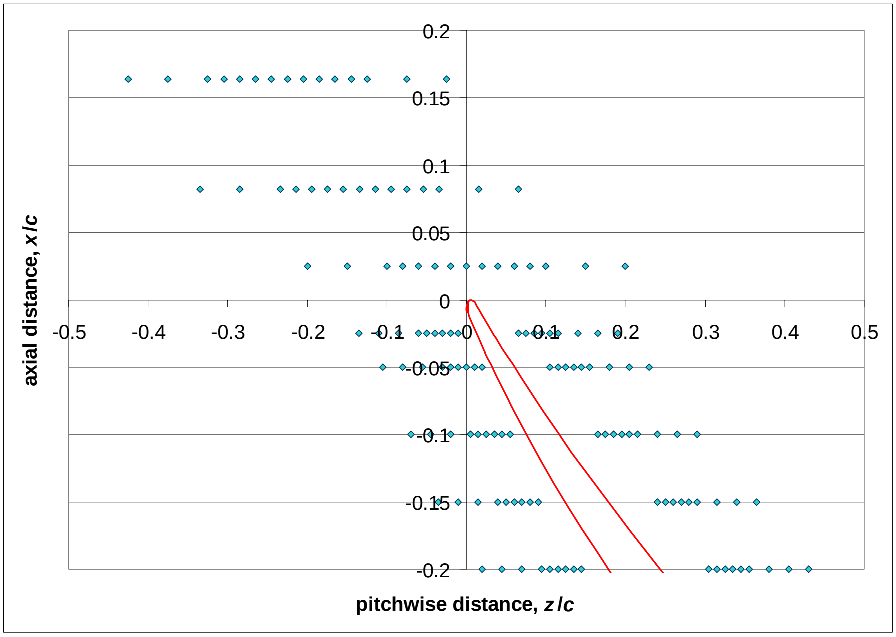

Figure 4-34: Measurement locations for normal-to-span cross-sections surrounding blade trailing-edge

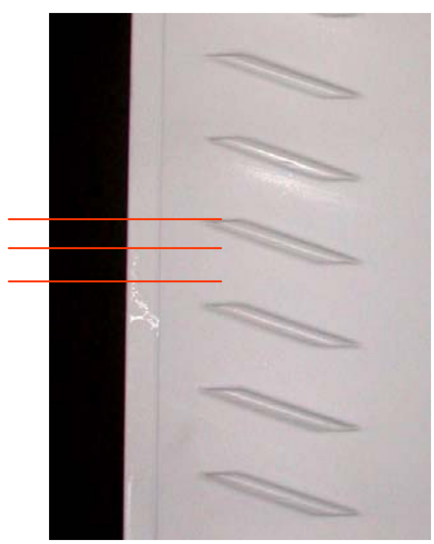

Figure 4-35: Three spanwise locations for Kuethe vane normal-to-span cross-sections: $0.84c_a$, $0.92c_a$ and $0.97c_a$

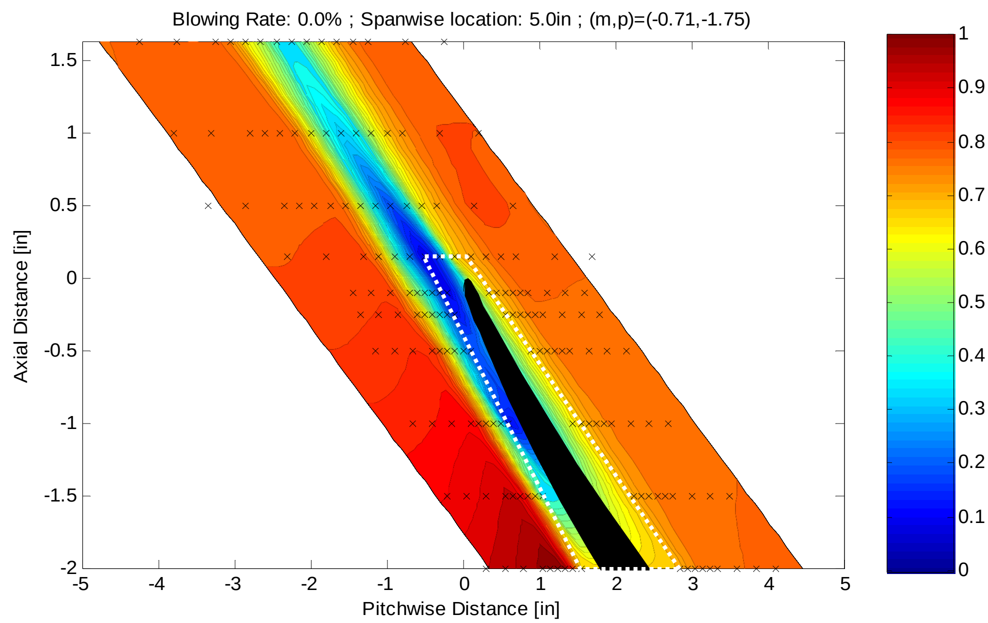

Figure 4-36: Simple blowing U/U_{ref} normal-to-span cross-section (0%) at mid-span

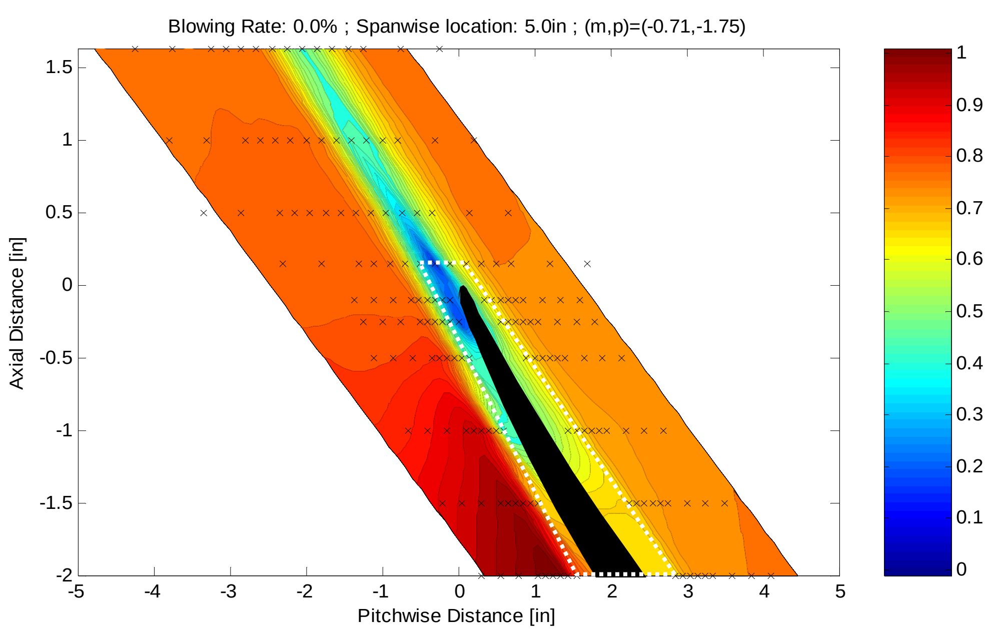

Figure 4-37: Simple blowing U/U_{ref} normal-to-span cross-section (passive suction) at mid-span

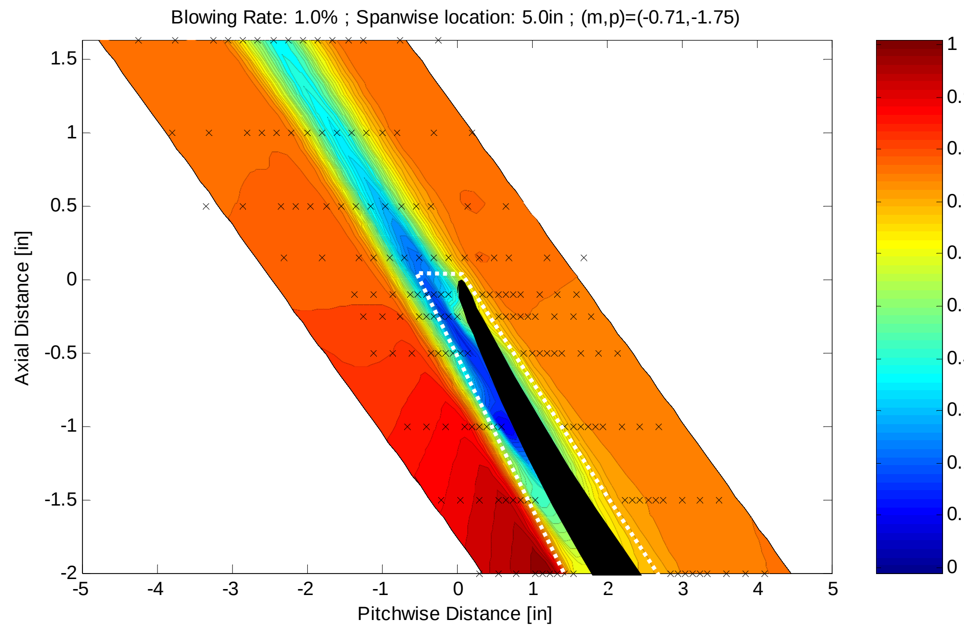

Figure 4-38: Simple blowing U/U_{ref} normal-to-span cross-section (1.0%) at mid-span

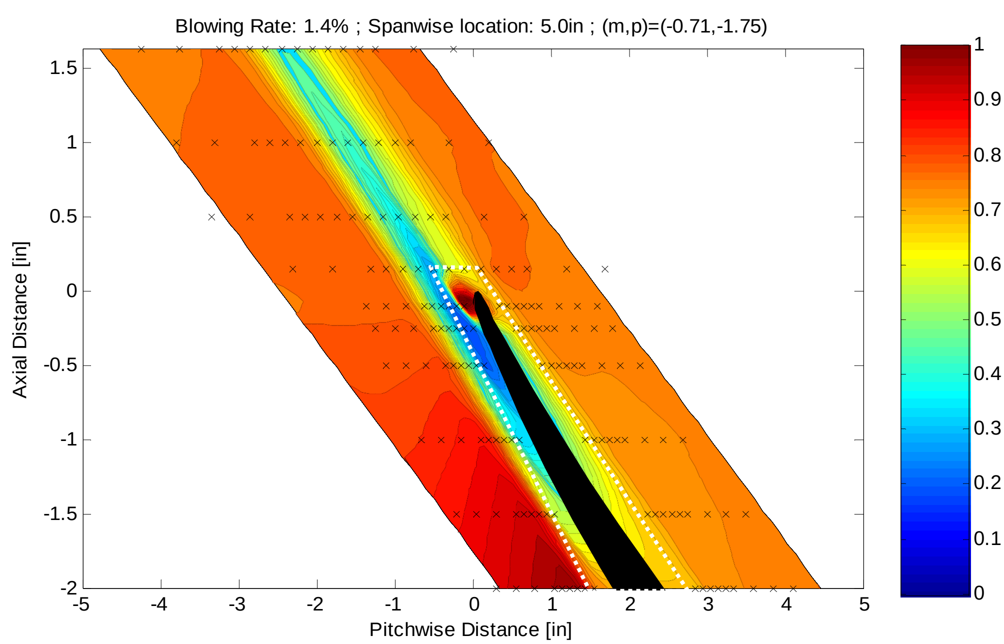

Figure 4-39: Simple blowing U/U_{ref} normal-to-span cross-section (1.4%) at mid-span

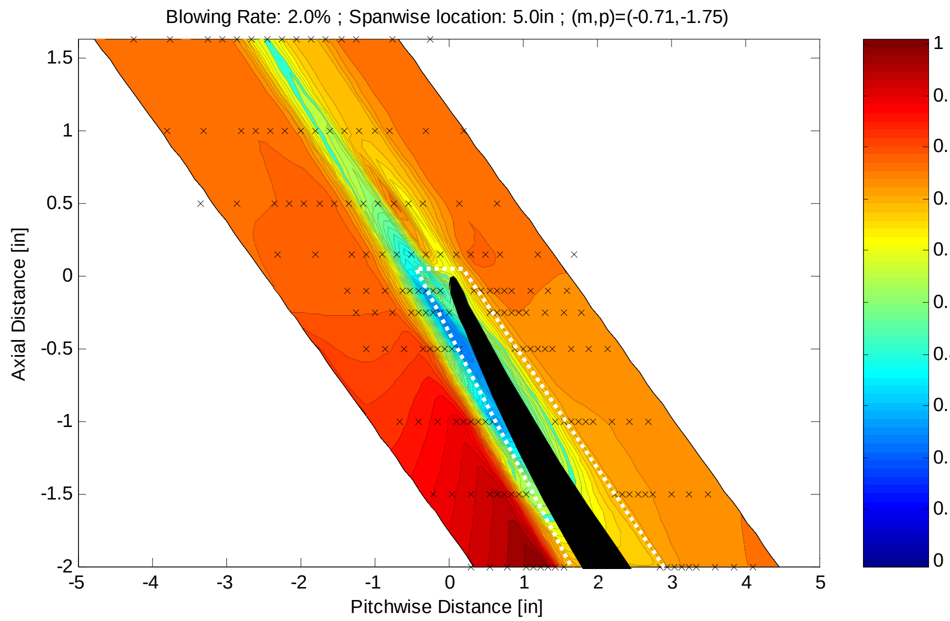

Figure 4-40: Simple blowing U/U_{ref} normal-to-span cross-section (2.0%) at mid-span

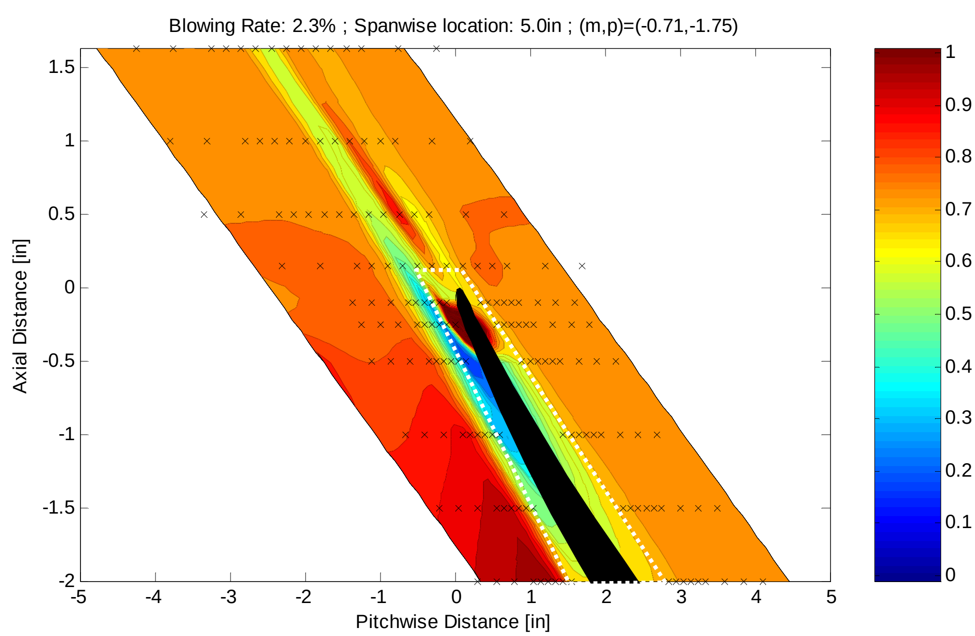

Figure 4-41: Simple blowing U/U_{ref} normal-to-span cross-section (2.3%) at mid-span

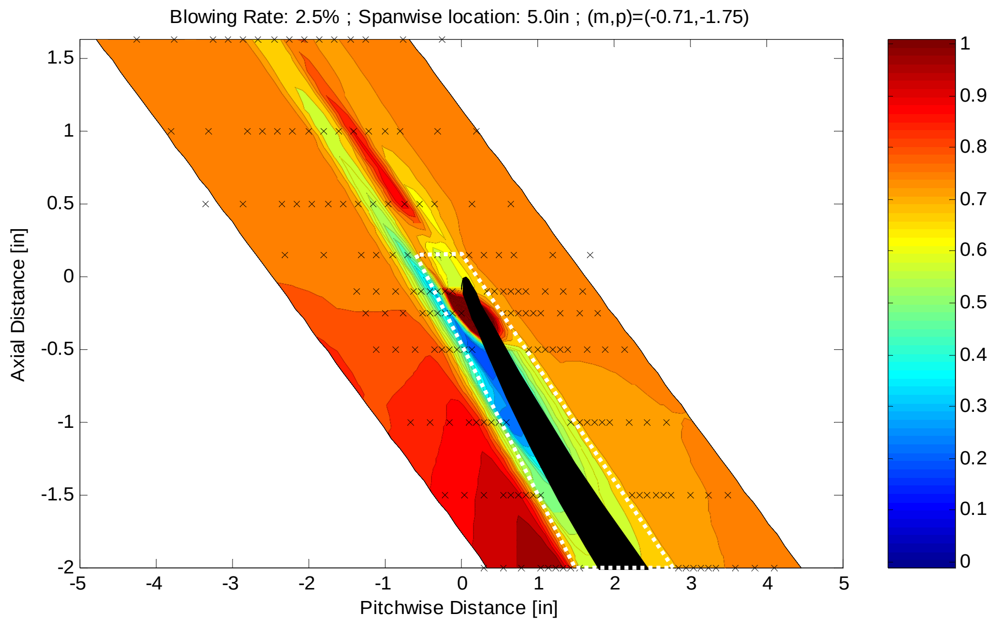

Figure 4-42: Simple blowing U/U_{ref} normal-to-span cross-section (2.5%) at mid-span

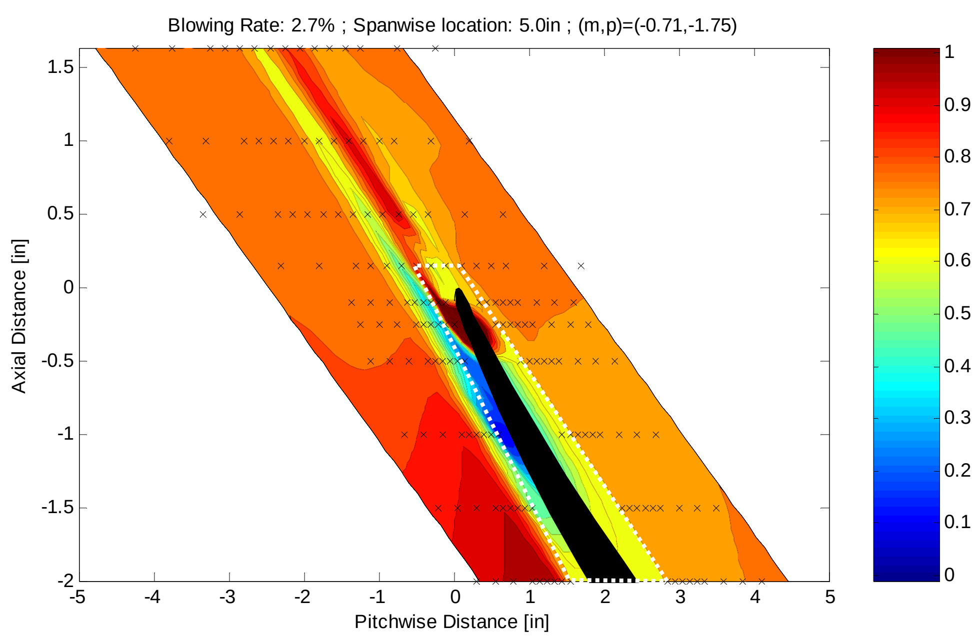

Figure 4-43: Simple blowing U/U_{ref} normal-to-span cross-section (2.7%) at mid-span

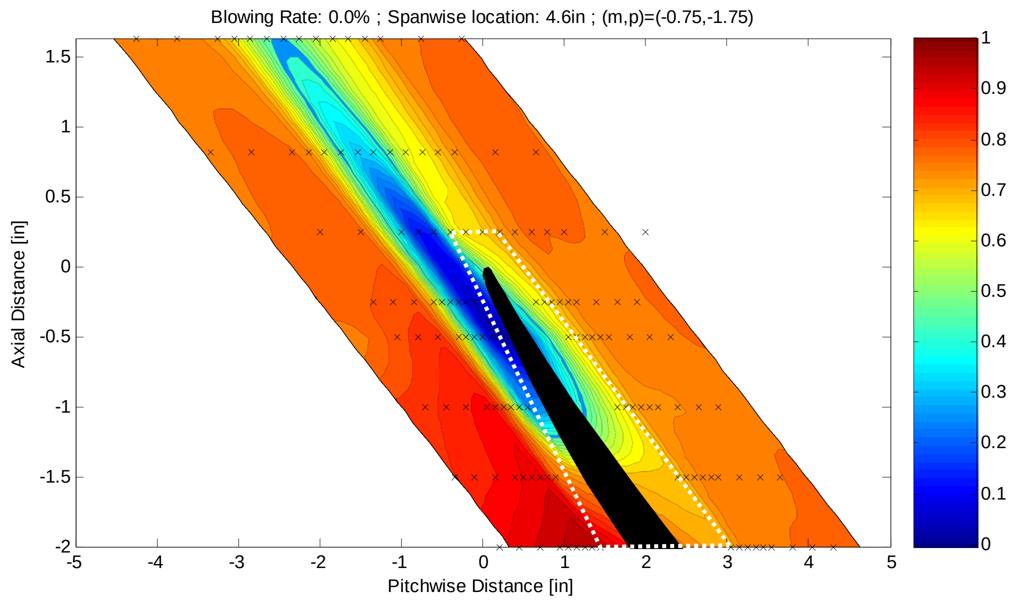

Figure 4-44: Kuethe vane U/U_{ref} normal-to-span cross-section (0%) at y/c_a = 0.84

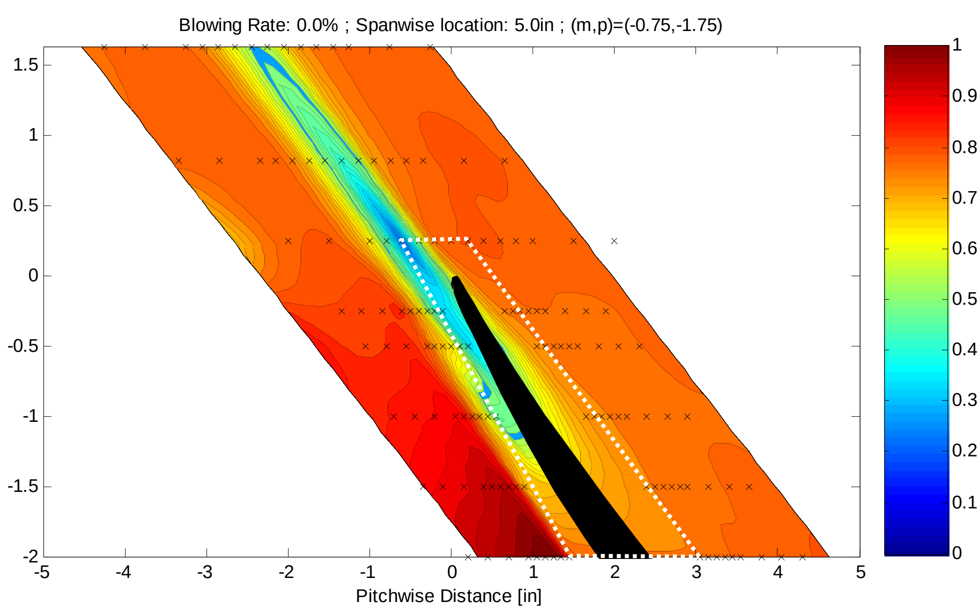

Figure 4-45: Kuethe vane U/U_{ref} normal-to-span cross-section (0%) at y/c_a = 0.92

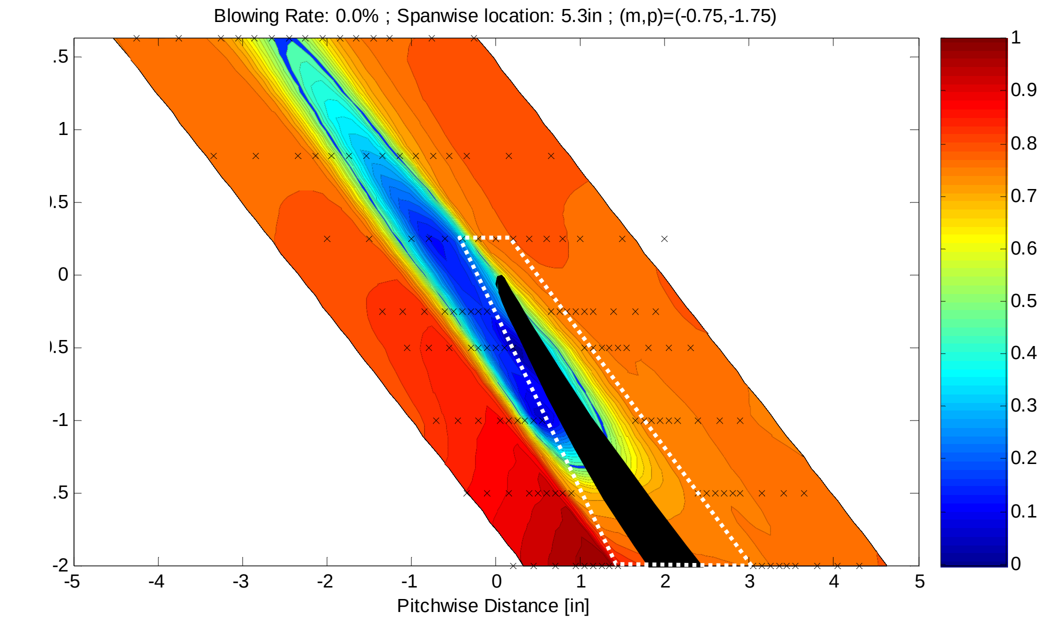

Figure 4-46: Kuethe vane U/U_{ref} normal-to-span cross-section (0%) at y/c_a = 0.97

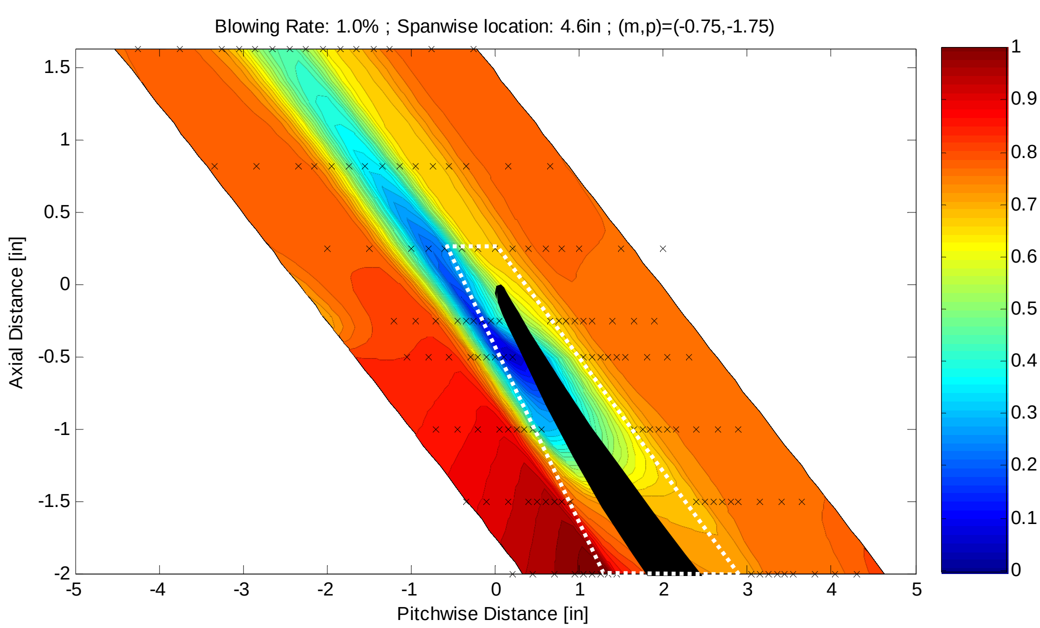

Figure 4-47: Kuethe vane U/U_{ref} normal-to-span cross-section (1.0%) at y/c_a = 0.84

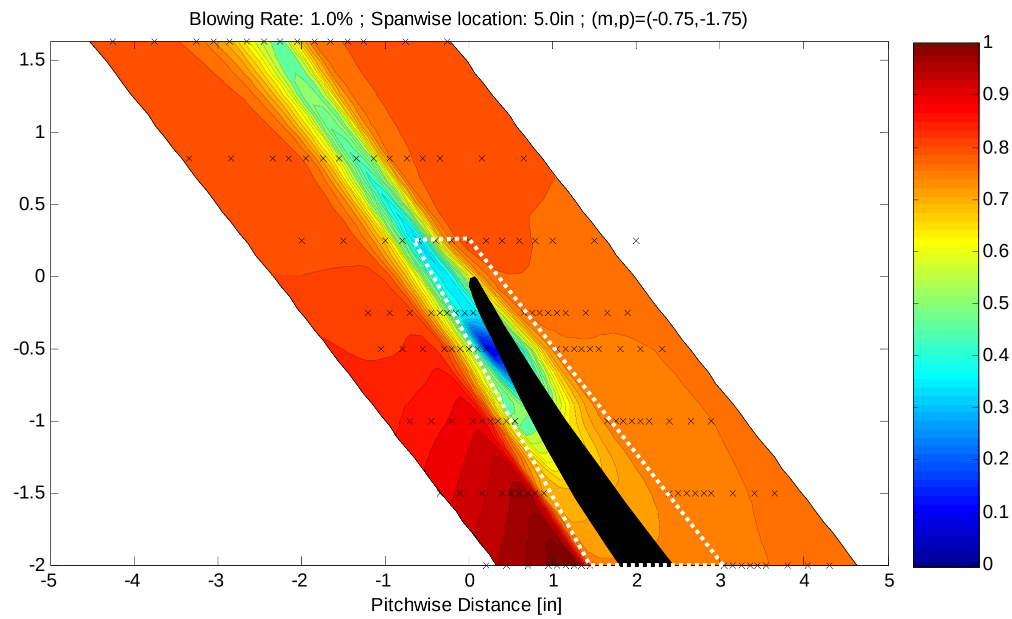

Figure 4-48: Kuethe vane U/U_{ref} normal-to-span cross-section (1.0%) at y/c_a = 0.92

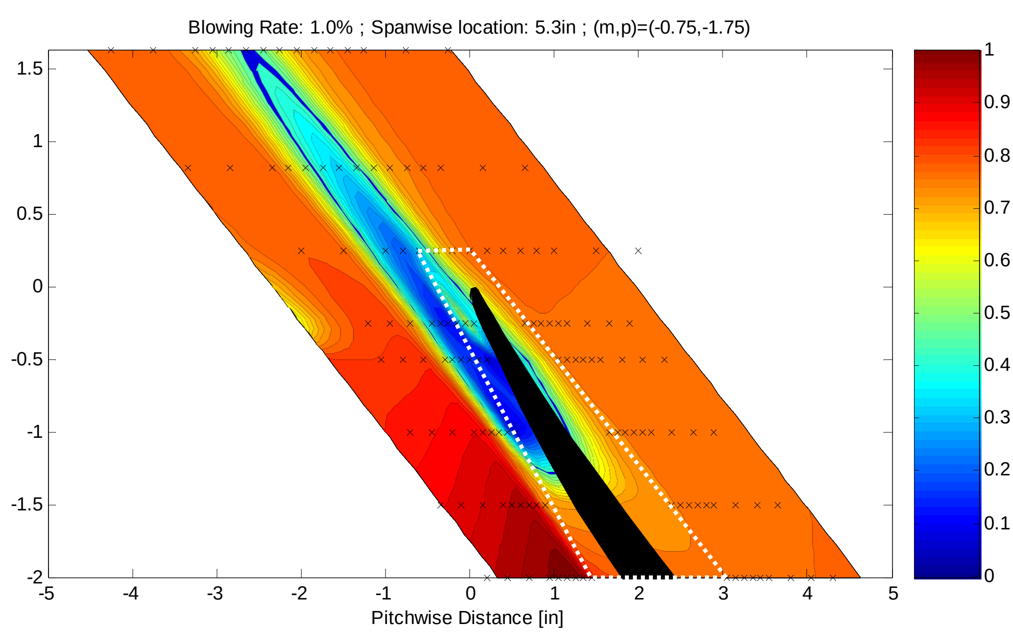

Figure 4-49: Kuethe vane U/U_{ref} normal-to-span cross-section (1.0%) at y/c_a = 0.97

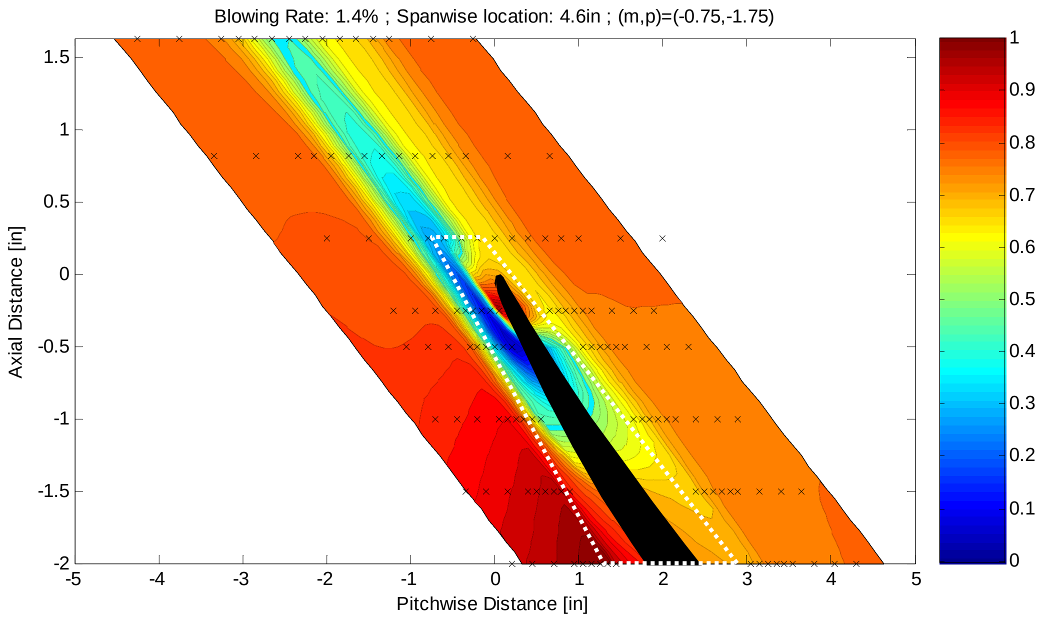

Figure 4-50: Kuethe vane U/U_{ref} normal-to-span cross-section (1.4%) at y/c_a = 0.84

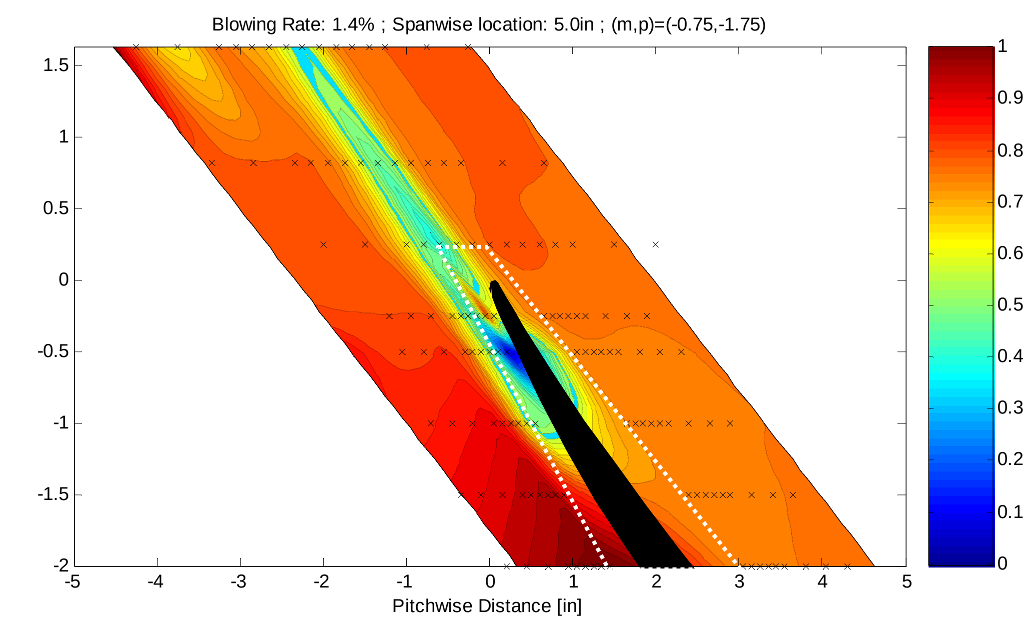

Figure 4-51: Kuethe vane U/U_{ref} normal-to-span cross-section (1.4%) at y/c_a = 0.92

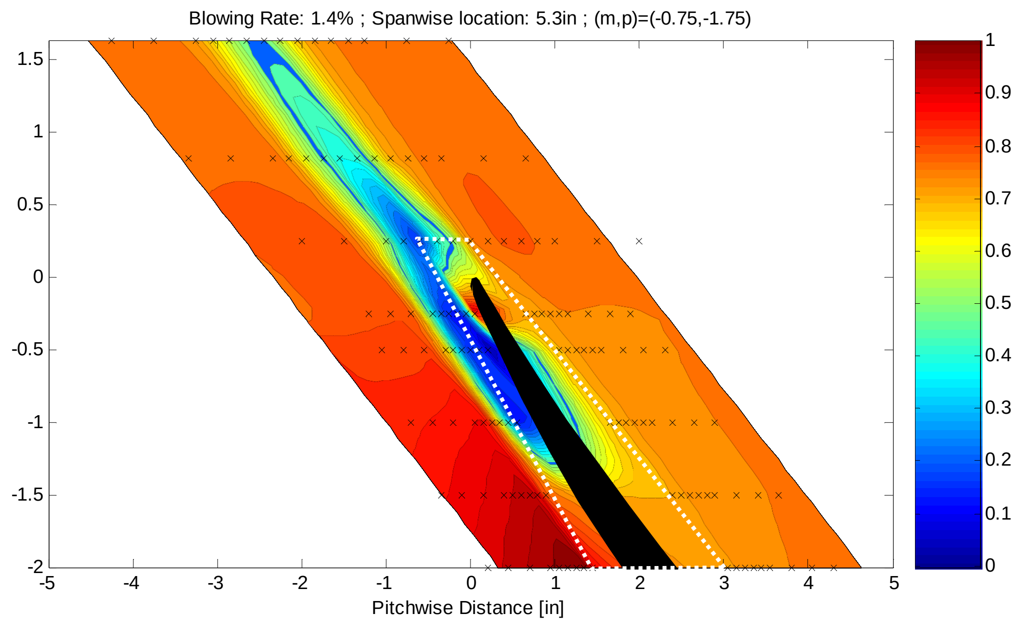

Figure 4-52: Kuethe vane U/U_{ref} normal-to-span cross-section (1.4%) at y/c_a = 0.97

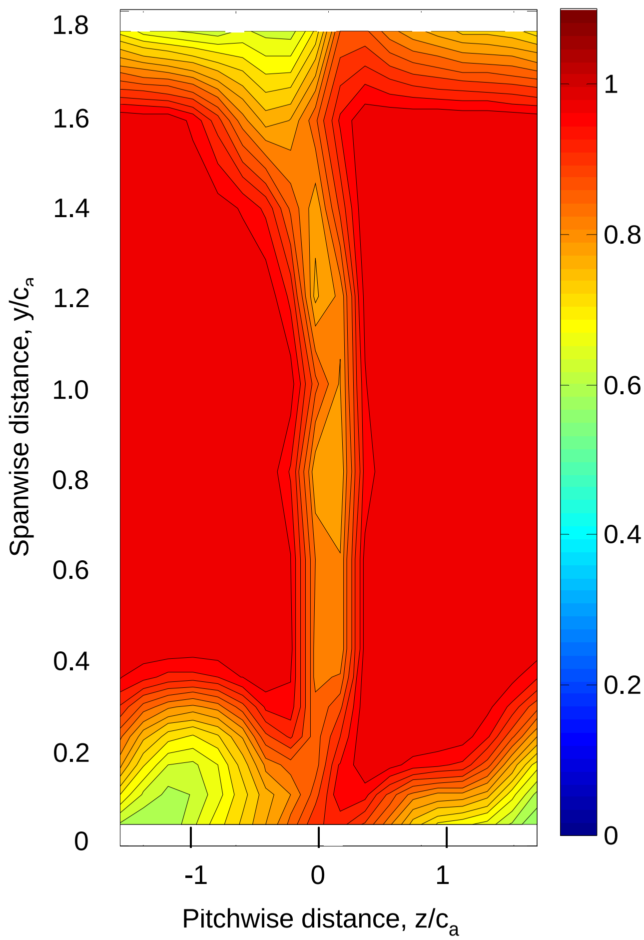

Figure 4-53: Simple blowing C_{p0} cross-section (passive suction) at x/c_a = 0.839 and tip-gap 0.004125*c*

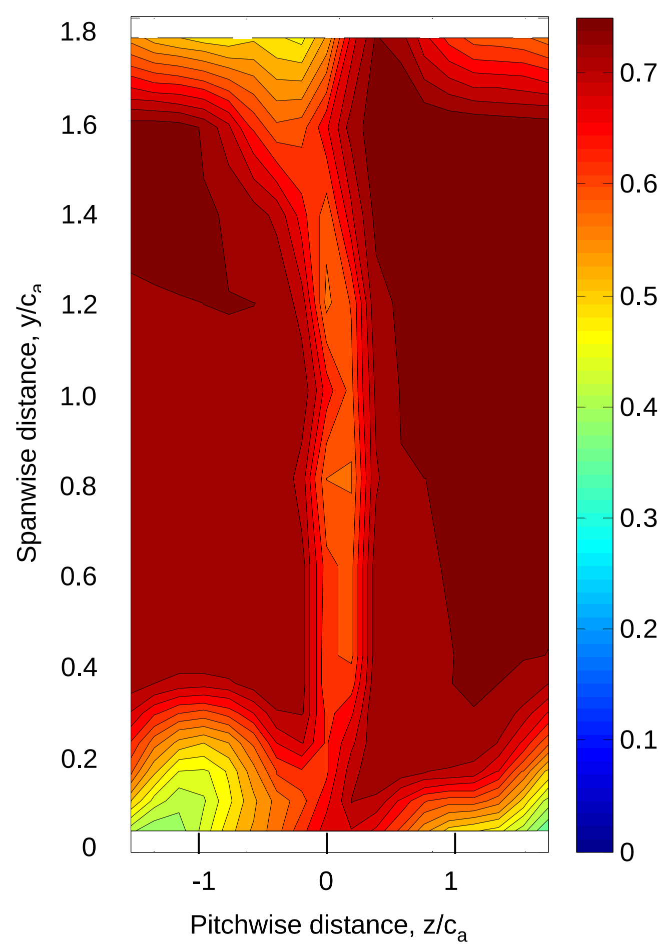

Figure 4-54: Simple blowing U/U_{ref} cross-section (passive suction) at x/c_a = 0.839 and tip-gap 0.004125*c*

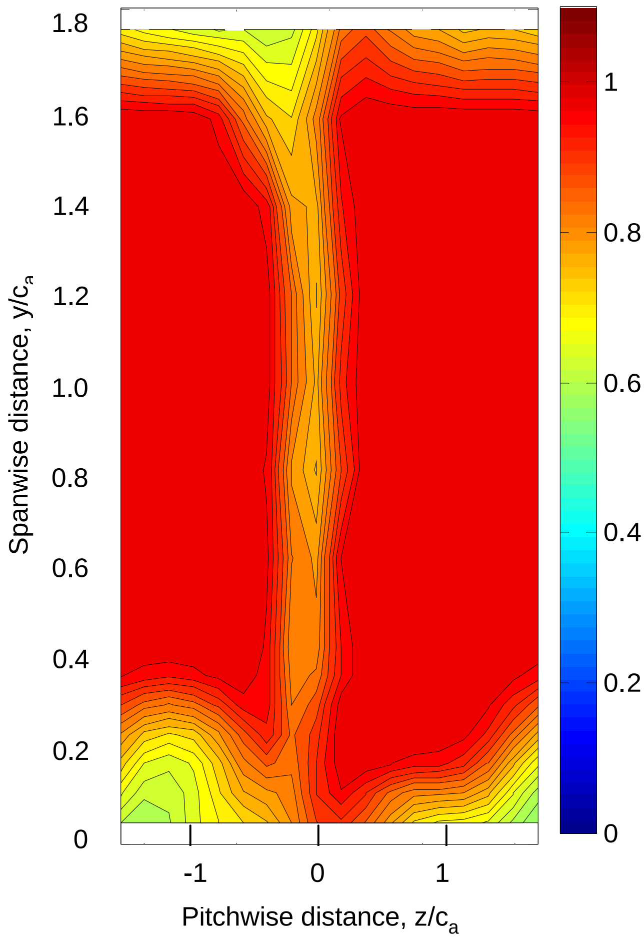

Figure 4-55: Simple blowing C_{p0} cross-section (1.4%) at x/c_a = 0.839 and tip-gap 0.004125*c*

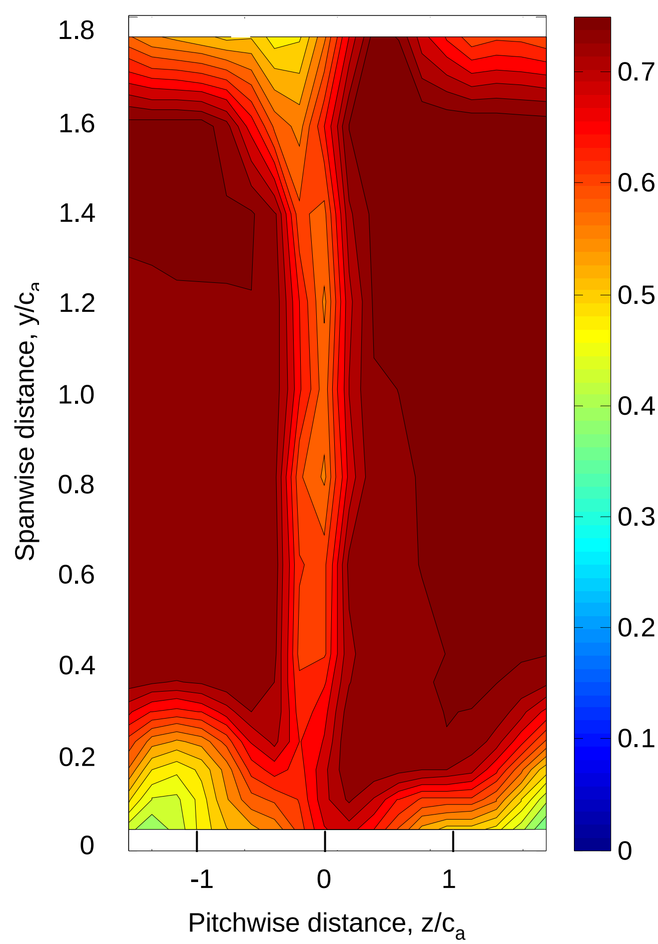

Figure 4-56: Simple blowing U/U_{ref} cross-section (1.4%) at x/c_a = 0.839 and tip-gap 0.004125*c*

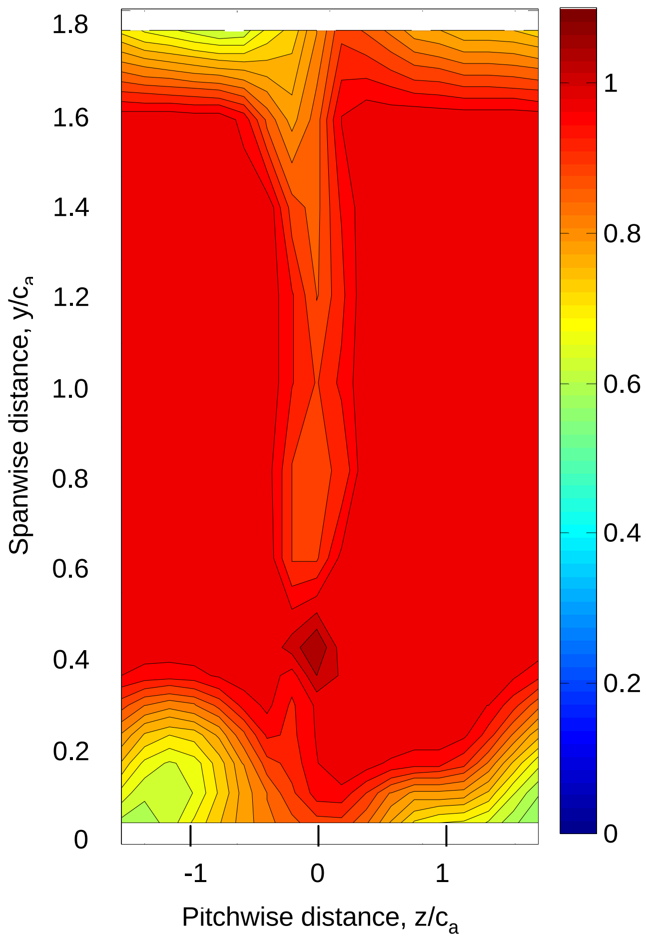

Figure 4-57: Simple blowing C_{p0} cross-section (2.0%) at x/c_a = 0.839 and tip-gap 0.004125c

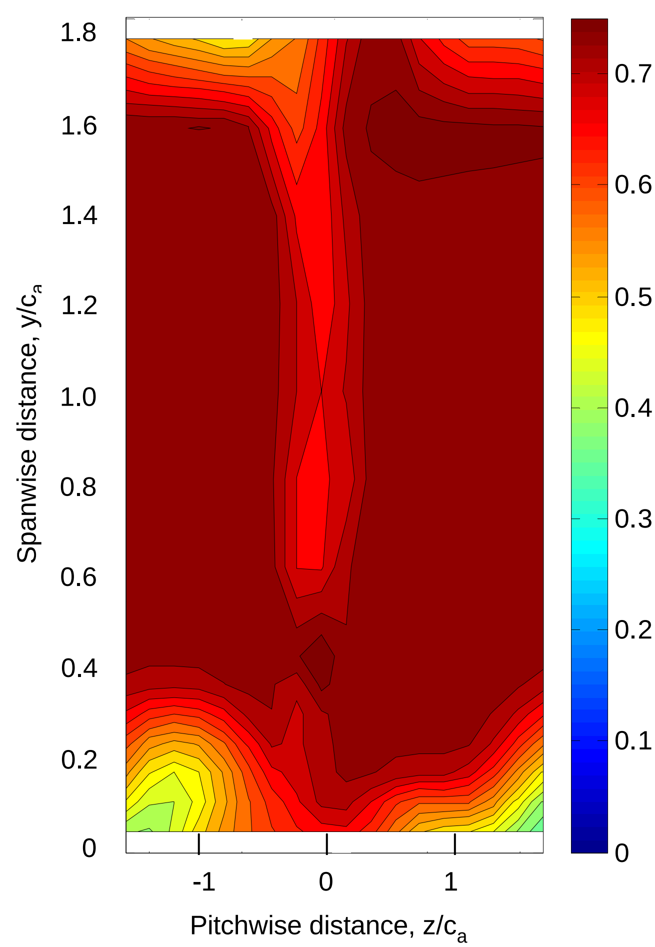

Figure 4-58: Simple blowing U/U_{ref} cross-section (2.0%) at x/c_a = 0.839 and tip-gap 0.004125c

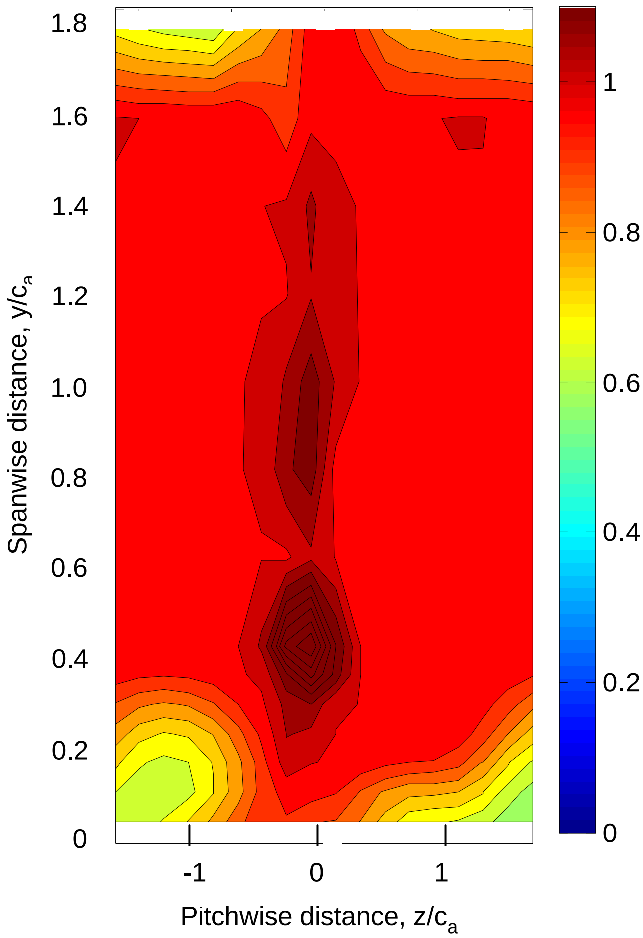

Figure 4-59: Simple blowing C_{p0} cross-section (2.6%) at x/c_a = 0.839 and tip-gap 0.004125c

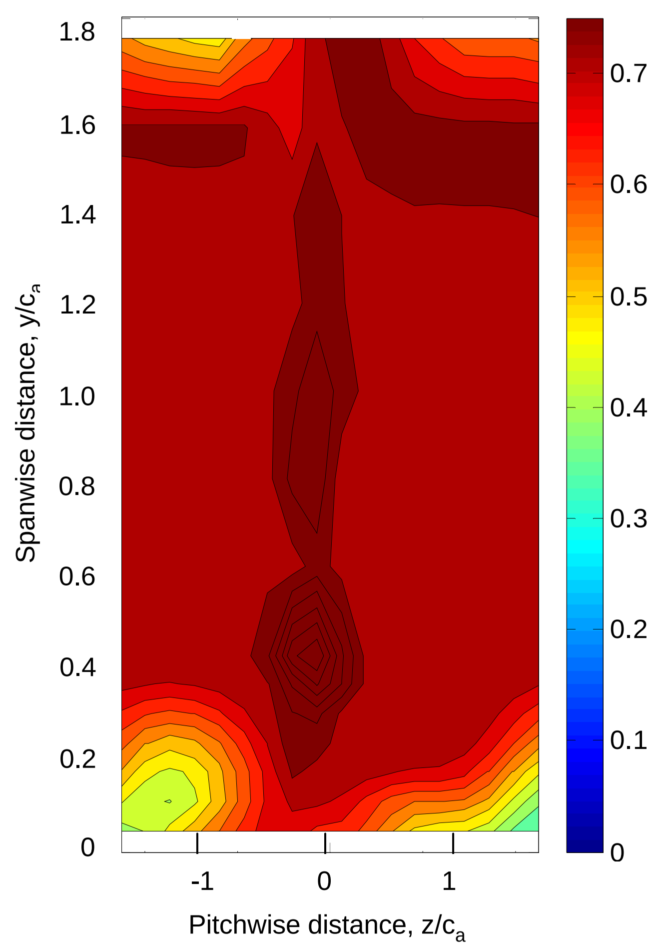

Figure 4-60: Simple blowing U/U_{ref} cross-section (2.6%) at x/c_a = 0.839 and tip-gap 0.004125c

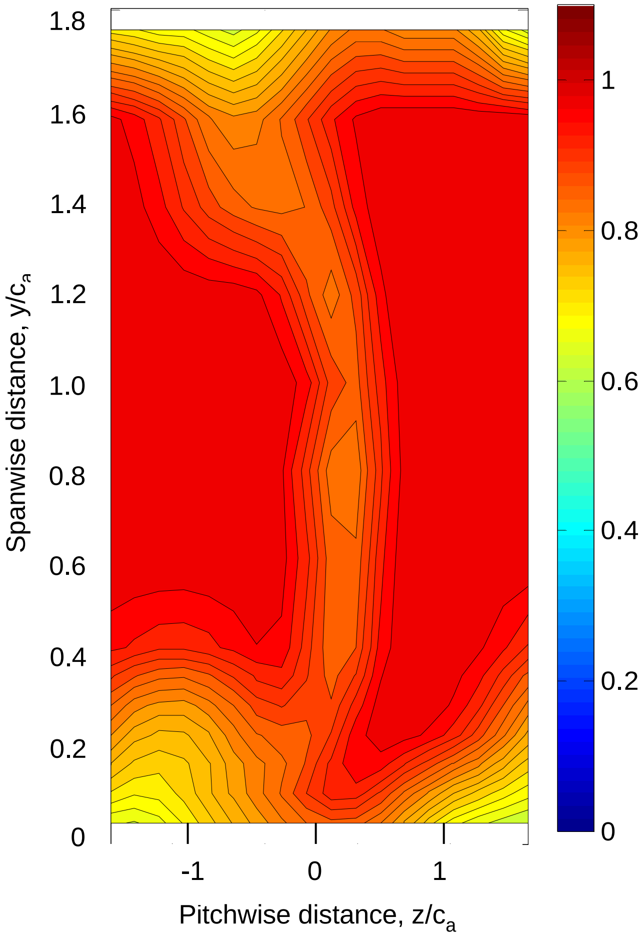

Figure 4-61: Simple blowing C_{p0} cross-section (passive suction) at x/c_a = 1.877 and tip-gap 0.004125c

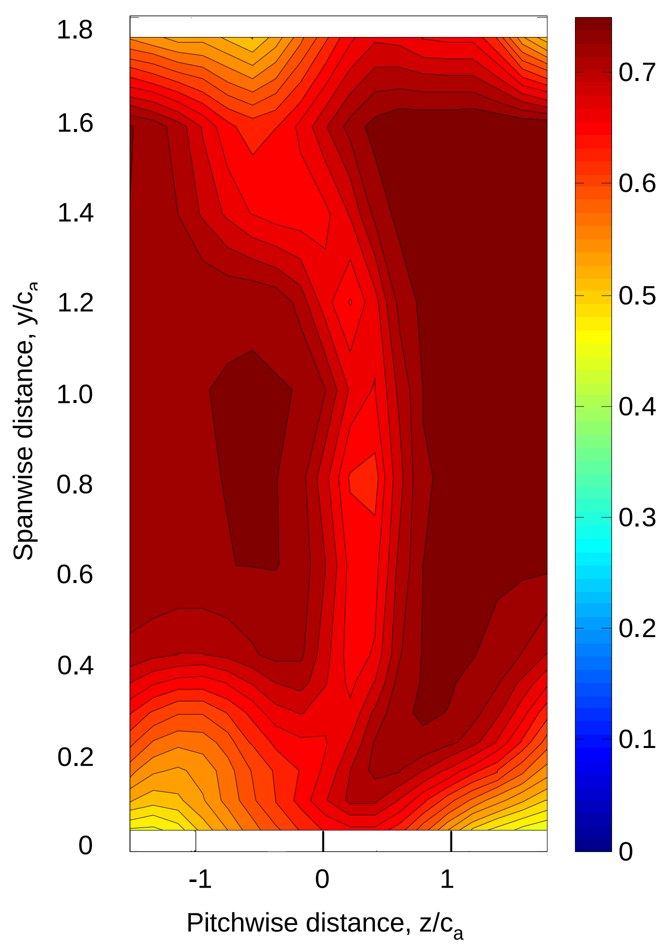

Figure 4-62: Simple blowing U/U_{ref} cross-section (passive suction) at x/c_a = 1.877 and tip-gap 0.004125c

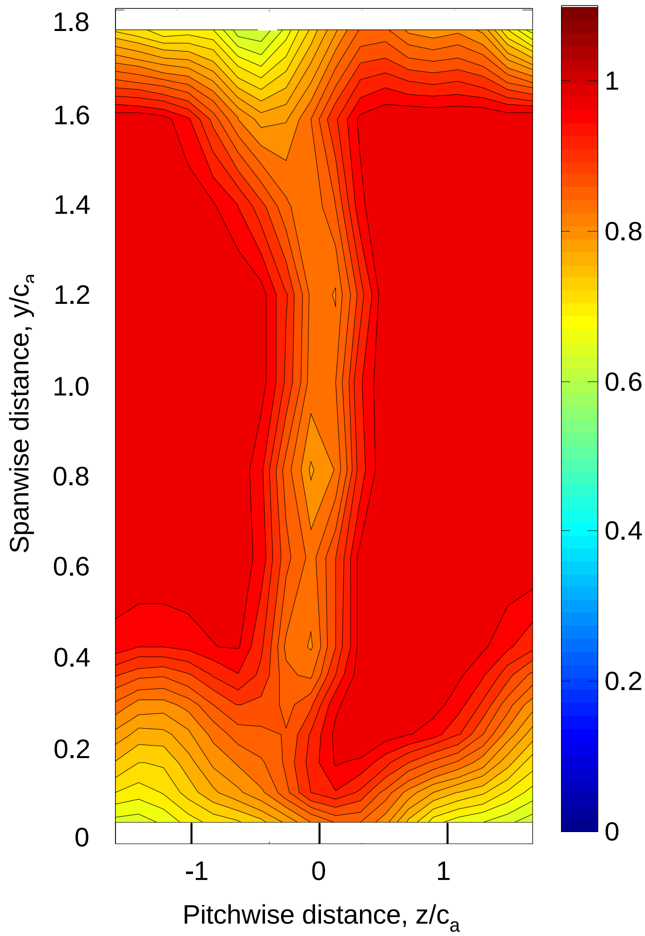

Figure 4-63: Simple blowing C_{p0} cross-section (1.4%) at x/c_a = 1.877 and tip-gap 0.004125c

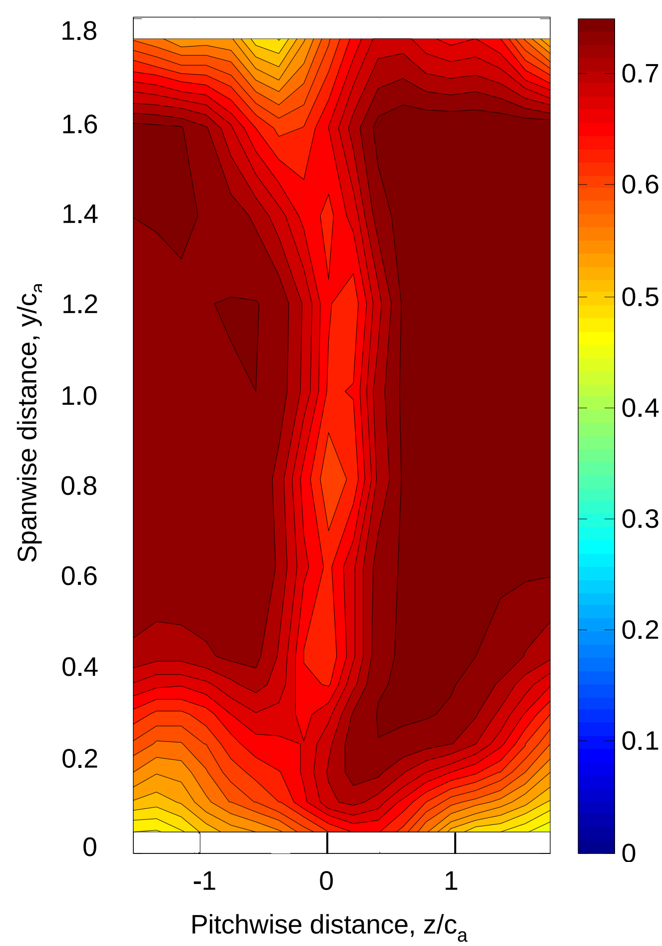

Figure 4-64: Simple blowing U/U_{ref} cross-section (1.4%) at x/c_a = 1.877 and tip-gap 0.004125c

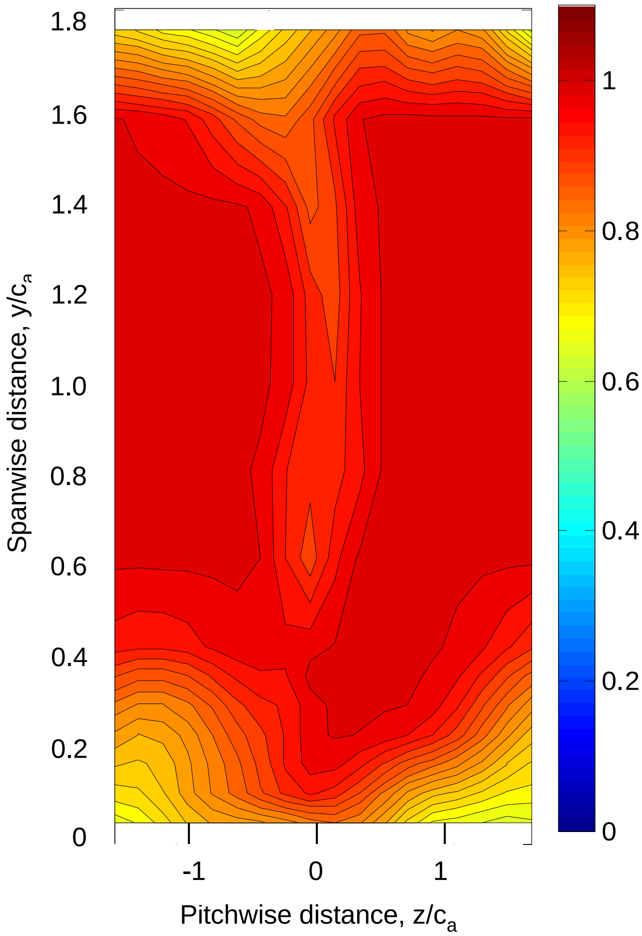

Figure 4-65: Simple blowing C_{p0} cross-section (2.0%) at x/c_a = 1.877 and tip-gap 0.004125c

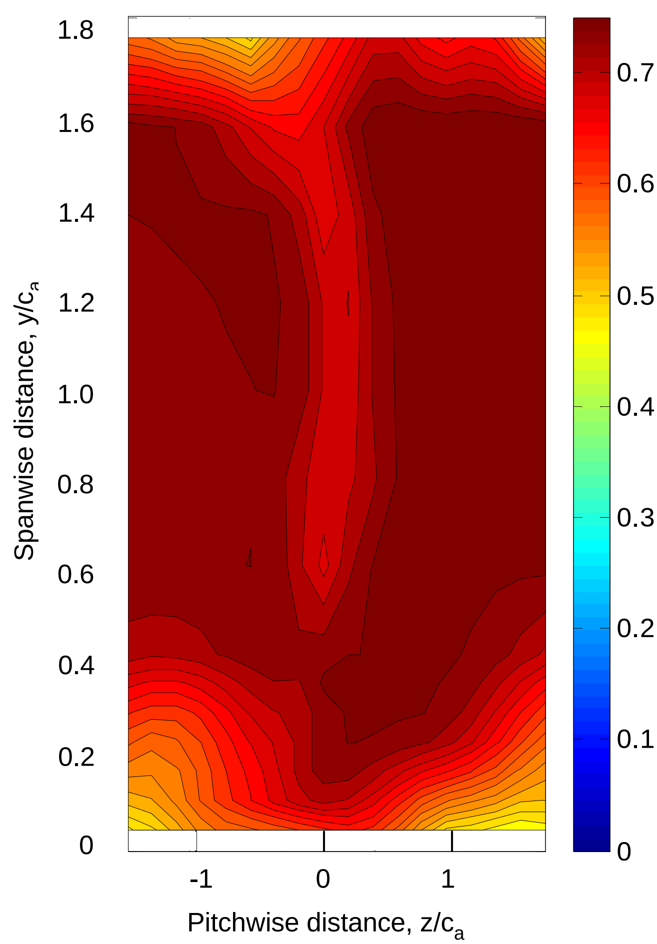

Figure 4-66: Simple blowing U/U_{ref} cross-section (2.0%) at x/c_a = 1.877 and tip-gap 0.004125c

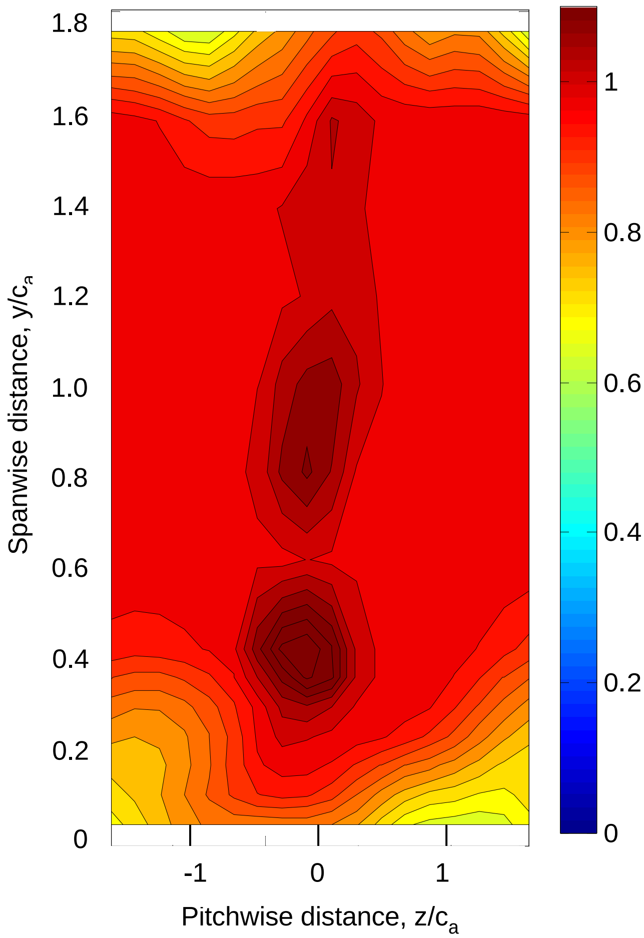

Figure 4-67: Simple blowing C_{p0} cross-section (2.6%) at x/c_a = 1.877 and tip-gap 0.004125c

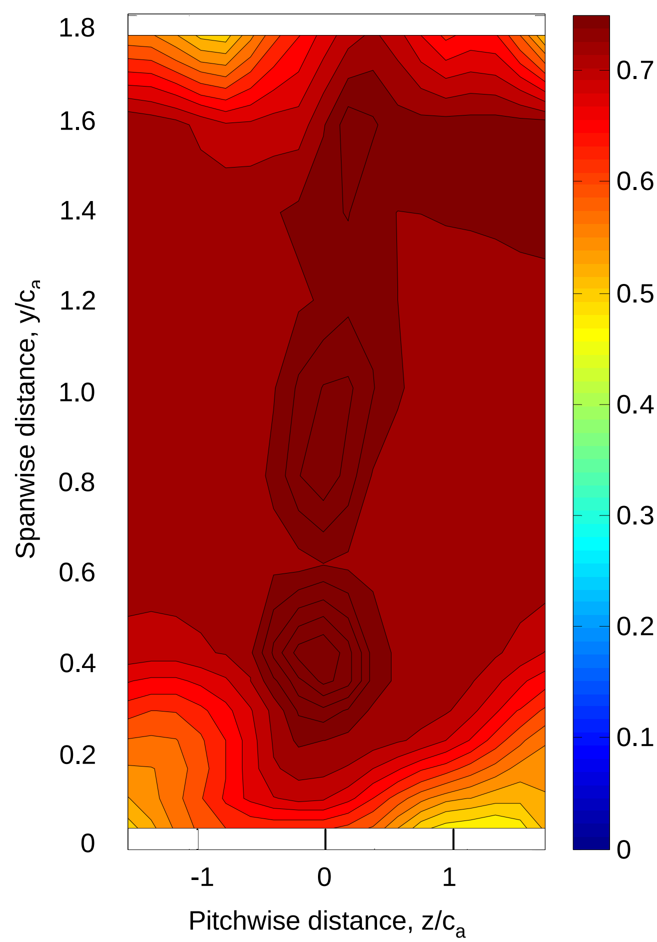

Figure 4-68: Simple blowing U/U_{ref} cross-section (2.6%) at x/c_a = 1.877 and tip-gap 0.004125c

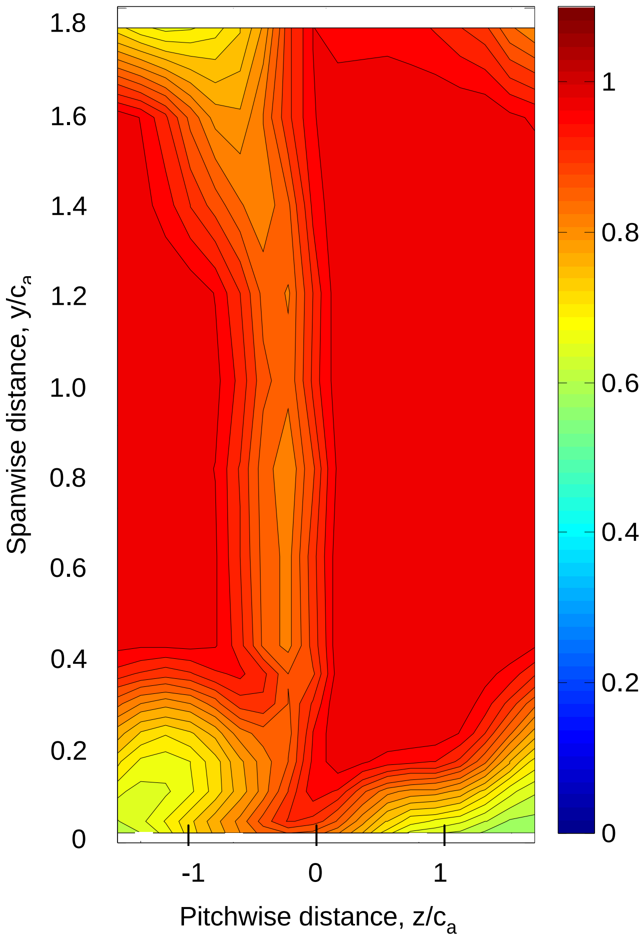

Figure 4-69: Kuethe vane C_{p0} cross-section (passive suction) at x/c_a = 0.839 and tip-gap 0.004125c

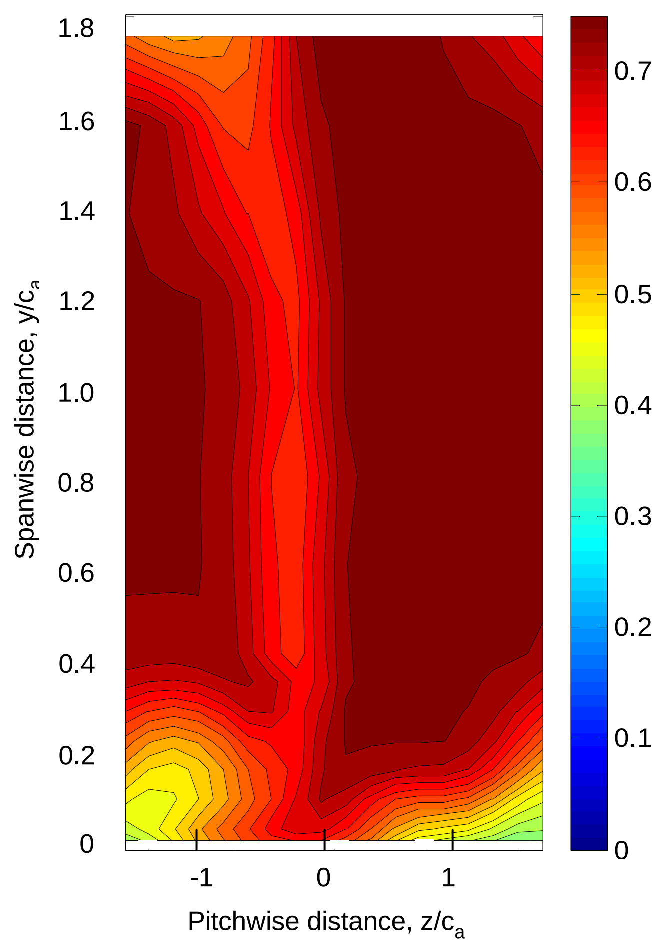

Figure 4-70: Kuethe vane U/U_{ref} cross-section (passive suction) at x/c_a = 0.839 and tip-gap 0.004125c

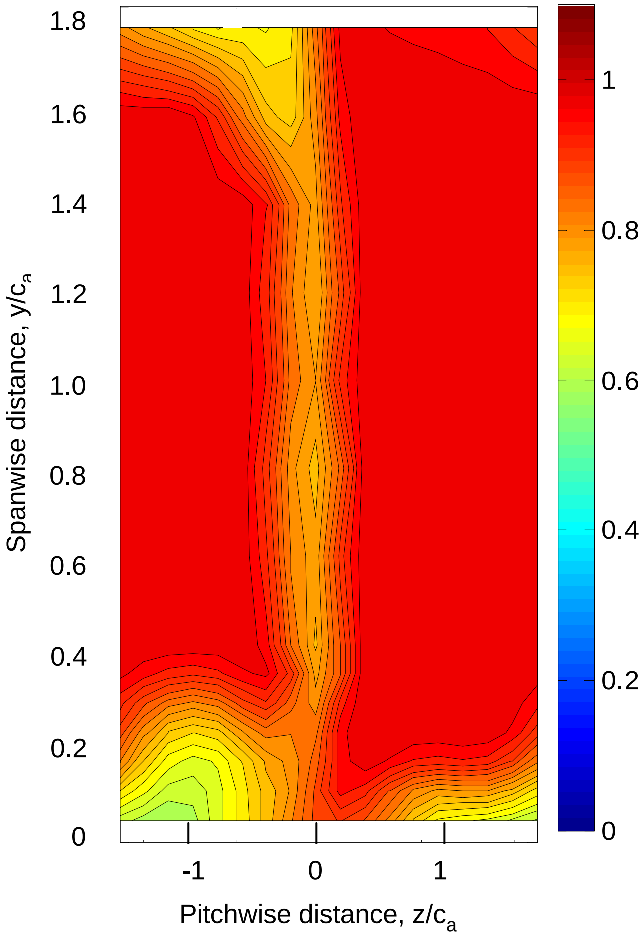

Figure 4-71: Kuethe vane C_{p0} cross-section (1.4%) at x/c_a = 0.839 and tip-gap 0.004125*c*

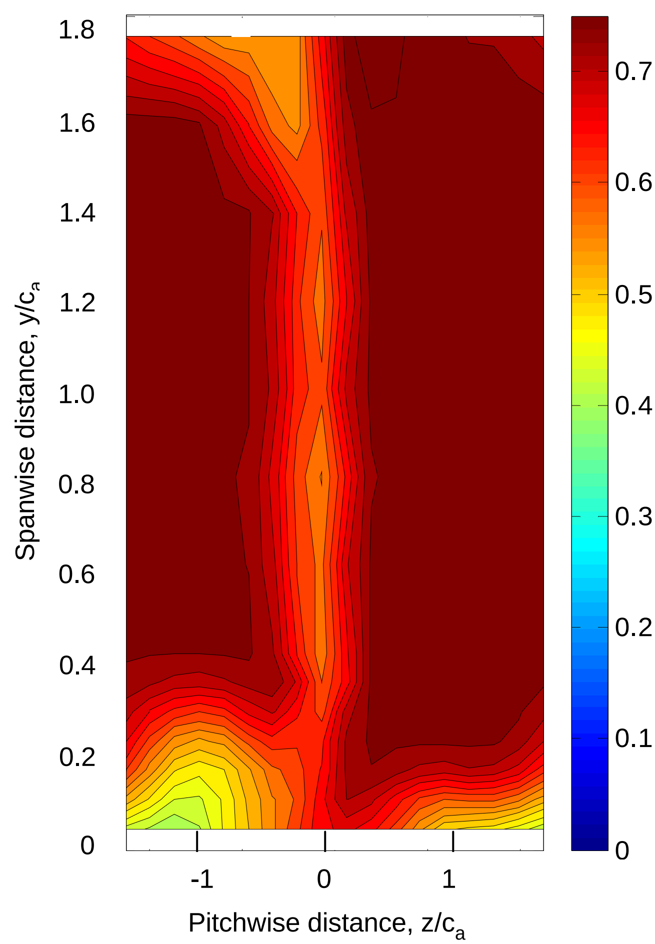

Figure 4-72: Kuethe vane U/U_{ref} cross-section (1.4%) at x/c_a = 0.839 and tip-gap 0.004125*c*

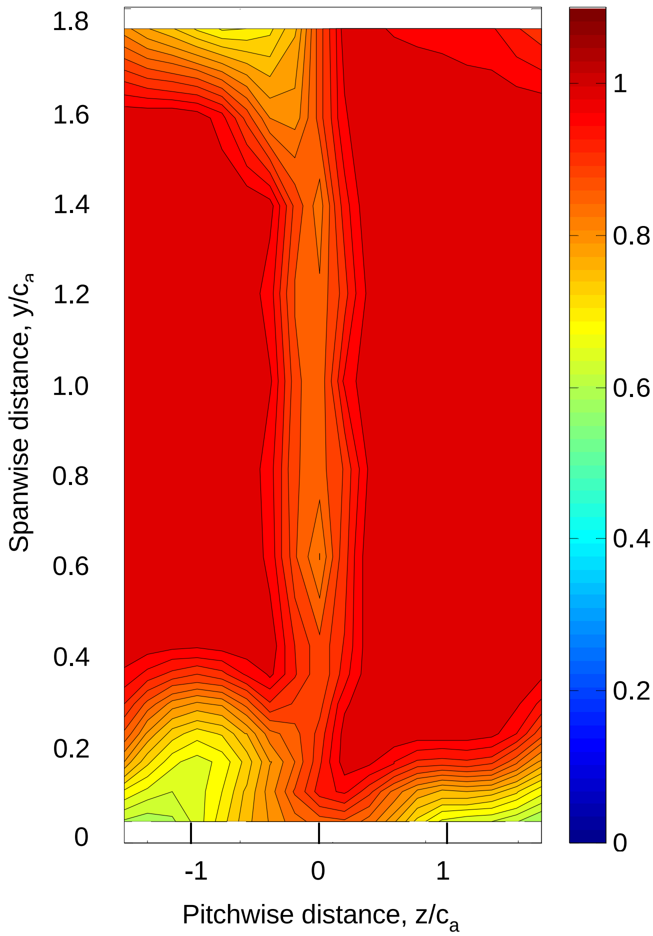

Figure 4-73: Kuethe vane C_{p0} cross-section (2.0%) at x/c_a = 0.839 and tip-gap 0.004125c

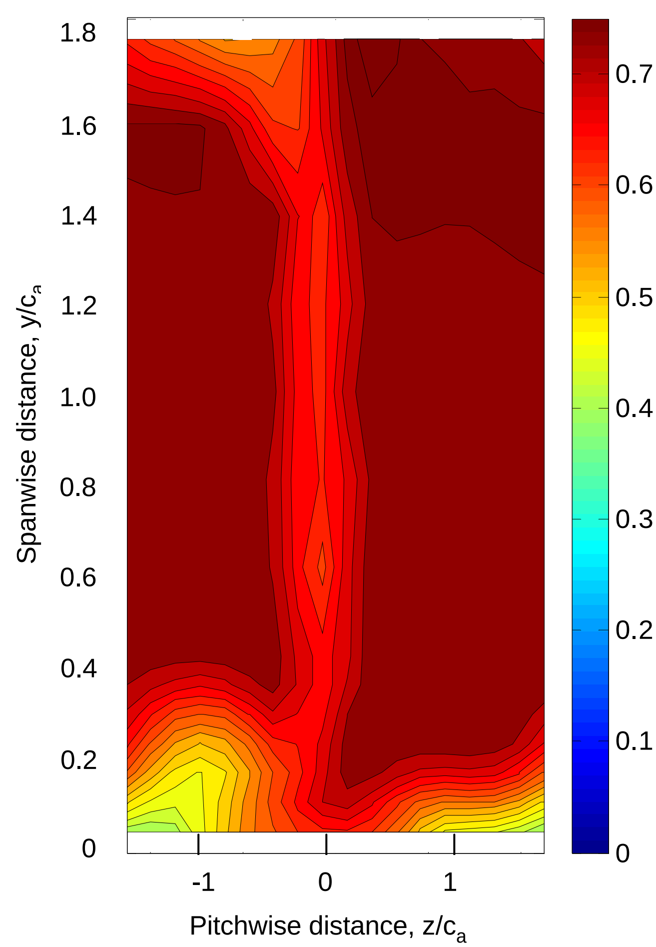

Figure 4-74: Kuethe vane U/U_{ref} cross-section (2.0%) at x/c_a = 0.839 and tip-gap 0.004125c

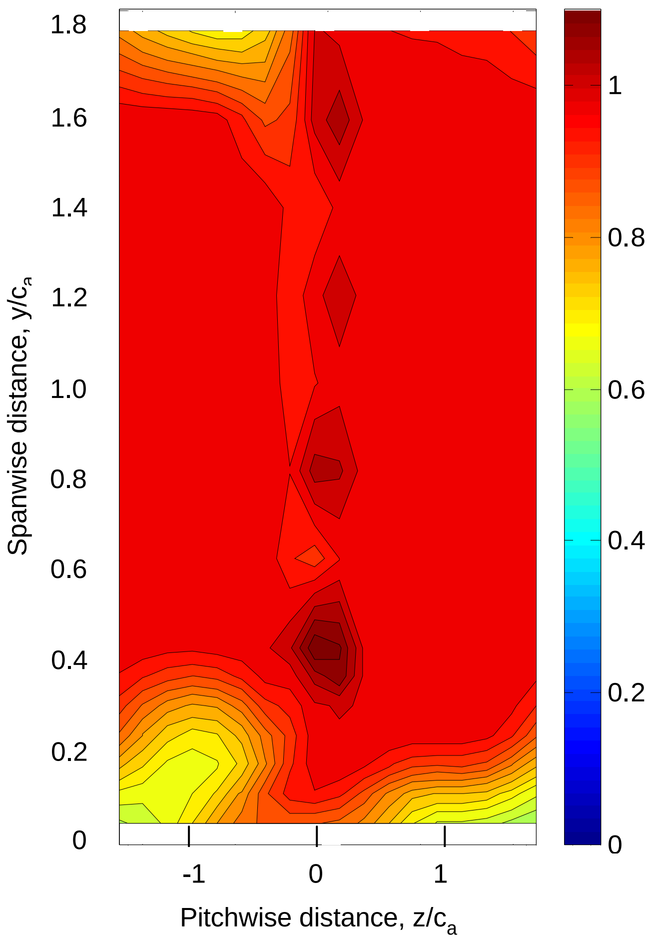

Figure 4-75: Kuethe vane C_{p0} cross-section (2.6%) at x/c_a = 0.839 and tip-gap 0.004125*c*

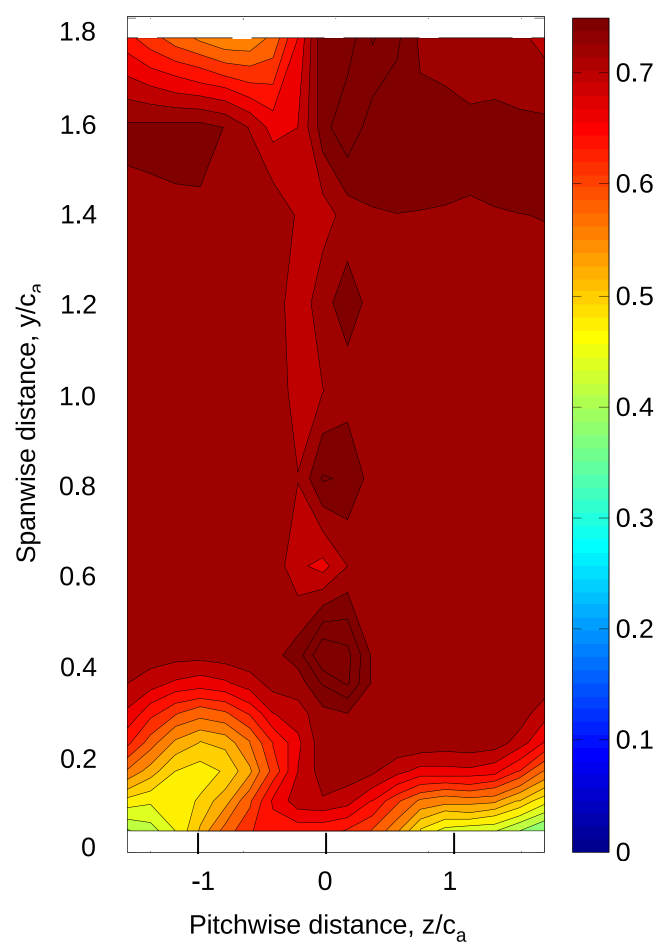

Figure 4-76: Kuethe vane U/U_{ref} cross-section (2.6%) at x/c_a = 0.839 and tip-gap 0.004125*c*

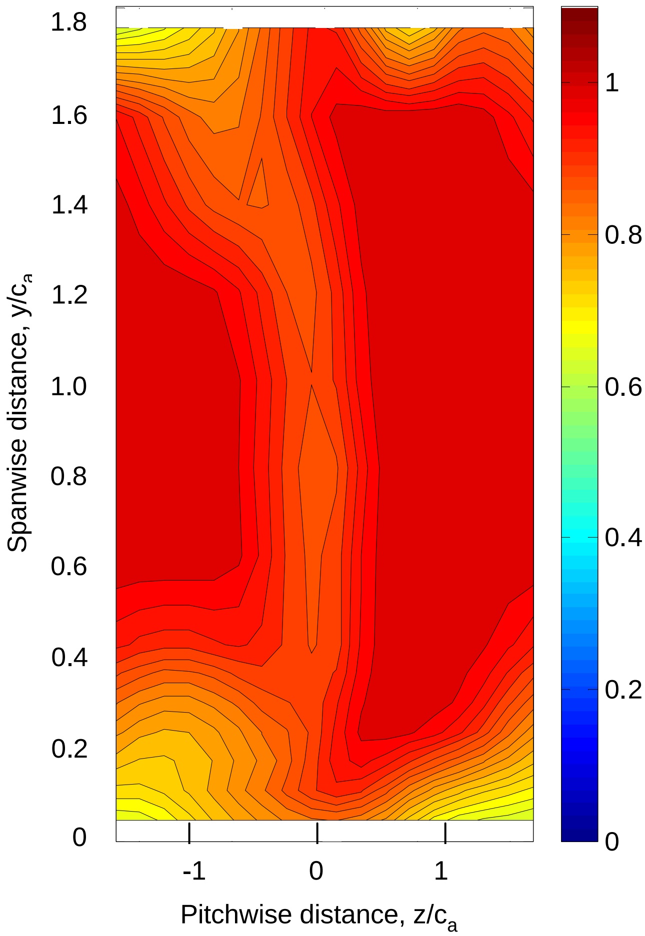

Figure 4-77: Kuethe vane C_{p0} cross-section (passive suction) at x/c_a = 1.877 and tip-gap 0.004125c

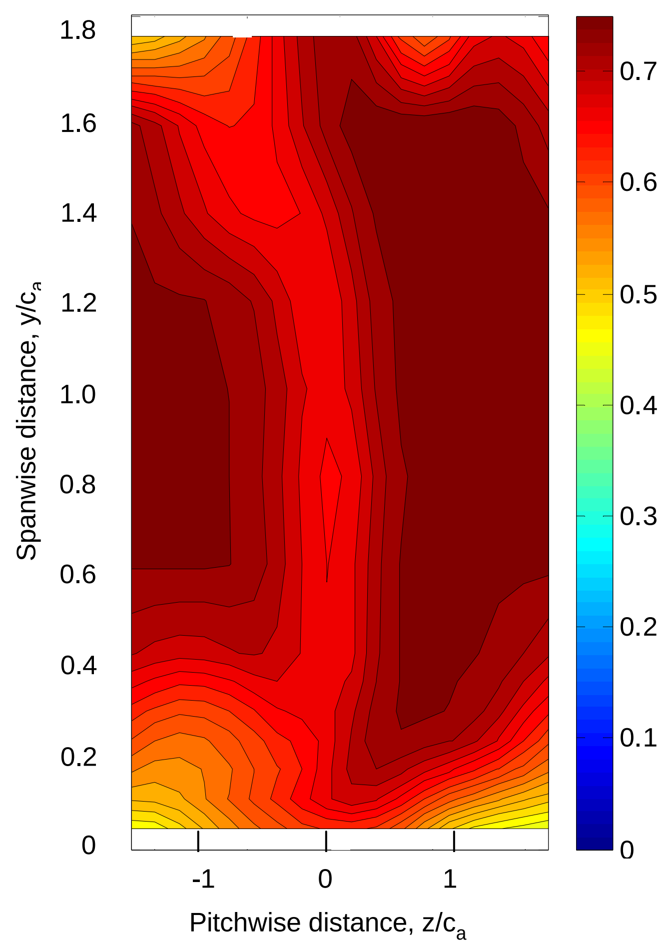

Figure 4-78: Kuethe vane U/U_{ref} cross-section (passive suction) at x/c_a = 1.877 and tip-gap 0.004125c

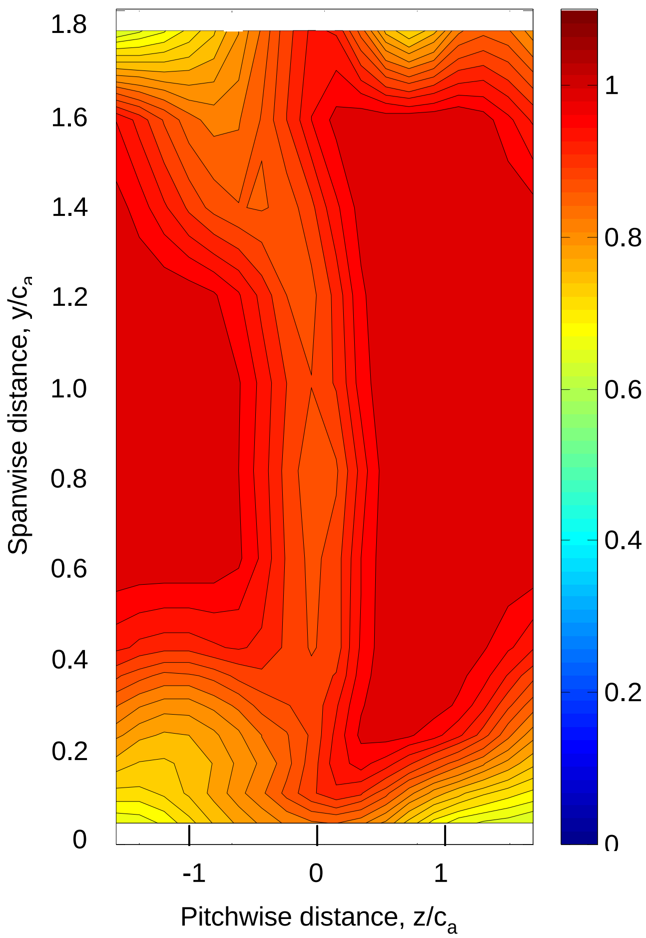

Figure 4-79: Kuethe vane C_{p0} cross-section (1.4%) at x/c_a = 1.877 and tip-gap 0.004125c

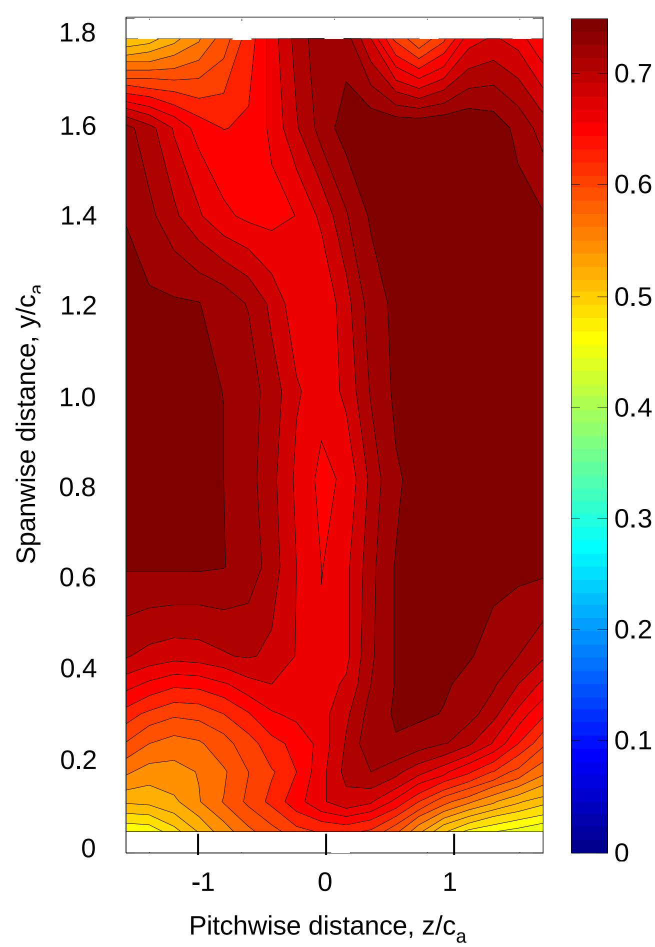

Figure 4-80: Kuethe vane U/U_{ref} cross-section (1.4%) at x/c_a = 1.877 and tip-gap 0.004125c

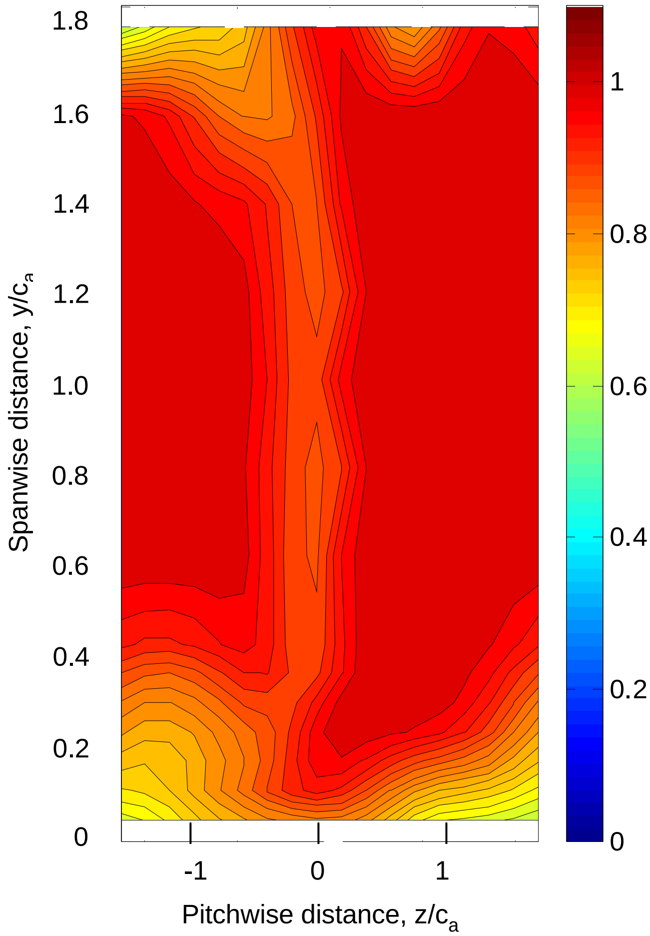

Figure 4-81: Kuethe vane C_{p0} cross-section (2.0%) at x/c_a = 1.877 and tip-gap 0.004125*c*

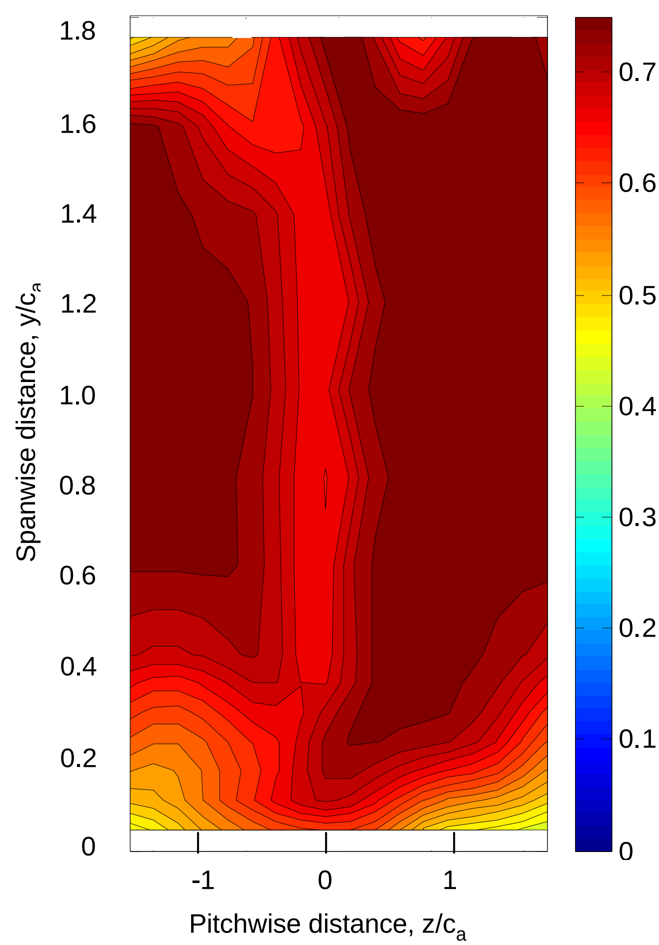

Figure 4-82: Kuethe vane U/U_{ref} cross-section (2.0%) at x/c_a = 1.877 and tip-gap 0.004125*c*

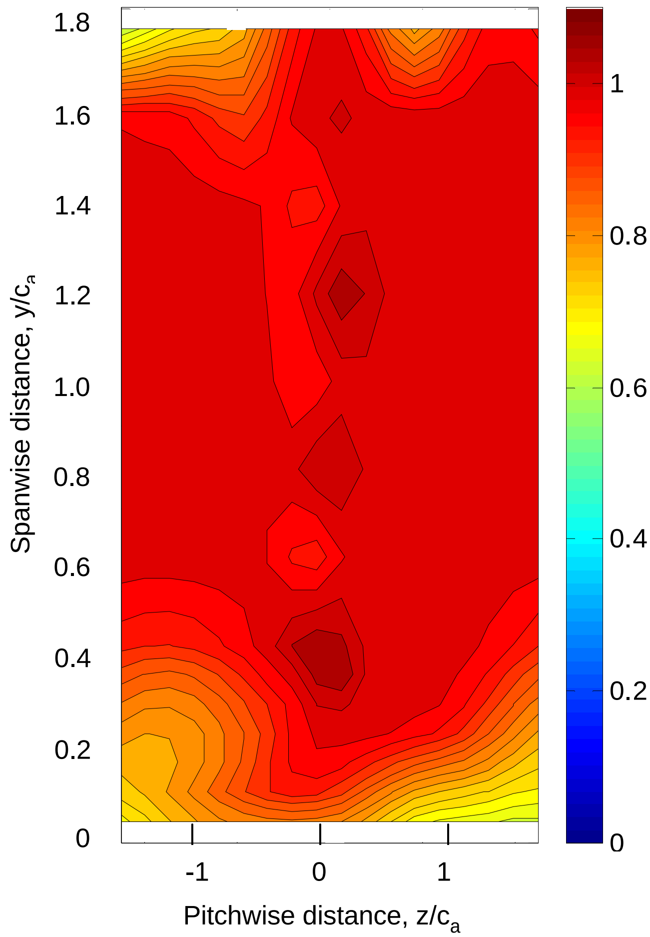

Figure 4-83: Kuethe vane C_{p0} cross-section (2.6%) at x/c_a = 1.877 and tip-gap 0.004125c

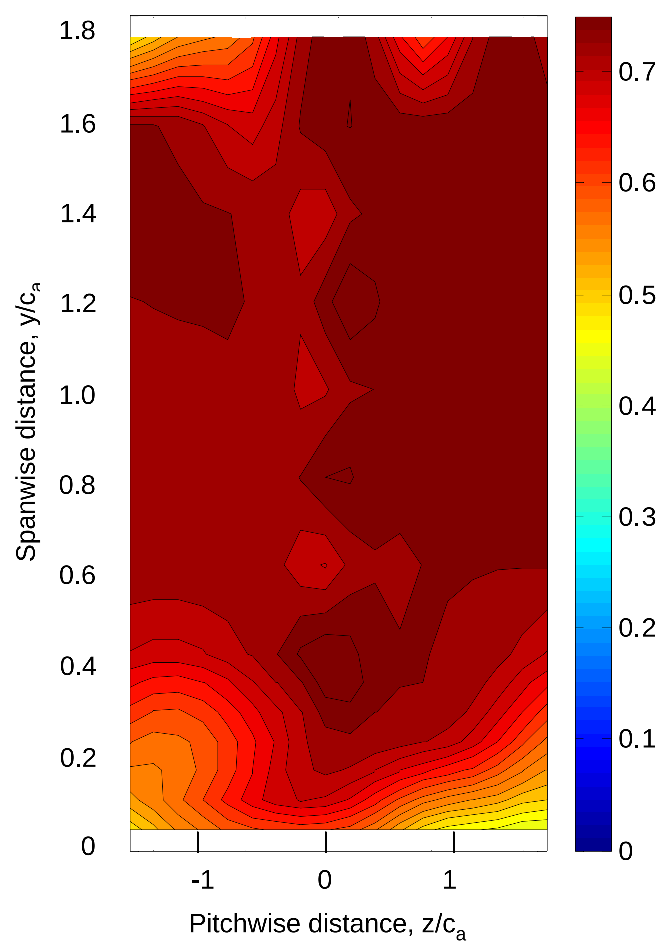

Figure 4-84: Kuethe vane U/U_{ref} cross-section (2.6%) at x/c_a = 1.877 and tip-gap 0.004125c

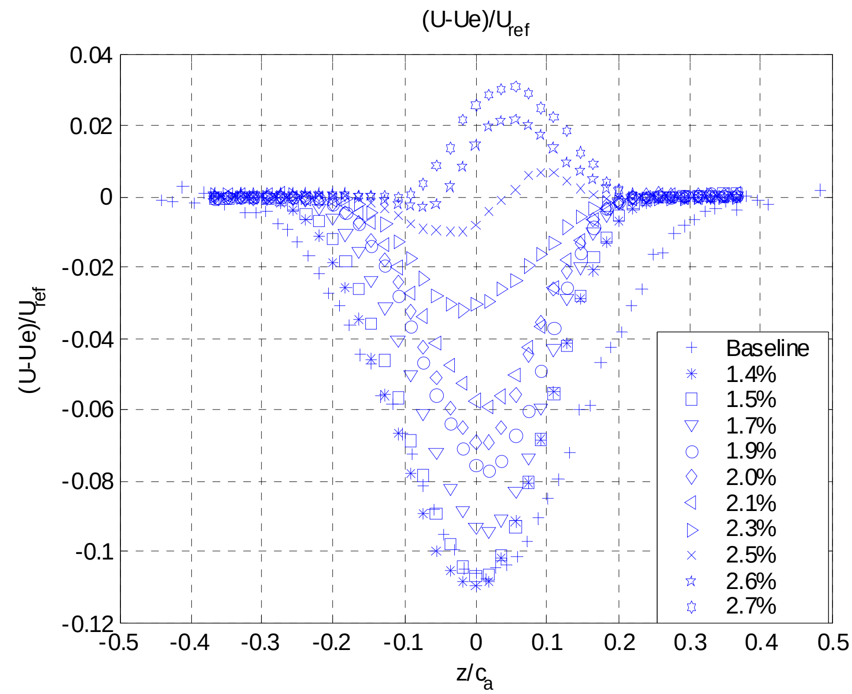

Figure 4-85: Simple blowing streamwise mean velocity profile $(U\text{-}U_e)/U_{ref}$ at x/c_a = 1.819

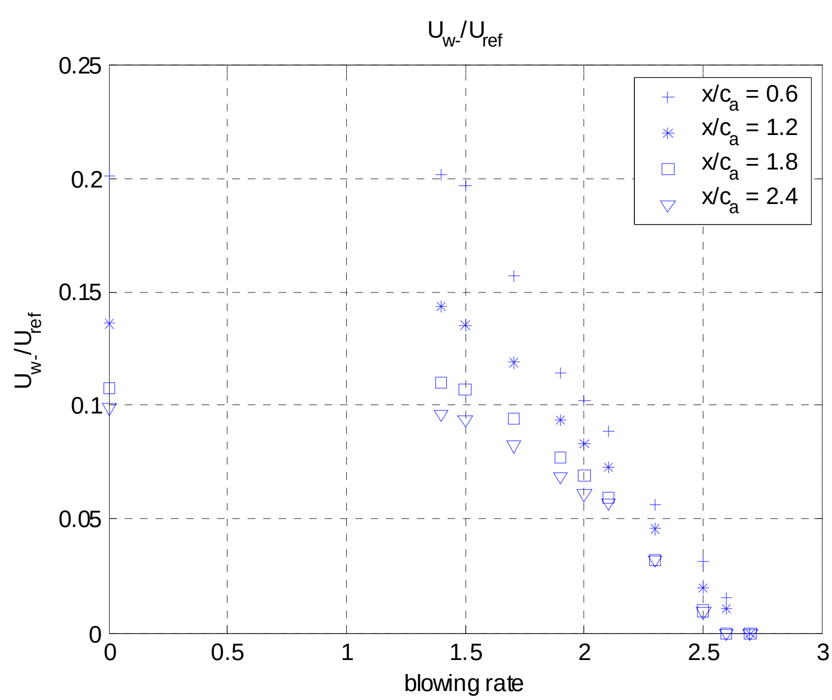

Figure 4-86: Simple blowing maximum pitchwise velocity deficit $U_{w\text{-}}/U_{ref}$ at x/c_a = 0.608, 1.178, 1.819 and 2.382.. The non-blowing baseline is included as 0%.

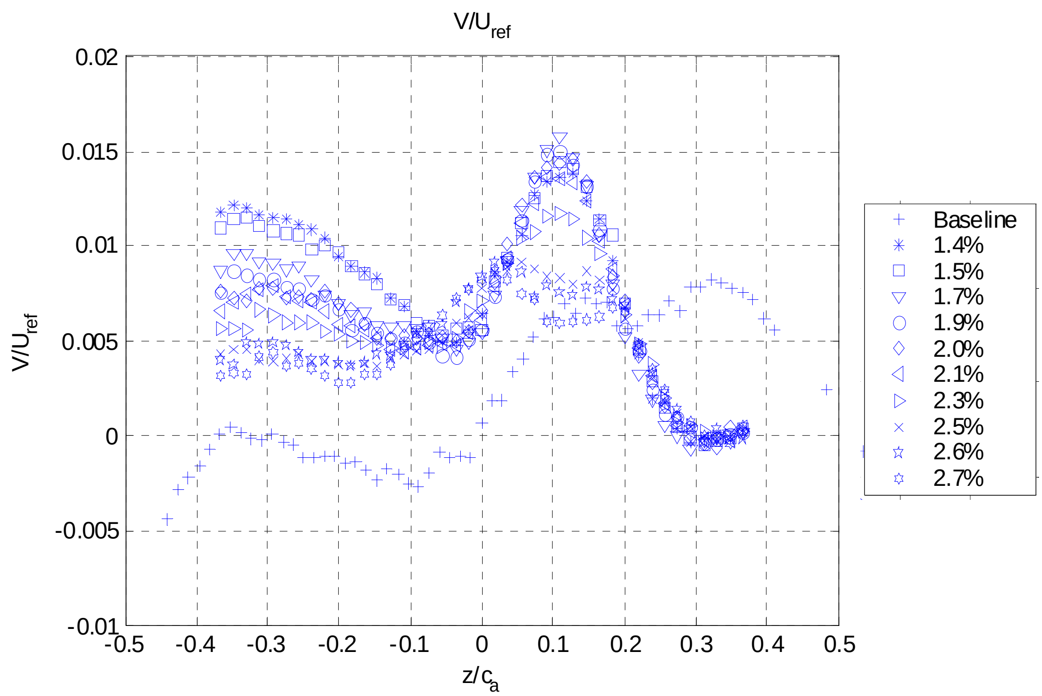

Figure 4-87: Simple blowing spanwise mean velocity profile V/U_{ref} at x/c_a = 1.819

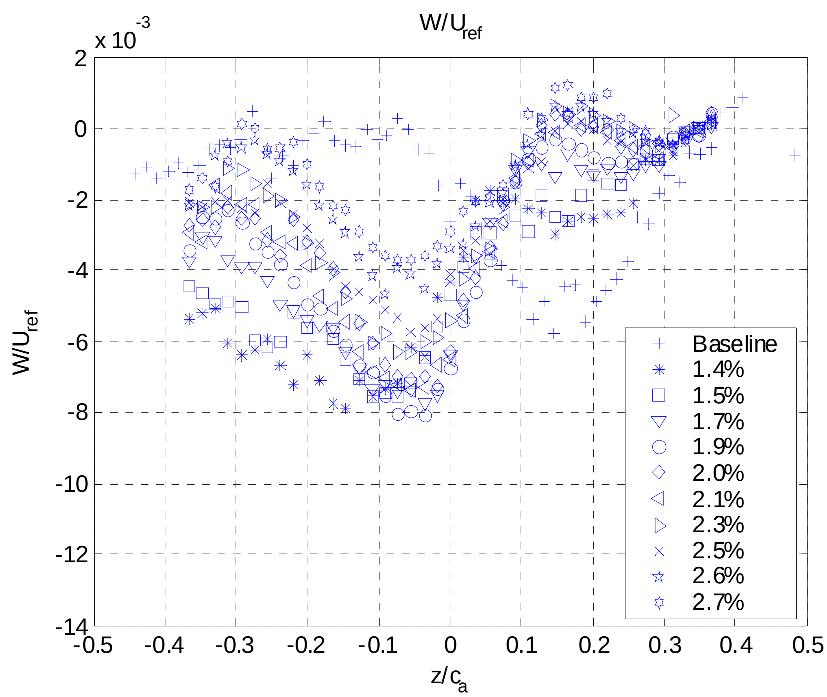

Figure 4-88: Simple blowing cross-wake mean velocity profile W/U_{ref} at x/c_a = 1.819

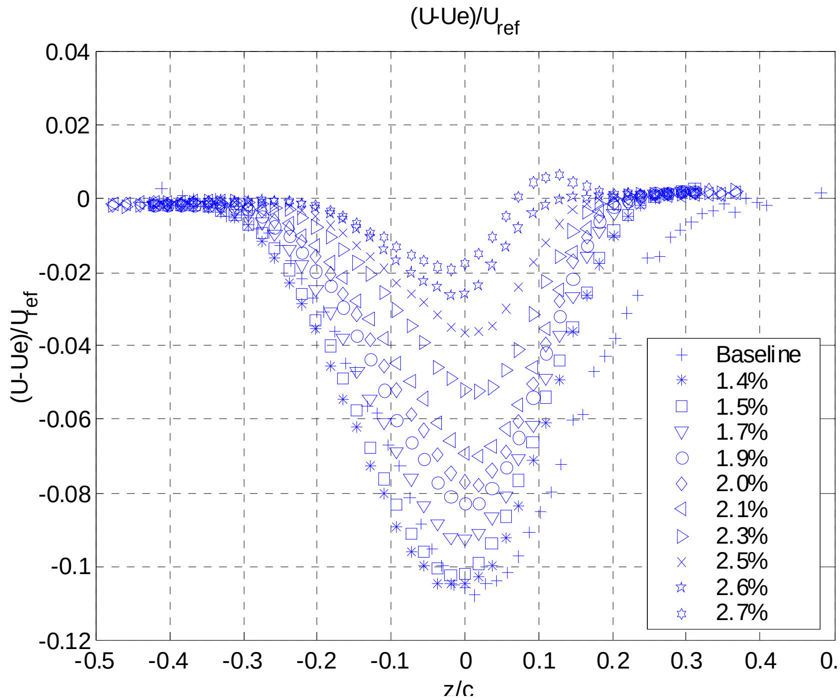

Figure 4-89: Kuethe vane streamwise mean velocity profile $(U\text{-}U_e)/U_{ref}$ at x/c_a = 1.819

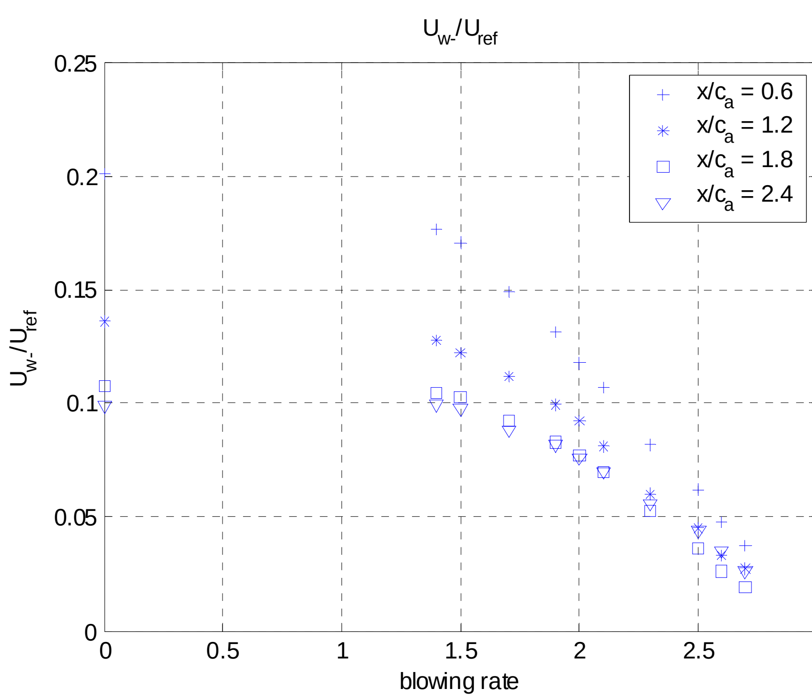

Figure 4-90: Kuethe vane maximum pitchwise velocity deficit U_{w-}/U_{ref} at x/c_a = 0.608, 1.178, 1.819 and 2.382. The non-blowing baseline is included as 0%.

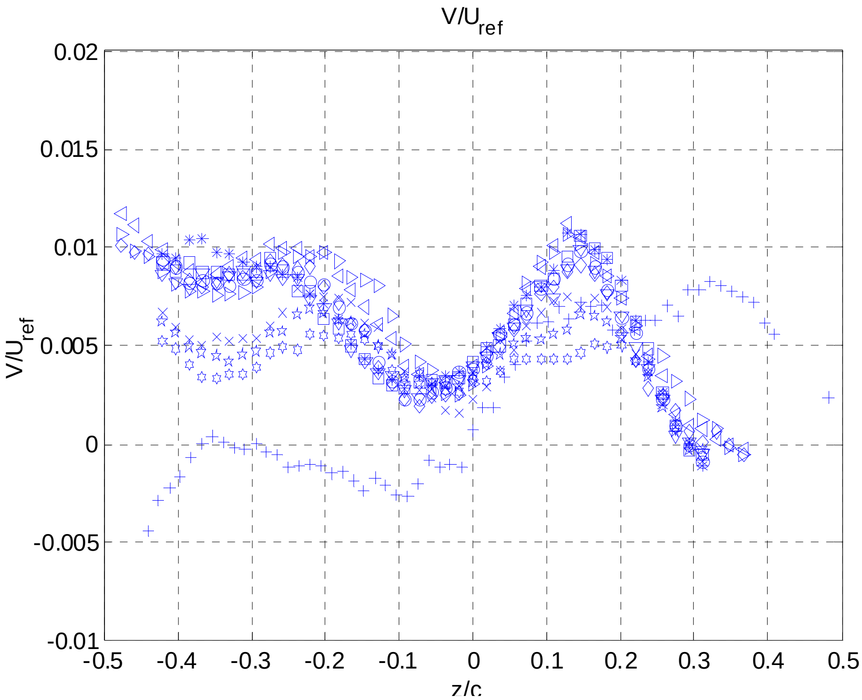

Figure 4-91: Kuethe vane spanwise mean velocity profile V/U_{ref} at x/c_a = 1.819

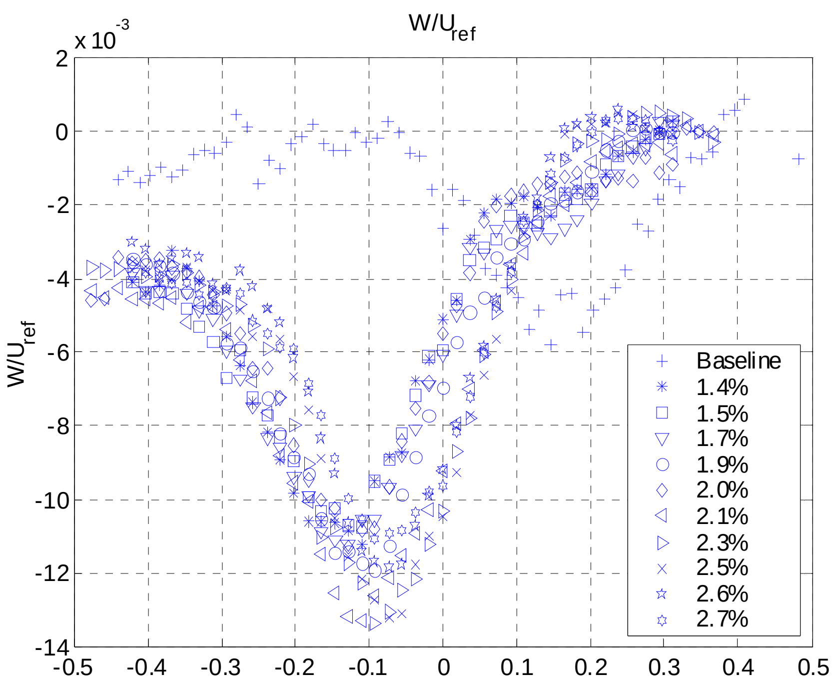

Figure 4-92: Kuethe vane cross-wake mean velocity profile W/U_{ref} at x/c_a = 1.819

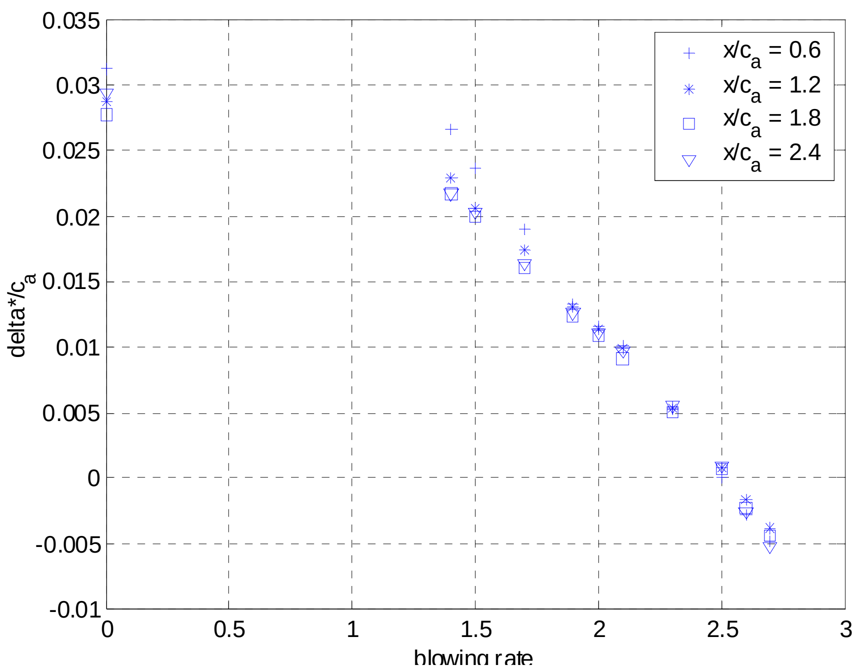

Figure 4-93: Simple blowing wake-aligned displacement thickness δ^*/c_a at x/c_a = 0.608, 1.178, 1.819 and 2.382. The non-blowing baseline is included as 0%.

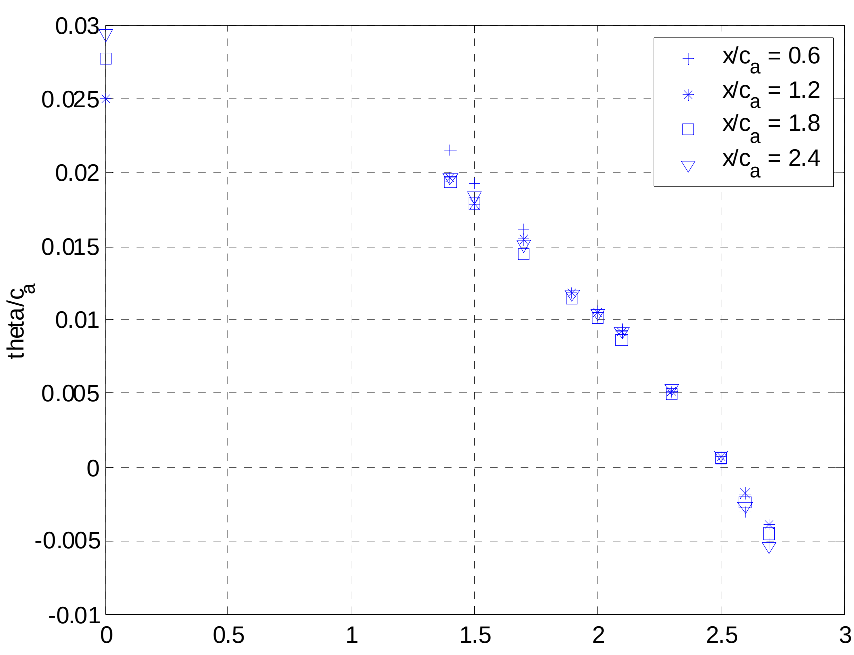

Figure 4-94: Simple blowing wake-aligned momentum thickness θ/c_a at x/c_a = 0.608, 1.178, 1.819 and 2.382. The non-blowing baseline is included as 0%.

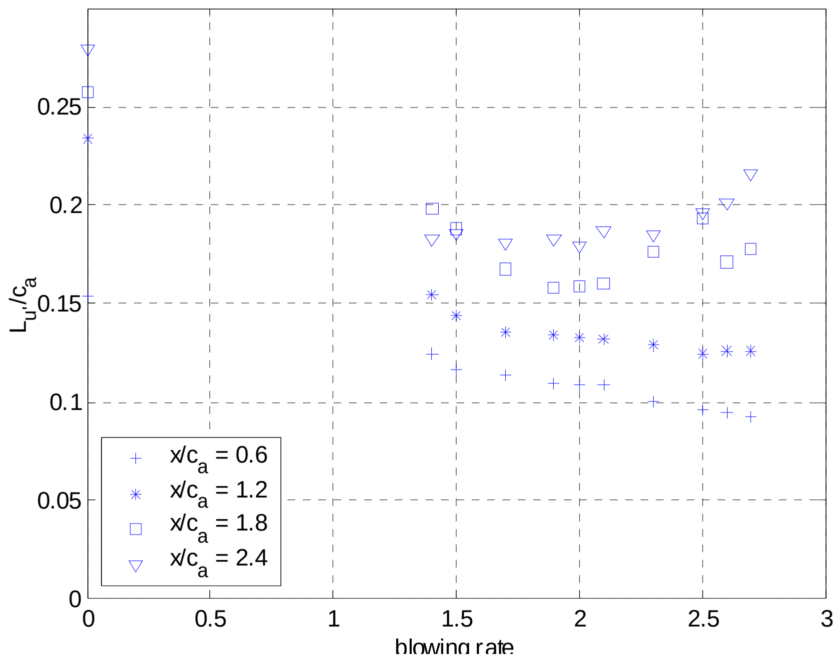

Figure 4-95: Simple blowing wake-aligned wake half-width $L_{u'}/c_a$ at x/c_a = 0.608, 1.178, 1.819 and 2.382. The non-blowing baseline is included as 0%.

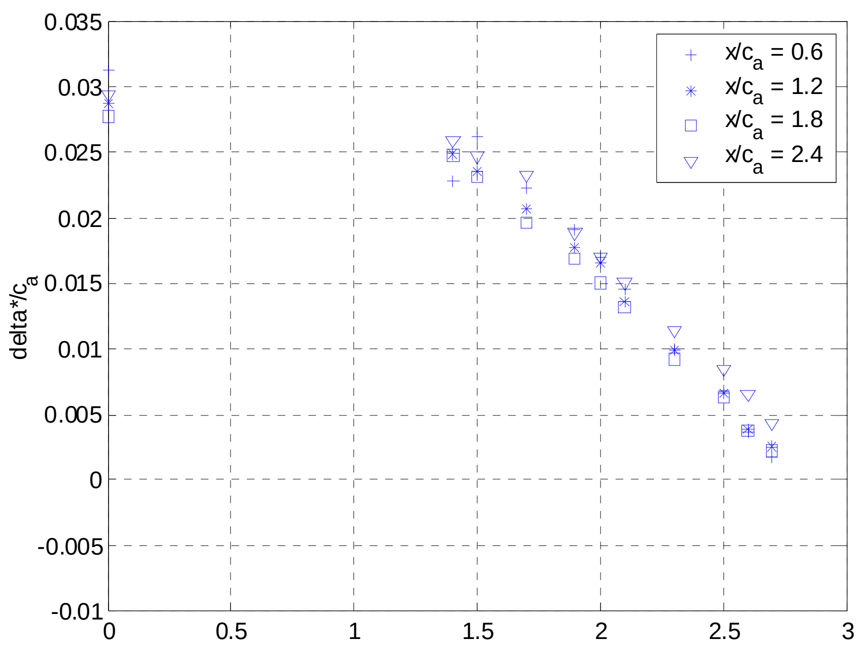

Figure 4-96: Kuethe vane wake-aligned displacement thickness δ^*/c_a at x/c_a = 0.608, 1.178, 1.819 and 2.382. The non-blowing baseline is included as 0%.

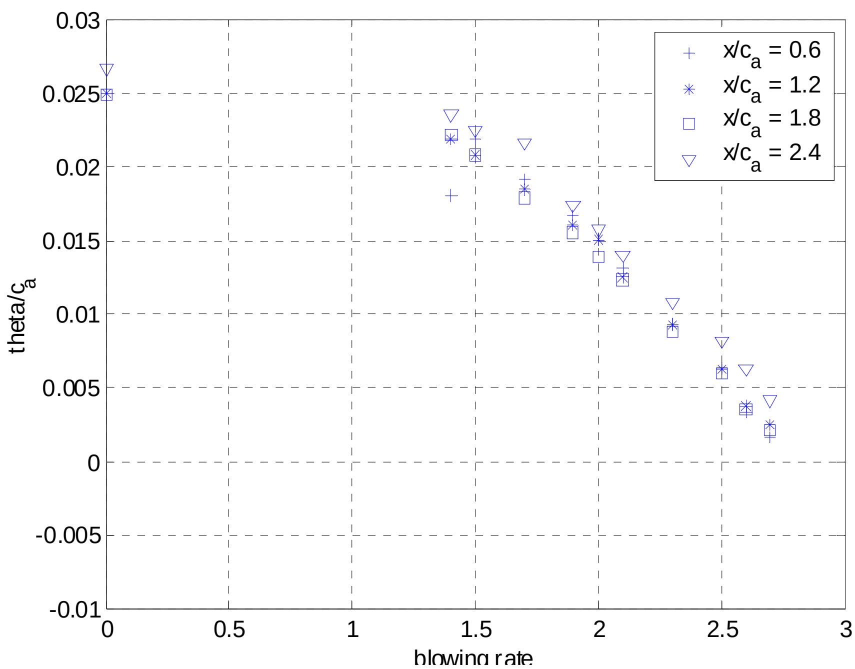

Figure 4-97: Kuethe vane wake-aligned displacement thickness θ/c_a at x/c_a = 0.608, 1.178, 1.819 and 2.382. The non-blowing baseline is included as 0%.

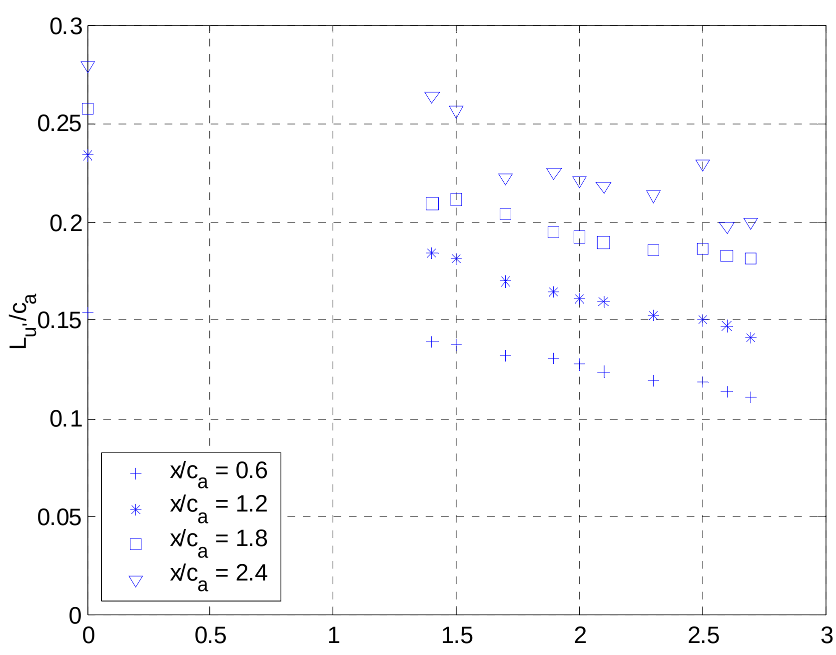

Figure 4-98: Kuethe vane wake-aligned wake half-width $L_{u'}/c_a$ at x/c_a = 0.608, 1.178, 1.819 and 2.382. The non-blowing baseline is included as 0%.

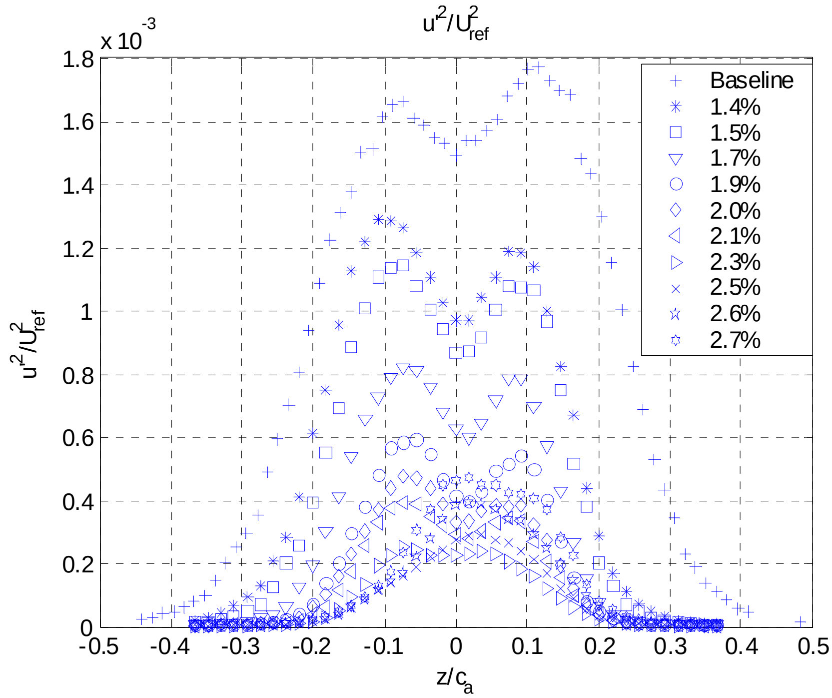

Figure 4-99: Simple blowing streamwise Reynolds normal stress profile u'^2/U_{ref}^2 at x/c_a = 1.819

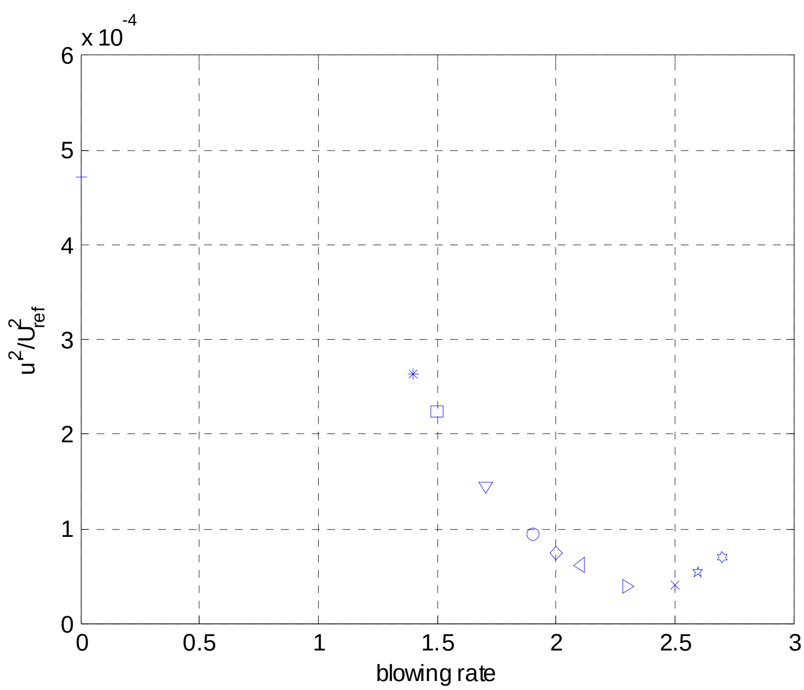

Figure 4-100: Simple blowing pitchwise-averaged streamwise Reynolds normal stress profile u'^2/U_{ref}^2 at x/c_a = 1.819

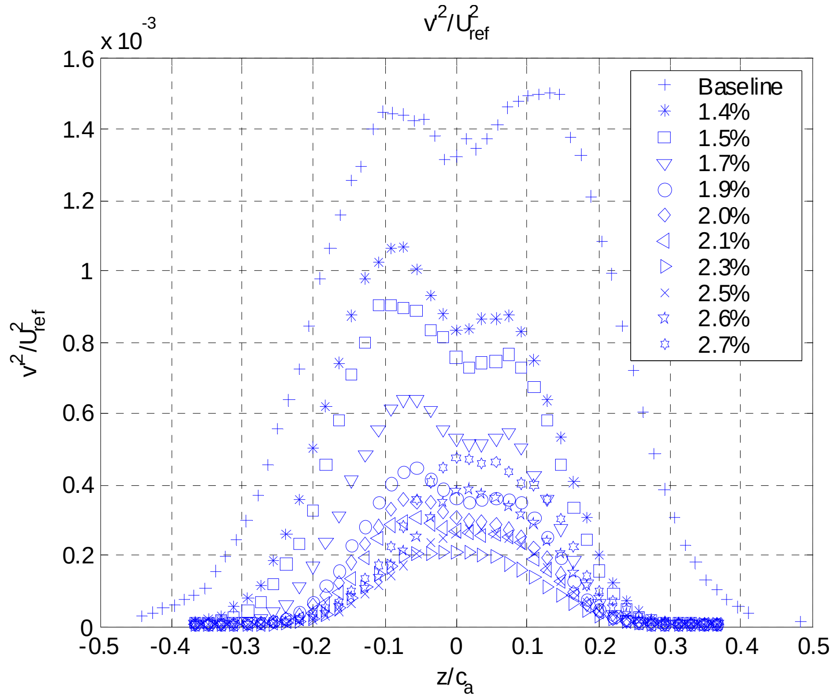

Figure 4-101: Simple blowing spanwise Reynolds normal stress profile v'^2/U_{ref}^2 at x/c_a = 1.819

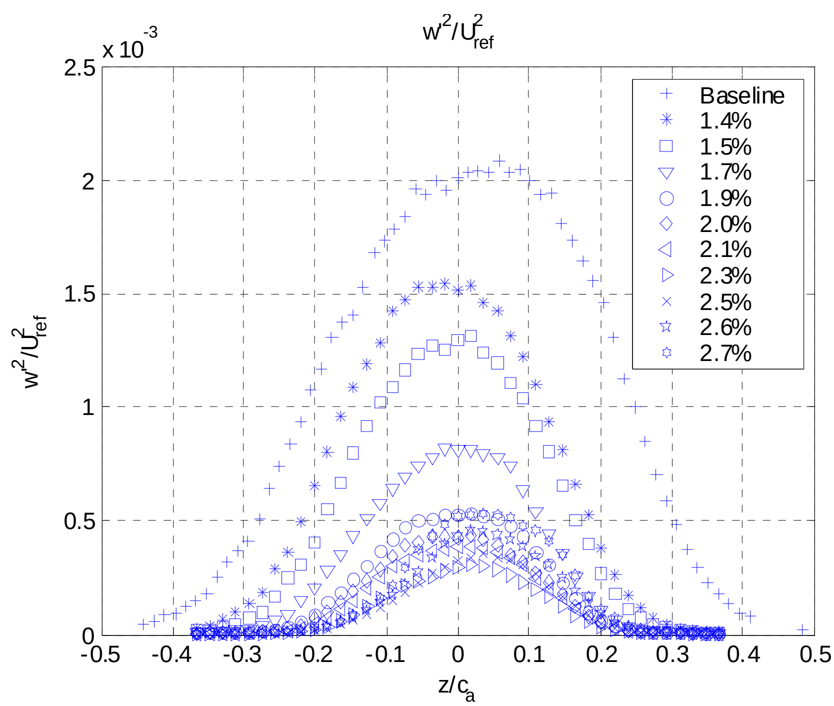

Figure 4-102: Simple blowing pitchwise Reynolds normal stress profile w'^2/U_{ref}^2 at x/c_a = 1.819

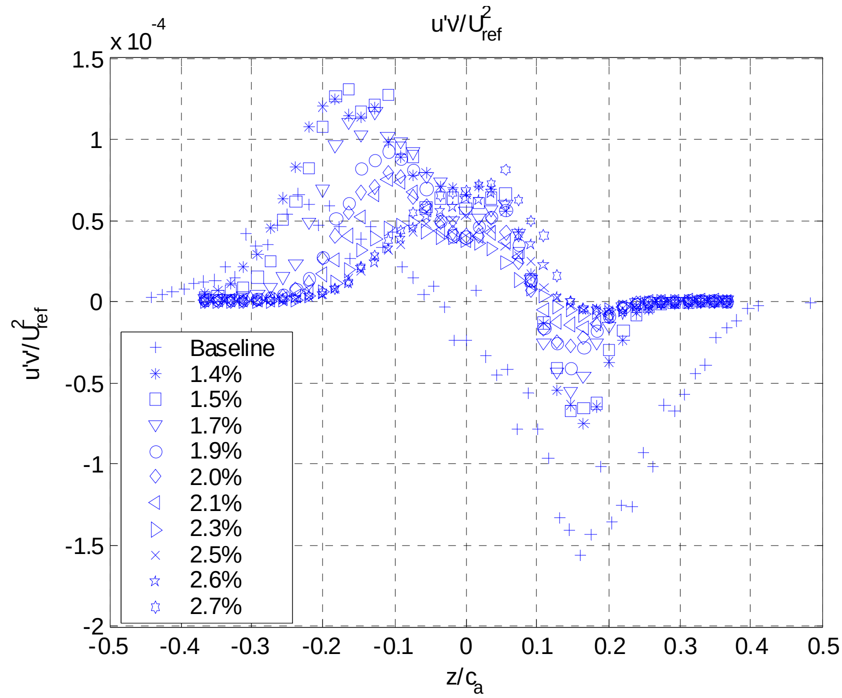

Figure 4-103: Simple blowing Reynolds shear stress profile $u'v'/U_{ref}^2$ at x/c_a = 1.819

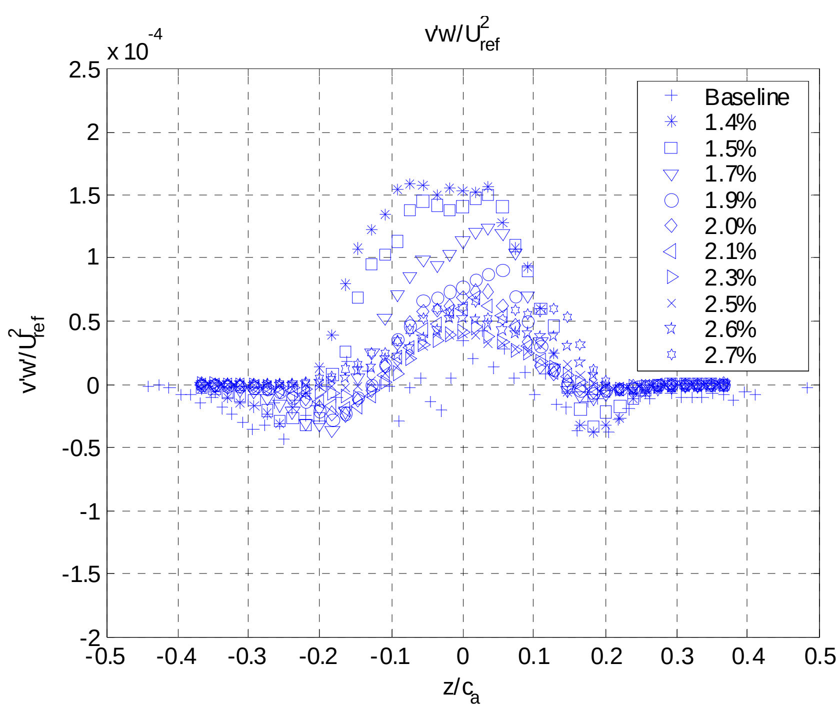

Figure 4-104: Simple blowing Reynolds shear stress profile $v'w'/U_{ref}^2$ at x/c_a = 1.819

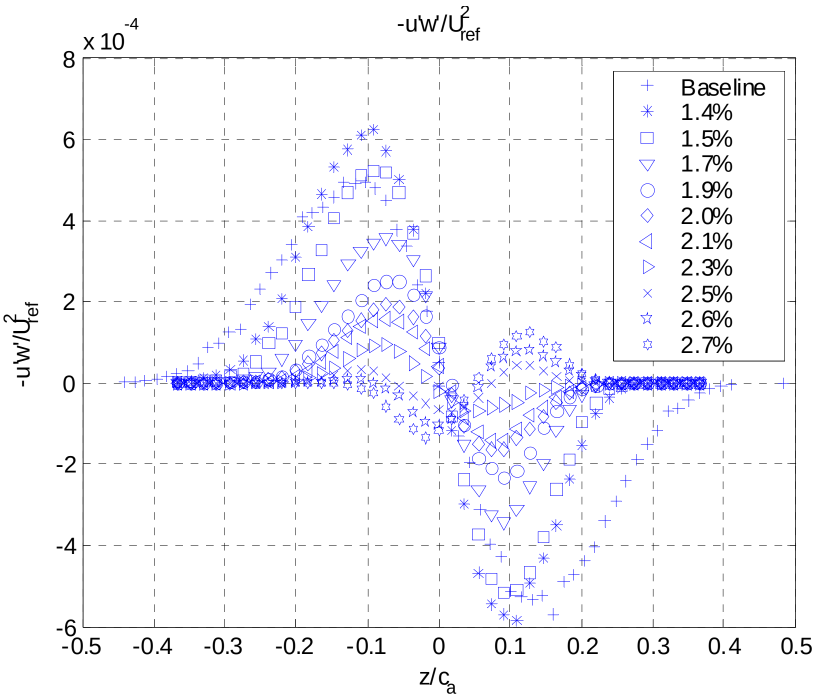

Figure 4-105: Simple blowing Reynolds shear stress profile $-u'w'/U_{ref}^2$ at x/c_a = 1.819

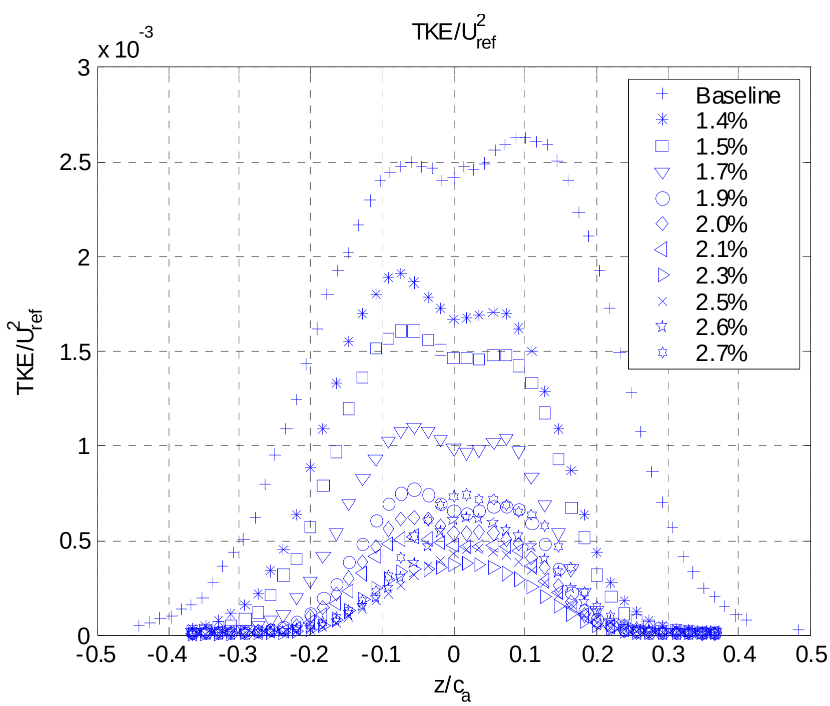

Figure 4-106: Simple blowing turbulent kinetic energy profile k/U_{ref}^2 at x/c_a = 1.819

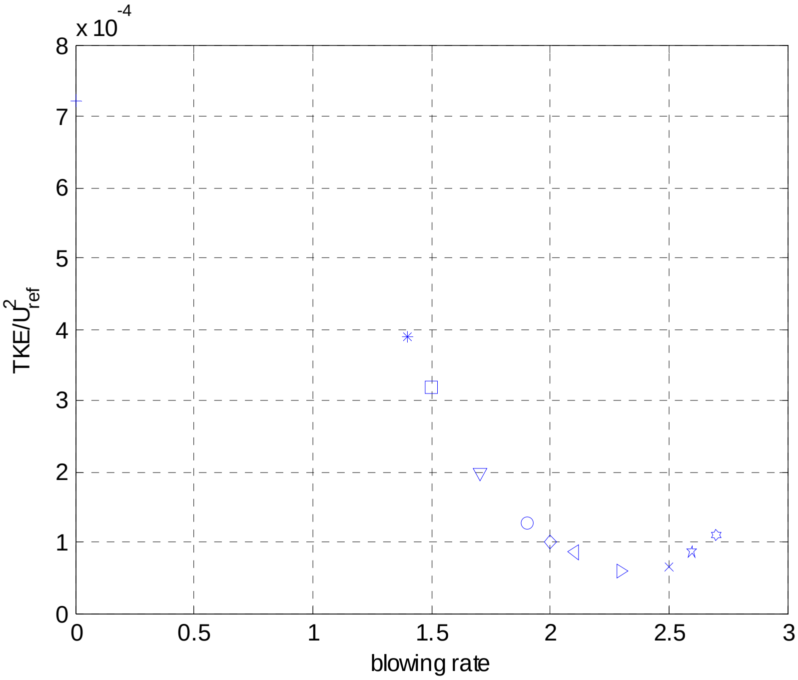

Figure 4-107: Simple blowing pitchwise-averaged turbulent kinetic energy profile k/U_{ref}^2 at x/c_a = 1.819

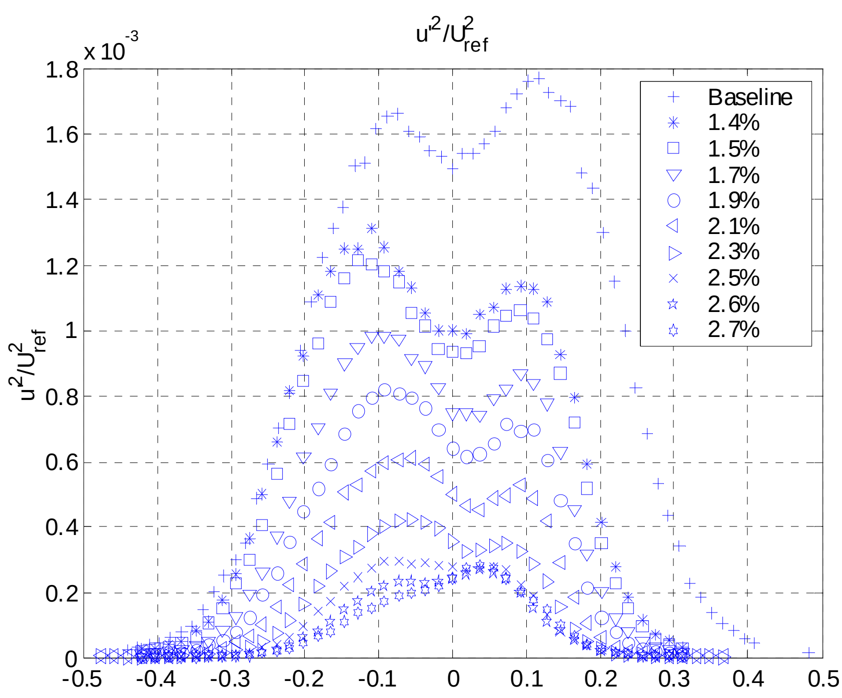

Figure 4-108: Kuethe vane streamwise Reynolds normal stress profile u'^2/U_{ref}^2 at x/c_a = 1.819

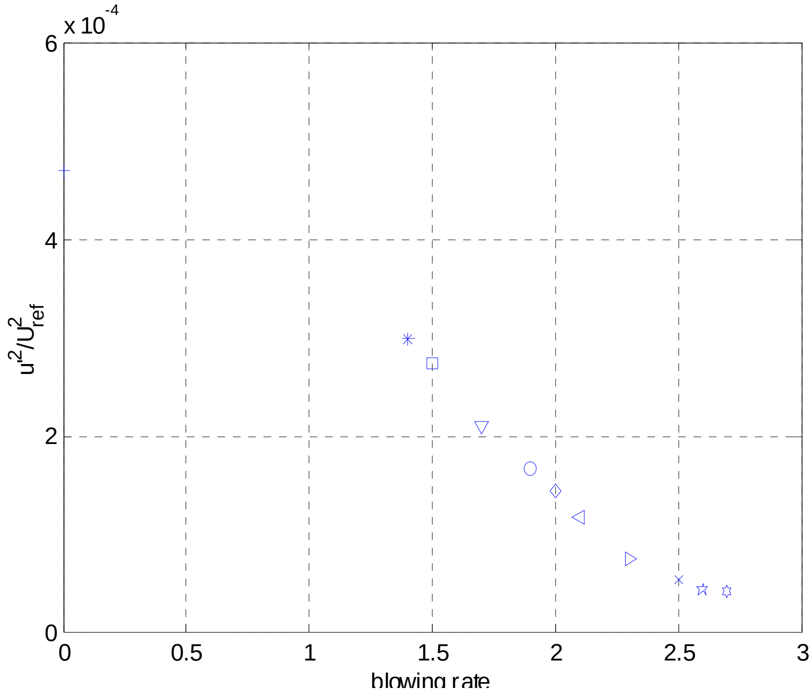

Figure 4-109: Kuethe vane pitchwise-averaged streamwise Reynolds normal stress profile u'^2/U_{ref}^2 at x/c_a = 1.819

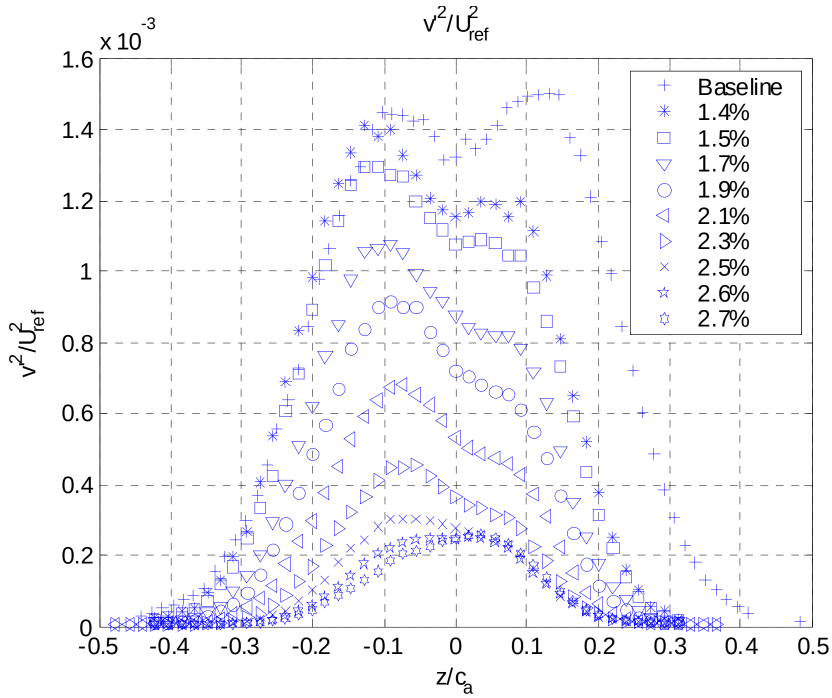

Figure 4-110: Kuethe vane spanwise Reynolds normal stress profile v'^2/U_{ref}^2 at x/c_a = 1.819

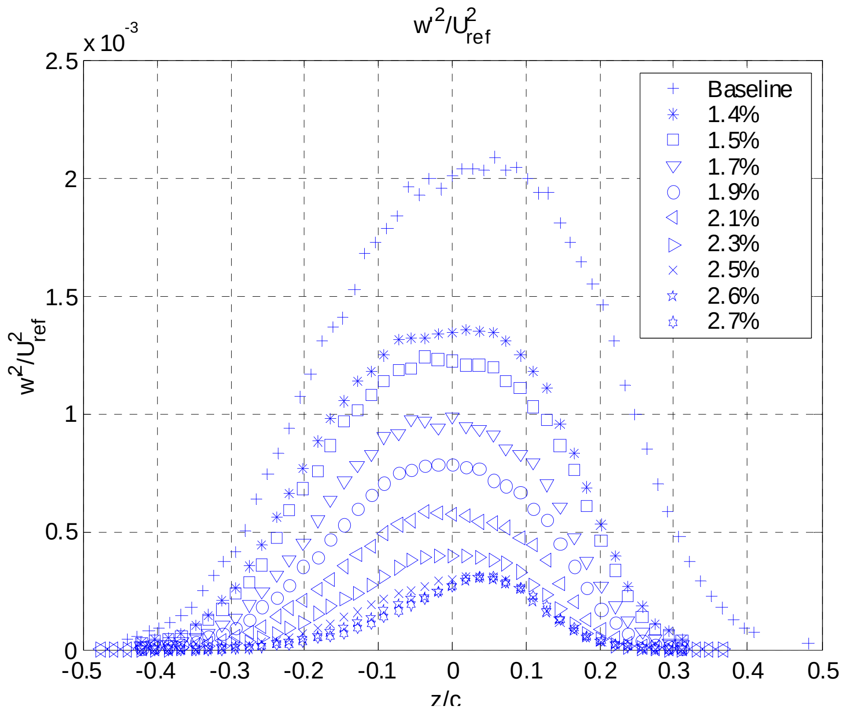

Figure 4-111: Kuethe vane pitchwise Reynolds normal stress profile w'^2/U_{ref}^2 at x/c_a = 1.819

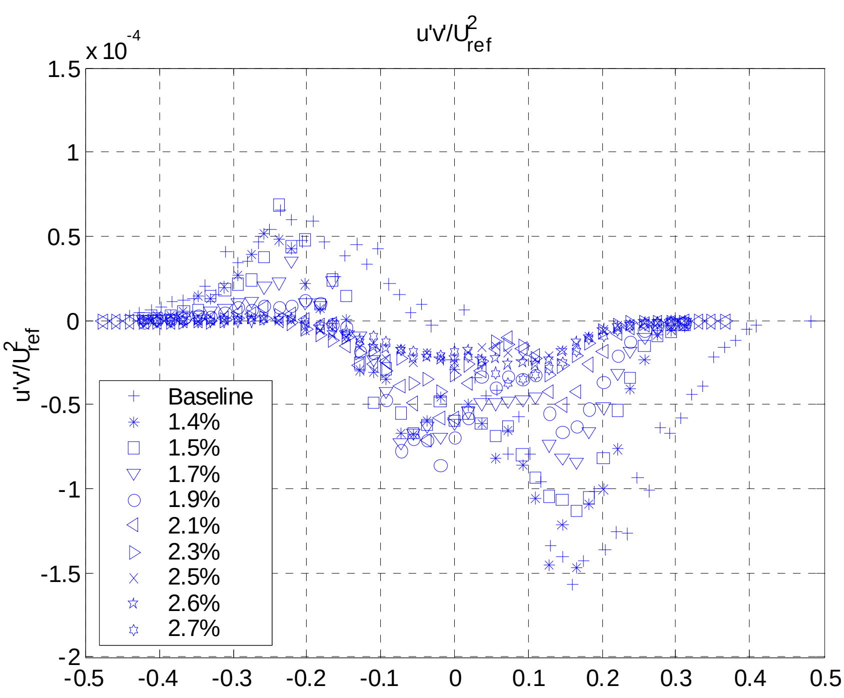

Figure 4-112: Kuethe vane Reynolds shear stress profile $u'v'/U_{ref}^2$ at x/c_a = 1.819

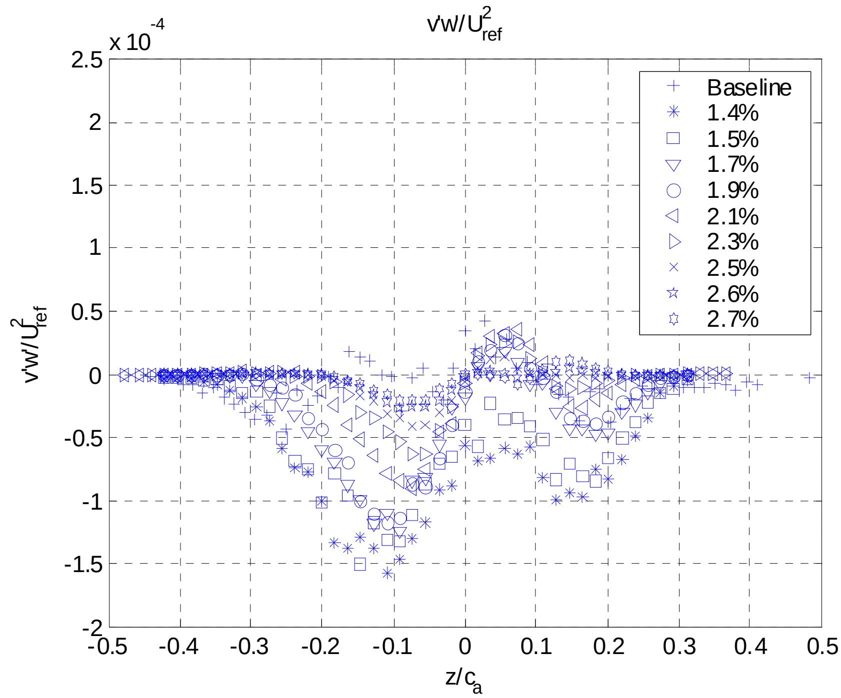

Figure 4-113: Kuethe vane Reynolds shear stress profile $v'w'/U_{ref}^2$ at x/c_a = 1.819

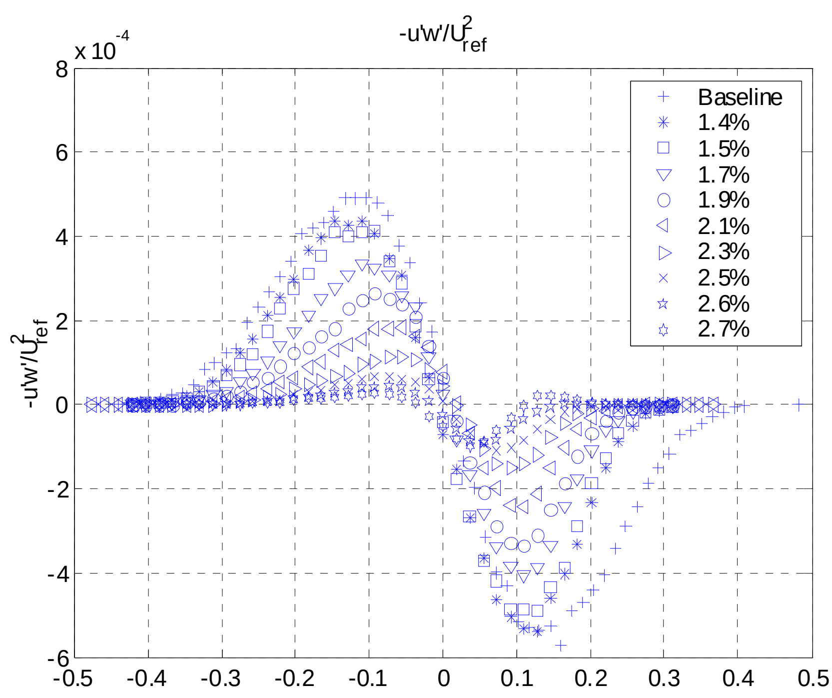

Figure 4-114: Kuethe vane Reynolds shear stress profile $-u'w'/U_{ref}^2$ at x/c_a = 1.819

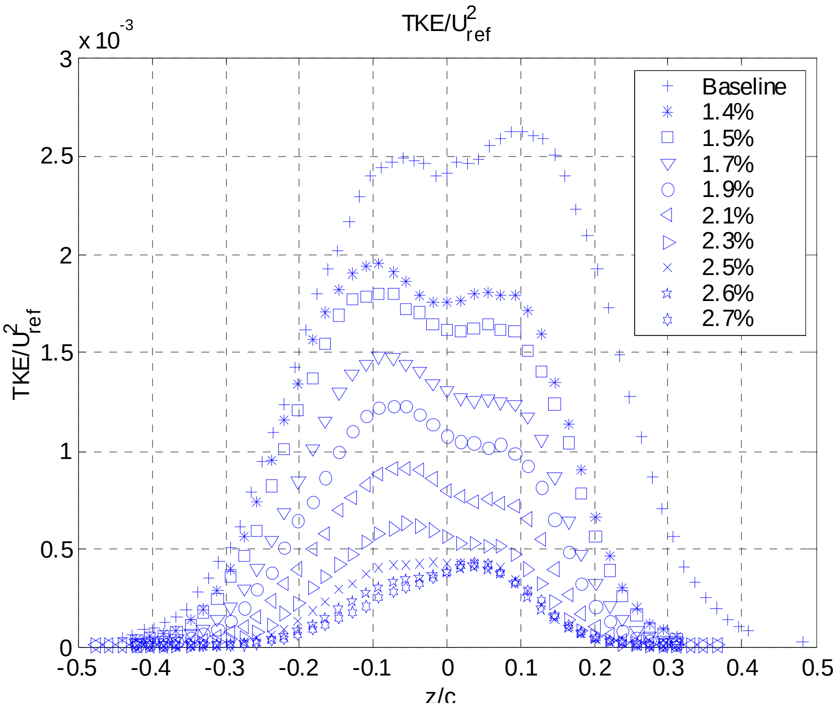

Figure 4-115: Kuethe vane turbulent kinetic energy profile k/U_{ref}^2 at x/c_a = 1.819

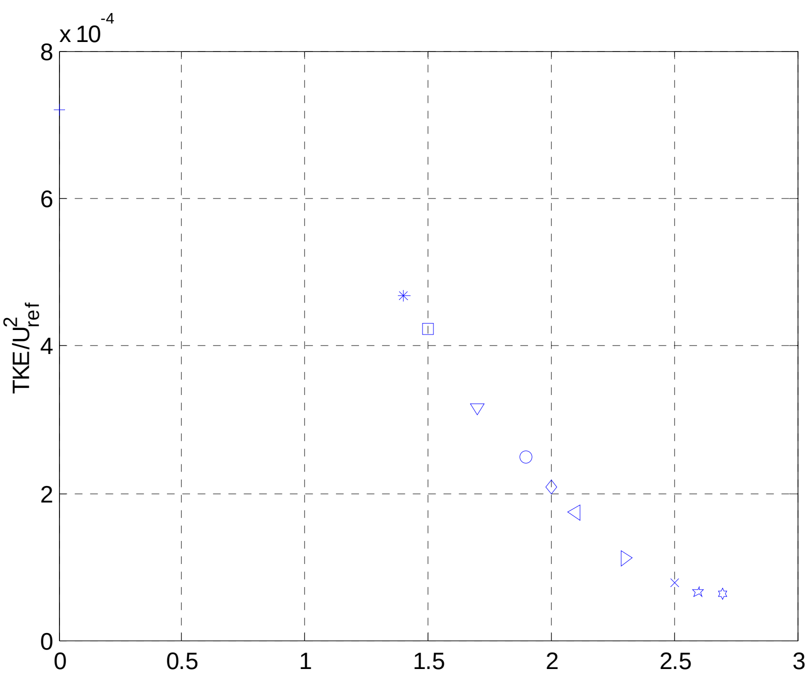

Figure 4-116: Kuethe vane pitchwise-averaged turbulent kinetic energy profile k/U_{ref}^2 at x/c_a = 1.819

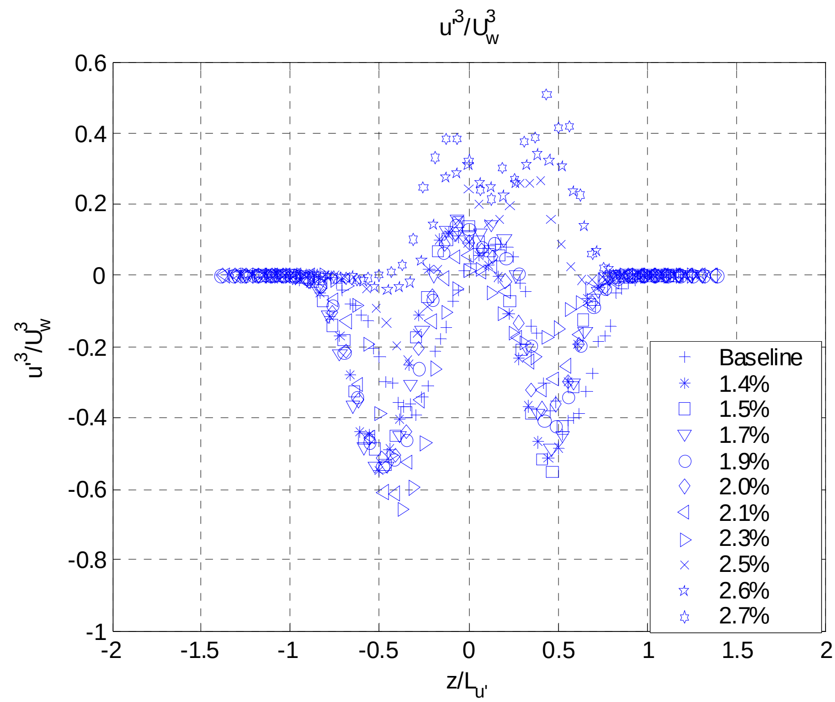

Figure 4-117: Simple blowing triple product profile u'^3/U_w^3 at x/c_a = 1.819

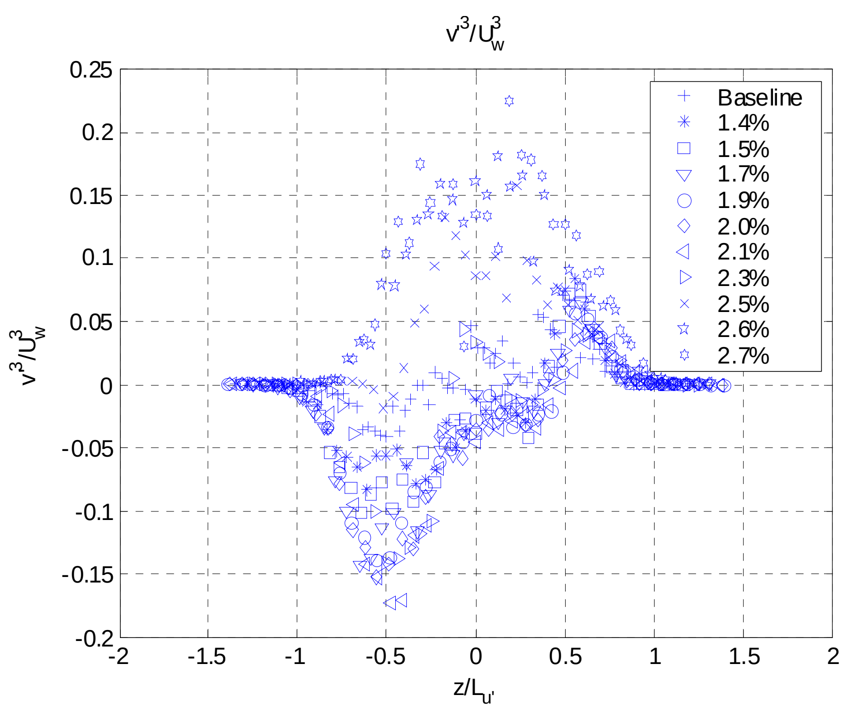

Figure 4-118: Simple blowing triple product profile v'^3/U_w^3 at x/c_a = 1.819

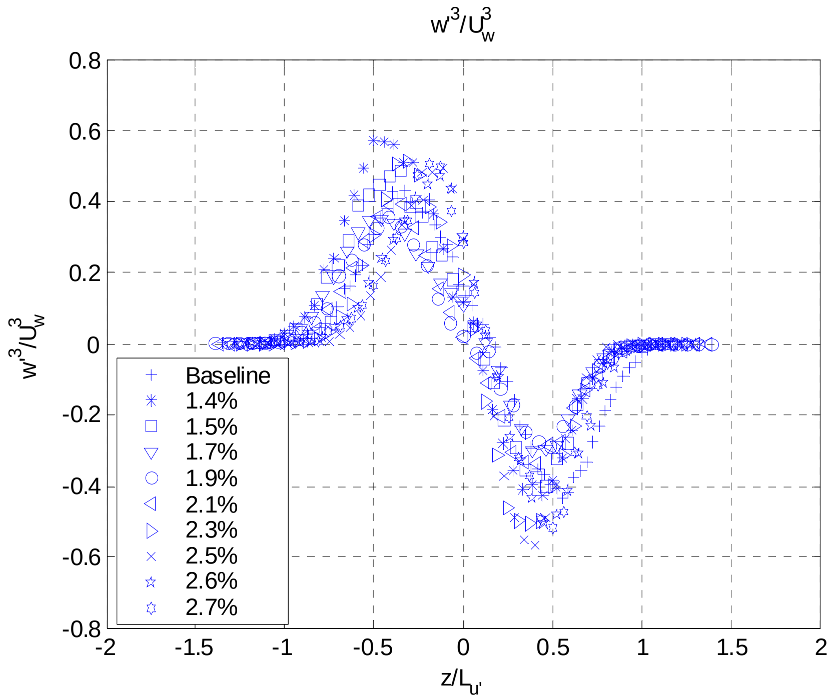

Figure 4-119: Simple blowing triple product profile w'^3/U_w^3 at $x/c_a = 1.819$

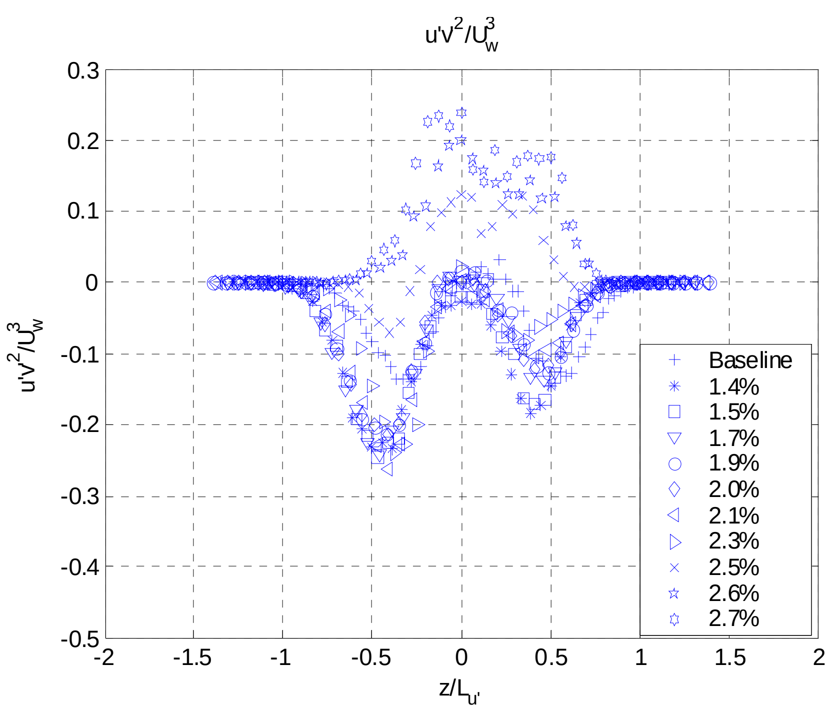

Figure 4-120: Simple blowing triple product profile $u'v'^2/U_w^3$ at $x/c_a = 1.819$

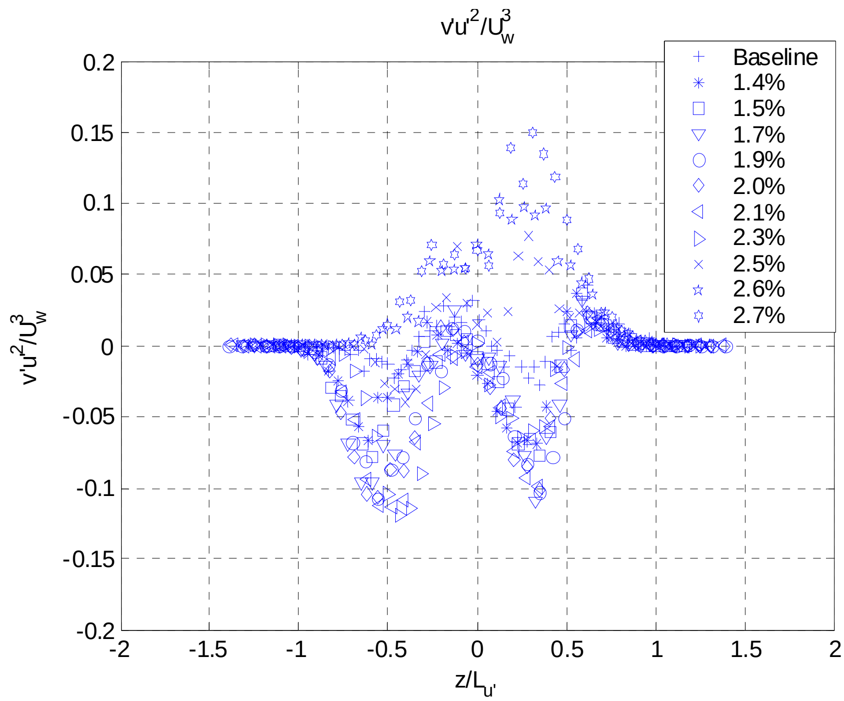

Figure 4-121: Simple blowing triple product profile $v'u'^2/U_w^3$ at x/c_a = 1.819

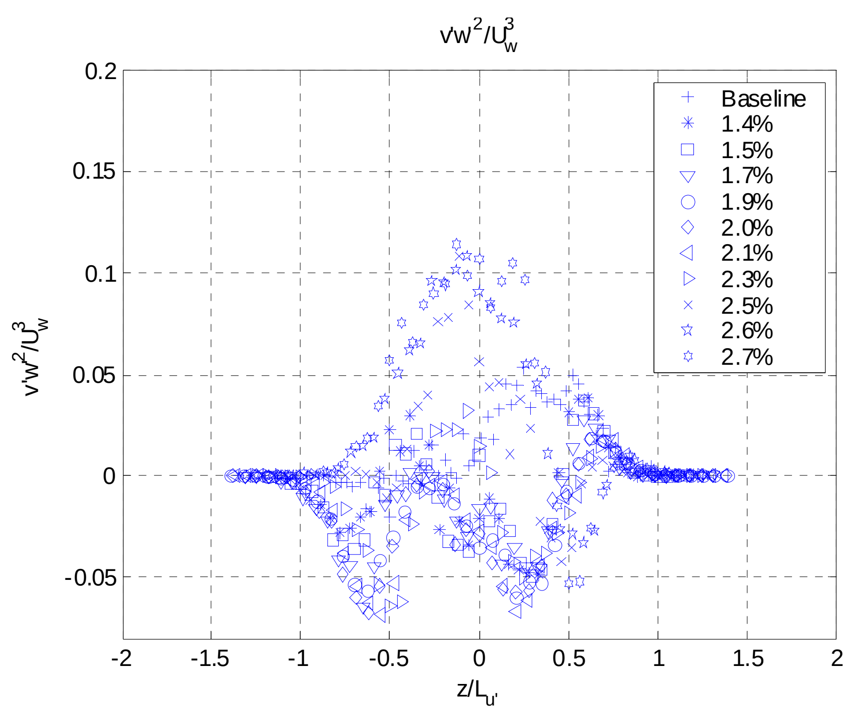

Figure 4-122: Simple blowing triple product profile $v'w'^2/U_w^3$ at x/c_a = 1.819

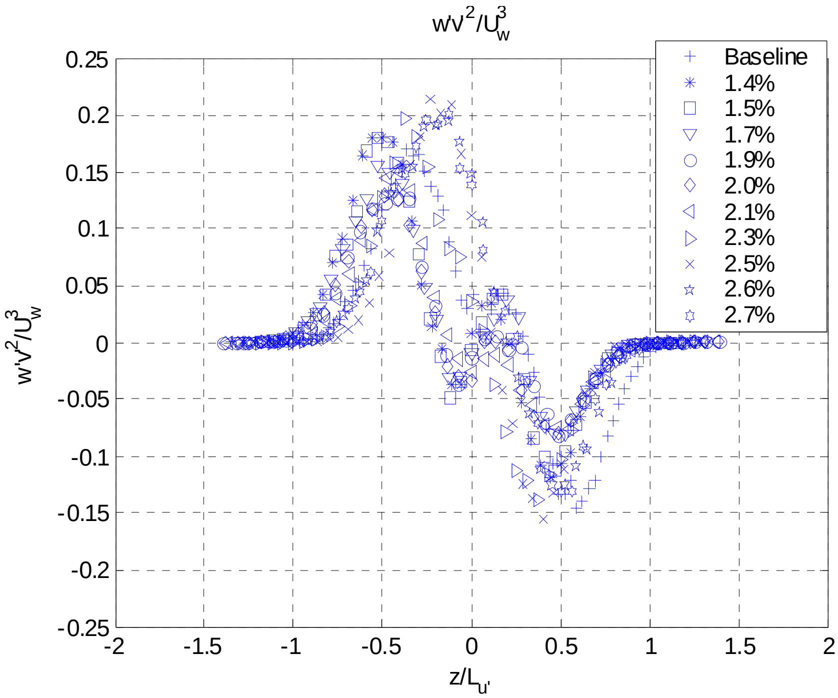

Figure 4-123: Simple blowing triple product profile $w'v'^2/U_w^3$ at x/c_a = 1.819

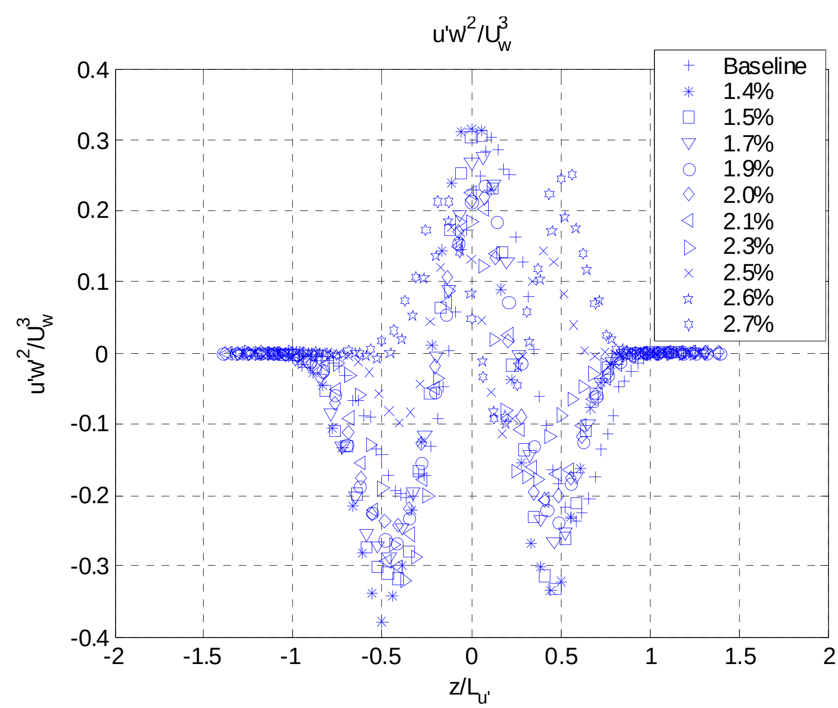

Figure 4-124: Simple blowing triple product profile $u'w'^2/U_w^3$ at x/c_a = 1.819

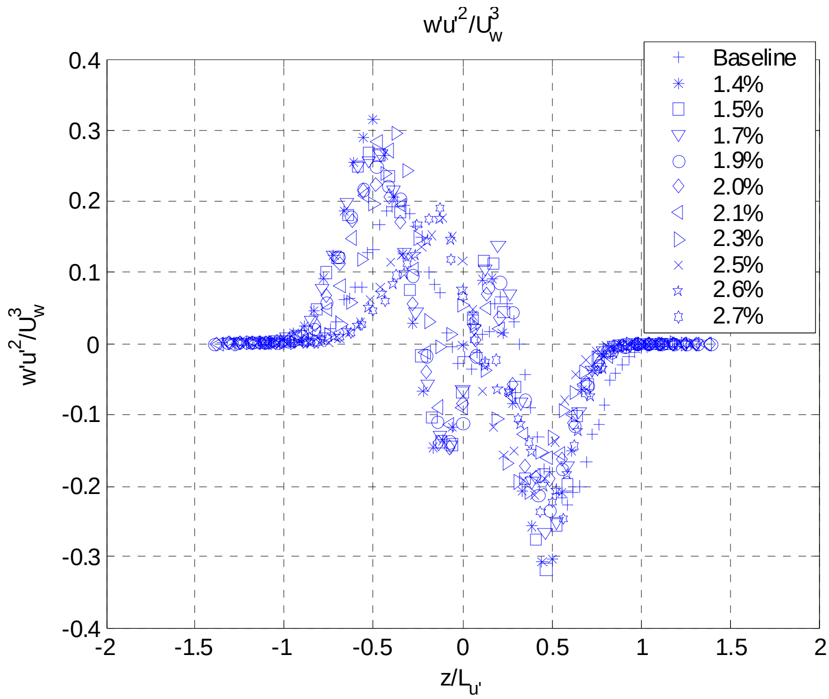

Figure 4-125: Simple blowing triple product profile $w'u'^2/U_w^3$ at x/c_a = 1.819

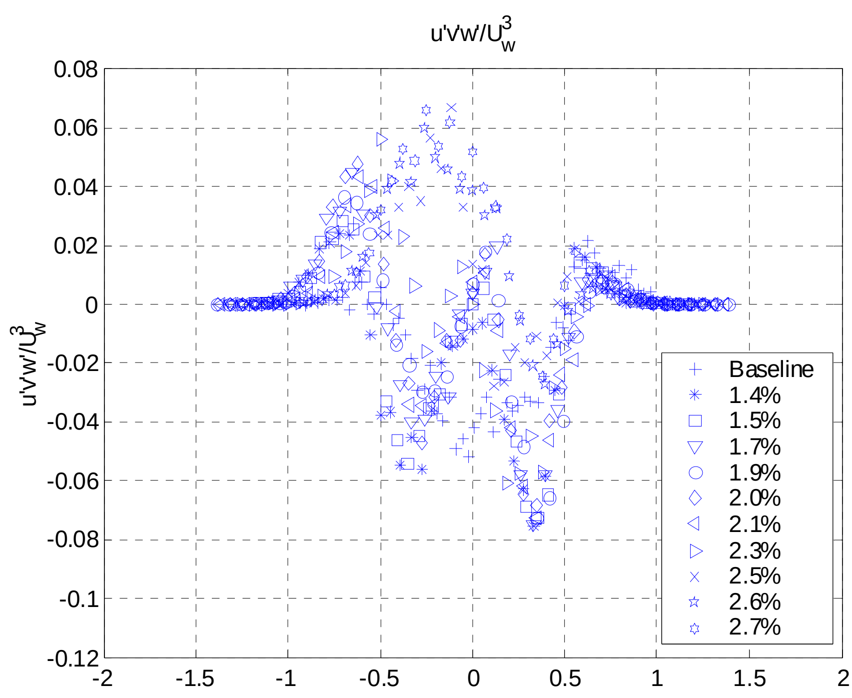

Figure 4-126: Simple blowing triple product profile $u'v'w'/U_w^3$ at x/c_a = 1.819

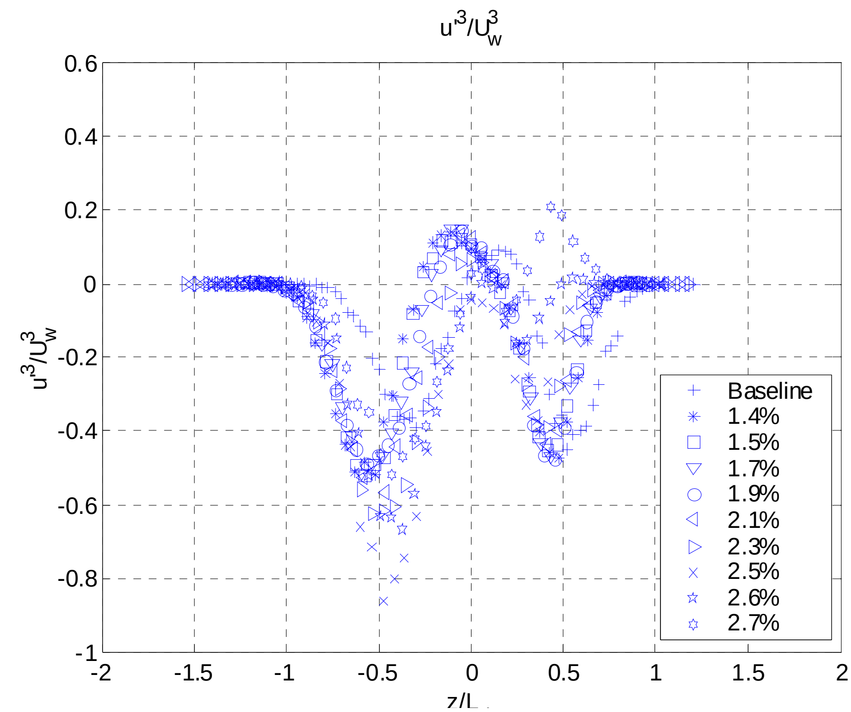

Figure 4-127: Kuethe vane triple product profile u'^3/U_w^3 at $x/c_a = 1.819$

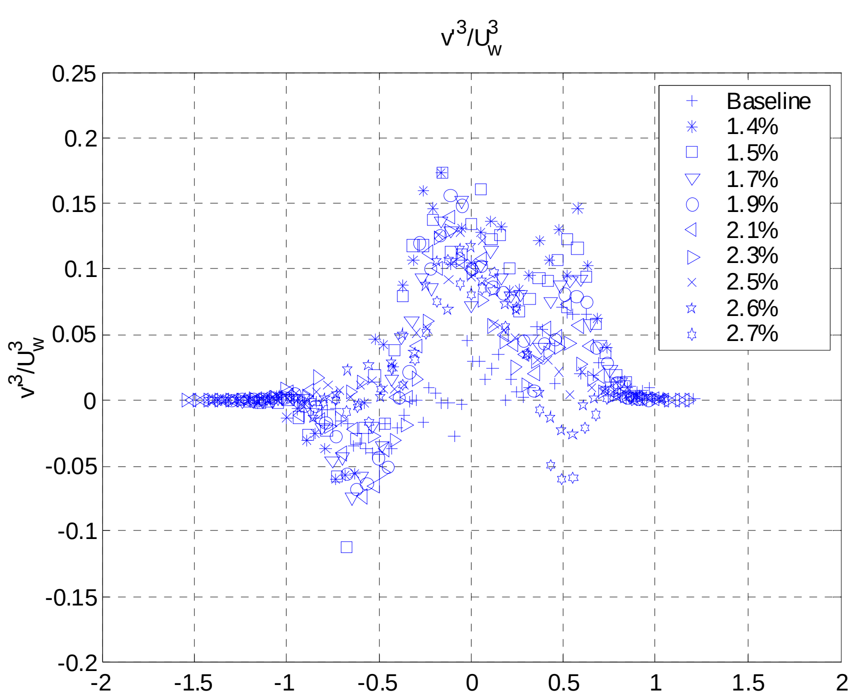

Figure 4-128: Kuethe vane triple product profile v'^3/U_w^3 at $x/c_a = 1.819$

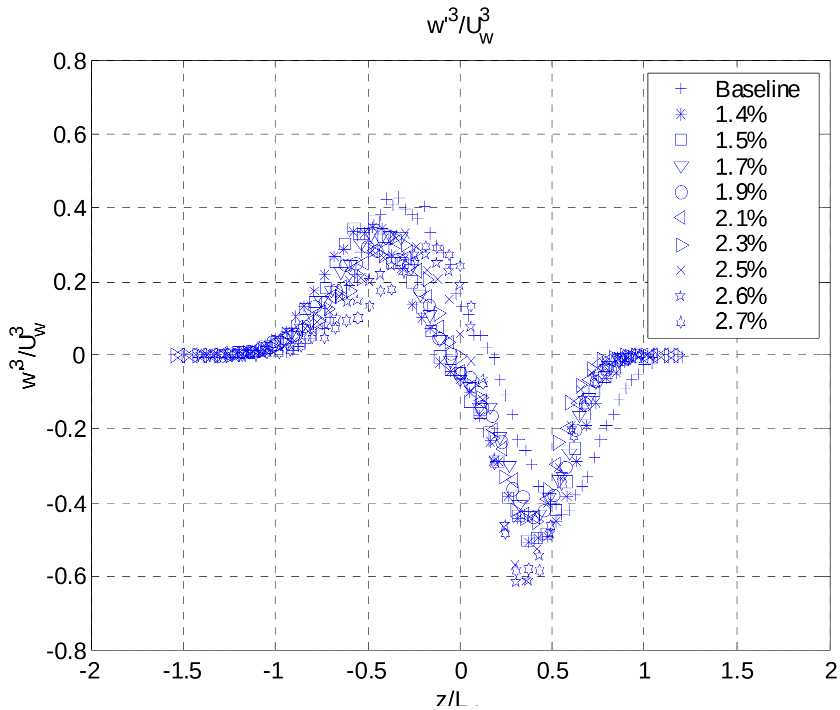

Figure 4-129: Kuethe vane triple product profile $w'^3/U_w{}^3$ at x/c_a = 1.819

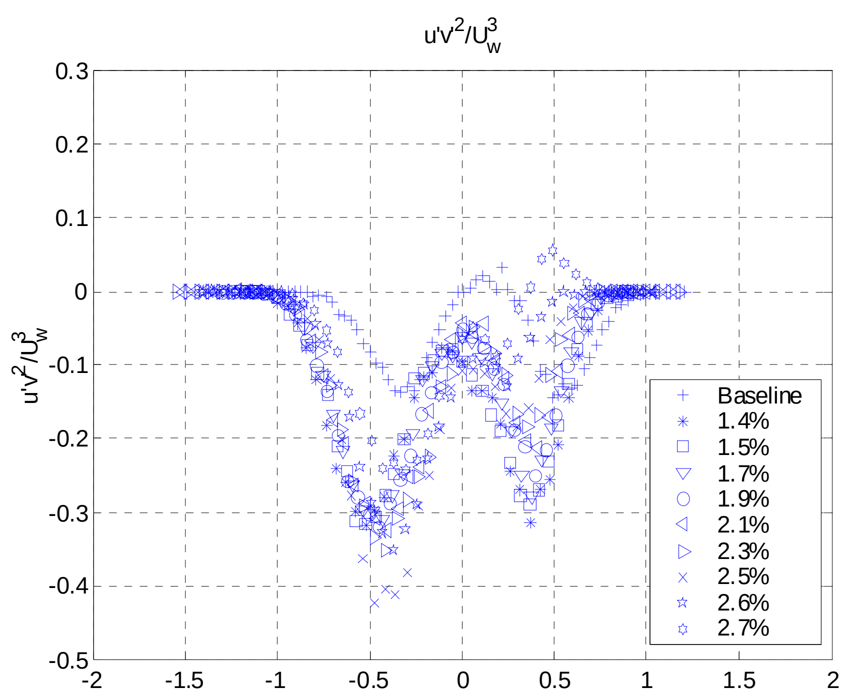

Figure 4-130: Kuethe vane triple product profile $u'v'^2/U_w{}^3$ at x/c_a = 1.819

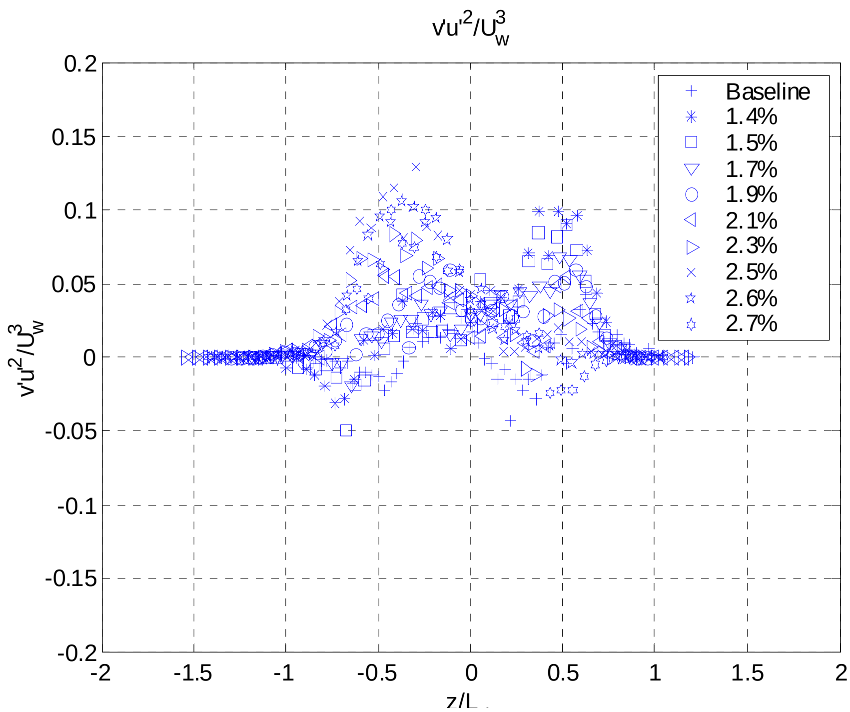

Figure 4-131: Kuethe vane triple product profile $v'u'^2/U_w^3$ at x/c_a = 1.819

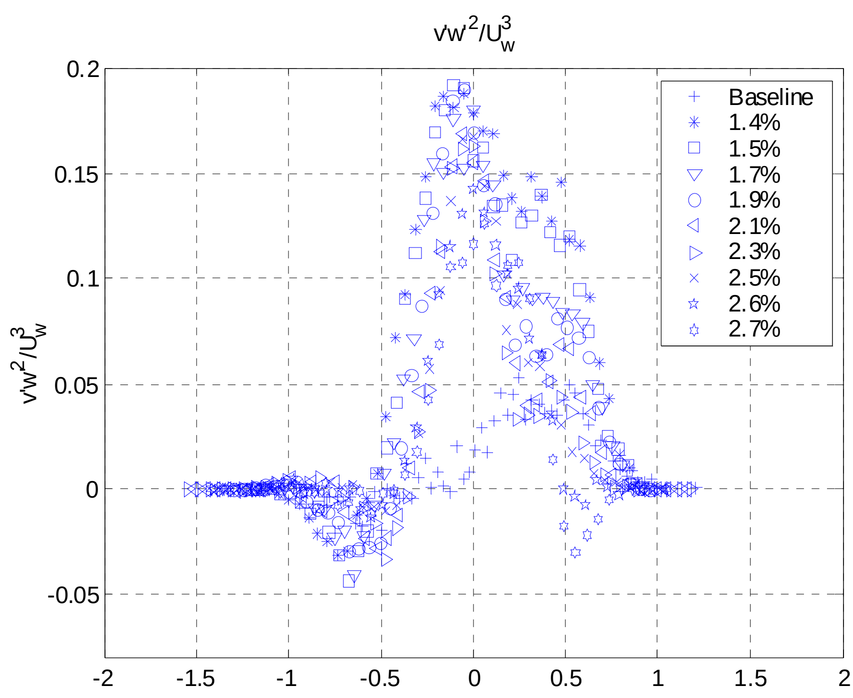

Figure 4-132: Kuethe vane triple product profile $v'w'^2/U_w^3$ at x/c_a = 1.819

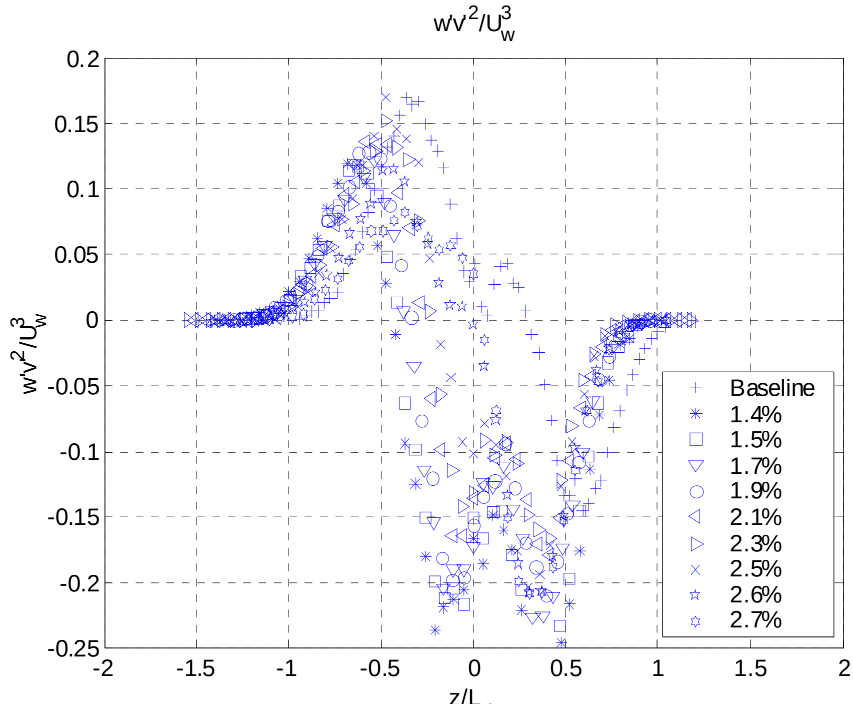

Figure 4-133: Kuethe vane triple product profile $w'v'^2/U_w^3$ at x/c_a = 1.819

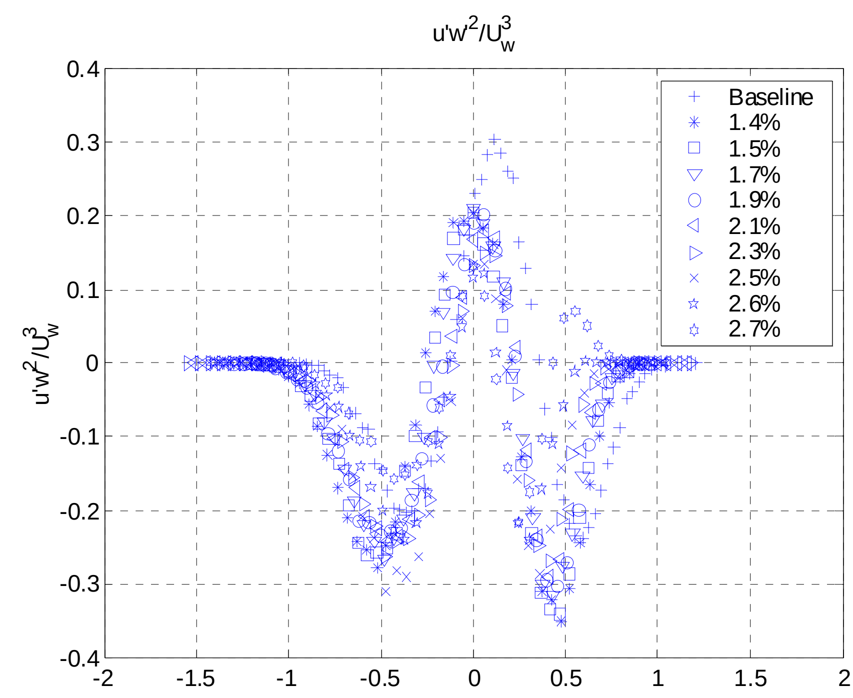

Figure 4-134: Kuethe vane triple product profile $u'w'^2/U_w^3$ at x/c_a = 1.819

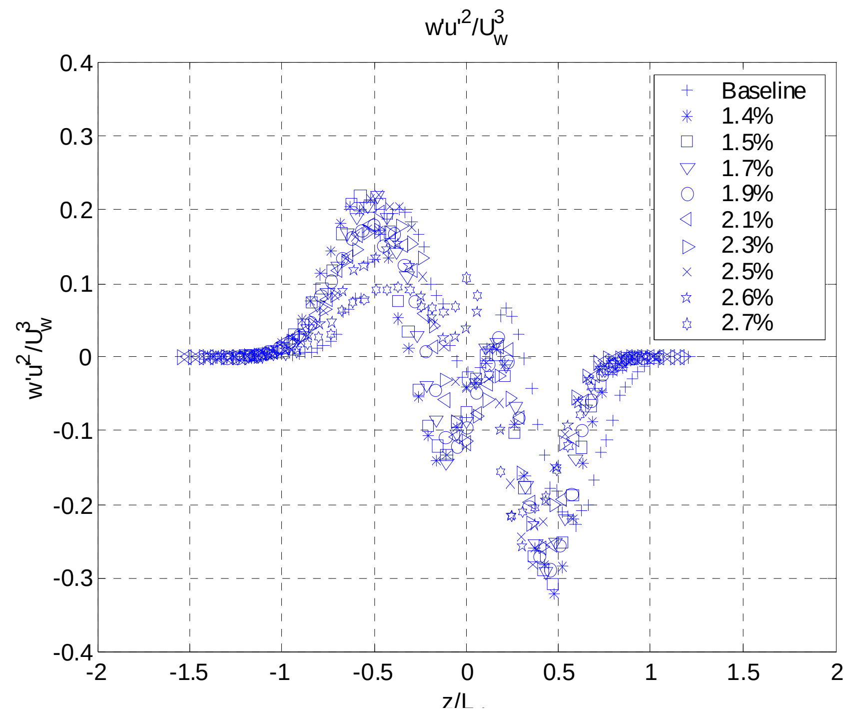

Figure 4-135: Kuethe vane triple product profile $w'u'^2/U_w^3$ at $x/c_a = 1.819$

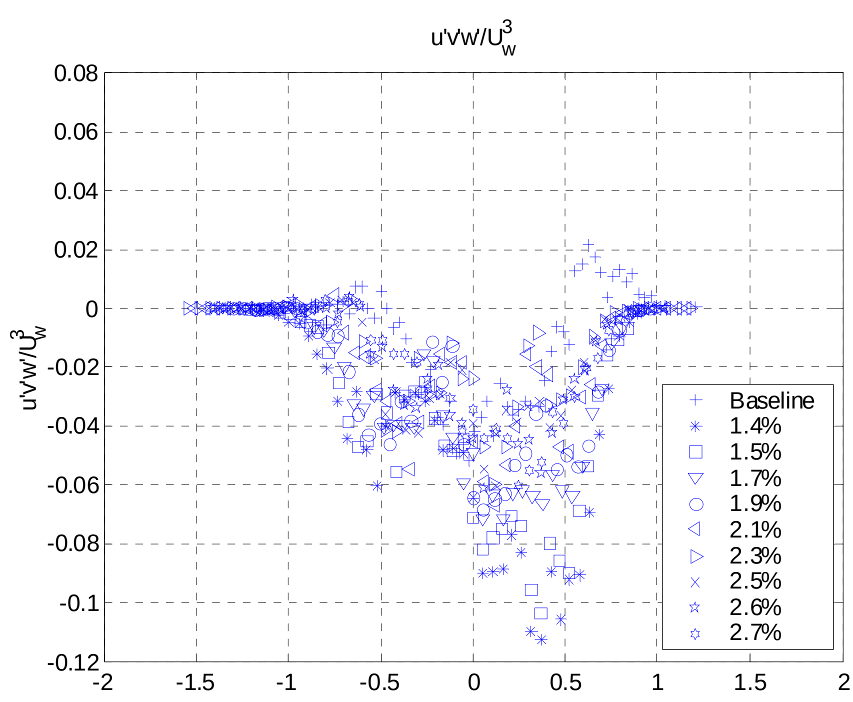

Figure 4-136: Kuethe vane triple product profile $u'v'w'/U_w^3$ at $x/c_a = 1.819$

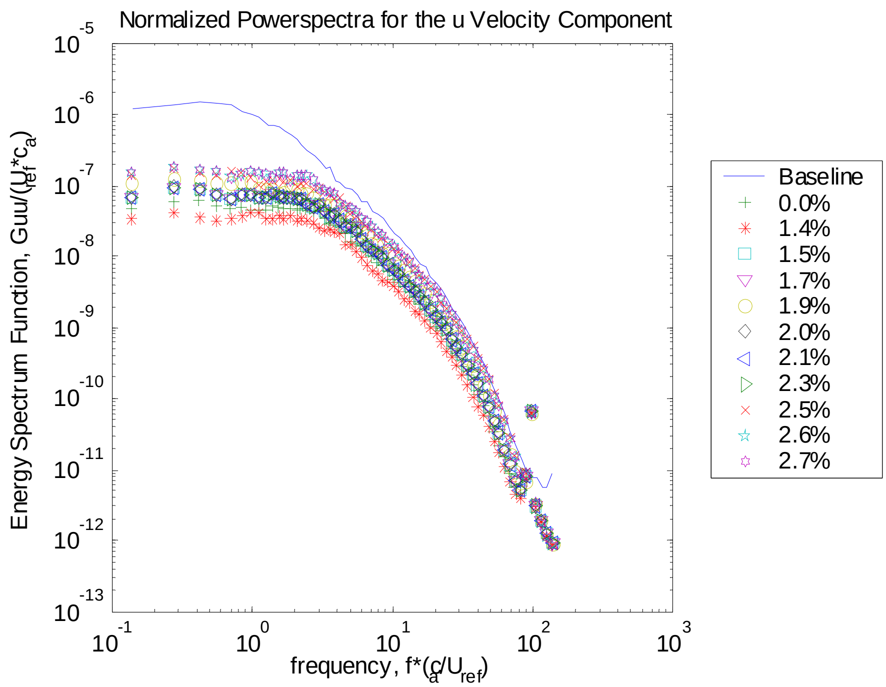

Figure 4-137: Simple blowing streamwise spectra at x/c_a = 1.819, at point of maximum streamwise turbulence

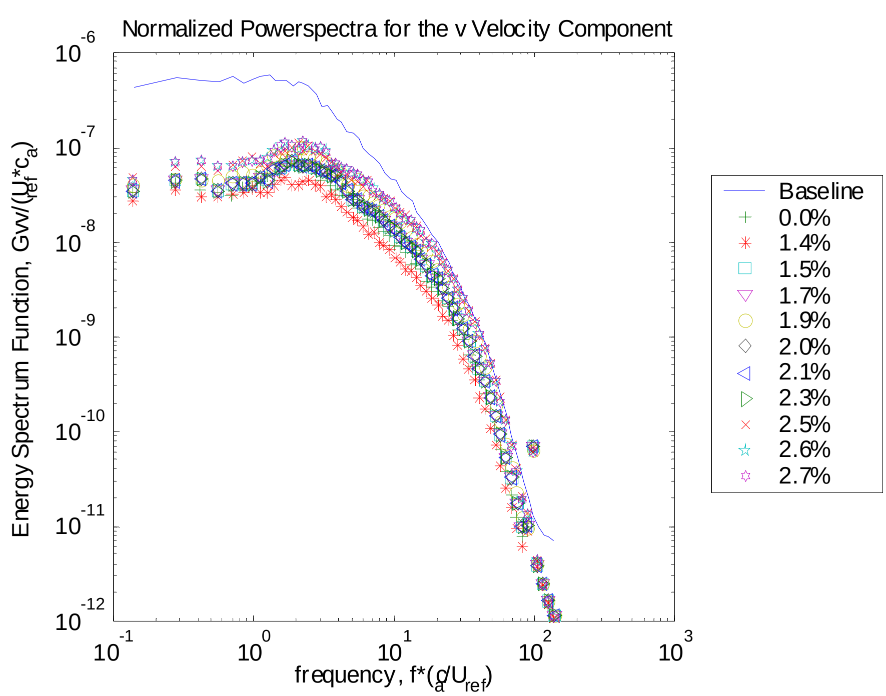

Figure 4-138: Simple blowing spanwise spectra at x/c_a = 1.819, at point of maximum streamwise turbulence

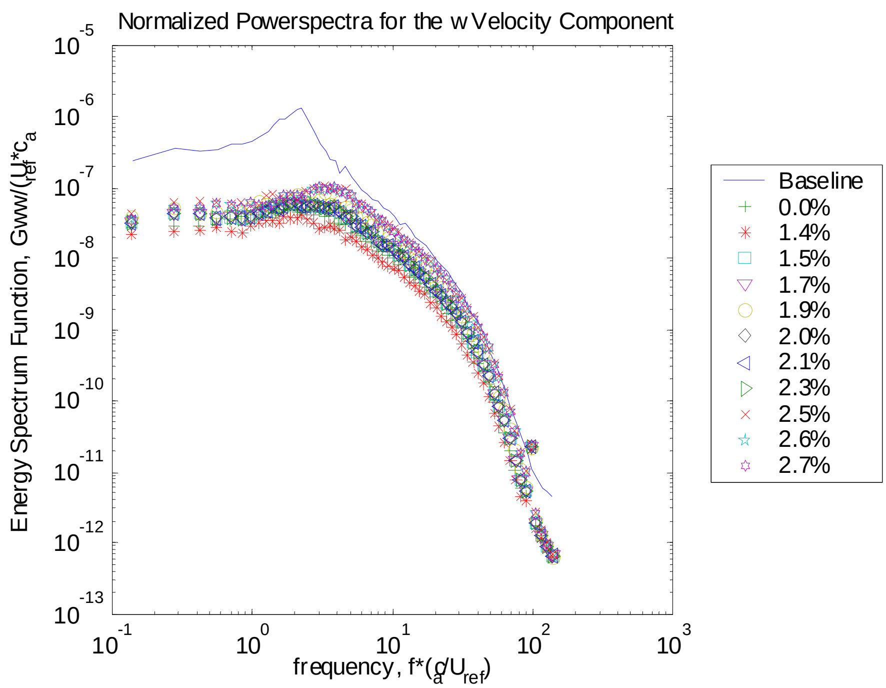

Figure 4-139: Simple blowing cross-wake spectra at x/c_a = 1.819, at point of maximum streamwise turbulence

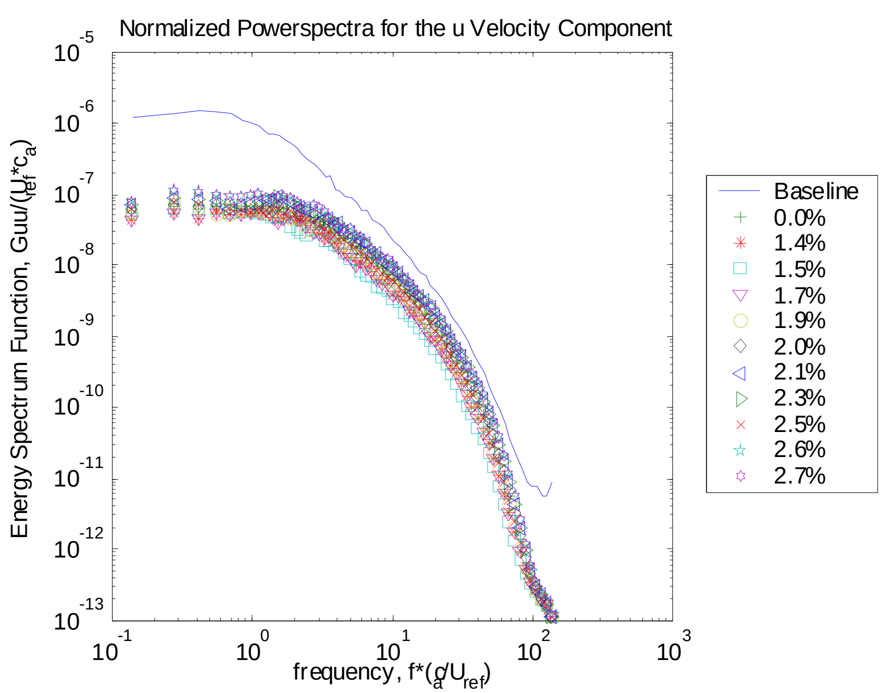

Figure 4-140: Kuethe vane streamwise spectra at x/c_a = 1.819, at point of maximum streamwise turbulence

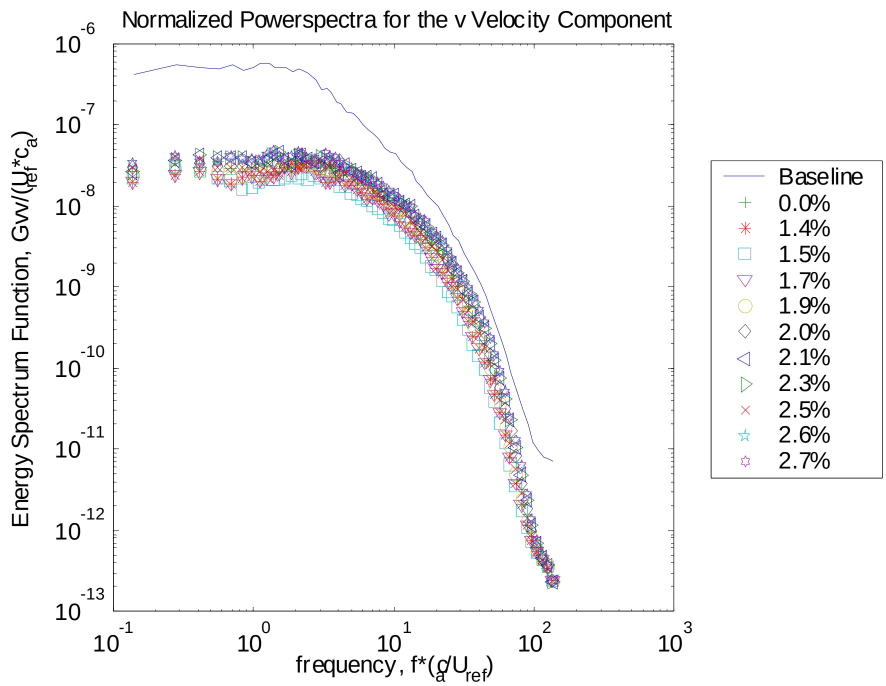

Figure 4-141: Kuethe vane spanwise spectra at x/c_a = 1.819, at point of maximum streamwise turbulence

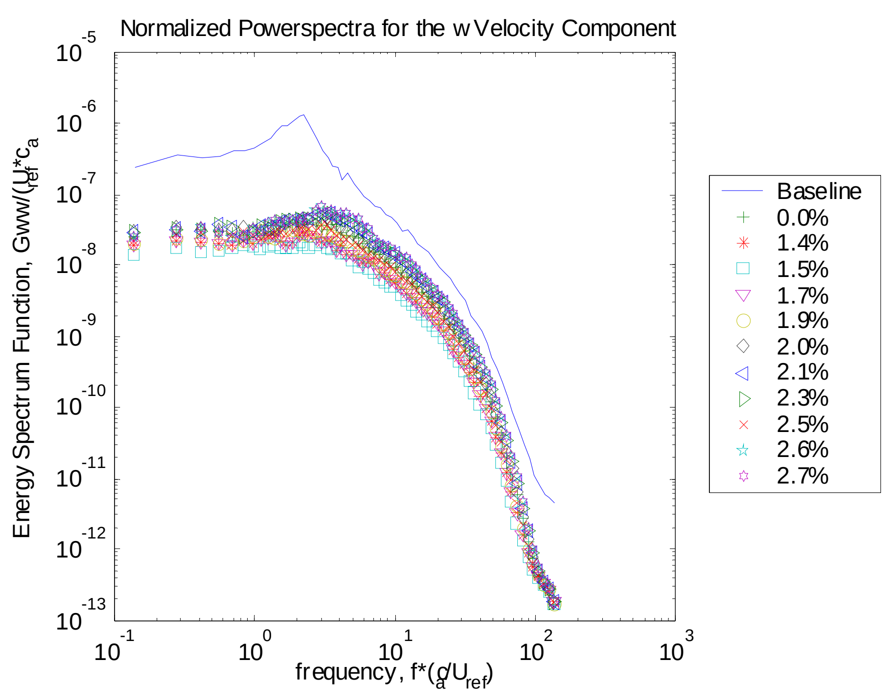

Figure 4-142: Kuethe vane cross-wake spectra at x/c_a = 1.819, at point of maximum streamwise turbulence

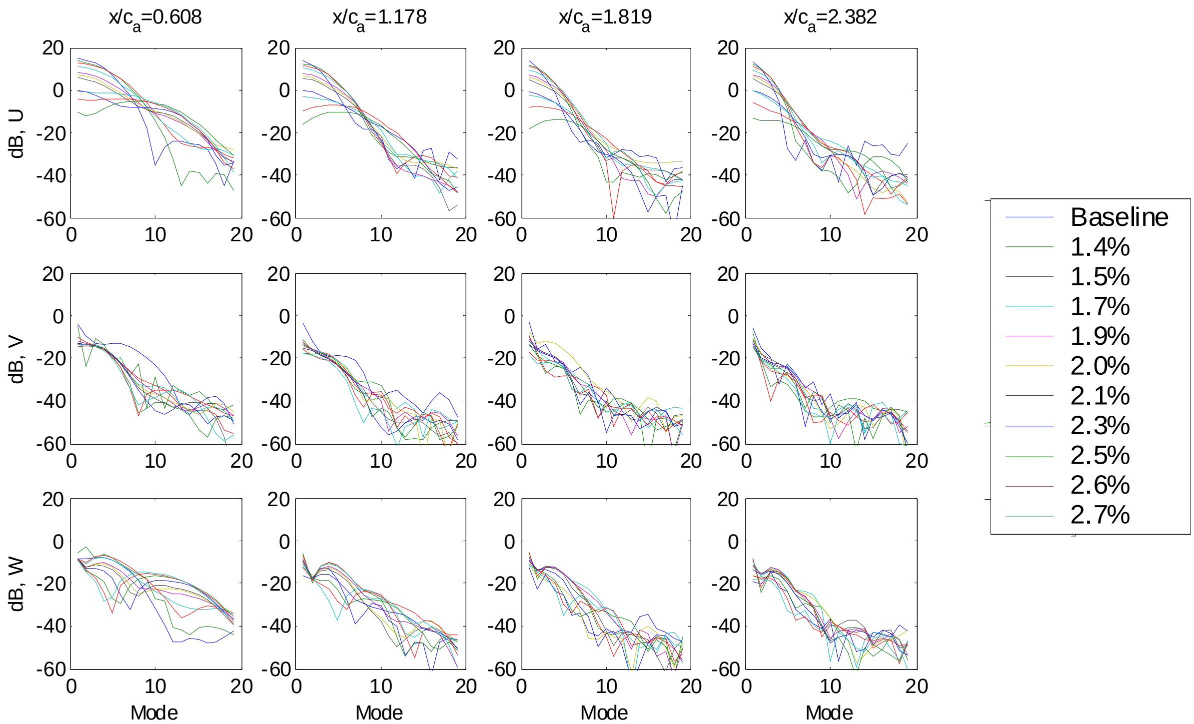

Figure 4-143: Non-blowing baseline and simple blowing three-component spectral levels at x/c_a = 0.608, 1.178, 1.819 and 2.382

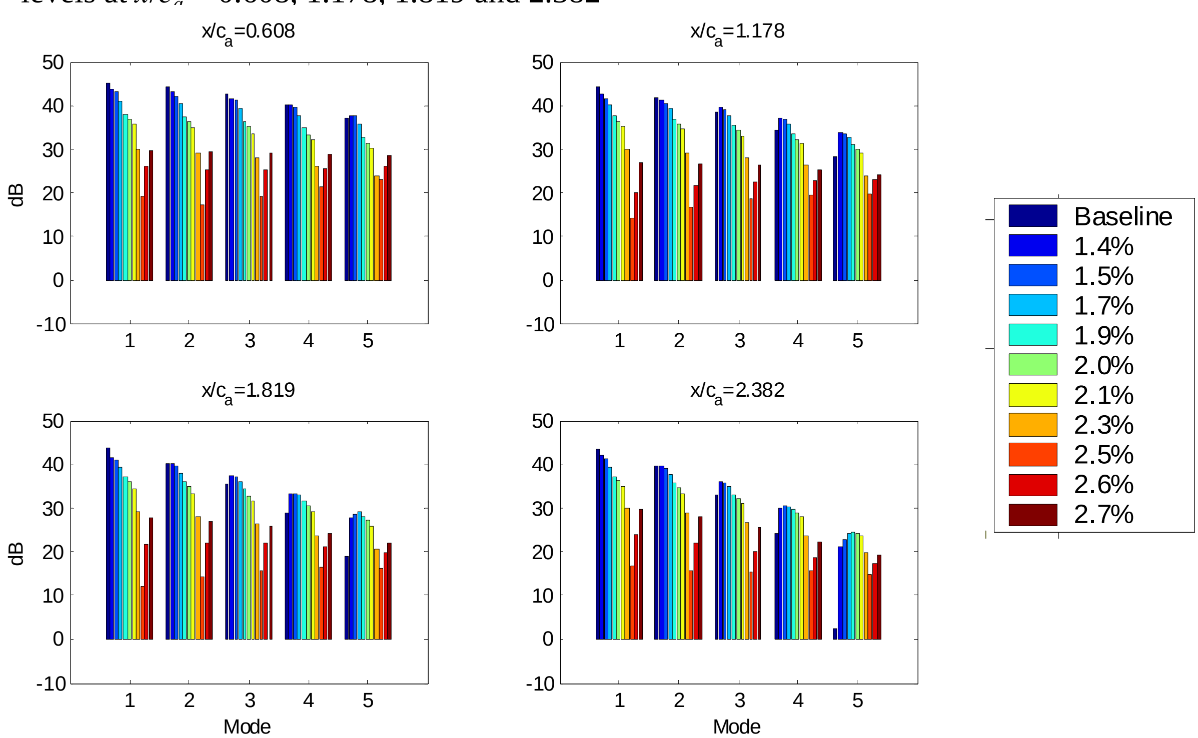

Figure 4-144: Non-blowing baseline and simple blowing streamwise spectral levels for the first five modes at x/c_a = 0.608, 1.178, 1.819 and 2.382

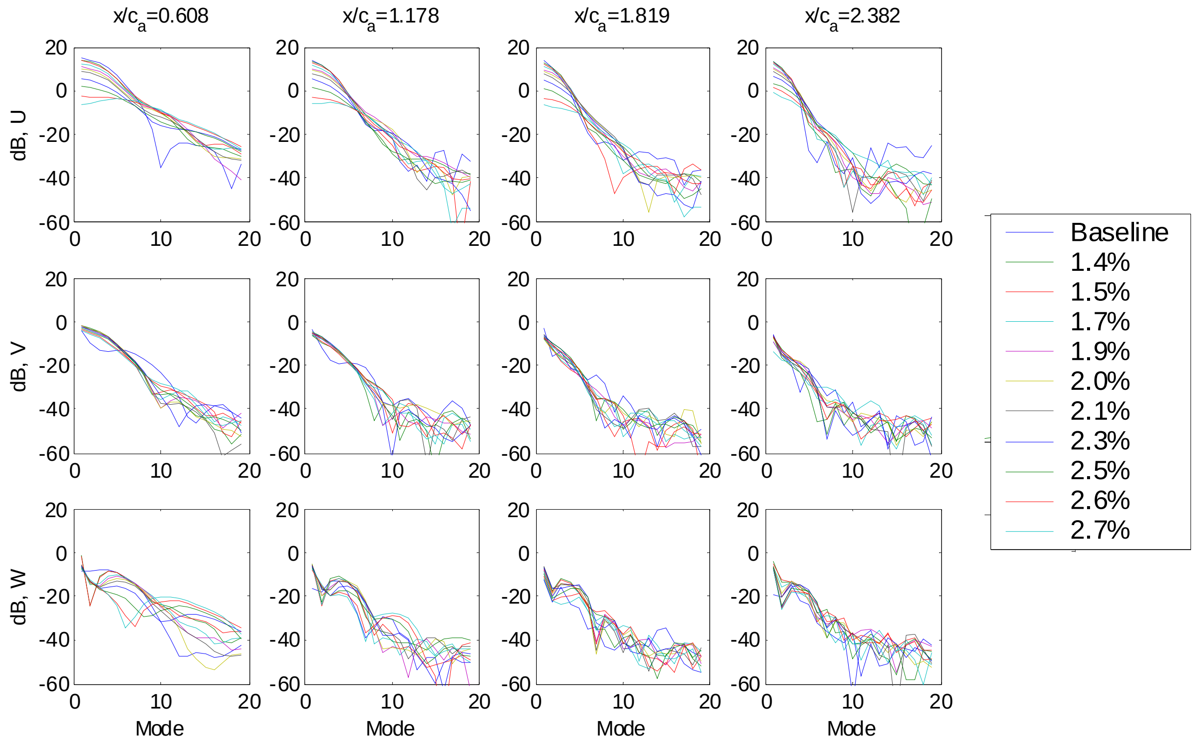

Figure 4-145: Non-blowing baseline and Kuethe vane three-component spectral levels at x/c_a = 0.608, 1.178, 1.819 and 2.382

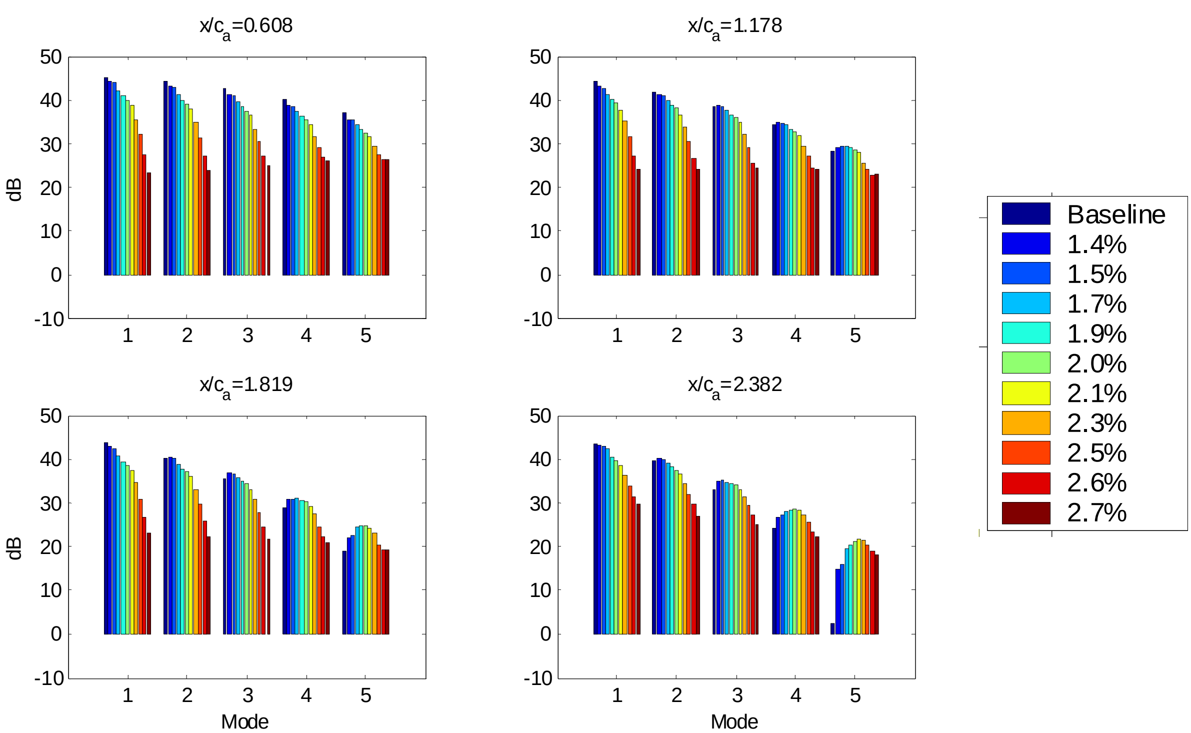

Figure 4-146: Non-blowing baseline and Kuethe vane streamwise spectral levels for the first five modes at x/c_a = 0.608, 1.178, 1.819 and 2.382

5. CONCLUSION

The dominant noise source in high-bypass ratio engines is the unsteady loading on the stators due to the wakes of the upstream rotors. The component of this loading that is periodic on the blade passing frequency is called tone noise. The purpose of this study was to investigate the wake management technique of trailing-edge blowing for the reduction of tone noise. Despite the number of previous studies on this subject, a sufficient basis for the development of CFD codes does not exist to properly model the flow. That basis was developed here for blown wakes with realistic rotor blade geometries through the testing of two sets of blowing blades in the Virginia Tech low-speed linear cascade tunnel. The cascade provides a practical arrangement for this testing, since there are no rotational forces with a stationary reference frame, and because there are no stators, the blade exit angle does not have to be matched to the stator inlet angle. The blowing blades (simple blowing and Kuethe vane) were designed to replicate the loading of the baseline GE Rotor B blades, which simulate the loading and flow generated by a subsonic high-bypass ratio aircraft engine at takeoff conditions. The original tunnel configuration and baseline flow were presented, specifically the blade loading, Pitot-static cross-sections at 0.839 and 1.877 axial chords downstream, and multiple mid-span profiles at streamwise locations of 0.608, 1.178, 1.819 and 2.382. Then the modified tunnel configuration and trailing-edge blowing flows were described and compared to the baseline flow.

5.1. Conclusions Regarding the Simple Blowing Blades

Measurements made on the simple blowing blades include blade loading with static pressure ports, blowing slot uniformity and normal-to-span cross-sections at mid-span with a single-sensor hot-wire, oil flow visualizations, Pitot-static full cross-sections at two downstream locations and mid-span profiles at four downstream locations with a four-sensor hot-wire. These measurements indicated the following:

a) The blade loading diverges from the baseline at the trailing-edge on the suction side for all blowing rates. The 1.4% case is the most similar to the baseline, while the 0% case is the least representative, despite eliminating the trailing-edge bluntness due to the blowing slot by covering the trailing-edge with tape.

b) Blowing slot uniformity measurements show a spanwise set of regions of higher velocity corresponding to the locations of the blade internal passages. The blowing becomes more spanwise uniform as blowing rate is increased.

c) The blown wakes are angled towards the pressure side of the blade, as compared to the wake with passive suction. The normal-to-span cross-sections also reveal that wake filling begins at 2.3% and the wake is largely overblown by 2.7%.

d) The wake with 1.4% blowing is noticeably deeper than the wake of the baseline in the Pitot-static full cross-sections. As blowing is increased to 2.0%, the tip region experiences some overblowing, and by 2.6% nearly the entire wake is overblown.

e) Results of the mid-span velocity profiles confirm that the wake deficit at 1.4% is larger than that of the baseline. The wake deficit decreases with increasing blowing rate between 1.5% and 2.3%. Optimum blowing appears to occur at 2.5%, with both wake-like and jet-like components. The wakes at 2.6% and 2.7% are clearly overblown.

f) The normalized displacement thicknesses and momentum thicknesses do not vary with streamwise location. For a given location, both the displacement thicknesses and momentum thicknesses at all blowing rates are lower than those of the baseline.

g) For a given location, the wake half-widths at all blowing rates are lower than those of the baseline. At x/c_a = 0.608 and 1.178, the wake half-widths decrease with increasing blowing rate. At x/c_a = 1.819 and 2.382, the wake spreading effect dominates and the wake half-widths begin to increase above roughly 2.0%.

h) Reynolds normal stresses and turbulent kinetic energy are at least 25% lower than the baseline at all blowing rates between 1.4% and 2.7%.

i) Spectral measurements show energy reductions for all blowing rates at normalized frequencies below $2*10^1$.

j) Fourier decomposition suggests tone noise benefits over the baseline at all tested blowing rates. At the blade passing frequency, the maximum attenuation of 33dB was achieved at x/c_a = 1.819 for a blowing rate of 2.5%.

5.2. Conclusions Regarding the Kuethe Vane Blades

The same sets of measurements made on the simple blowing blades were made on the Kuethe vane blades. Normal-to-span cross-sections were taken at two additional spanwise locations. The effects of the Kuethe vanes are:

a) Blade loadings at all blowing rates significantly differ from the baseline at the trailing-edge on both the suction and pressure sides. The 0% case is the most similar to the baseline here.

b) Spanwise regions of higher velocity associated with the blade internal passages are visible. An additional spanwise pattern due to the presence of the vortex generators is visible at the slot exit. Blowing becomes more spanwise uniform with increasing blowing rate.

c) The blown wakes are angled towards the pressure side of the blade. At a given blowing rate, the wake at the blade mid-span (which is also at a generator mid-span) has a slightly smaller deficit than at the other measured spanwise locations.

d) Pitot-static full cross sections indicate that the wake at 1.4% may be deeper than the baseline wake. The deficit decreases by 2.0%, and partial overblowing in select spanwise locations is evident at 2.6%.

e) The wake deficit at 1.4% is nearly the same as the baseline deficit. As blowing rate is increased, the deficit decreases. By 2.7%, only the extreme pressure side of the wake has been canceled, indicating that the optimum blowing rate has not yet been achieved.

f) The normalized displacement thicknesses and momentum thicknesses do not vary with streamwise location. For a given location, both the displacement thicknesses and momentum thicknesses at all blowing rates are lower than those of the baseline.

g) For a given location, the wake half-widths at all blowing rates are lower than those of the baseline. At all four axial locations, the wake half-widths decrease with increasing blowing rate, although by a smaller margin at x/c_a = 2.382. The blowing is still more effective than wake spreading this far downstream.

h) Reynolds normal stresses and turbulent kinetic energy are lower than the baseline at all blowing rates between 1.4% and 2.7%.

i) Spectral measurements show energy reductions for all blowing rates over the entire range of normalized frequencies.

j) Fourier decomposition suggests tone noise benefits over the baseline at all tested blowing rates. At the blade passing frequency, the maximum attenuation of 23dB was achieved at x/c_a = 0.608 at a blowing rate of 2.7%.

APPENDIX -- UNCERTAINTY ANALYSIS

Uncertainties for 20:1 odds for the pressure measurements and the single-component and three-component hot-wire measurements were calculated based on the methods of Kline and McClintock (1953).

Velocity Uncertainty Analysis

Uncertainty in hot-wire measurements depends on A/D conversion error and uncertainties in the velocity calibration and freestream velocity. The A/D converter can be represented by the following equation:

$$e_i = M_i i_i + c_i$$

where the subscript *i* denotes the i-th sensor and:

$$e_i = output$$
$$M_i = slope$$
$$i_i = input$$
$$c_i = offset$$

For each sensor, there is an A/D conversion random error $\delta_c(e_i)$, an A/D offset bias error $\delta(c_i)$, and an A/D slope bias error $\delta(M_i)$. The two bias errors can be included with the velocity calibration, leaving only the rms random error $\delta_c(e_i)$. According to specifications for the Agilent 1432, this is $45\mu V_{RMS}$.

An angle calibration was performed after a sensor replacement, as well as a velocity calibration based on King's law prior to each use. Errors associated with these processes include random A/D converter error $\delta_c(e_i)$, calibration curve error $\delta(U_i)$ and calibration curve slope error $\delta(\partial U_i/\partial e_i)$ for both mean and fluctuating velocity components.

Single-component hot-wire uncertainty estimates

Quantity	Uncertainty
$\delta(U)/U_{ref}$	1%
$\delta(u'^2)/U_{ref}{}^2$	3%

Three-component hot-wire uncertainty estimates

Quantity	Uncertainty
$\delta(U)/U_{ref}$	1%
$\delta(V)/U_{ref}, \delta(W)/U_{ref}$	2%
$\delta(u'^2)/U_{ref}{}^2$	3%
$\delta(v'^2)/U_{ref}{}^2, \delta(w'^2)/U_{ref}{}^2$	6%
$\delta(u'v')/U_{ref}{}^2, \delta(v'w')/U_{ref}{}^2, \delta(-u'w')/U_{ref}{}^2$	4%
$\delta(k)/k$	4%

For the above estimates, the uncertainty in the freestream velocity measured by the reference Pitot-static probe was taken as $\delta(U_{ref})$ = 0.00326m/s, according to Ma (2003).

Mean Pressure Uncertainty

The static pressure coefficient, C_p, is defined by the ratio $\frac{P - P_\infty}{P_{0\infty} - P_\infty}$ as explained in Section 3.3.1. Similar transducers were used to measure the quantities in the numerator and the denominator, leading to an assumption that $\delta(P - P_\infty) = \delta(P_{0\infty} - P_\infty)$. The uncertainty of C_p can then be calculated as follows:

$$\frac{\delta C_p}{C_p} = \delta(P - P_\infty)\sqrt{\frac{1}{(P - P_\infty)^2} + \frac{1}{(P_{0\infty} - P_\infty)^2}}$$

$$\delta(P - P_\infty) = \sqrt{\delta^2(P - P_\infty)\big|_{Rand}\ \delta^2(P - P_\infty)\big|_{Bias}}$$

The random component of the uncertainty was found to be 1.24Pa, which is half of the resolution of the digital manometer used. The bias component was found to be negligible, leading to a total uncertainty in the pressure coefficient of close to 1%.

BIBLIOGRAPHY

Ahn, W.J. and Sung, H.J., "Prediction of Two-Dimensional Momentumless Wake by k-ε-γ Model", AIAA Journal, Vol. 33, No. 4, 1995, pp. 611-617.

Brookfield, J.M., 1998, "Turbofan Stator/Rotor Interaction Noise Reduction Through Trailing Edge Blowing", PhD dissertation, Dept. of Aeronautics and Astronautics, Massachusetts Institute of Technology.

Brookfield, J.M. and Waitz, I.A., "Trailing-Edge Blowing for Reduction of Turbomachinery Fan Noise", Journal of Propulsion and Power, Vol. 16, No. 1, 2000, pp. 57-64.

Chevepanov, P.Y. and Babenko, V.A., "Experimental and Numerical Study of Flat Momentumless Wake", International Journal of Heat and Fluid Flow, 19, 1998, pp. 608-622.

Cimbala, J.M. and Park, W.J., "An Experimental Investigation of the Turbulent Structure in a 2-D Momentumless Wake", Journal of Fluid Mechanics, Vol. 213, 1990, pp. 479-509.

Corcoran, T.E., 1992, "Control of the Wake from a Simulated Blade by Trailing-Edge Blowing: A Study Using Particle Image Velocimetry", M.S. thesis, Dept. of Mechanical Engineering, Lehigh University.

de la Riva, D.H., 2001, "Turbulence Interaction in a Highly Staggered Cascade-Propulsor Configuration", MS thesis, Aerospace and Ocean Engineering Dept., Virginia Polytechnic Institute and State University. http://scholar.lib.vt.edu/theses/available/etd-04272001-172809/

de la Riva, D.H., Devenport, W.J., Muthanna, C. and Glegg, S.A.L., "Behavior of Turbulence Flowing Through a Compressor Cascade", AIAA Journal, Vol. 42, No. 7, 2004, pp. 1302-1313.

Devenport, W.J., Muthanna, C., Ma, R. and Glegg, S.A.L., 1999, "Measurement and Modeling of the Two-Point Correlation Tensor in a Plane Wake for Broadband Noise Prediction", Report to NASA Langley, Aerospace and Ocean Engineering Dept., Virginia Polytechnic Institute and State University.

Dmitrenko, Y.M., Kovalev, I.I., Luchko, N.N. and Cherenpanov, P.Y., "Plane Turbulent Wake with Zero Excess Momentum", Journal of Engineering Physics, Vol. 52, No. 5, 1987, pp. 536-542.

Envia, E., "Fan Noise Reduction: An Overview", 39th AIAA Aerospace Sciences Meeting and Exhibit, 8-11 January 2001, Reno, NV, AIAA 2001-0661.

Geiger, D.H., 2005, “Comparative Analysis of Serrated Trailing Edge Designs on Idealized Aircraft Engine Fan Blades for Noise Reduction”, Aerospace and Ocean Engineering Dept., Virginia Polytechnic Institute and State University. http://scholar.lib.vt.edu/theses/available/etd-01102005-202530/

Kline, S.J. and McClintock, F.A., “Describing uncertainties in single sample experiments”, Mechanical Engineering, vol. 75, 1953, pp. 3.

Krammer, P., Rued, K. and Truebenbach, J., “Technology Preparation for Green Aero Engines”, AIAA/ICAS International Air and Space Symposium and Exhibition: The Next 100 Years, 14-17 July 2003, Dayton, OH, AIAA 2003-2790.

Kuethe, A.M., “Effect of Streamwise Vortices on Wake Properties Associated with Sound Generation”, Journal of Aircraft, Vol. 9, No. 10, 1972, pp. 715-718.

Leitch, T.A., Sanders, C.A. and Ng, W.F., “Reduction of Unsteady Stator-Rotor Interaction Using Trailing Edge Blowing”, Journal of Sound and Vibration, Vol. 235, No. 2, 2000, pp. 235-245.

Ma, R., 2003, “Unsteady Turbulence Interaction in a Tip Leakage Flow Downstream of a Simulated Axial Compressor Rotor”, PhD dissertation, Aerospace and Ocean Engineering Dept., Virginia Polytechnic Institute and State University. http://scholar.lib.vt.edu/theses/available/etd-06172003-122153/

“Making Future Commercial Aircraft Quieter”, NASA – Quiet Aircraft Facts, FS-1999-07-003-GRC. http://www.nasa.gov/centers/glenn/about/fs03grc.html

Mish, P.F., 2003, “An Experimental Investigation of Unsteady Surface Pressure on Single and Multiple Airfoils”, PhD dissertation, Aerospace and Ocean Engineering Dept., Virginia Polytechnic Institute and State University. http://scholar.lib.vt.edu/theses/available/etd-03312003-173021/

Moore, J., Moore, J.G. and Liu, B., 1996, “CFD computation to aid noise research, progress report, 2/96-10/96”, Mechanical Engineering Dept., Virginia Polytechnic Institute and State University.

Muthanna, C., 1998, "Flowfield Downstream of a Compressor Cascade with Tip Leakage", MS thesis, Aerospace and Ocean Engineering Dept., Virginia Polytechnic Institute and State University. http://scholar.lib.vt.edu/theses/available/etd-110798-235327/

Muthanna, C., 2002, “The Effects of Free Stream Turbulence on the Flow Field through a Compressor Cascade”, PhD dissertation, Aerospace and Ocean Engineering Dept., Virginia Polytechnic Institute and State University. http://scholar.lib.vt.edu/theses/available/etd-08222002-194441/

Muthanna, C., “Effects of Free Stream Turbulence on the Viscous Flow Field of a Compressor Cascade”, 37th AIAA/ASME/SAE/ASEE Joint Propulsion Conference and Exhibit, 8-11 July 2001, Salt Lake City, Utah, AIAA 2001-3210.

Muthanna, C., Wittmer, K.S. and Devenport, W.J., “Turbulence Structure of the Flow Downstream of a Compressor Cascade with Tip Leakage”, 36th AIAA Aerospace Sciences Meeting, 12-15 January 1998, Reno, Nevada, AIAA 98-0420.

Naumann, R.G., 1992, “Control of the Wake from a Simulated Blade by Trailing-Edge Blowing”, MS thesis, Dept. of Mechanical Engineering, Lehigh University.

Park, W.J. and Cimbala, J.M., “The Effect of Jet Injection Geometry on 2-D Momentumless Wakes”, Journal of Fluid Mechanics, Vol. 224, 1991, pp. 29-47.

Pope S. B., 2001, “Turbulent Flows”, Cambridge University Press, New York.

Rao, N.M., Feng, J., Burdisso, R.A. and Ng, W.F., “Experimental Demonstration of Active Flow Control to Reduce Stator-Rotor Interaction”, AIAA Journal, Vol. 39, No. 3, 2001, pp. 458-464.

Schetz, J.A., 1993, “Boundary Layer Analysis”, Prentice Hall, New Jersey.

Sell, J., 1997, “Cascade Testing to Assess the Effectiveness of Mass Addition/Removal Wake Management Strategies for Reduction of Rotor-Stator Interaction Noise”, MS thesis, Dept. of Aeronautics and Astronautics, Massachusetts Institute of Technology.

Staubs, J.K., 2005, “Correlation between Unsteady Loading and Tip Gap Flow Occurring in a Linear Cascade with Simulated Rotor-Stator Interaction”, Aerospace and Ocean Engineering Dept., Virginia Polytechnic Institute and State University. http://scholar.lib.vt.edu/theses/available/etd-06092005-125521/

“StreamLine Research CTA System – For High-Precision CTA Measurements”, Dantec Dynamics. http://www.dantecmt.com/CTA/System/system/

Sutliff, D.L., Tweedt, D.L., Fite, E.B. and Envia, E., “Low-Speed Fan Noise Reduction with Trailing Edge Blowing”, 8th AIAA/CEAS Aeroacoustic Conference Exhibit, 17-19 June 2002, Breckenridge, Colorado, AIAA 2002-2992.

Takami, H. and Maekawa, H., “Experimental Investigation of Turbulent Structures in a Two-Dimensional Momentumless Wake”, JSME International Journal, B63, No. 608, 1997, pp. 1145-1153.

Thomas, C.S., Hume, K.I. and Hooper, P.D., "Aircraft Noise, Airport Growth, and Regional Development", 10th AIAA/CEAS Aeroacoustics Conference, 10-12 May 2004, Manchester, United Kingdom, AIAA 2004-2806.

Wang, Y., 2000, "Tip Leakage Flow Downstream of a Compressor Cascade with Moving Endwall", MS thesis, Aerospace and Ocean Engineering Dept., Virginia Polytechnic Institute and State University http://scholar.lib.vt.edu/theses/available/etd-04052000-14200057/

Wang, Y. and Devenport, W.J., "Wake of a Compressor Cascade with Tip Gap, Part 2: Effects of Endwall Motion", AIAA Journal, Vol. 42, No. 11, 2004, pp. 2332-2340.

Wenger, C., 1999, "Analysis of Two-point Turbulence Measurements for Aeroacoustics", MS thesis, Aerospace and Ocean Engineering Dept., Virginia Polytechnic Institute and State University. http://scholar.lib.vt.edu/theses/available/etd-010699-132153/

Wenger, C., Devenport, W.J., Wittmer, K.S. and Muthanna, C., "Two-point Measurements in the Wake of a Compressor Cascade", 29th AIAA Fluid Dynamics Conference, 15-18 June 1998, Albuquerque, NM, AIAA 1998-2556.

Wisler, D.C., 1977, "Core Compressor Exit Stage Study, Volume I – Blading Design", NASA CR-135391.

Wisler, D.C., 1981, "Core Compressor Exit Stage Study, Volume IV – Data and Performance Report for the Best Stage Configuration", NASA CR-165357.

Wittmer K.S., Devenport W.J., Zsoldos J.S. and Follin, G.J., "A Four-sensor Hot-wire Probe System for Three-component Velocity Measurements", Experiments in Fluids, Vol. 24, 1998, pp. 416-423.

Wo, A.M., Lo. A.C. and Chang. W.C., "Flow Control via Rotor Trailing Edge Blowing in Rotor/Stator Axial Compressor", Journal of Propulsion and Power, Vol. 18, No. 1, 2002, pp. 93-99.